Doctoral Dissertation
博士論文

Observational Studies of Photonuclear Reactions Triggered by Lightning Discharges
(雷放電による光核反応の観測的研究)

A Dissertation Submitted for the Degree of Doctor of Philosophy

December 2019

令和元年 12 月 博士 (理学) 申請

Department of Physics, Graduate School of Science,
The University of Tokyo
東京大学大学院理学系研究科
物理学専攻

Yuuki Wada
和田 有希

Abstract

Lightning and thunderstorms are closely associated with high-energy phenomena in the atmosphere. Terrestrial gamma-ray flashes (TGFs) are powerful and instant emissions coincident with lightning discharges, serendipitously discovered and now routinely detected by in-orbit satellites. In addition to space-borne observations, on-ground experiments have also detected high-energy phenomena in thunderstorms. We have performed the Gamma-Ray Observation of Winter thunderclouds experiment during winter thunderstorms in Japan since 2006. During more than 10 years of its operation, minute-lasting gamma-ray glows and sub-second-lasting short bursts have been detected. While the former was found to be bremsstrahlung photons from electrons accelerated in thunderclouds, the origin of short bursts was, however, unresolved due to insufficient observations with a single detector.

In 2016, we developed brand-new compact gamma-ray detectors, and constructed a gamma-ray monitoring network with 10 detectors along the coast of the Sea of Japan. On February 6th, 2017, four detectors installed in Kashiwazaki successfully recorded a short burst lasting for $\sim$200 ms. Immediately after the short burst, two of them also recorded the annihilation line lasting for $\sim$1 minute. Based on the observation, we demonstrated that a downward TGF, an analogous phenomenon to TGFs but beamed downward, took place coincident with a lightning discharge, triggered photonuclear reactions such as $^{14}\mathrm{N}(\gamma, n)^{13}\mathrm{N}$ in the atmosphere, and proton-rich nuclei produced by the reactions emitted positrons via β^{+}-decay. During 2016-2017 and 2017-2018 winter seasons, in total 5 short bursts were detected, and all events originated from photonuclear reactions in lightning. Therefore, short bursts are evidence of atmospheric photonuclear reactions triggered by downward TGFs.

We then considered all the major photonuclear channels in the atmosphere, and performed Monte-Carlo simulations of photonuclear reactions and propagation of electrons, gamma rays, neutrons, and positrons in the atmosphere. The simulations were utilized to construct models of on-ground doses by downward TGFs, spectra of de-excitation gamma rays by neutron captures, and gamma-ray spectra of positron annihilation to quantitatively evaluate photonuclear reactions and downward TGFs. The models successfully reproduced our measurements of three short-burst events detected in Kashiwazaki. Furthermore, the positions of downward TGFs were estimated with an accuracy of $<$500 m, and their source altitudes to be 1.4–2.7 km. In a single downward TGF, 10^{18}–10^{19} energetic electrons were estimated to be produced, and then 10^{13}–10^{14} neutrons by photonuclear reactions. Since the number of energetic electrons is the same order of magnitude as those of upward TGFs observed from space, the downward TGFs in the present study are suggested to be intrinsically the same phenomena as upward TGFs.

Contents

Chapter 1

Introduction

Recent observational and theoretical studies have made us convinced that lightning and thunder-storms work as particle accelerators in nature. In 1991, the Burst And Transient Source Experiment (BATSE) detector onboard the Compton Gamma-Ray Observatory (CGRO) serendipitously detected millisecond-lasting gamma-ray bursts coming from the Earth's atmosphere [Fishman et al., 1994]. This phenomenon, later named "terrestrial gamma-ray flash" (TGF), contains gamma-ray photons with energy of >20 MeV, lasts for hundreds of microseconds to several milliseconds, and coincides with lightning discharges [Briggs et al., 2011, Mailyan et al., 2016, Marisaldi et al., 2010, Smith et al., 2005, Tavani et al., 2011]. Since the gamma-ray spectra of TGFs are consistent with bremsstrahlung radiation from energetic electrons going upward into the space, it is suggested that lightning discharges can accelerate electrons up to tens of MeV. More recently, a similar phenomenon but beamed downward, called "downward TGF", has been discovered by ground-based observations [Abbasi et al., 2018, Dwyer et al., 2004, 2003, Hare et al., 2016, Tran et al., 2015]. These findings have been establishing a new academic field called "high-energy atmospheric physics".
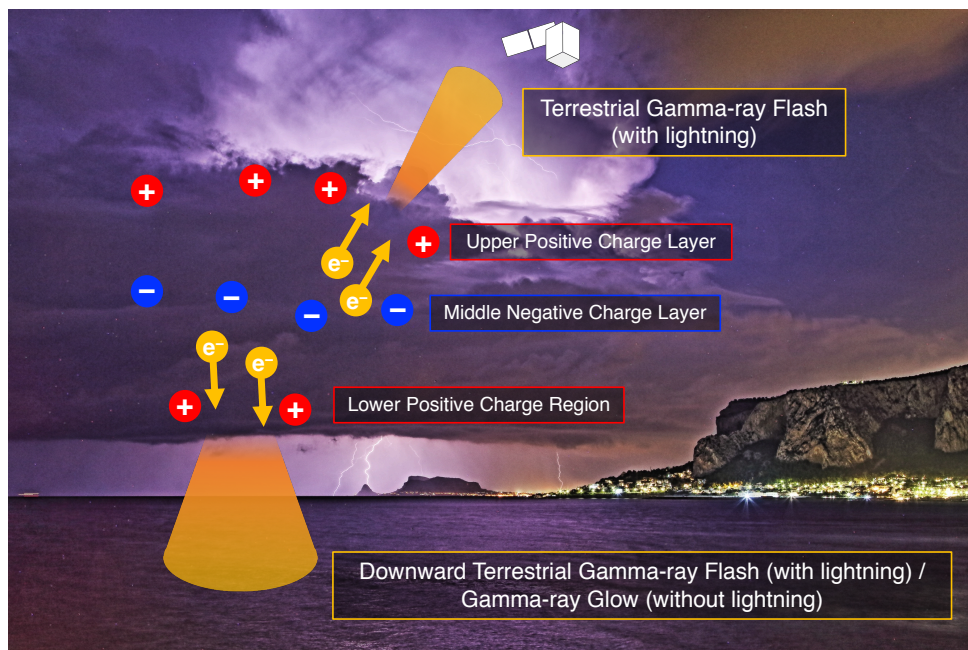

Figure 1.1: A schematic diagram of high-energy phenomena in thunderstorms.[1]

As proven by Benjamin Franklin in 1752, lightning and thunderstorm activities are electric phenomena. Figure 1.1 shows a schematic diagram of thunderstorms and related high-energy phenomena. There are several charged layers inside thunderclouds, and highly electrified regions can exist between two opposite charge layers. The strength of electric fields sometimes reaches 0.3–0.4 MV m^{-1} (Gurevich et al. [1992]; converted to an equivalent value at sea level). Wilson [1925] suggested that electrons can be accelerated to relativistic energies in such highly electrified regions by a process called "runaway electron". In the dense atmosphere, electrons usually lose their energy via collisional ionization and radiative processes. If the Coulomb force of electric fields exceeds the drag force, electrons are accelerated by overcoming the energy-loss processes. The total drag force to electrons is shown in Figure 1.2. The force gets minimum, 0.216 MeV m^{-1}, at 1.0 MeV in the atmosphere at sea level. When an electric-field strength of 0.4 MeV m^{-1}, a plausible value in thunderclouds [Gurevich et al., 1992], is assumed, the Coulomb force of electric fields exceeds the drag force at kinetic energies of electrons from 0.13 to 40 MeV. This indicates that electrons with initial energies of >0.13 MeV can be accelerated up to 40 MeV in the strong electric fields if the electric fields hold enough length for the acceleration. Gurevich et al. [1992] introduced multiplication processes of electrons into this theory, by considering acceleration of secondary electrons produced by ionization. The entire process of the electron acceleration and multiplication in the atmosphere, called "relativistic runaway electron avalanche" (RREA), is now widely accepted as the basic mechanism to produce energetic electrons in thunderstorms.
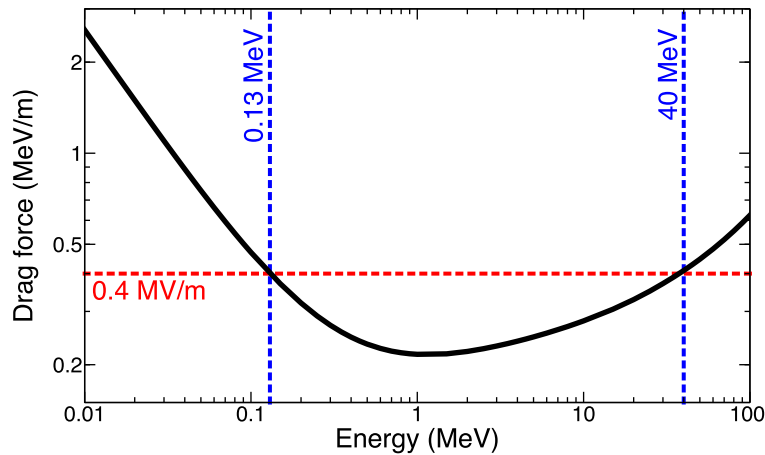
Figure 1.2: The drag force to electrons by ionization and radiation processes in the standard atmosphere at 1 atm, as a function of kinetic energies of electrons. Data are retrieved from NIST/EStar.[2]

This mechanism to accelerate electrons in the atmosphere has been revealed to take place both in instantaneous electric fields of lightning discharges and quasi-stable fields inside thunderclouds. The former case corresponds to TGFs. Energetic electrons produced by e.g. cosmic rays are thought to be accelerated and multiplied by electric fields in a time scale of less than hundreds of milliseconds. However, the estimated number of electrons produced by a single TGF cannot be explained by the RREA process with seed electrons of cosmic-ray origin; much more seed electrons are needed to produce the gamma-ray fluxes of TGFs detected by satellites [Dwyer, 2008]. While several models have been proposed (e.g. Celestin and Pasko [2011],

---

[1]Photo in Sicily by the author. EOS 6D + EF24-105mm F4L IS USM, 35 mm, 30 sec, F8.0, ISO400.

[2]https://physics.nist.gov/PhysRefData/Star/Text/ESTAR.html

Dwyer [2003]), the mechanism and condition of TGF production remain a big mystery in high-energy atmospheric physics.

The latter is associated with another high-energy phenomenon called "gamma-ray glow", also referred to as "long burst", or "thunderstorm ground enhancement" when detected at ground level. It is a gamma-ray enhancement originating from electron acceleration inside thunderclouds lasting for tens of seconds to several minutes, or sometimes tens of minutes [Chilingarian et al., 2010, McCarthy and Parks, 1985, Torii et al., 2002]. It has been observed by both airborne and ground experiments.

Based on these initial findings, we started the Gamma-Ray Observation of Winter Thunder-clouds (GROWTH) experiment in 2006 to observe gamma-ray glows during winter thunderstorms in coastal areas of the Sea of Japan. While winter thunderstorms are quite rare phenomena, they allow us to observe high-energy phenomena at sea level because winter thunderclouds develop at a lower altitude than summer ones, and hence high-energy photons reach the ground more easily. During observations over more than 10 years, we succeeded in detecting gamma-ray glows when thunderclouds were passing above our detectors. We revealed from their energy spectra that gamma-ray glows originate from bremsstrahlung of energetic electrons accelerated up to >10 MeV inside thunderclouds [Tsuchiya et al., 2007, 2011].

Besides gamma-ray glows, another phenomenon called "short burst" has been detected by the GROWTH experiment [Umemoto et al., 2016]. Short bursts are gamma-ray bursts coinciding with lightning discharges and lasting for hundreds of milliseconds. While it is obvious that they are distinguished from TGFs due to their longer duration, their origin remained a mystery.

At the same time, a possibility of atmospheric photonuclear reactions in lightning and thunderstorms such as

$$^{14}\text{N} + \gamma \rightarrow {}^{13}\text{N} + n \tag{1.1}$$

has been discussed because TGFs and gamma-ray glows contain photons of >10 MeV, high enough to trigger this reaction [Babich, 2006, 2007, Carlson et al., 2010]. The reaction emits a fast neutron and a proton-rich radioactive nucleus ^{13}N. Since ^{13}N decays with a half-life of 10 minutes and emits a positron, the annihilation line at 0.511 MeV should be detected. In fact, detections of neutrons [Bowers et al., 2017, Chilingarian et al., 2010, Gurevich et al., 2012, Shah et al., 1985] and positrons [Dwyer et al., 2015, Umemoto et al., 2016] have been reported, and they have thought to originate from photonuclear reactions in the atmosphere. However, such separated detections of neutrons and positrons cannot rule out possibilities of neutron productions by nuclear fusions or positron productions by pair creations. Therefore, a simultaneous detection of neutrons and positrons is the definitive way to demonstrate photonuclear reactions in lightning.

In 2016, we developed compact gamma-ray detectors and started a new operation with 4 detectors at Kashiwazaki-Kariwa Nuclear Power Station. On February 6th, 2017, the four detectors caught a short burst, and furthermore, two of them detected annihilation signals lasting for tens of seconds immediately after the short burst. The present thesis verifies our hypothesis that a downward TGF coinciding with a lightning discharge triggered photonuclear reactions, and their byproducts were observed as the short burst and the annihilation gamma rays.

This thesis is organized as follows. In Chapter 2, we review observations of high-energy phenomena in lightning and thunderclouds, theoretical views of electron acceleration in the atmosphere, and basics of neutron physics. Chapter 3 introduces Instruments utilized in the thesis and our observational target, winter thunderstorms in Japan. In Chapter 4, we summarize short-burst events and demonstrate photonuclear reactions in the atmosphere, based on a paper previously published as Enoto et al. [2017]. In Chapters 5 and 6, the downward TGFs which triggered photonuclear reactions are quantitatively evaluated based on observations and

Monte-Carlo simulations of positrons and neutrons. The downward TGFs are also evaluated by dose measurements and Monte-Carlo simulations in Chapter 7, based on a paper previously published as Wada et al. [2019b]. In Chapter 8, the evaluations of the downward TGFs by three methods (positron, neutron, and TGF dose measurements) are compared, and Chapter 9 summarizes the present thesis.

The errors described in the present thesis is at 1σ confidence level unless otherwise noted. We use "thunderstorm" as a word including both lightning discharge and thundercloud. Time in this thesis is described in local time (japan standard time: JST) unless otherwise noted.

Chapter 2

Review

Since 1980s, high-energy phenomena in the atmosphere have been detected by satellite, aircraft, balloon, and on-ground experiments. As briefly mentioned in Chapter 1, they have been found to originate from electron acceleration in strong electric fields of lightning discharges or thunderclouds. This chapter reviews current observational understandings of high-energy atmospheric phenomena such as TGFs, X-ray emissions from lightning, gamma-ray glows, then theories of electron acceleration proposed to explain these phenomena. Section 2.6 introduces basic physics of neutrons utilized to interpret observation data of neutron origin.

2.1　Terrestrial Gamma-ray Flash

2.1.1　Gamma-ray observations with space-borne detectors

Lightning discharges are known to release enormous energy via three ways, optical flashes, sonic booms, and radio-frequency emissions in various wavelengths. In addition to the three ways, gamma rays are recognized as the forth way, discovered by an in-orbit spacecraft in 1991. The Compton Gamma-Ray Observatory (CGRO), developed by National Aeronautics and Space Administration (NASA) to detect celestial high-energy emissions, was launched into a low-Earth orbit of the 500-km altitude. The Burst and Transient Source Experiment (BATSE) onboard CGRO was sensitive to X and gamma rays above 50 keV, and searched for transient emissions from the whole sky such as gamma-ray bursts. During its initial operation from April 1991 to October 1993, BATSE serendipitously detected 12 gamma-ray flashes of terrestrial origin [Fishman et al., 1994]. Figure 2.1 shows count rate histories of the 12 flashes. These flashes have a duration of several hundred microseconds to a few milliseconds. The energy of their gamma-ray photons exceeded 300 keV, which is the maximum range of BATSE. When the gamma-ray flashes were detected, BATSE passed above active thunderstorms, and hence the relation between the gamma-ray flashes and thunderstorm activities was suggested. In addition, radio-frequency emissions in very low frequency (VLF: 3-30 kHz) and extremely low frequency (ELF: <3 kHz) bands were detected at the Antarctica Palmer station coincident with a gamma-ray flash observed by BATSE in 1994. Since the radio-frequency emissions originated from a lightning discharge and came from where BATSE detected the gamma-ray flash, it was confirmed that such gamma-ray flashes coincided with lightning discharges. Today, these phenomena are called terrestrial gamma-ray flashes (TGFs).

Up to date, TGFs have been observed by successive space-borne gamma-ray detectors, such as the Reuven Ramaty High Energy Solar Spectroscopic Imager (RHESSI), the Astro-Rivelatore Gamma a Immagini Leggero (AGILE) satellite, and the Fermi satellite. RHESSI,
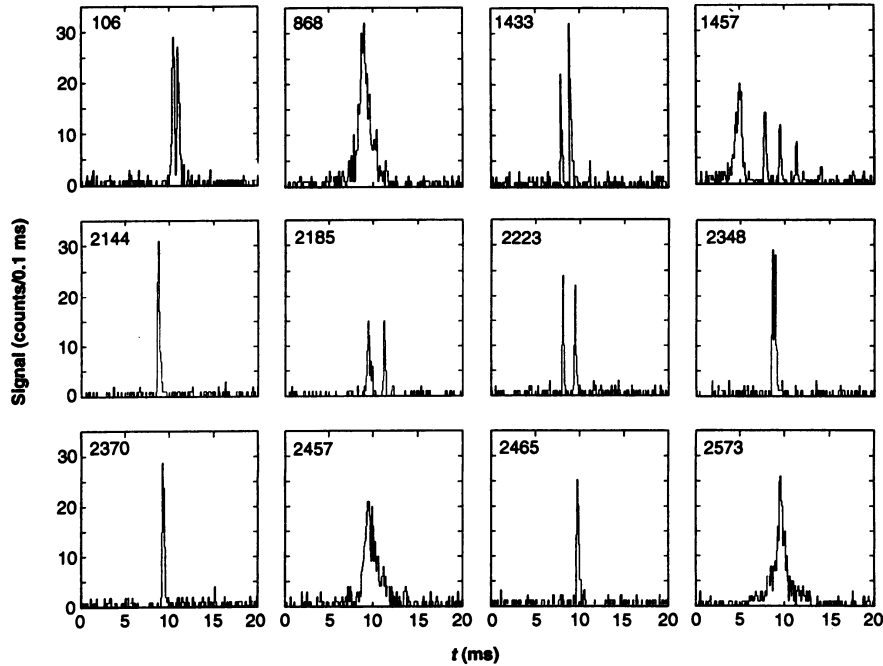
Figure 2.1: Count rate histories of 12 TGFs detected by the BATSE detector onboard the CGRO. Adapted from Fishman et al. [1994].

to observe high-energy solar phenomena, was launched into a 500-km low-Earth orbit by NASA. The Germanium Detector onboard RHESSI, sensitive to gamma rays up to 20 MeV, observed 86 TGFs during 4 months of its initial operation [Smith et al., 2005]. Figure 2.2 shows count-rate histories of 4 representative events, and an accumulated energy spectra of the 86 events. The RHESSI Germanium Detector obtained TGF spectra for the first time, owing to its wide energy range and good energy resolution. The obtained average spectrum follows a power-law function, and extends up to 20 MeV. The average spectrum can be reproduced by a bremsstrahlung spectrum from 35-MeV monochromatic electrons, and hence it is strongly suggested that electrons can be accelerated up to tens of MeV in lightning discharges. Dwyer et al. [2005] performed Monte-Carlo simulations to calculate electron acceleration and atmospheric attenuation, and compared the results with the average spectrum. They estimated a TGF altitude as 15–21 km from spectral features in low-energy range which are affected by atmospheric attenuation. The number of avalanche electrons above 1 MeV was also estimated to be 1×10^{16}–2×10^{17}.

The Italian gamma-ray astronomy satellite "Astro-rivelatore Gamma a Immagini Leggero", has detected TGFs since its launch in April 2007 [Marisaldi et al., 2010]. AGILE is equipped with the Mini-Calorimeter (MCAL), which is sensitive to 0.3–100 MeV gamma-ray photons. The stacked energy spectra, shown in Figure 2.3 left, extends up to 100 MeV, which exceeds the upper range of RHESSI Germanium detector [Tavani et al., 2011]. This high-energy component suggests that high voltage of several hundred MV in thunderclouds should contribute to the TGF production. TGFs have been also detected by the Gamma-ray Burst Monitor (GBM) onboard NASA's Fermi Gamma-ray Space Telescope, launched in June 2008 [Briggs et al., 2010]. GBM is sensitive to 0.01-40.0 MeV photons. TGFs obtained by Fermi GBM contain ∼100 photons and last for 100 ± 10 μs (full width at half maximum: FWHM) on average [Briggs et al., 2013]. Two fifth of them consist of multiple pulses, called "multi-pulse TGFs" [Foley et al., 2014].
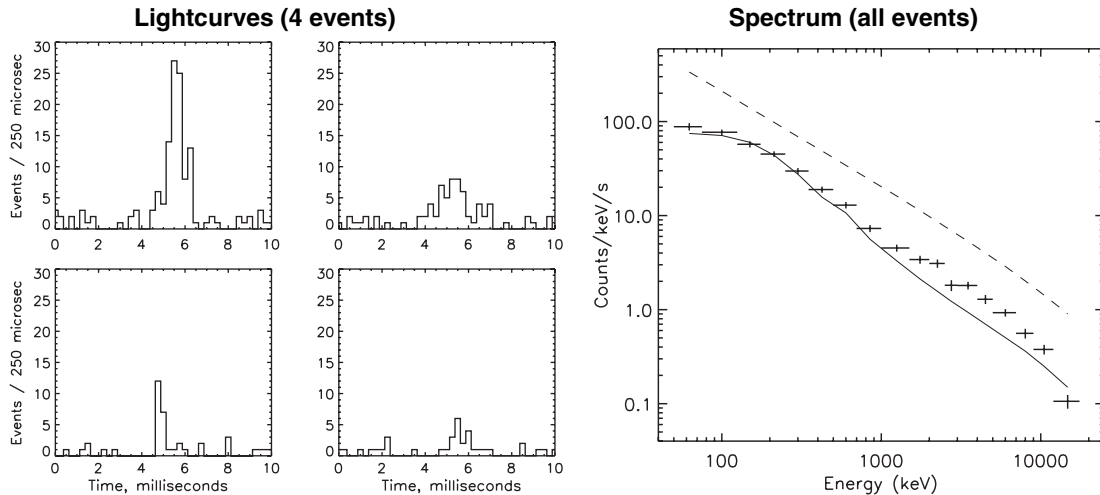
12

Figure 2.2: Count-rate histories (left) and an accumulated spectrum (right) of TGFs detected by the RHESSI Germanium detector. Adapted from Smith et al. [2005].

Mailyan et al. [2016] compared individual Fermi TGF spectra with Monte-Carlo simulations, and estimated the number of avalanche electrons above 1 MeV generated in a TGF as 4×10^{16}–3×10^{19}, and 2×10^{18} on average. More than 1000 TGFs have been detected by CGRO, RHESSI, AGILE and Fermi until now. The active missions, AGILE and Fermi, have detected $\sim$1000 and $\sim$850 TGFs per year, respectively [Sarria et al., 2017].

Energy spectra of several Fermi TGFs exhibit a 511-keV line, indicating ambient electron-positron annihilations (Figure 2.3 right: [Briggs et al., 2011]). Positrons in their cases are thought to be produced by pair creation with TGF photons in the atmosphere, and propagate to the spacecraft along the geomagnetic field. As well, electrons produced by TGF photons in the atmosphere reach spacecrafts. They are sometimes detected as a delayed pulse because they propagate more slowly than photons. When electrons reach an altitude where atmospheric interactions are negligible, they are drifted by geomagnetism and separated from the parent gamma-ray photons. In some cases, only electrons can hit the space-borne detectors. These events of electron origin are called "terrestrial electron beams" (TEBs: Briggs et al. [2013]).

2.1.2 Radio-frequency observations of TGF-associated lightning discharges

After the association between TGFs and radio-frequency (RF) emissions from lightning discharges were confirmed [Inan et al., 1996], simultaneous observations of TGFs and spherics in various wavelength have been performed. Lightning discharges consist of two phase: one is that high electric-field regions called "stepped leaders" extends from a charge region and form lightning paths, and the other is that the stepped leaders reach another charge region and then large-current processes called "return strokes" take place (Figure 2.4). When stepped leaders reach the ground and a discharge occurs between a thundercloud and the ground, this phenomenon is called "cloud-to-ground discharge" (CG). Discharges in a thundercloud and between two thunderclouds but not connected to the ground are called "intracloud discharges" and "intercloud discharges" respectively, or called together "in-cloud discharges" (ICs).

High-frequency (HF: 3–30 MHz) and very-high-frequency (VHF: 30–300 MHz) bands are dominant emissions from stepped leaders. ELF, VLF, and low-frequency (LF: 30–300 kHz) bands are dominant from high-current processes such as return strokes. Receiving RF pulses
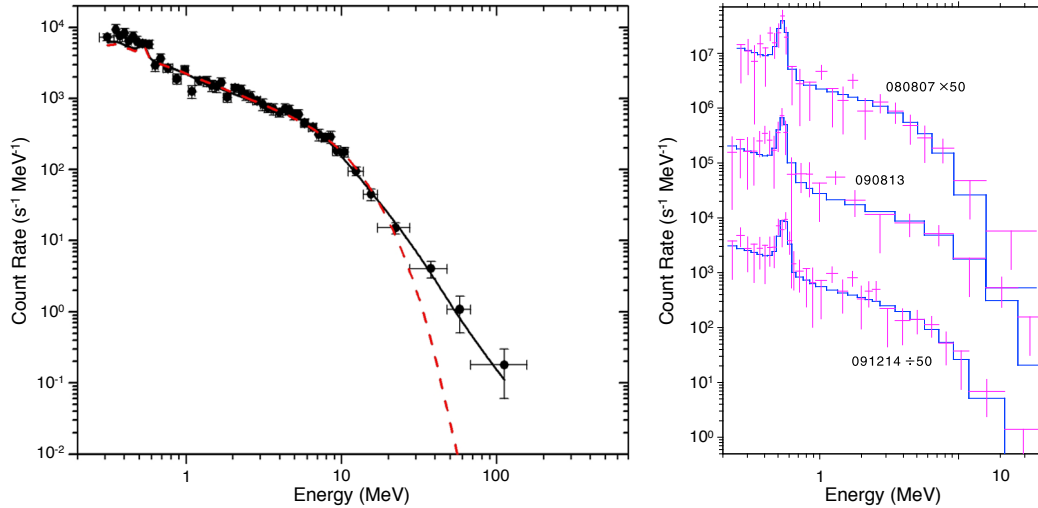
Figure 2.3: An accumulated spectrum of AGILE TGFs (left) and TGF spectra showing positron annihilation obtained by Fermi (right). Adapted from Tavani et al. [2011] and Briggs et al. [2011]

with multiple antennas allows us to locate where they come from. In particular, broadband interferometry [Mardiana et al., 2002, Morimoto et al., 2004, 2016] and time-of-arrival method in the VHF bands are of great importance to visualize evolution of discharge processes including initial breakdown and leader progression. They three-dimensionally locate sources of VHF spherics with high timing and spatial resolution, while attenuation of VHF limits observation ranges. In contrast, time-of-arrival and magnetic-direction-finder methods using polarimetry in VLF/LF bands are useful to locate return strokes. They cover wide areas and hence are employed by world-wide and national lightning detection services such as World Wide Lightning Location Network (WWLLN: Rodger et al. [2009]), National Lightning Detection Network (NLDN: Holle et al. [2016], Nag et al. [2011]) and Japanese Lightning Detection Network (JLDN: Ishii et al. [2013], Matsui et al. [2015]). Observations of RF emissions are essential to examine characteristics of lightning discharges associated with TGFs.

Lightning location systems covering wide areas are suitable to examine correlations between lightning discharges and TGFs detected by spacecrafts. WWLLN covers all over the world by a VLF detection network, and has a 30–35% detection efficiency to lightning discharges of > 50 kA [Rodger et al., 2009]. Among 50 TGFs detected by Fermi, 15 events coincided with WWLLN-detected discharges within 50 μs. Estimated locations of discharges were located within 300 km from where Fermi detected the associated TGFs [Connaughton et al., 2010]. [Mailyan et al., 2018] surveyed associations between TGFs and RF emissions taking place around North America using NLDN, which provides more accurate location and peak current of discharges than WWLLN.

Detailed observations in LF and VHF bands give insights into individual TGFs. Lu et al. [2010] for the first time succeeded in three-dimensionally visualizing a lightning discharge associated with a RHESSI TGF using a lightning mapping array (LMA: Krehbiel et al. [2000], Rison et al. [1999]) installed in Alabama, US. LMA is a lightning location system employing the time-of-flight technique in the VHF band. They suggested that the TGF was produced during an upward leader progression, and leader processes might be responsible for TGFs. Cummer et al. [2014, 2015] monitored LF waveforms from TGF-associated lightning discharges,
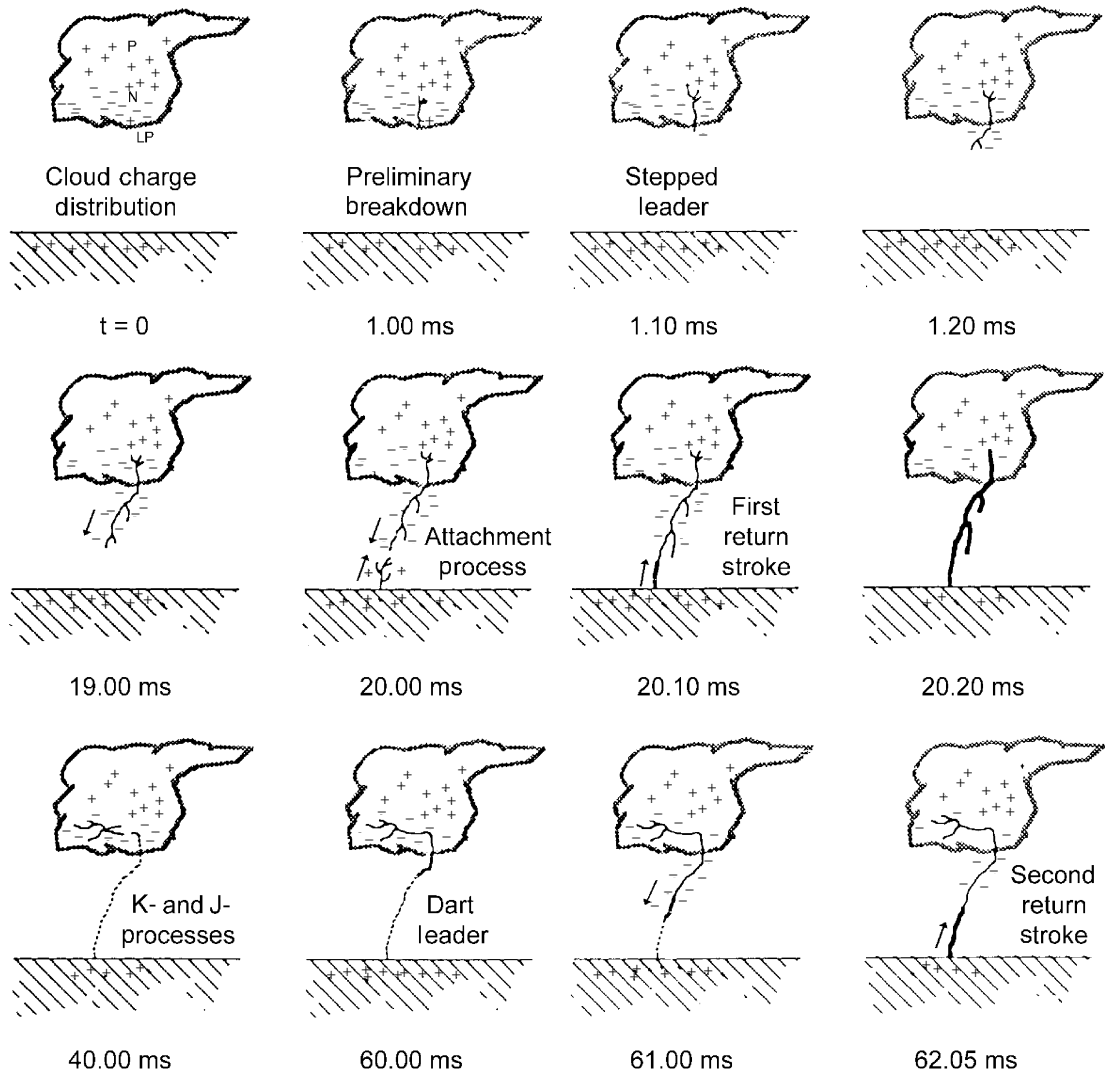
Figure 2.4: Discharge processes of a cloud-to-ground discharge. Adapted from Rakov and Uman [2003].

and employed a method to estimate pulse heights of the LF sources, by identifying reflection pulses from the ionosphere and the ground [Smith et al., 2004]. Their results in the LF band also suggested that TGFs were produced in the middle of upward leader development several milliseconds after leader initiation. Cummer et al. [2014] detected TGF-associated LF pulses at 11–12-km altitude, and suggested that TGFs took place in the upper part of thunderclouds. More recently, Lyu et al. [2015, 2016] have identified a new type of lightning discharges named "energetic in-cloud pulses" (EIPs), which are characterized by high estimated peak currents of >200 kA, and proposed a strong connection to TGFs.

2.1.3 Downward TGFs observed at ground level

At present, TGFs are widely accepted as upward-beamed emissions from thunderclouds mainly observed with space-borne detectors. However, despite less common cases, TGF-like but downward-beamed emissions have been detected by on-ground facilities. They are now called
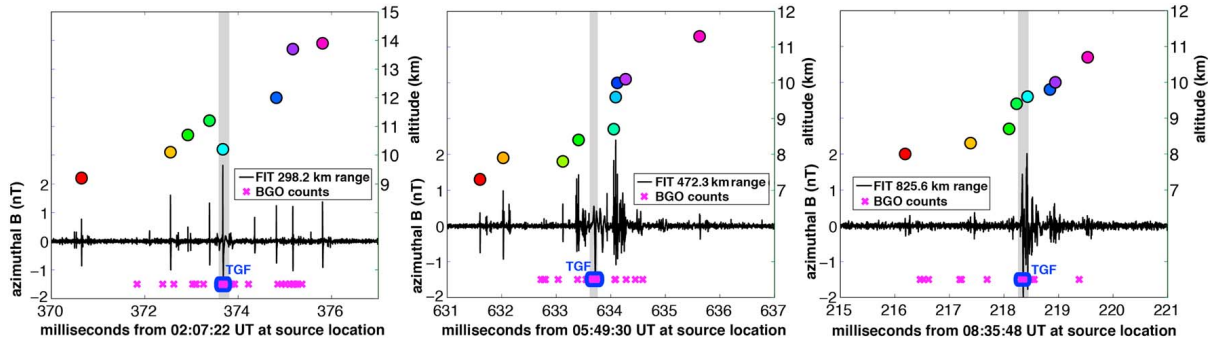
15

Figure 2.5: LF waveforms and leader altitude progression during TGFs. Adapted from Cummer et al. [2015].

"downward TGFs". Downward TGFs were detected coincident with rocket-triggered lightning discharges. International Center for Lightning Research and Testing (ICLRT), University of Florida performed rocket-triggered lightning experiments, which make artificial lightning leaders by launching metal wires attached to a small rocket toward thunderclouds, and inducing CGs. Dwyer et al. [2004] and Hare et al. [2016] installed multiple sodium iodide and plastic scintillators around the launch point, and detected gamma-ray photons with energies of >8 MeV coincident with successful rocket-triggered CGs in August 2003 and August 2014, respectively. In the case in 2003 [Dwyer et al., 2004], 227 photons were detected during 300 μs, and its energy spectrum extended to 10 MeV, as shown in Figure 2.6. An LMA observation in the 2014 event revealed that a downward TGF took place at the tip of an upward positive leader from the launched rocket. ICLRT and another facility of University of Florida observed other events of downward TGFs, coincident with natural lightning discharges [Dwyer et al., 2012a, Tran et al., 2015]. They lasted for several tens of millisecond with photons of >10 MeV.

The Telescope Array (TA) experiment is performed on a wilderness at a 1400 m altitude in Utah, US, to detect ultra-high energy cosmic rays exceeding 10^{20} eV. It covers an area of 700 km^2 with 507 surface detectors consisting of plastic scintillators, installed in a grid of a 1.2-km width [Abu-Zayyad et al., 2013]. Since 2010, surface detectors have observed gamma-
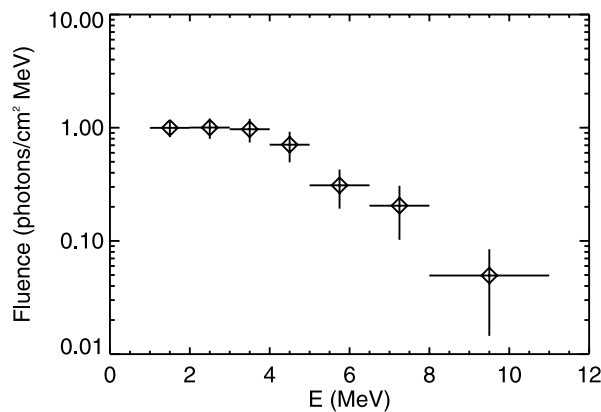

Figure 2.6: The energy spectrum of a downward TGF obtained at ICLRT. Adapted from Dwyer et al. [2004].

16

ray signals different from those of cosmic-ray origin, coincident with lightning discharges detected by NLDN [Abbasi et al., 2017]. The gamma-ray signals lasted for $\sim$10 μs, and were simultaneously detected by several to tens of surface detectors (Figure 2.7). An LMA installed at the TA site in 2013 observed negative leader progression of CGs or ICs associated with downward TGFs [Abbasi et al., 2018]. By comparing with Monte-Carlo simulations, they suggested that gamma rays of more than several MeV hit surface detectors, and 10^{12}–10^{14} photons of >0.1 MeV were produced in a downward TGF. These results presented that TA is capable of studying weak TGFs which cannot be detected by spacecrafts in detail. The Pierre Auger observatory in Argentina, aiming at detecting ultra-high energy cosmic rays likewise TA, also detected high-energy radiation events coincident with lightning discharges [Colalillo, 2017].
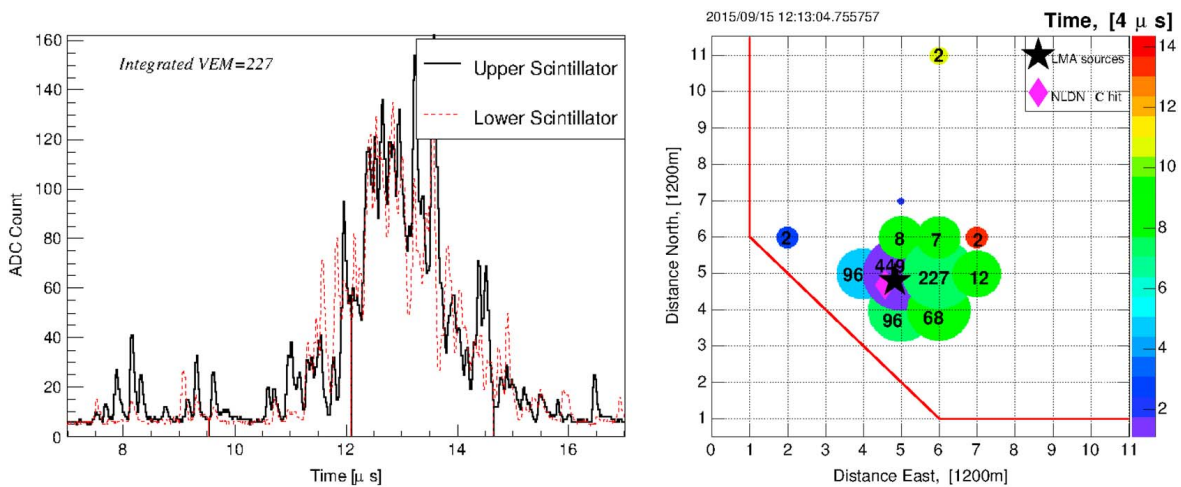

Figure 2.7: Waveforms from surface detectors (left) and a spatial distribution of energy deposits (right) in a downward TGF event observed by the TA experiment. Adapted from Abbasi et al. [2018].

2.2 Lightning-associated X-ray Emissions

Besides TGFs, another type of emissions has been recorded by ground-level measurements. In 2000, Moore et al. [2001] detected X-ray and gamma-ray photons coincident with lightning discharge, by using sodium iodide scintillators installed at South Baldy Peak in New Mexico, US. The photons were produced 1–2 milliseconds before return strokes, and some of them had energies of >1 MeV. Similar events have been detected at ICLRT [Dwyer et al., 2005, 2003, Saleh et al., 2009, Schaal et al., 2012], at 2500-m altitude of the Pyrenees, Spain [Montanyà et al., 2014], and by a sea-level experiment during winter thunderstorms in Japan [Yoshida et al., 2008]. Dwyer et al. [2005], by high-energy photon and electric-field measurements at ICLRT, revealed that X-ray photons of several hundreds of keV were emitted at each leader step, as shown in Figure 2.8 left.

This phenomenon shares characteristics with TGFs such as coincidence with lightning discharges and duration of sub-milliseconds to several milliseconds. However, energy spectra of this phenomenon have a steep cutoff at a few MeV, while those of TGFs extend to >10 MeV (Dwyer et al. [2004]; Figure 2.8 right). Therefore, it is thought that the X-ray emissions can
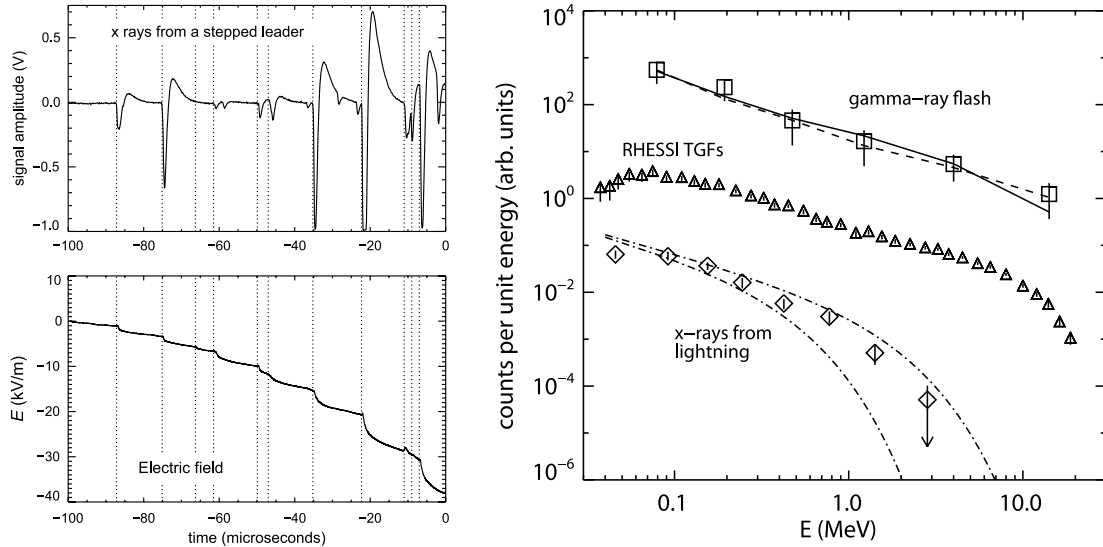
Figure 2.8: X-ray pulses (left top) and associated electric-field changes (left bottom) observed at ICLRT [Dwyer et al., 2005], and a comparison between energy spectra of RHESSI TGFs, a downward TGF, and a X-ray emission from lightning [Dwyer et al., 2012a].

be distinguished from TGFs, and its production mechanism should be different from those of TGFs [Dwyer et al., 2012a].

2.3 Gamma-ray Glow

In contrast to high-energy phenomena coincident with lightning discharges such as TGFs and X-ray bursts, X-ray and gamma-ray emissions coming from thunderclouds and lasting for more than seconds have been observed. The first report was made by Parks et al. [1981] and McCarthy and Parks [1985]. They equipped NASA's F-106 aircraft with an X-ray detector and a photo-multiplier tube (PMT) without X-ray absorbers for noise monitoring. During its flights inside thunderclouds in Oklahoma and Virginia, US, X-ray bursts were detected for tens of seconds to a minute, as shown in Figure 2.9. No lightning discharges were confirmed while the X-ray bursts were being observed. They concluded that high-energy electrons produced in active thunderstorms emitted bremsstrahlung X-rays.

This phenomenon is now called "gamma-ray glow", and has been observed inside thunder-clouds by aircrafts and balloons, and below thunderclouds at mountain-top observatories. Eack et al. [1996] performed a balloon flight with X-ray and atmospheric electric-field monitors. As strength of electric fields exceeded 50 kV m^{-1} at an 4-km altitude, a significant increase in X-rays was detected, as shown in Figure 2.10. Since the strength of electric fields during the gamma-ray glow was less than two third of that needed for relativistic runaway acceleration [Wilson, 1925], they speculated that there was another stronger electric fields which facilitate electron acceleration near the balloon, or an unknown mechanism to accelerate electrons even in weak electrostatic fields.

Recently, airborne observations at high altitude have been performed. Kelley et al. [2015] detected a gamma-ray glow at a 14 km altitude in Colorado, US, with the Airborne Detector for Energetic Lightning Emissions onboard Gulfstream V aircraft (Figure 2.11). Based on detector responses, gamma-ray photons, whose spectrum extended to >5 MeV, propagated downward.
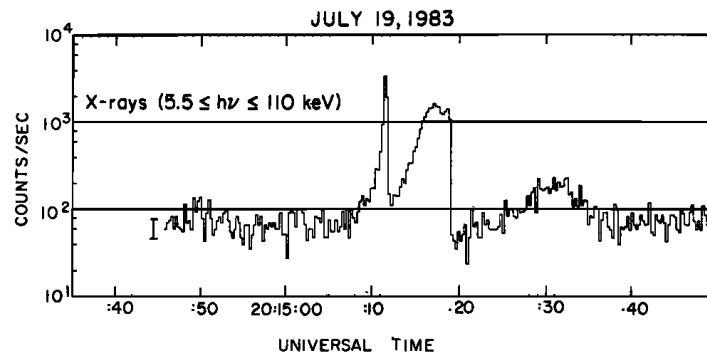
18

Figure 2.9: One of the first gamma-ray glow observations by airborne detectors. Adapted from McCarthy and Parks [1985].
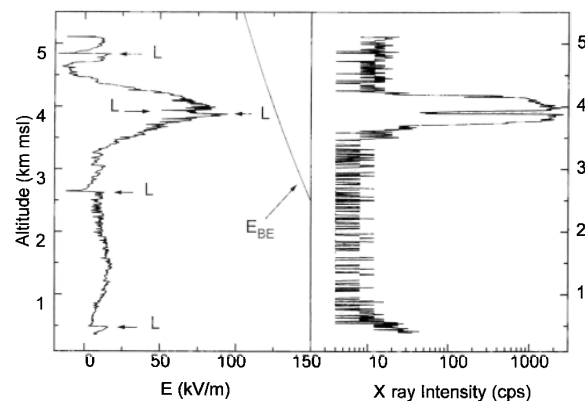

Figure 2.10: X-ray intensity and electric-field strength measured by a balloon flight. Adapted from Eack et al. [1996].

As the aircraft was flying at the cloud top of a thundercloud during the glow detection, they concluded that electrons were accelerated downward between a positive charge layer and a negative charge layer above called "screen layer". Kochkin et al. [2017] observed gamma-ray glows lasting for 20–30 seconds at a 12-km altitude in North Australia, with X-ray and gamma-ray detectors onboard an Airbus A340 aircraft, and Østgaard et al. [2019] observed ones at a 20-km altitude in Georgia, US, with gamma-ray and electric-field monitors onboard NASA's ER-2 aircraft.

On high-altitude mountains, on-ground observations of high-energy radiation can be performed inside or near thunderclouds. Since 2000s, cosmic-ray observatories around the world have recorded minute-lasting gamma-ray emissions associated with thunderstorm activities [Alexeenko et al., 2002, Chubenko et al., 2000]. In Japan, observatories at Mount Norikura (2770-m altitude: Tsuchiya et al. [2009]) and Mount Fuji (3776-m: Torii et al. [2009]) have recorded gamma-ray glows. The longest-lasting gamma-ray glow, lasting for ∼40 minutes, was observed at Yangbajing International Cosmic Ray Observatory. The highest photon energy of the glow exceeded 40 MeV [Tsuchiya et al., 2012]. Aragats Space Environmental Center (ASEC) at a 3200-m altitude slope of Mount Aragats in Armenia has continuously performed gamma-ray, electrons, and neutron monitoring with solar neutron telescopes and cosmic-ray monitors. They have detected increases in gamma rays and electrons associated with thunder-
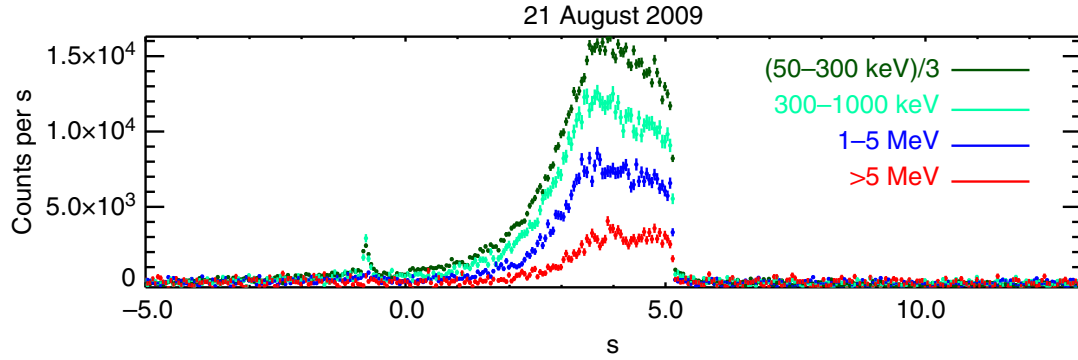
Figure 2.11: The brightest gamma-ray glow detected by the Airborne Detector for Energetic Lightning Emissions experiment. Adapted from Kelley et al. [2015].
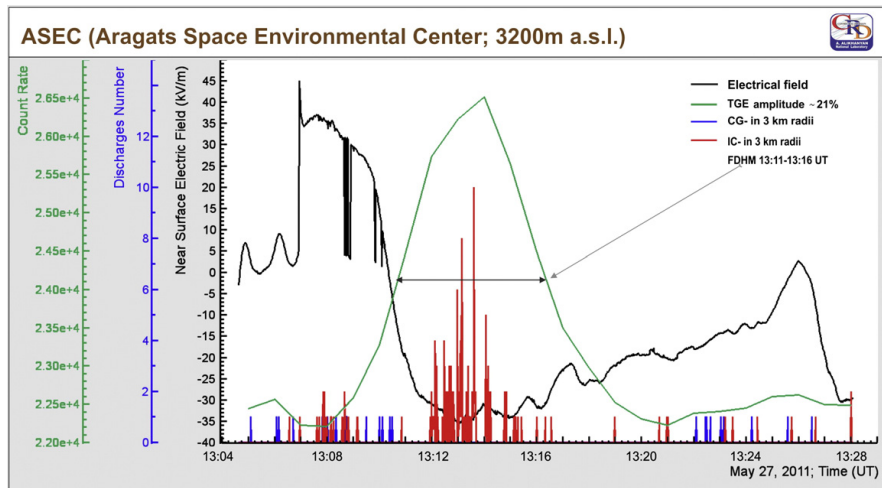

Figure 2.12: A thunderstorm ground enhancement and electric-field variation recorded at Aragats Space Environmental Center. Adapted from Chilingarian and Mkrtchyan [2012].

storms, named "thunderstorm ground enhancements" (TGEs: Chilingarian et al. [2010, 2011]). TGEs and gamma-ray glows are thought to be intrinsically the same phenomena. By comparing TGEs with electric-field perturbations shown in Figure 2.12, Chilingarian and Mkrtchyan [2012] speculated that electron acceleration and multiplication could take place in a strong electric field between a middle-layer negative charge region and a lower positive charge region. ASEC is the site where the largest number of TGEs has been registered, as ∼300 TGEs were detected there in 2008–2012.

Typical summer thunderclouds have cloud bases of >3 km altitudes, and hence gamma-ray glows cannot be detected at sea level as photons and electrons are attenuated. On the other hand, low could bases of winter thunderstorms in Japan enable us to detect gamma-ray glows at sea level. Torii et al. [2002], with radiation monitoring stations installed in the nuclear facility "Monju" faced on the Sea of Japan, recorded dose increases lasting for ∼1 minute associated with passage of thunderclouds (Figure 2.13). In addition, an observation with multiple monitoring stations allowed Torii et al. [2011] to measure time lags of a gamma-ray glow at each
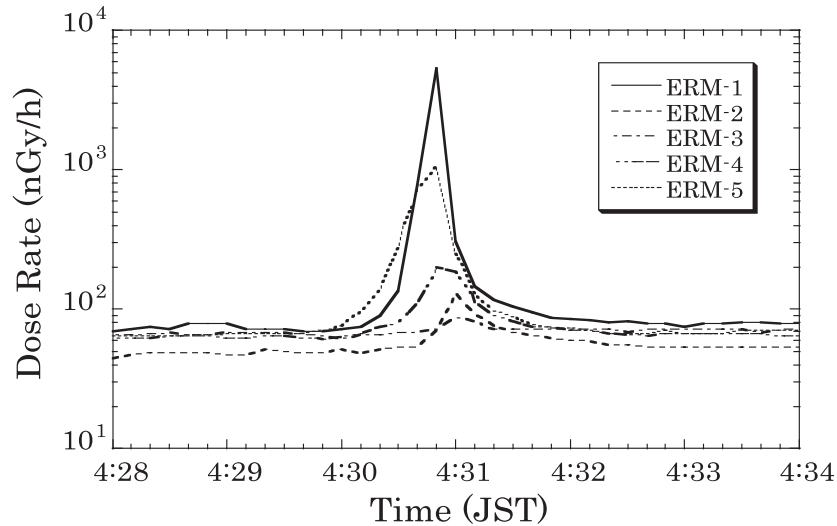
20

Figure 2.13: A dose-rate enhancement measured by environmental radiation monitors installed at the nuclear reactor Monju during a winter thunderstorm in Japan. Adapted from Torii et al. [2002].

station, and then to estimate the height of the gamma-ray source as ∼300 m. Since 2006, the Gamma-Ray Observation of Winter Thunderclouds(GROWTH) experiment has been performed at Kashiwazaki-Kariwa Nuclear Power Station in Niigata. Tsuchiya et al. [2007] for the first time succeeded in obtaining an energy spectrum of a gamma-ray glow. The energy spectrum presenting a power-law function extending up to 10 MeV indicated that gamma-ray photons originated from bremsstrahlung of relativistic electrons accelerated in thunderclouds (Figure 2.14). Tsuchiya et al. [2011] estimated total electron numbers during their detection as 10^9–10^{11}, and their source height as 100–700 m. Kuroda et al. [2016] revealed that gamma-ray photons came from zenith during a gamma-ray glow detection, at Ohi Nuclear Power Station in Fukui with Plastic Anti-Neutrino Detector Array.

Gamma-ray glows are widely thought to originate from strong electric fields inside thunderclouds, not directly associated with lightning discharges themselves. On the other hand, on-ground and airborne experiments have observed sudden termination of gamma-ray glows coincident with lightning discharges [Alexeenko et al., 2002, Chilingarian et al., 2015, Eack et al., 1996, Kelley et al., 2015, Kochkin et al., 2017, McCarthy and Parks, 1985, Tsuchiya et al., 2013]. Since lightning discharges can be remotely observed in the RF bands, glow termination is an opportunity to observe gamma-ray glows besides high-energy bands. Chilingarian et al. [2017] performed electric-field monitoring during TGEs and their termination. They revealed that negative charge layers inside thunderclouds were discharged when TGEs were terminated, and suggested that the negative layers were responsible for electron acceleration of TGEs. Wada et al. [2018] observed a glow termination during a winter thunderstorm in Japan with gamma-ray, LF, and electric-field monitors. Two-dimensional lightning mapping with broadband LF receivers revealed that the gamma-ray glow was terminated by leader development of an IC which horizontally extended ∼70 km.
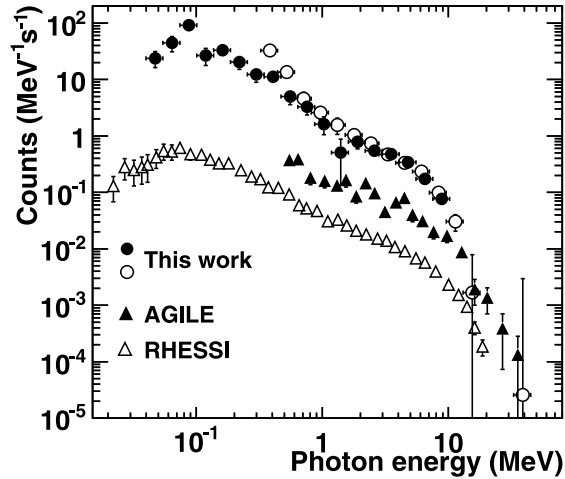
Figure 2.14: Energy spectra of gamma-ray glow during winter thunderstorms and TGFs detected by AGILE and RHESSI. Adapted from Tsuchiya et al. [2011].

2.4   Neutron Production in the Atmosphere

Besides electrons, X-rays and gamma rays, possibility of neutron production by lightning discharges has been discussed since 1970s. Neutron production in the atmosphere is of great importance because it leads to producing a carbon isotope ^{14}C, which is used for radiocarbon dating in archaeology, via a nuclear reaction $^{14}N + n \rightarrow^{14} C + p$ [Babich, 2017, Libby and Lukens, 1973]. Shah et al. [1985] reported detection of neutrons coincident with lightning discharges by cosmic-neutron monitors installed in the Himalayan region. They estimated that 10^7–10^{10} neutrons were generated per a lightning discharge. At that time, the most probable scenario of neutron production in lightning was thought to be nuclear fusion; deutrons in vapor molecules are heated in lightning paths, and eventually trigger deutron-deutron reactions $^2H +^2 H \rightarrow^3 He + n$. In that reaction, a neutron with an energy of 2.45 MeV is produced. However, Babich [2006, 2007] concluded that deutron-deutron reactions are not plausible in lightning, because cross section of the reactions under the condition in lightning is too low to produce an observable number of neutrons.

After the discovery of TGFs in 1994 [Fishman et al., 1994], neutron production via photonuclear reactions has been discussed because energy spectra of TGFs were confirmed to extend to >10 MeV [Smith et al., 2005]. Photonuclear reaction is one of nuclear reactions that a photon kicks a neutron off from a nucleus. Nuclei in the atmosphere such as ^{14}N and ^{16}O are involved in the reactions $^{14}N + \gamma \rightarrow^{13} N + n$ and $^{16}O + \gamma \rightarrow^{15} O + n$, with the threshold photon energies of 10.55 MeV and 15.66 MeV, respectively. Babich [2006, 2007] suggested that 10^{15} neutrons can be generated in a lightning discharge. Furthermore, Carlson et al. [2010] performed a simulation study with parameters of RHESSI TGFs, and presented that 3×10^{11}–3×10^{12} neutrons per a TGF could be generated via photonuclear reactions.

Several reports on neutron detection associated with thunderstorm activities have been recently made. Gurevich et al. [2012] detected thermal neutrons associated with lightning discharges by ^3He neutron monitors, installed at a 3340-m-altitude cosmic-ray observatory in Kazakhstan. They reported that neutron fluxes were (3–5) $\times 10^{-2} cm^{-2} s^{-1}$ on average. In addition, neutrons have been detected during gamma-ray glows. Chilingarian et al. [2010] and Chilingarian and Mkrtchyan [2012] reported detection of neutrons associated with TGEs by ^{10}Be proportional counters of Aragats Solar Neutron Telescope. Kuroda et al. [2016] also
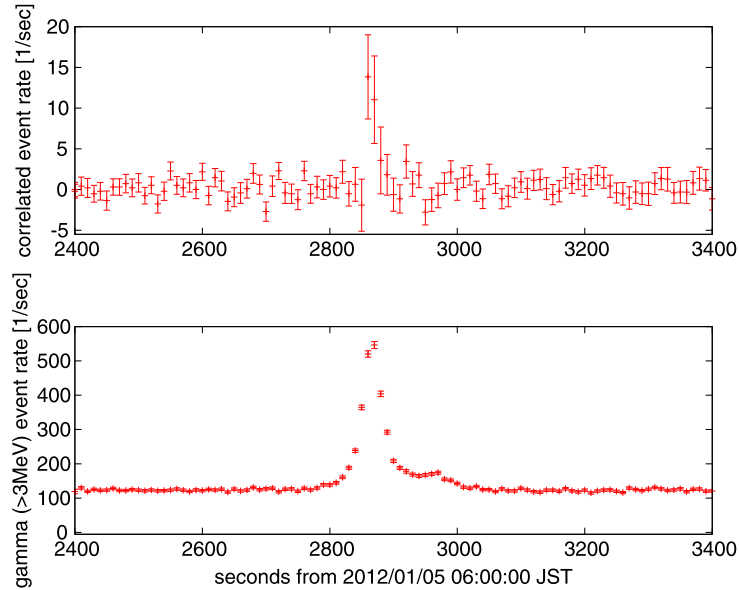
Figure 2.15: Count-rate histories of neutrons (top) and gamma rays (bottom) during a winter thunderstorm in Japan. Adapted from Kuroda et al. [2016].

reported a neutron burst during a gamma-ray glow in a winter thunderstorm, as shown in Figure 2.15. These two neutron bursts were not associated with lightning discharges, and hence photonuclear reactions triggered by photons of gamma-ray glows are the only possibility for neutron production. On the other hand, proton-rich nuclei such as ^{13}N and ^{15}O should be generated in such reactions. These nuclei eventually emit positrons via β^+ decay, with half-lives of 10 and 2 minutes, respectively. When photonuclear reactions take place, a signature of positrons can be detected besides neutrons. In fact, Umemoto et al. [2016] reported a signature of electron-positron annihilation detected immediately after a lightning discharge. However, occurrence of photonuclear reactions in the atmosphere has never been demonstrated because simultaneous detection of positrons and neutrons has never been reported.

2.5 Theories of Electron Acceleration in Thunderstorms

2.5.1 Relativistic runaway electron avalanche

Wilson [1925] proposed an idea that electrons can be accelerated by strong electric fields in the atmosphere for the first time. Then, Gurevich et al. [1992] developed this idea into "relativistic runaway electron avalanche" (RREA) by considering acceleration of secondary electrons. As well known [Knoll, 2000], the drag force to electrons by ionization is presented as the Bethe formula

$$F_{\text{ion}} = 2\pi r_{\text{e}}^2 m_{\text{e}} c^2 \rho N_{\text{A}} \frac{Z}{A} \frac{1}{\beta^2} \left[\ln \frac{\epsilon m_{\text{e}} c^2 \beta^2 \gamma^2}{2I^2} - \ln \left(\frac{4}{\gamma} - \frac{3}{\gamma^2} \right) + \frac{1}{\gamma^2} + \frac{1}{8} \left(1 - \frac{1}{\gamma} \right)^2 \right], \quad (2.1)$$

where ϵ, r_{e}, $m_{\text{e}} c^2$, ρ, Z, A, N_{A}, β, γ, I are kinetic energy of an electron, the classical electron radius, rest energy of an electron, density, atomic number and atomic weight of targets, the Avogadro constant, a ratio of electron velocity to speed of light, the Lorenz factor, and ionization
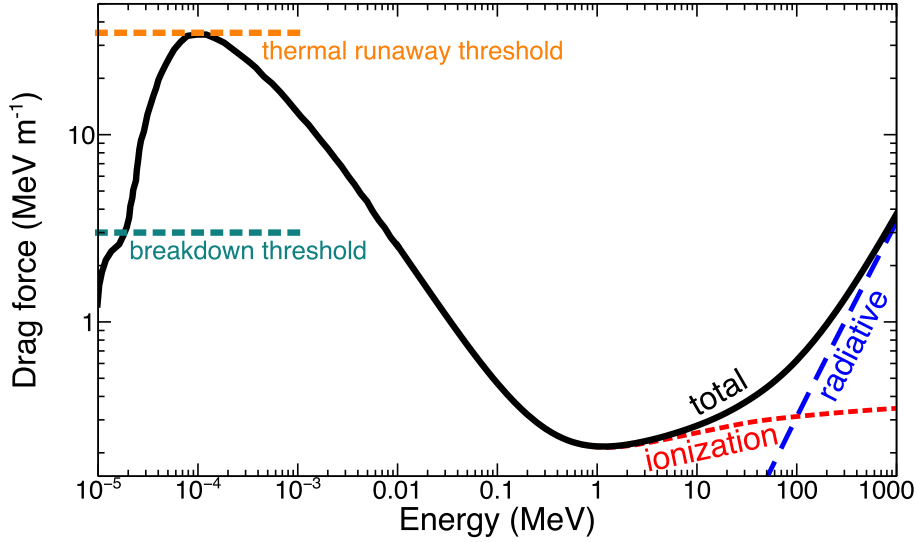
23

Figure 2.16: The drag force to electrons in the standard atmosphere. Data points are provided by NIST/EStar and Dwyer [2004].

energy of targets, respectively. In relativistic energies, radiative drag force also affects electrons. This force is formulated as [Knoll, 2000]

$$F_{\rm rad} = \alpha r_{\rm e}^2 \rho N_{\rm A} \frac{Z(Z+1)}{A} \epsilon \left[4 \ln \frac{2\epsilon}{m_{\rm e} c^2} - \frac{4}{3} \right], \qquad (2.2)$$

where α the fine structure constant. The total force to electrons is the summation of ionization and radiative forces $F_{\rm tot} = F_{\rm ion} + F_{\rm rad}$. More precise values of drag forces to electrons are provided by the EStar database provided by National Institute of Standards and Technology (NIST). The drag force in the standard atmosphere ($\rho = 1.293 \times 10^{-3}$ g cm^{-3}) is shown in Figure 2.16. In non-relativistic energy, drag force decreases as electron energy increases. In contrast, both ionization and radiative forces increase as electron energy increases in relativistic energy. Therefore, the drag force has a minimum at ~ 1 MeV

$$F_{\rm min} = 0.216 \text{ MeV m}^{-1} \times \frac{\rho}{1.293 \times 10^{-3} \text{ g cm}^{-3}}. \qquad (2.3)$$

When a higher electric field than this minimum exists in the atmosphere, acceleration force by the electric field and drag force are balanced at two point in relativistic energy. The lower-energy point is unstable: electrons with slightly lower energy decelerate, and those with slightly higher energy accelerate. On the other hand, the higher point is stable: electrons with slightly lower energy accelerate, and those with slightly higher energy decelerate. Therefore, electrons with energy higher than the lower energy point can be accelerated to the higher energy point in the electric field.

Then, acceleration of secondary electrons produced by ionization processes is considered [Gurevich et al., 1992]. In non-relativistic energy range, the formula of drag force is approximated as [Landau et al., 1984]

$$F = 2\pi r_{\rm e}^2 m_{\rm e} c^2 \rho N_{\rm A} \frac{1}{\beta^2} \ln \left(\frac{m_{\rm e} c^2}{Z \epsilon_i} \beta^2 \right). \qquad (2.4)$$

In relativistic energy range as

$$F \approx 2\pi r_e^2 m_e c^2 \rho N_A \ln\left(\frac{m_e c^2}{\epsilon_1}\gamma\right), \tag{2.5}$$

where $\epsilon_i = 15$ eV and $\epsilon_1 = 270$ eV. The minimum of the drag force is shown as

$$\begin{aligned}
F_{\min} &\approx 2\pi r_e^2 m_e c^2 \rho N_A \ln\left(\frac{m_e c^2}{Z\epsilon_i}\right) \\
&= 0.2 \text{ MeV m}^{-1} \times \frac{\rho}{1.293 \times 10^{-3} \text{ g cm}^{-3}}.
\end{aligned} \tag{2.6}$$

Here a non-dimentinal parameter

$$\delta_0 = \frac{eE}{F_{\min}} = \frac{E}{0.2 \text{ MV m}^{-1}} \frac{1.293 \times 10^{-3} \text{ g cm}^{-3}}{\rho} \tag{2.7}$$

is introduced. When $\delta_0 > 1$, the balance equation between electric fields and drag force $eE - F = 0$ has two solutions, hence runaway electrons are produced.

The runaway electrons produce secondary electrons via ionization processes. Assuming that primary electrons penetrate along electric fields, the angle between primary and secondary electron's velocity vectors is given as θ, and $\mu = \cos\theta$. Secondary electrons tend to be emitted into the perpendicular direction to primary electron's velocity vector, and hence the initial value of μ is ~ 0. Then velocity v and momentum angle μ of the secondary electrons are affected by the drag force and the electric field. The equation of motion of the secondary particles for their forward direction is introduced as

$$m_e \frac{dv}{dt} = eE\mu - F(v), \tag{2.8}$$

where, m_e is the electron mass. Time variation of $\mu = \vec{v} \cdot \vec{E}/vE$ is also introduced as

$$\begin{aligned}
\frac{d\mu}{dt} &= \frac{d}{dt}\left(\frac{\vec{v}\cdot\vec{E}}{vE}\right) \\
&= \frac{1}{vE}\left[E\cos\theta\left(\frac{eE\mu}{m_e} - \frac{F(v)}{m_e}\right) + E\sin\theta \times \frac{eE}{m_e}\sin\theta\right] \\
&\approx \frac{eE}{m_e v}\sin^2\theta = \frac{eE}{m_e v}(1-\mu^2).
\end{aligned} \tag{2.9}$$

Here the electron velocity can be replaced by a dimension-less parameter $u = v^2/c^2$. In the non-relativistic case, the two equations of motion derive a differential equation of u and μ

$$\frac{du}{d\mu} = \frac{2}{1-\mu^2}\left[\mu u - \frac{1}{\delta_0}\left\{1 + \frac{\ln u}{\ln(m_e c^2/Z\epsilon_i)}\right\}\right]. \tag{2.10}$$

The solution of this equation predicts the movement of secondary electrons in the $\mu - u$ plane. Figure 2.17 left shows examples of electron trajectories under a condition of $\delta_0 = 3$ and the initial value of $\mu = 0$, calculated by the two-stage second-order Runge-Kutta method. While secondary electrons move toward $\mu = 1$, they accelerate with higher initial velocity than a threshold, and decelerate with lower initial velocity than the threshold. The relation between δ_0 and the threshold initial velocity u_{init} is shown in Figure 2.17 right. The threshold u_{init} exists
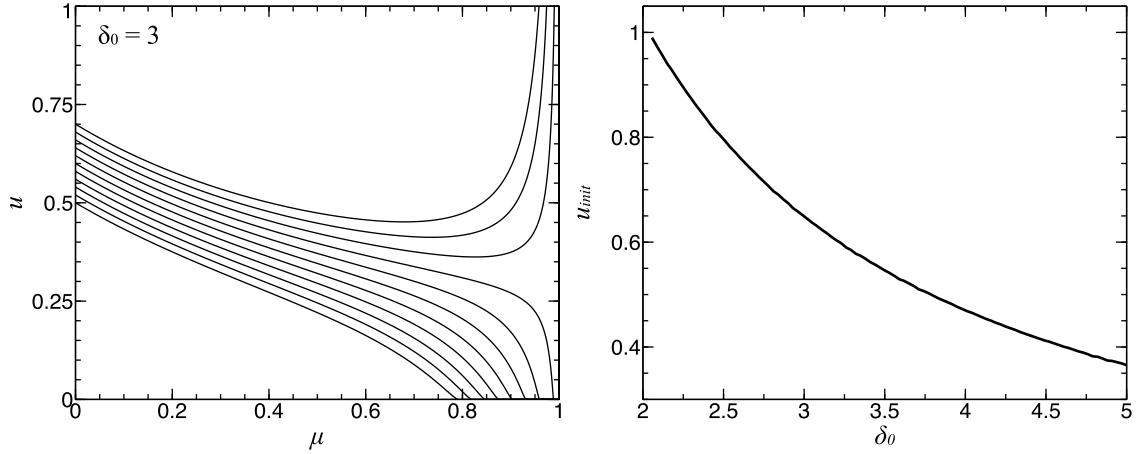
Figure 2.17: Trajectories of secondary electrons in the $\mu - u$ plane at $\delta_0 = 3$ (left) and the relation between δ_0 and u_{init} (right) in the standard atmosphere.

when δ_0 is higher than 2.1. Since δ_0 depends on atmospheric density and electric fields, the threshold electric-field strength where secondary electrons can run away is

$$E_{\text{th}} = 0.42 \, \text{MV m}^{-1} \times \frac{\rho}{1.293 \times 10^{-3} \, \text{g cm}^{-3}}. \tag{2.11}$$

The initial velocity of secondary electrons must exceed u_{init} so that they become runaway electrons. Their kinetic energy is then $\epsilon_{10} = \frac{1}{2} m_e c^2 u_{\text{init}}$. When energy of primary electrons far exceeds ϵ_{10}, an average length λ_e in which a primary electron produces secondary one is

$$\lambda_e = \frac{u_{\text{init}}}{2\pi r_e^2 \rho N_A}. \tag{2.12}$$

Since the number of secondary electrons produced per a unit length is proportional to the number of runaway electrons and inversely proportional to λ_e, a differential equation

$$\frac{dN}{dx} \propto \frac{N}{\lambda_e} \tag{2.13}$$

is obtained. Ignoring the altitudinal variation of atmospheric density, the solution is $N \propto N_0 \exp(x/\lambda_e)$, where N_0 is the number of energetic seed electrons. Namely, the number of runaway electrons exponentially increases with longer length of acceleration region.

This model has been developed with computer-based simulations. Dwyer [2003] confirmed by a Monte-Carlo simulation that RREA processes take place with electric fields higher than the threshold E_{th}:

$$E_{\text{th}} = 0.284 \, \text{MV m}^{-1} \times \frac{\rho}{1.293 \times 10^{-3} \, \text{g cm}^{-3}}. \tag{2.14}$$

Babich et al. [2004] independently obtained a consistent result with Dwyer [2003]. The threshold field E_{th} is higher than the runaway threshold F_{min}/e, since Coulomb and Møller scatterings affect electron avalanches.

Electron multiplication in the RREA process is characterized by the acceleration length λ. Electron flux $F(L)$ is introduced as

$$F(L) = F_0 \exp(\xi), \, \xi = \int_0^L \frac{dz}{\lambda} \tag{2.15}$$
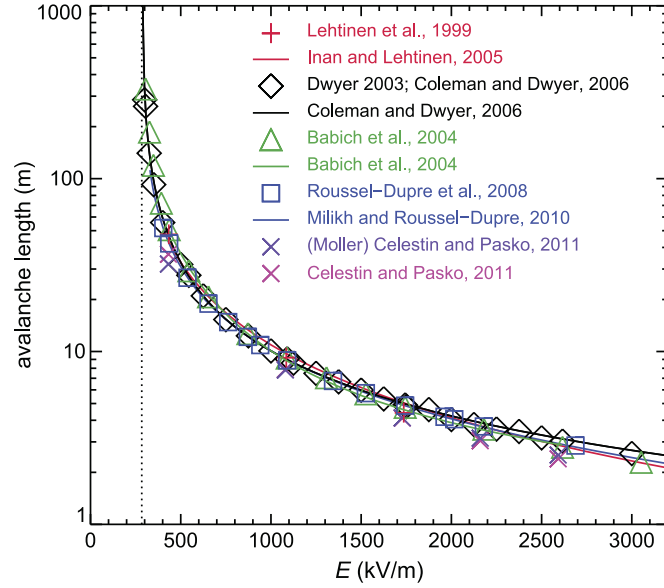
26

Figure 2.18: The relation between electric-field strength and avalanche length obtained by various simulations. Adapted from Dwyer et al. [2012b].

where L is a length from where electron acceleration begins, and F_0 is a seed electron flux at $L = 0$. This formula is simplified as an exponential function $F(L) = F_0 \exp(L/\lambda)$ when an uniform electric field is considered. The relation between electric-field strength and λ is obtained by simulation studies by Babich et al. [2004], Coleman and Dwyer [2006], Dwyer [2003], Inan and Lehtinen [2005], Lehtinen et al. [1999], Milikh and Roussel-Dupré [2010], Roussel-Dupré et al. [2008], and Celestin and Pasko [2011]. Dwyer et al. [2012b] reviewed these results, as shown in Figure 2.18. The relation in the standard atmosphere is empirically obtained as

$$\lambda \approx \frac{7.3 \text{ MeV}}{eE - 0.276 \text{ MV m}^{-1}}.$$ (2.16)

Furthermore, Sarria et al. [2018] inspected these results with different simulation frameworks such as `Geant4` [Agostinelli et al., 2003, Allison et al., 2006, 2016], GRanada Relativistic Runaway Simulator [Luque, 2014] and Runaway Electron Avalanche Model [Dwyer, 2003, 2007].

The energy spectrum of electrons in RREA is thought to settle down in a steady state after accelerated for a few acceleration length. Because the electron flux f_e increases $e \approx 2.71$ times as electrons travel λ, its temporal evolution is expressed with an electron velocity v and the avalanche e-fold time $\tau = \lambda/v$ as

$$\frac{f_e}{\tau} = \frac{df_e}{dt}.$$ (2.17)

Since electrons obtain energy per a unit time $d\epsilon/dt = v(eE - F_d)$,

$$\frac{df_e}{dt} = \frac{d\epsilon}{dt}\frac{df_e}{d\epsilon} = v(eE - F_d)\frac{df_e}{d\epsilon}$$ (2.18)

is obtained. Therefore, the electron spectrum is formulated as

$$f(\epsilon) \propto f_0 \exp\left(-\frac{\epsilon}{7.3 \text{ MeV}}\right).$$ (2.19)
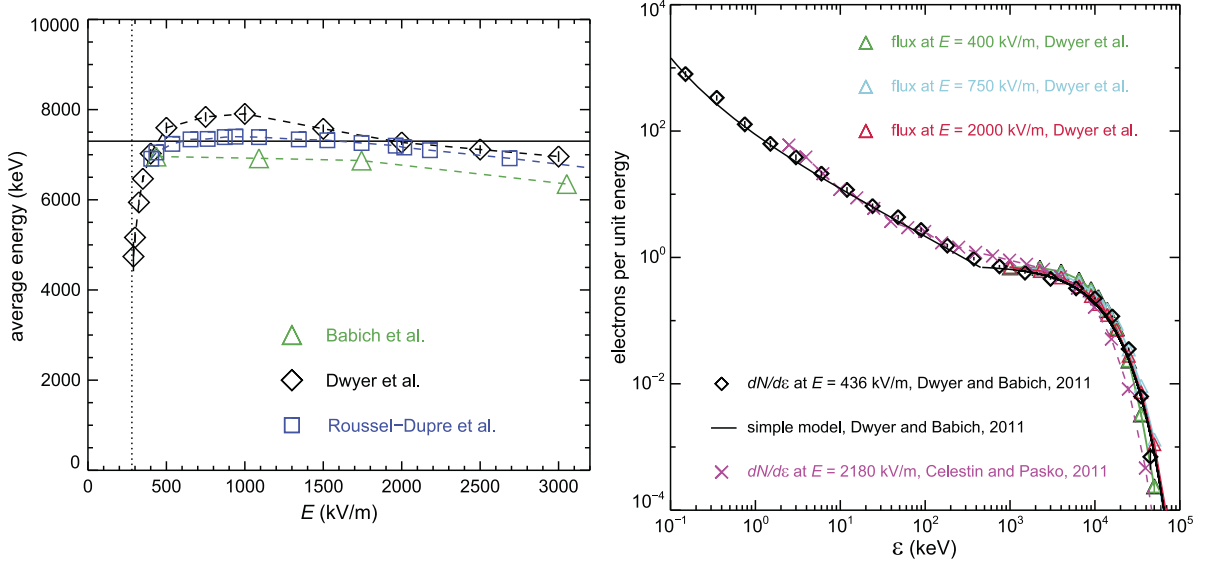
Figure 2.19: Average energy of avalanche electrons in a function of electric-field strength (left) and simulation results of electron spectra in RREA (right). Adapted from Dwyer et al. [2012b].

Figure 2.19 left shows average electron energy in RREA, obtained by Monte-Carlo simulations. When an electric field higher than 400 kV m^{-1} exists in the standard atmosphere, the average electron energy is approximately 7.3 MeV, regardless of electric-field strength. Therefore, with this electric-field condition, Equation 2.19 does not depend on electric-field strength. In fact, Monte-Carlo simulations confirmed that RREA spectrum follows an exponential function with a cutoff at ∼7.3 MeV above a few hundreds of keVs, as shown in Figure 2.19 right.

The accelerated electrons collide with ambient atmospheric nuclei, then emit bremsstrahlung. In the case of thin target, where electrons interact with the target once, a bremsstrahlung spectrum from electrons with monochromatic energy is proportional to ϵ^{-1}, where ϵ is an energy of bremsstrahlung photons, and exhibits a steep cutoff at the electron energy [Kotoku et al., 2007]. The bremsstrahlung spectrum from avalanche electrons F_γ is a convolution of a bremsstrahlung spectrum from monochromatic electrons and the electron spectrum. Therefore, it is approximately derived as [Dwyer, 2008]

$$F_\gamma \propto \epsilon^{-1} \times \exp\left(-\frac{\epsilon}{7.3 \text{ MeV}}\right). \tag{2.20}$$

This can reproduce the TGF spectrum obtained by RHESSI [Smith et al., 2005]. More precisely, this spectrum could be affected by atmospheric absorption and scattering.

Around the RREA threshold E_{th}, Coulomb scatterings significantly affect the RREA processes [Coleman and Dwyer, 2006]. Thus, Equation 2.16 is empirically modified around 300 kV m^{-1} as

$$\lambda \approx \frac{5.1 \text{ MeV}}{eE - 0.285 \text{ MeV m}^{-1}}. \tag{2.21}$$

This RREA process in relatively low electric fields can be applied to discussions on gamma-ray glows. It is noted that λ becomes longer than several kilometers when electric fields are almost E_{th}. In this case, these empirical relations cannot be applied because typical thunderstorms cannot maintain such large electric fields to realize the steady state of the RREA processes [Coleman and Dwyer, 2006, Cramer et al., 2017].
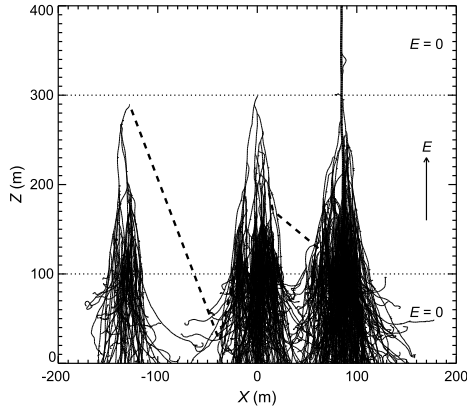
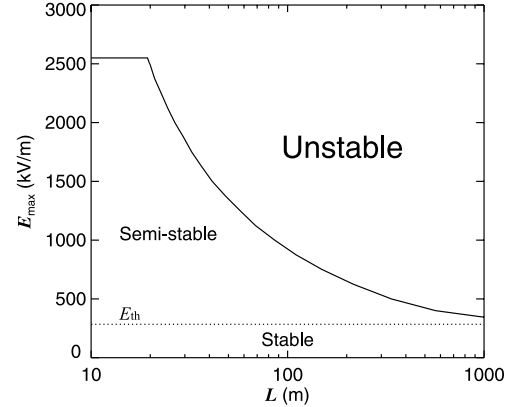Figure 2.20: Examples of electron avalanches and relativistic feedback. Adapted from Dwyer et al. [2012b].

Figure 2.21: The maximum electric field strength to host stable electron acceleration in a function of acceleration length in the standard atmosphere. Adapted from Dwyer [2003].

2.5.2 Relativistic feedback processes

The biggest problem of TGFs at the present is seed electrons. As in Equation 2.15, the simple RREA process provides larger multiplication ratio with longer acceleration distance L, while longer distance than several kilometers is not plausible in thunderstorms. In fact, Dwyer [2007] suggested that a multiplication factor of RREA $\exp(\xi)$ cannot exceed 10^5. In this case, the number of seed electrons is important to explain the enormous amount of energetic electrons in TGFs. However, Dwyer [2008] estimated that the flux of seed electrons required for TGFs detected by RHESSI is 5×10^5 times larger than the maximum flux of atmospheric cosmic rays. Therefore, another mechanism to produce seed electrons is required.

Dwyer [2003] introduced the relativistic feedback model, as a complementary process of RREA. This model describes that secondary particles created in RREA supply energetic seed electrons by themselves (Figure 2.20). Photons and electrons are thought to play a feedback role in this model. Bremsstrahlung photons emitted from runaway electrons travel to various directions, and produce energetic electrons via Compton scattering and photoabsorption. When these secondary electrons are produced in the upper of acceleration region, they can behave as seed electrons and trigger another avalanche. In the case of positron feedback, bremsstrahlung photons from avalanche electrons with energies of >1 MeV produce positrons via pair creation. In highly electrified region, they can become "runaway positrons" and move backward. Secondary electrons generated by the positrons via ionization also become seed electrons. These processes recursively increase the number of runaway electrons, not depending on the number of initial seed electrons in the atmosphere. Therefore, the relativistic feedback processes are a candidate to solve the seed-electron problem of TGFs.

Let us consider a temporal evolution of electron flux by the relativistic feedback processes F_{RF} [Dwyer, 2007]. As shown in Equation 2.15, electron flux in normal RREA is $F_{\mathrm{RREA}} = F_{\mathrm{seed}} \exp(\xi)$. Introducing an e-folding time τ, F_{RF} at a time point t is a sum of total runaway electrons generated by the feedback $F_n(t)$, formulated as

$$F_{\mathrm{RF}} = \sum_{n=0}^{t/\tau} F_n(t),\tag{2.22}$$

where n is the generation of feedback. $F_n(t)$ is included in a recursion formula with feedback parameter γ

$$F_{n+1}(t) = \gamma \int_0^t D(t - t') F_n(t') dt'. \tag{2.23}$$

The transportation function $D(t - t')$ is approximated with the Dirac delta function σ as $D(t - t') = \sigma(t - \tau - t')$. Therefore, using the relation $F_{n+1}(t) = \gamma F_n(t - \tau)$,

$$F_n(t) = \begin{cases} 0 & (t < n\tau) \\ \gamma^n F_{\text{seed}} \exp(\xi) & (t \geq n\tau) \end{cases} \tag{2.24}$$

and

$$F_{\text{RF}} = F_{\text{seed}} \exp(\xi) \sum_{n=0}^{t/\tau} \gamma^n \tag{2.25}$$

are obtained. The formula of sequence summation

$$\sum_{n=0}^{t/\tau} \gamma^n = \begin{cases} \frac{\gamma^{(t/\tau)+1} - 1}{\gamma - 1} & \gamma \neq 1 \\ (t/\tau) + 1 & \gamma = 1 \end{cases} \tag{2.26}$$

derives

$$F_{\text{RF}} = \begin{cases} F_{\text{seed}} \exp(\xi) \exp(t/\tau')/(\gamma - 1), \ \tau' \equiv \tau/\ln(\gamma) & \gamma > 1 \\ F_{\text{seed}} (t/\tau) \exp(\xi) & \gamma = 1 \\ F_{\text{seed}} \exp(\xi)/(\gamma - 1) & \gamma < 1 \end{cases} \tag{2.27}$$

valid in a time domain of $t \gg \tau$.

When $\gamma < 1$, the feedback processes are in a semi-steady state. Namely, electron flux does not depend on time, and quasi-stable acceleration continues. This state is thought to be applied to gamma-ray glows with high electron fluxes [Kelley et al., 2015]. On the other hand, electron flux diverges as time goes in the case of $\gamma \geq 1$. In electric fields of $\gg$500 kV m^{-1}, τ is less than 2 microseconds (see FIG.8 in Dwyer [2007]). Therefore, the number of runaway electrons is divergent in time scale of milliseconds or shorter, and TGFs can take place [Dwyer, 2007]. The parameter γ depends on electric-field strength and acceleration length. Figure 2.21 shows the condition where $\gamma = 1$ in the E-field–acceleration length plane. When electric fields are weak and acceleration length is short, semi-stable feedback with $\gamma < 1$ takes place. When long and strong electric fields exist, electron flux would be divergent with $\gamma \geq 1$ and the electric field would short-circuit.

2.5.3 Thermal runaway process

Another model to explain the problem of TGF seed electrons is thermal runaway electron production. As in Figure 2.16, the drag force to electrons by ionization has the maximum at $\sim$130 eV ($\sim$30 MV m^{-1}: thermal runaway threshold [Gurevich, 1961]). This is 10 times higher than the breakdown threshold (3 MV m^{-1}). When ambient electric fields are higher than the thermal runaway threshold, even thermal electrons with energies of a few eV can accelerate to relativistic energy, by getting over the maximum of the drag force. Whether such extremely high electric fields can exist has not been clear, but recent studies suggest their existence in lightning processes [Celestin and Pasko, 2011, Celestin et al., 2015, Moss et al., 2006].

In the tip of stepped leaders, a filament-like structure called streamer develops, which has lower conductivity than leaders. Moss et al. [2006] and Celestin and Pasko [2011] confirmed
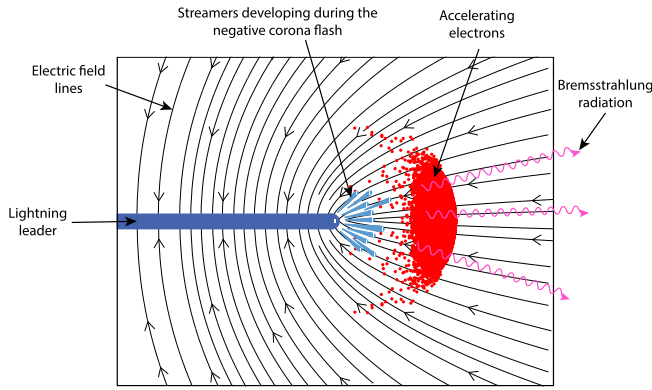
Figure 2.22: A schematic view of thermal runaway electron production in the tip of streamers. Adapted from Celestin et al. [2015].
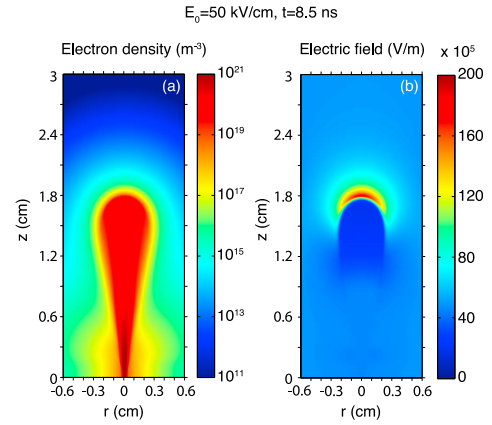

Figure 2.23: Cross-sectional views of electron density (left) and electric field (right) developed in an ambient electric field of 5 MV m^{-1}. Adapted from Celestin and Pasko [2011].
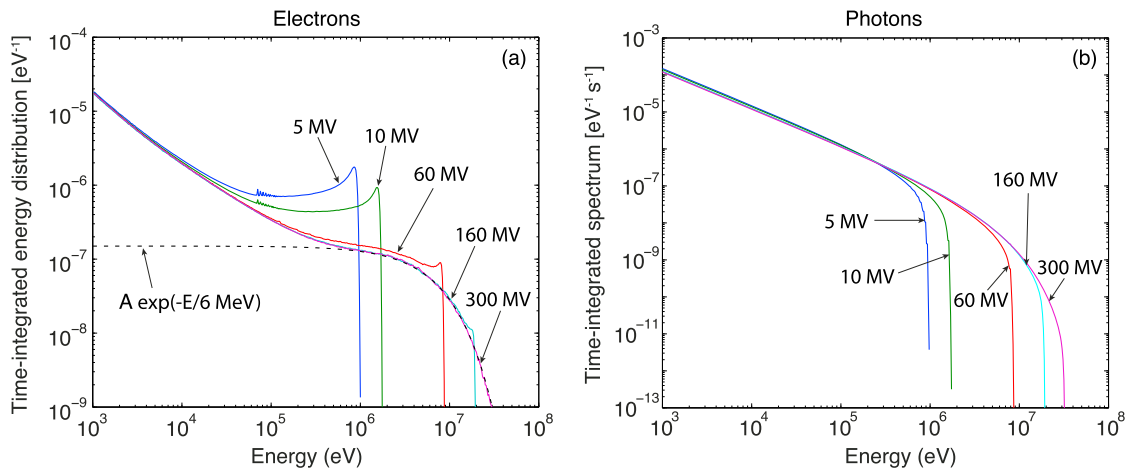

Figure 2.24: Electron and gamma-ray spectra produced in potential drops around electron-seeding streamers. Adapted from Celestin et al. [2015].

by simulations that electric fields 10 times higher than the breakdown threshold can be locally created in the tip of streamers by concentration of electric fields. In such highly-electrified region, thermal electrons can become runaway electron, and be accelerated up to 100 keV, on average 60 keV [Celestin and Pasko, 2011]. These electrons cannot emit MeV photons, but they can further accelerate to tens of MeV if electric fields of >300 kV m^{-1} with enough acceleration distance exist around the streamers. A streamer is calculated to produce 10^{19} electrons s^{-1}. Assuming that 10^6 streamers are produced in the tip of a stepped leader, 10^{16} electrons with energies of several tens of keV can be produced in 1 ns. If these electrons are accelerated to MeV or tens of MeV, the number of energetic electrons is comparable to that in TGFs ($\sim 10^{17}$: Dwyer and Smith [2005]) without any further avalanche processes. In addition, if ambient electric-field potential surrounding streamers reaches 300 MV, the electron spectrum in the thermal runaway electron process approximately follows $\exp(\epsilon/6\,\mathrm{MeV})$, whose bremsstrahlung

spectrum is consistent with observed TGF spectra (Figure 2.24: Celestin et al. [2015]).

2.5.4 Modification of spectra

Even in lower electric fields than the RREA threshold, charged particles in secondary cosmic rays can be accelerated against atmospheric attenuation [Dorman and Dorman, 2005, Muraki et al., 2004]. When electric fields are weaker than the runaway (0.216 MV m^{-1} at sea level) and avalanche (0.284 MV m^{-1}) threshold, they cannot produce runaway electrons nor trigger avalanches. However, the electron spectrum of secondary cosmic rays extending to several hundreds of MeVs can be changed by the electric fields. This process is called "Modification of Spectra" (MOS: Chilingarian et al. [2014, 2012]) Chilingarian et al. [2014, 2012] and Cramer et al. [2017] performed Monte-Carlo simulations that they input the cosmic-ray spectrum provided by EXPACS/PARMA model [Sato, 2015, 2016] into a weak electric field. Figure 2.25 shows a comparison between an original cosmic-ray-induced gamma-ray spectrum and an excess component by MOS. The excess component is $\sim$10% of the original component, and extends to several tens of MeVs. This model is thought to be applied to gamma-ray glows and TGEs with low gamma-ray fluxes. This mechanism is also considered for acceleration and deceleration of muons. In fact, Hariharan et al. [2019] demonstrated an existence of 1.3 GV potential inside a thundercloud by monitoring muons with the muon telescope GRAPE-3 installed in India.
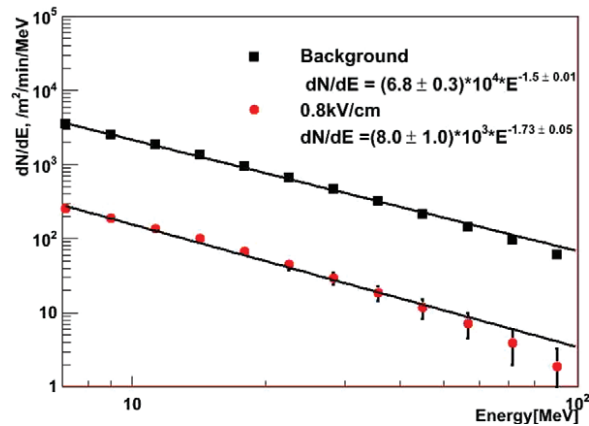

Figure 2.25: Gamma-ray spectra of secondary cosmic rays and an excess component created by MOS. Adapted from Chilingarian et al. [2014].

2.6 Basics of Neutron Physics

This section describes neutron reactions utilized in the present thesis. Here neutron energy is considered to be non-relativistic, which is justified by the fact that the typical energy of photoneutrons is less than 20 MeV, much lower than the neutron rest-mass energy of 940 MeV. Considering reactions with relatively light elements in the atmosphere or soil, there are four major reactions with neutrons: elastic and inelastic scatterings, neutron capture, and charged-particle production. Figure 2.26 shows cross sections of these reactions with nuclides considered in the present thesis such as ^{1}H, ^{14}N, ^{16}O, ^{27}Al, ^{28}Si, and ^{40}Ar.
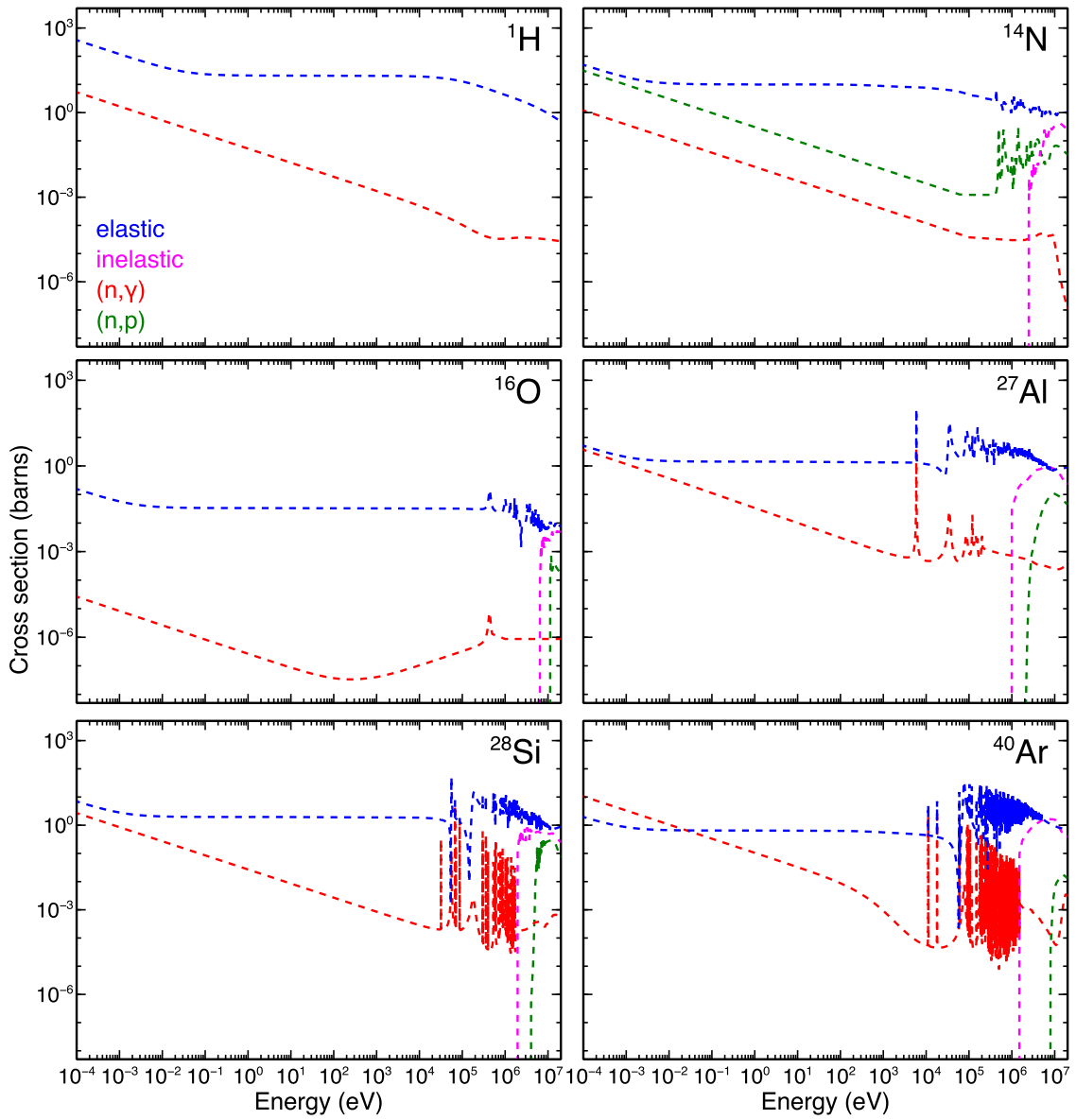
Figure 2.26: Cross sections of neutron reactions as a function of neutron kinetic energy, extracted from JENDL-4.0 [Shibata et al., 2011].

2.6.1 Elastic scattering

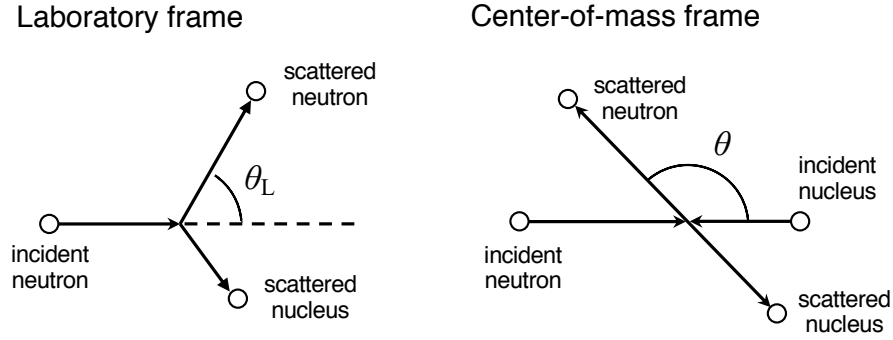Laboratory frame Center-of-mass frame

Figure 2.27: Diagrams of an elastic scattering with a neutron in the laboratory frame and in the center-of-mass frame.

Elastic scattering is the most major reactions with neutrons. Here kinetic energy of scattered neutrons is considered based on expertises in radiation engineering [Lamarsh and Baratta, 2001, The Institute of Electrical Engineers of Japan, 1982]. Let us consider the situation shown in Figure 2.27: a neutron is elastically scattered with an angle of θ_L in the laboratory frame, or θ in the-center-of-mass frame. Considering the laws of conservation of energy and momentum, the ratio of kinetic energies of a neutron before (E) to after (E') the scattering is

$$\frac{E'}{E} = \frac{A^2 + 1 + 2A\cos\theta}{(A+1)^2}, \tag{2.28}$$

where A is the ratio of the neutron mass to a mass of a target nucleus. When $\theta = \pi$, E' becomes its minimum as

$$E'_{\min} = \left(\frac{A-1}{A+1}\right)^2 E = \alpha E, \tag{2.29}$$

where $\alpha = [(A-1)/(A+1)]^2$ is the collision parameter. Also E' becomes its maximum as $E'_{\max} = E$ when $\theta = 0$ (i.e. no collisions occur). Considering the relation between the laboratory and center-of-mass frames, θ_L is expressed as

$$\cos\theta_L = \frac{A\cos\theta + 1}{\sqrt{A^2 + 1 + 2\cos\theta}}. \tag{2.30}$$

In the center-of-mass frame, the scattered neutron is emitted isotropically. Namely, the probability dP of neutron emission per unit steradian is

$$dP = \frac{\sin\theta d\theta}{2}. \tag{2.31}$$

By differentiating Equation 2.28,

$$\frac{dP}{d\theta} = \frac{2A\sin\theta}{(A+1)^2}E, \tag{2.32}$$

and hence,

$$\frac{dP}{dE'} = \frac{dP}{d\theta} \times \frac{d\theta}{dE'} = \frac{(A+1)^2}{4AE} = \text{const.} \tag{2.33}$$

are obtained. Namely, the energy distribution is constant in the range of $\alpha E \leq E' \leq E$, like a square-wave shape. Therefore, the average of E' is calculated as

$$\overline{E'} = \int_{\alpha E}^{E} E' \frac{dP}{dE'} dE' = E \left[1 - \frac{2A}{(A+1)^2} \right]. \tag{2.34}$$

It is convenient to introduce the lethargy $\xi = \langle \ln E/E' \rangle$ to consider averaged neutron energies after multiple elastic scatterings. By utilizing the equations derived above,

$$\xi = \langle \ln E/E' \rangle = \frac{\int_{\alpha E}^{E} \ln \frac{E}{E'} \frac{dP}{dE'} dE'}{\int_{\alpha E}^{E} \frac{dP}{dE'} dE'} = 1 + \frac{(A-1)^2}{2A} \ln \frac{A-1}{A+1} \tag{2.35}$$

is obtained. When considering nuclei with a large atomic number A, ξ can be approximated as

$$\xi \approx \frac{2}{A + 2/3}. \tag{2.36}$$

Therefore, when a neutron with an initial energy of E_0 is elastically scattered n-times, its expected energy after n-th scatterings E_n is expressed as

$$E_n = E_0 \exp(-n\xi). \tag{2.37}$$

2.6.2 Inelastic scattering

As well as elastic scatterings, inelastic scatterings can also occur when kinetic energy of incident neutrons is higher than the lowest excitation level of target nuclei. In this case, the kinetic energy of incident neutrons are distributed not only to kinetic energies of the scattered neutron and nucleus, but also to excitation energy of the target nucleus. The excited nucleus immediately goes back to the ground state by emitting de-excitation gamma-ray lines.

2.6.3 Neutron capture

One of the major reactions which absorb neutrons is neutron captures. In this reaction, a target nucleus absorb a neutron, and transforms into an isotope. Furthermore, the produced isotope is excited by the binding energy of the neutron, and immediately goes back to the ground state by emitting de-excitation gamma-ray lines. The energy of de-excitation gamma rays corresponds to excitation levels of the produced isotope. Table 2.1 summarizes energies and branch ratios of de-excitation gamma rays by neutron captures with ^{14}N, ^{27}Al and ^{28}Si.

2.6.4 Charged-particle production

It is possible that another nucleon is emitted when a neutron is absorbed by a target nucleus. The reaction absorbing a neutron and emitting a proton is called charged-particle production. Only ^{14}N is capable of charged-particle production with low-energy neutrons among nuclides considered in the present thesis. ^{14}C, the product of charged-particle productions by ^{14}N, is an important isotope for radiocarbon dating. They are usually produced by neutrons of cosmic-ray origin.

Table 2.1: De-excitation gamma-ray lines from neutron captures with ^{14}N, ^{27}Al and ^{28}Si.

^{14}N		^{27}Al		^{28}Si	
Energy (MeV)	Ratio (%)	Energy (MeV)	Ratio (%)	Energy (MeV)	Ratio (%)
1.678	26.66	0.031	100.00	1.273	24.05
1.885	62.86	0.983	15.77	2.093	27.85
2.000	13.76	1.408	11.11	3.539	100.00
2.520	18.69	1.623	16.49	4.934	93.50
3.532	29.94	2.108	10.04	6.38	16.04
3.678	48.63	2.283	16.85	7.199	10.04
4.509	55.96	2.59	15.05		
5.269	100.00	2.821	13.98		
5.298	71.10	3.034	31.54		
5.533	65.57	3.465	25.09		
5.562	35.77	3.591	16.85		
6.322	61.05	3.849	11.11		
7.299	31.45	4.133	24.73		
8.310	13.80	4.260	24.37		
10.829	47.89	4.691	16.49		
		4.734	19.71		
		4.903	11.11		
		5.134	10.75		
		7.693	11.83		
		7.724	96.06		

Chapter 3

Instrumentation and Observation

Since 2006, we have been performing the Gamma-Ray Observation of Winter Thunderclouds (GROWTH) experiment, an on-ground observation program for high-energy phenomena during winter thunderstorms in Japan [Tsuchiya et al., 2007, 2011, 2013, Umemoto et al., 2016]. In 2015, we launched a mapping observation program; observation network with compact gamma-ray detectors has been constructed in coastal areas of the Japan Sea [Enoto et al., 2018, 2017, Wada et al., 2018, 2019a,b,c]. Because of gamma-ray attenuation in the atmosphere, a single detector can cover only an area within 1-2 km from its location. It is therefore important to deploy multiple gamma-ray detectors for covering wider area and for increasing the number of event detections. In addition, detections of an identical event by multiple detectors allow us to examine more detailed nature of the event such as spatial distribution of gamma-ray fluxes than by a single detector.
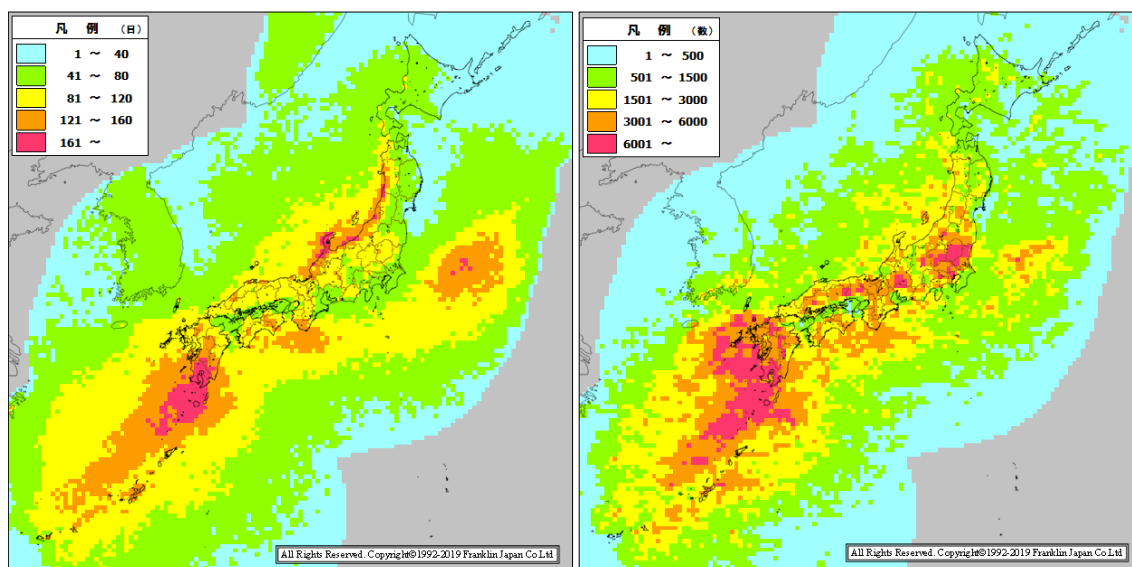

Figure 3.1: Contour maps of thunder days (left) and density (right) around Japan. Provided by Franklin Japan Co., Ltd.[3] Thunder day is defined as the number of days that Japanese Lightning Detection Network (JLDN) recorded one or more lightning discharges in a region. Density of lightning is as the number of lightning discharges JLDN recorded in a region. The data is accumulated in 5 years from 2014–2018.

---

[3]https://www.franklinjapan.jp/contents/lightning/data/

3.1 Winter Thunderstorms

Winter thunderstorms in coastal areas of the Sea of Japan provide unique features comparing to other thunderstorms in the world (e.g. Rakov and Uman [2003]), and they have been studied by sferics and radar observations since 1970s. During winter seasons in Japan, seasonal northwest winds are provided by Siberian Anticyclone staying on the Eurasian Continent and depressions on the Sea of Okhotsk and the Pacific. When these dried and cold winds pass over the Sea of Japan, water vapor is provided by the Tsushima Warm Current, which flows in the Sea of Japan from west to north. Then the winds bring heavy snow in coastal and mountainous areas in Japan. If ascending air currents take place in coastal areas, the winds also provide thunderstorms.

Figure 3.1 presents contours of the number of days with lightning (or thunder days) and density around Japan. Notably, lightning flashes occur in more than 30 days per year along the north coast of the main island of Japan. The Japan Meteorological Agency reports that Kanazawa City, Ishikawa Prefecture in the Hokuriku area shows the greatest number of thunder days in Japan: 42.4 days per year on average from 1981 to 2010.[4] On the other hand, the number of lightning strikes in Kanazawa is not as many as those in other regions. This indicates that winter thunderstorms frequently take place in Kanazawa, but each thunderstorm hosts a smaller number of lightning discharges in its lifecycle than summer ones. This unique feature of winter lightning is called "single-flash thunderclouds", as Michimoto [1993] reported.
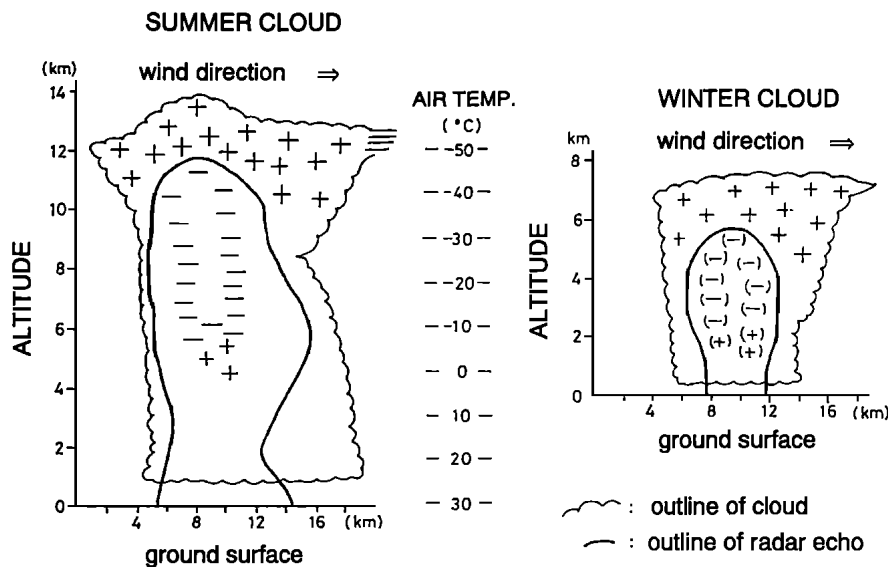

Figure 3.2: Comparison of thundercloud structures in summer and winter. Adapted from Kitagawa and Michimoto [1994].

Winter thunderstorms taking place in coastal areas of the Sea of Japan have some unique features which do not appear in summer thunderstorms. The most important one is the cloud structure developed at a lower altitude than summer [Kitagawa, 1992, Kitagawa and Michimoto, 1994]. Figure 3.2 shows structures of summer and winter thunderclouds. Typical thunderclouds have a tripolar structure of charges produced by collisions of ice crystals and droplets [Takahashi, 1978]. The altitude with a temperature of $-10°C$, where a negative charge region forms, is 5–6 km in summer, while $\sim$2 km in winter. The cloud top is at $\sim$15 km in summer while

---

[4]https://www.jma.go.jp/jma/kishou/know/toppuu/thunder1-1.html

38

5–7 km in winter, and cloud bases in winter also get lower around 0.2–0.8 km [Goto and Narita, 1992]. The lower altitude of cloud bases makes several distinctive features: In winter thunderstorms, the ratio of positive lightning, which discharges positive charges in thunderclouds to the ground, to negative lightning is higher than in summer [Miyake et al., 1992]. Upward lightning also frequently occurs, whose leaders develop from a tip of tall buildings into thunderclouds [Miyake et al., 1990].

The lower cloud bases of winter thunderclouds make on-ground radiation measurements feasible. Electron ranges in the standard atmosphere at sea level are 3.8 m and 40.2 m at 1 MeV and 10 MeV, respectively, while mean free paths of gamma-ray photons are 122 m and 380 m at 1 MeV and 10 MeV, respectively. Since electrons and gamma rays generated above 1-km altitudes are absorbed before reaching the ground, gamma-ray glows produced in summer thunderstorms, whose cloud bases are higher than a 3 km altitude, cannot be detected at sea level. On the other hand, gamma rays generated in winter thunderstorms lower than 1 km can reach the ground. Based on these facts, on-ground radiation measurements during winter thunderstorms in Japan have been performed by Torii et al. [2002, 2004, 2011], Yoshida et al. [2008], and Kuroda et al. [2016] besides the GROWTH collaboration.

3.2 Detector Development

The present thesis employs original compact gamma-ray detectors with scintillation crystals which are sensitive to photons of several to tens of MeVs. We developed these detectors for the mapping observation program.

3.2.1 Scintillation crystals

We employ inorganic scintillation crystals as the main gamma-ray detection unit. Specification of representative inorganic crystals such as NaI, CsI, BGO ($Bi_4Ge_3O_{12}$), GSO (Gd_2SiO_5), $LaBr_3$, and a plastic scintillator EJ-200 for comparison is shown in table 3.1. When gamma-ray photons enter scintillators, either photoabsorption, Compton scattering or pair creation takes place stochastically. Figure 3.3 shows reaction probability between gamma rays and scintillators of 2.5 cm thickness. In general, scintillators including heavy nuclei such as Bi and Ge have large cross section of photoabsorption.

Table 3.1: Specification of scintillation crystals.[5,6,7]

type (doped element)	NaI (Tl)	CsI (Tl)	BGO	GSO (Ce)	LaBr$_3$ (Ce)	EJ-200
density (g cm^{-3})	3.67	4.51	7.13	6.71	5.08	1.02
refractive index	1.85	1.80	2.15	1.85	1.9	1.58
decay time (ns)	230	680	300	56	16	2
light output (photons MeV^{-1})	38,000	65,000	8,200	9,000	63,000	10,000
peak wavelength (nm)	415	540	480	440	380	425
deliquescence	yes	slightly	no	no	yes	no

[5]Knoll [2000] for NaI, CsI, BGO, and GSO.

[6]https://www.crystals.saint-gobain.com/products/standard-and-enhanced-lanthanum-bromide for LaBr$_3$.

[7]https://eljentechnology.com/products/plastic-scintillators/ej-200-ej-204-ej-208-ej-212 for EJ-200.

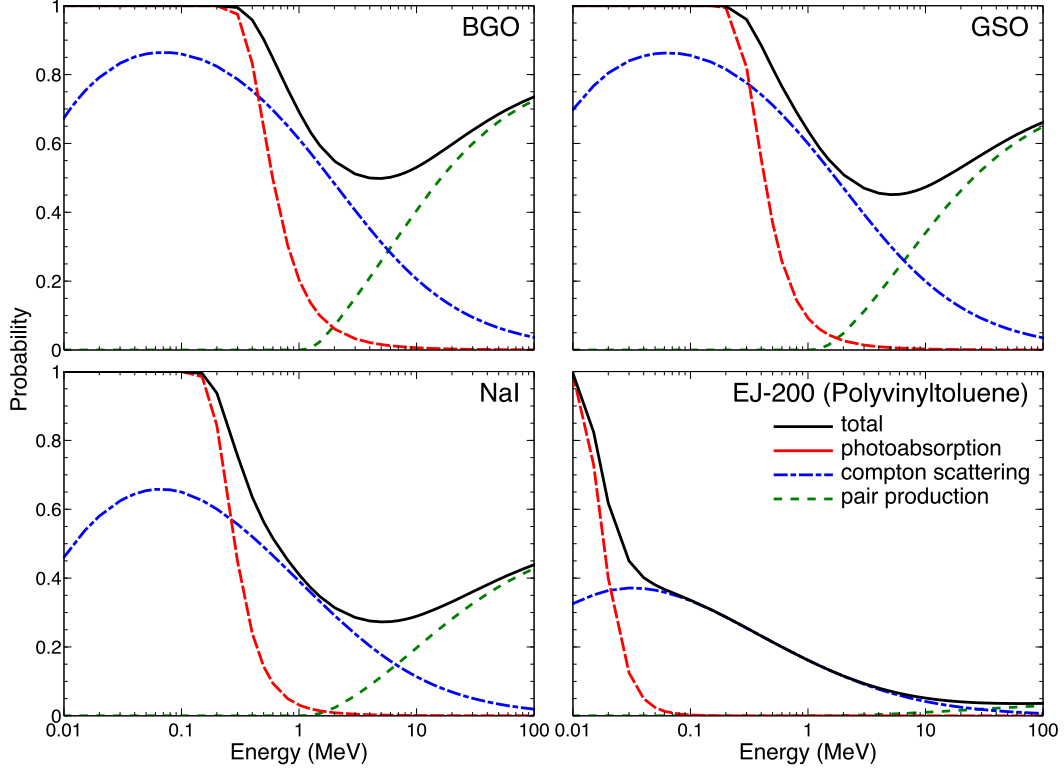[8]http://physics.nist.gov/PhysRefData/Xcom/html/xcom1.html

Figure 3.3: Probability of photoabsorption, Compton scattering, and pair production with gamma rays in 2.5-cm-thick scintillators, extracted from NIST/XCOM.[8]

In the present study, three types of scintillators, BGO, NaI, and GSO are employed. We utilized two types of shape for BGO crystals. Type 1 is a cuboid of $25.0 \times 8.0 \times 2.5$ cm^3, shown in Figure 3.4. The crystals are coupled with two photo-multipliers (PMTs: Hamamatsu R1924), and shielded by 3-mm-thick aluminum. They are provided by Sakurai Radioactive Isotope Group, RIKEN Nishina Center and Nuclear Experiment Group, The University of Tokyo. Type 2 is a cylinder of $\phi7.62$ cm $\times$ 7.62 cm, coupled with a PMT (Hamamatsu R6231) and shielded by 3-mm-thick aluminum. BGO crystals are suitable for detection of $\geq$10 MeV gamma rays due to large cross section and high density, although light output is only 22% of NaI. In addition, they are not suffered from high humidity in winter because they are not deliquescent. A NaI scintillator used in this study is also a cylinder of $\phi7.62$ cm $\times$ 7.62 cm, coupled with a photo-multiplier (Hamamatsu R1306) and shielded by 3-mm-thick aluminum.

GSO scintillators are a cuboid of $2.0 \times 2.0 \times 0.5$ cm^3, which are spares for the Hard X-ray Detector onboard the X-ray Astronomy Satellite "Suzaku". These are connected with a photo-multiplier of Hamamatsu R7600U. GSO scintillators are employed for neutron detection, rather than photon detection. Figure 3.5 shows cross sections of neutron-capture reactions with ^{155}Gd, ^{156}Gd, ^{157}Gd and ^{158}Gd included in GSO crystals Among Gd isotopes, nuclei containing an odd number of neutrons have a large cross section to neutrons, and they have been utilized as neutron detectors [Kuroda et al., 2012, Marti-Magro and Super-Kamiokande Collaboration, 2017, Oguri et al., 2014]. When the Gd nuclei capture a neutron, they emit de-excitation gamma rays; ^{155}Gd mainly emits gamma-ray lines at 88.97 and 199.22 keV, and ^{157}Gd at 79.51 and 181.94 keV. Since the de-excitation gamma-ray lines are self-absorbed in the GSO scintillators, the large cross section of GSO scintillators to neutrons allowed us to use them as thermal neutron
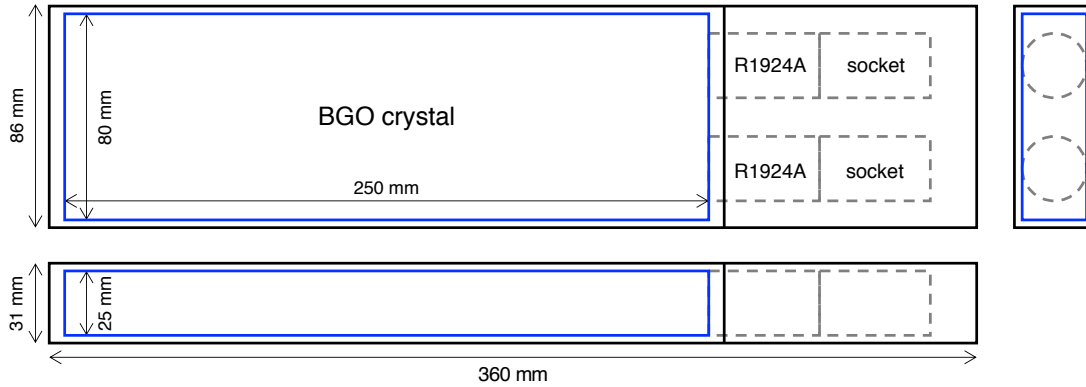
Figure 3.4: A schematic view of Type 1 BGO, a cuboid of $25.0 \times 8.0 \times 2.5$ cm^3.
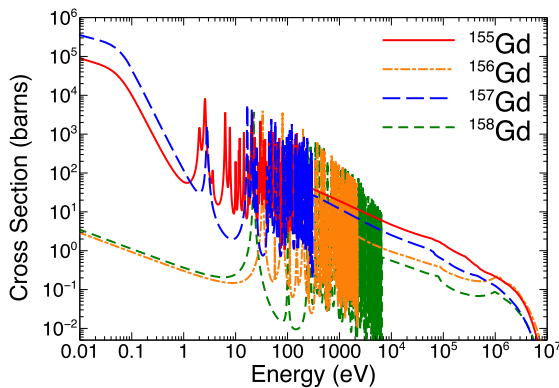

Figure 3.5: Cross sections of neutron capture with Gd isotopes, extracted from JENDL-4.0 [Shibata et al., 2011].
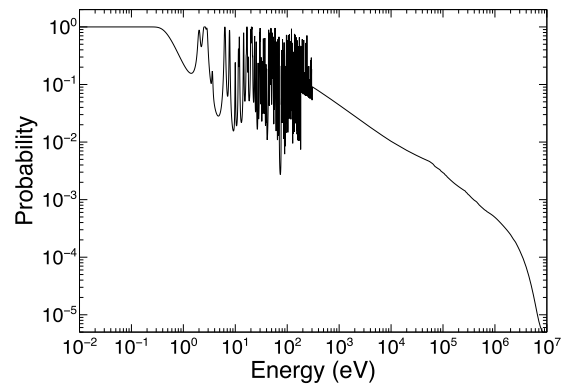
Figure 3.6: Probability of neutron capture in 5-mm-thick GSO scintillators, calculated with JENDL-4.0 [Shibata et al., 2011].

detectors. Neutron-capture probability of 5-mm-thick GSO scintillators used in this study is shown in Figure 3.6.

3.2.2 Data acquisition system

Minimizing data acquisition (DAQ) system is a key to develop compact gamma-ray detectors, because other components such as scintillators have to be as large as possible to enlarge effective areas to gamma rays. Therefore, we developed a dedicated DAQ system for the mapping observation program. It consists of three components: a field-programmable gate array/analog-to-digital converter (FPGA/ADC) board, an analog processing board to be connected with PMTs, and a small Linux computer Raspberry Pi. A summary of the DAQ system is shown in Figure 3.7.

The GROWTH FPGA/ADC board was developed by Dr. Takayuki Yuasa and Shimafuji Electric Incorporated.[9] Two 12 bit/2 ch flash ADC chips (Analog Devices AD9231; 4 ch in total) and an FPGA chip (Xilinx Artix-7 XC7A35T-2FTG256C) are onboard. The dimension of the FPGA/ADC board is 9.5×9.5 cm^2.
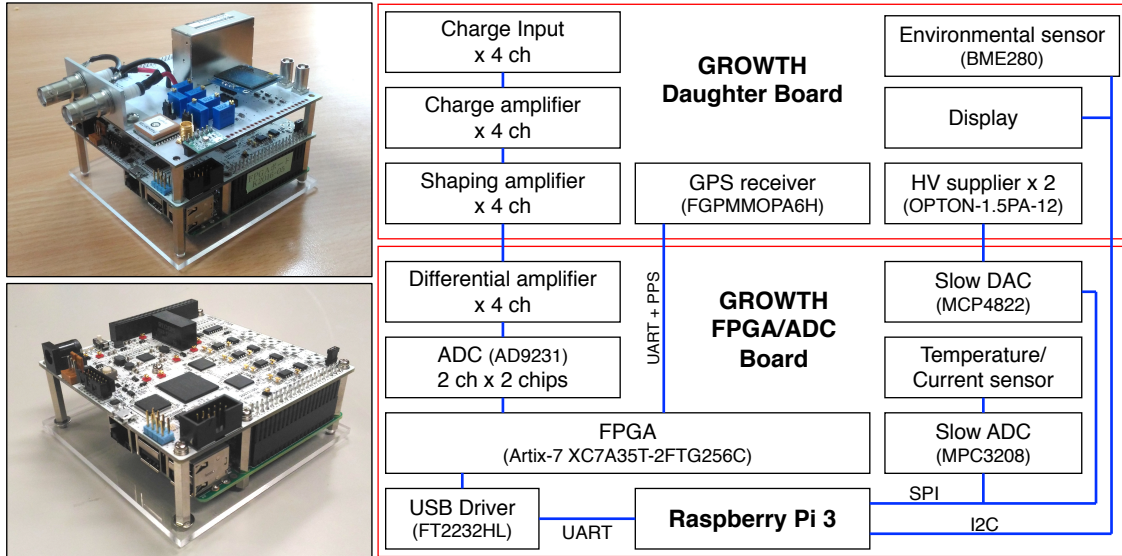
---

[9]http://www.shimafuji.co.jp/en/products/808

Figure 3.7: An overview of the DAQ system. Left-top: the GROWTH daughter board on the GROWTH FPGA/ADC board. Left-bottom: the GROWTH FPGA/ADC board with a Raspberry Pi. Right: a schematic diagram of the system.

This board obtains pulse signals by self-triggered and event-by-event schemes. Input signals (±5 V) are buffered by a differential amplifier, digital-sampled by a 50 MHz ADC. The digitized signals are then sent to the FPGA. The FPGA always store 20 samples (for 400 ns at 50 MHz sample rate). When the FPGA detects a signal exceeding a trigger threshold in the 20 samples, it stores following 500–1000 samples (10–20 μs at 50 MHz). Two types of trigger thresholds are employed: fixed thresholds and differential thresholds based on running average. In the stored samples, detection time, triggered channel, trigger number, the maximum, minimum, first, and last values are extracted. The trigger number counts up every detected event. If a pulse event is triggered but not properly transferred to Raspberry Pi, the corresponding trigger number is not registered in the event list. Detecting the unrecorded trigger number is utilized for the dead-time correction.

The FPGA can be connected with a global positioning system (GPS) receiver, and calibrate the detection time with better than 1 μs accuracy. The extracted data by the FPGA is transferred to a Raspberry Pi computer by the Universal Asynchronous Receiver/Transmitter (UART) protocol via a USB driving device FT2232HL. The theoretical maximum rate of data transfer is 36 kHz with the maximum speed of UART (8 Mbps). However, an effective transfer rate is limited up to $\sim$10 kHz because the processing ability of Raspberry Pi is not enough to receive all event packets.

In addition, another ADC (Microchip Technology MCP3208) and digital-analog convertor (DAC; Microchip Technology MCP4822) chips controllable by Raspberry Pi with Serial Peripheral Interface (SPI) are onboard. This ADC is connected to onboard current sensors, and monitors power supply modules to record housekeeping data of the DAQ system.

For analog processing, we utilize the GROWTH daughter board to read signals from PMTs with the GROWTH FPGA/ADC board. The daughter board was developed and designed by the author, manufactured and soldered by p-ban.com Corp. Its dimension is 9.5×9.5 cm^2, and can be stacked on the GROWTH FPGA/ADC board (the left-top picture of Figure 3.8). On the daughter board, 4 ch charge amplifiers, waveform-shaping amplifiers, and high-voltage
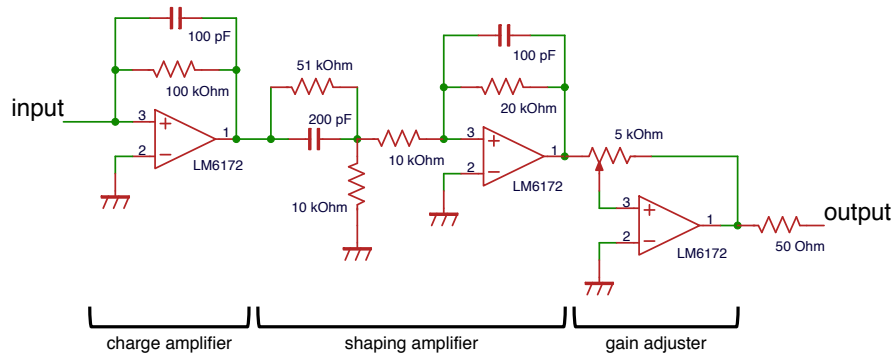
Figure 3.8: A circuit diagram of the charge and waveform-shaping amplifiers onboard the GROWTH daughter board.

(HV) supply modules to PMTs are mounted. A circuit diagram of the charge and waveform-shaping amplifiers is shown in Figure 3.8. The amplifiers consist of 3 channels of operation amplifiers (Texas Instruments LM6172). The time constants of charge and waveform-shaping amplifiers are 10 and 2 μs, respectively. We employ Matsusada OPTON-1.5PA-12 as a HV module for PMTs. Their output voltage is controlled by reference voltage or a potentiometer from 0 to 1500 V. In the present case, the reference voltage was produced by the Raspberry-Pi-controlled DAC and connected to the HV module via a buffer circuit. Besides the amplifiers and HV modules, a GPS receiver (Global Top FGPMMOPA6H), a small liquid-crystal display and an environmental sensor recording humidity, temperature, and pressure (Bosch Sensortec BME280) are onboard. Signals from these devices are transferred to the FPGA/ADC board and Raspberry Pi. The FPGA/ADC board, daughter board, HV module and Raspberry Pi consume 3.1, 1.7, <1.0 and <5 W, respectively.

3.2.3   Compact detectors

Compact gamma-ray detectors employed in this study consist of the DAQ system, scintillation crystals and a telecommunication device. The inside and outside of the detector system are shown in Figure 3.9. All components are packed in a water-proof box of $45 \times 35 \times 20$ cm^3 (Takachi BCAR354520T). In total eight compact detectors were manufactured. Seven of them contain a BGO type 1, and some are additionally equipped with a GSO scintillator. The other contains a BGO type 2.

Components of the detectors are mounted on a base aluminum plate. This plate is connected to another aluminum plate outside the detector with 4 aluminum M10 bolts to transfer the inner heat to outside. When a temperature is 25°C outside and 40°C in the water-proof box, in total 15 W can be exhausted via the aluminum bolts. This cooling system is required to keep the detector in a normal operating temperature (<50°C) especially when it is in fine weather.

High-speed network connection (4G LTE) is provided via a mobile router device (NEC Aterm MR05LN). Raspberry Pi is wire-connected to the router. To monitor the state of detectors, Raspberry Pi sends every 5 minutes a telemetry called house keeping data, consisting of device temperature, humidity, and atmospheric pressure. Also we can remotely connect to Raspberry Pi by the port-forwarding scheme.
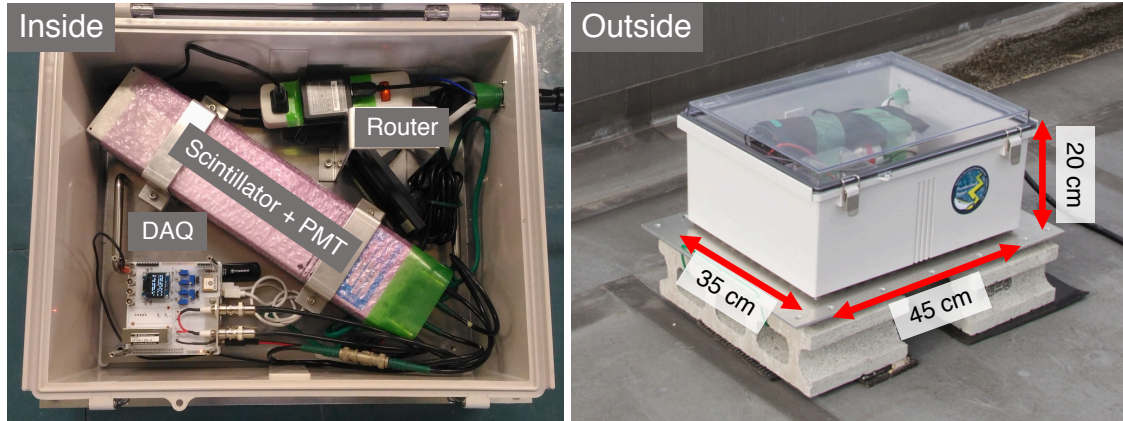
Figure 3.9: Inside and outside photos of a compact gamma-ray detector.

3.2.4 Stationary detectors in Kashiwazaki

Besides the compact detectors, two stationary detectors are employed, and were operated in Kashiwazaki, Niigata, Japan. One is developed for observation of gamma-ray glows. It is equipped with eight type 1 BGO crystals, and collimators made of lead are attached to six of them. Signals from 8 BGO crystals are read by two DAQ system. In this study, only one BGO which is not equipped with the collimator is used for analysis. Therefore, basic characteristics of this detector is the same as the compact detectors with the type 1 BGO.

The other was developed by Dr. Harufumi Tsuchiya in 2010 [Tsuchiya et al., 2013]. This detector in 2016 consist of a NaI scintillator and another DAQ system with self-triggered and event-by-event schemes. Signals from a PMT are amplified and digital sampled by a 12 bit ADC (Analog Devices AD7862-10), then timing and pulse height are recorded. The absolute timing of the DAQ system is conditioned by GPS signals with 100 μs accuracy. In 2017, a GSO scintillator coupled with the GROWTH FPGA/ADC board was additionally equipped with the detector.

Table 3.2: Configuration and operation log of radiation detectors in FY2016.

No.	area	type	crystal	range (MeV)	operation period
1	Kashiwazaki	compact	BGO type 1	0.35–13.0	2016.12.05–2017.04.12
2	Kashiwazaki	compact	BGO type 1	0.35–13.0	2016.12.05–2017.04.12
3	Kashiwazaki	stationary	BGO type 1	1.2–48.0	2016.12.05–2017.04.12
4	Kashiwazaki	stationary	NaI	0.2–27.0	2016.11.11–2017.04.12
5	Komatsu	compact	BGO type 1	0.7–15.0	2016.10.13–2017.04.14
6	Komatsu	compact	BGO type 1	0.35–14.0	2016.10.14–2017.04.14
7	Kanazawa	compact	BGO type 1	0.6–14.0	2016.10.13–2017.04.15
8	Kanazawa	compact	BGO type 1	0.35–12.0	2016.10.12–2017.04.14
9	Kanazawa	compact	BGO type 1	0.25–15.0	2016.10.10–2017.04.17
10	Suzu	compact	BGO type 2	0.2–7.0	2016.12.11–2017.03.21

Table 3.3: Configuration and operation log of radiation detectors in FY2017.

No.	area	type	crystal	range (MeV)	operation period
1	Kashiwazaki	compact	BGO type 1	0.2–18.0	2017.11.14–2018.03.19
			GSO	0.04–1.5	
2	Kashiwazaki	compact	BGO type 1	0.2–26.0	2017.11.14–2018.03.19
			GSO	0.04–1.1	
3	Kashiwazaki	stationary	BGO type 1	0.3–15.0	2017.11.14–2018.03.19
			GSO	0.04–1.1	
4	Kashiwazaki	stationary	NaI	0.1–27.0	2017.11.14–2018.03.19
			GSO	0.04–1.0	
5	Komatsu	compact	BGO type 1	0.4–24.0	2017.11.28–2018.03.15
6	Komatsu	compact	BGO type 1	0.4–22.0	2017.11.30–2018.03.15
7	Kanazawa	compact	BGO type 1	0.4–20.0	2017.11.27–2018.03.14
8	Kanazawa	compact	BGO type 1	0.4–20.0	2017.11.30–2018.03.13
9	Kanazawa	compact	BGO type 1	0.4–20.0	2017.12.01–2018.03.13

3.3   Detector Deployment

In the present thesis, data obtained in 2016-2017 (FY2016) and 2017-2018 (FY2017) winter seasons are analyzed. Configuration of detectors in each observation season is summarized in Tables 3.2–3.3. Observation sites are presented in Figure 3.10. Through the two seasons, we installed 4 detectors at Tokyo Electric Power Company Holdings (TEPCO) Kashiwazaki-Kariwa Nuclear Power Station, in Kashiwazaki, Niigata Prefecture, one detector each at Kanazawa Izumigaoka High School, Kanazawa University High School and Kanazawa University in Kanazawa, Ishikawa Prefecture, at Komatsu High School and Komatsu City Science Museum in Komatsu, Ishikawa Prefecture, and at Kanazawa University Noto School in Suzu, Ishikawa Prefecture. In each fiscal year, detectors were installed in November or December, and removed in March. It is noted that only Detector 3 and 4 in FY2017 employed the differential-threshold mode, and the other detectors in FY2017 and all in FY2016 employed the fixed-threshold mode.

During an observation season, detectors automatically continue radiation measurement. After the season, we search for radiation increases from background levels. Background signals mainly consist of cosmic rays and environmental gamma-ray lines. The environmental component contains gamma rays from decays of ^{40}K in rocks and concrete, ^{208}Tl in rocks, ^{214}Bi in the atmosphere, and so on. Figure 3.11 shows background spectra recorded by Detector 7 under different weather conditions. Data in a sunny day was obtained from 28 November 2017 13:00 to 14:00, data in a rainy day from 5 December 2017 13:00 to 14:00 when Kanazawa Weather Station reported 3.5 mm h^{-1} rainfall and data in a snowy day from 8 February 2018 5:00 to 6:00, when Kanazawa Weather Station reported a 85-cm depth of snow cover. While the cosmic-ray component only slightly varies, the environmental component varies on a large scale due to precipitation. A radioactive isotope ^{214}Bi is produced in the Uranium series decay chain starting from ^{238}U, as shown in Figure 3.12. In the middle of the decay chain, the noble gas nuclei ^{222}Rn can be released from rocks that contains ^{238}U, because ^{222}Rn has the long half-life of 3.8 days. As a result, their daughter nuclei ^{214}Bi flow in the atmosphere and are captured in vaper. Since they gather on the ground by precipitation, radiation dose increases during rainy days. This is called "radon washout". In fact, lines from ^{214}Bi are significant in the spectrum of the rainy day in Figure 3.11. On the other hand, ^{208}Tl, which is produced in the Thorium series decay chain starting from ^{232}Th, stay in rocks because the noble gas nuclei ^{220}Rn in the chain
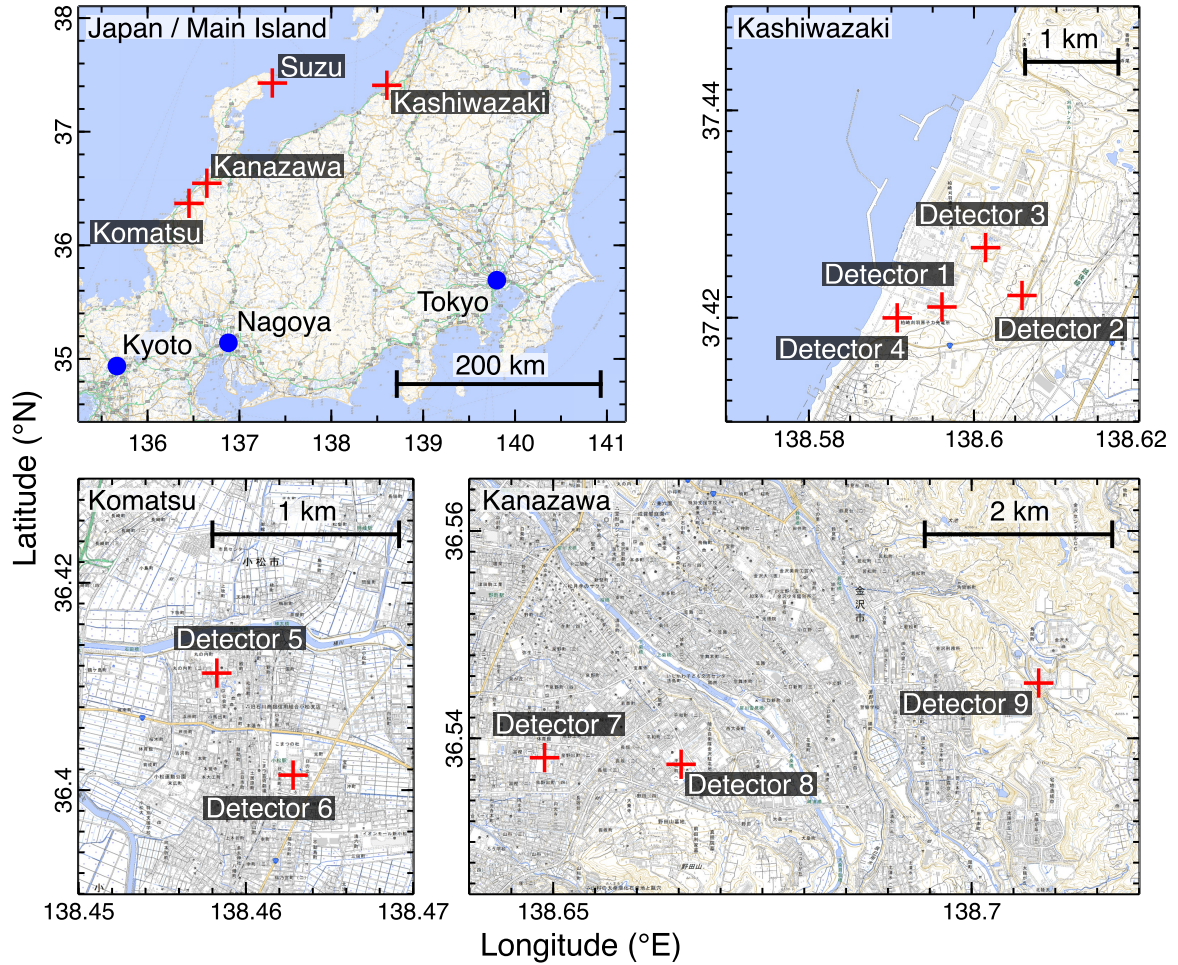
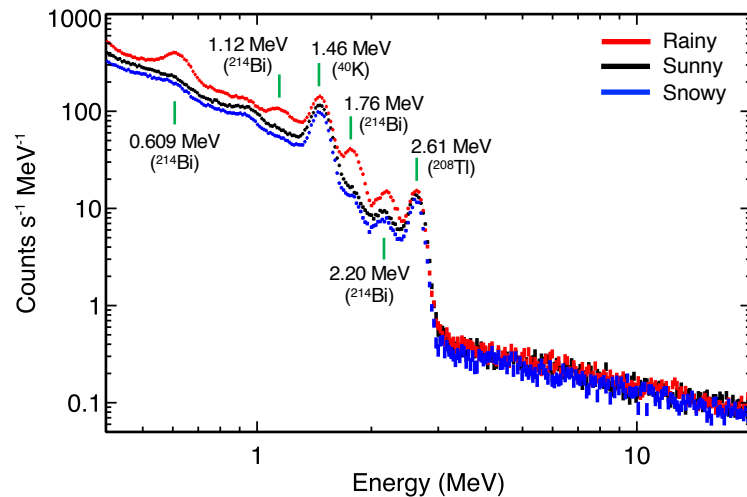Figure 3.10: Maps of observation sites in coastal areas of the Sea of Japan.

Figure 3.11: Background spectra obtained by detector 7 at Kanazawa Izumigaoka High School. The black, red and blue-colored data points present spectra in sunny, rainy and snowy days, respectively.
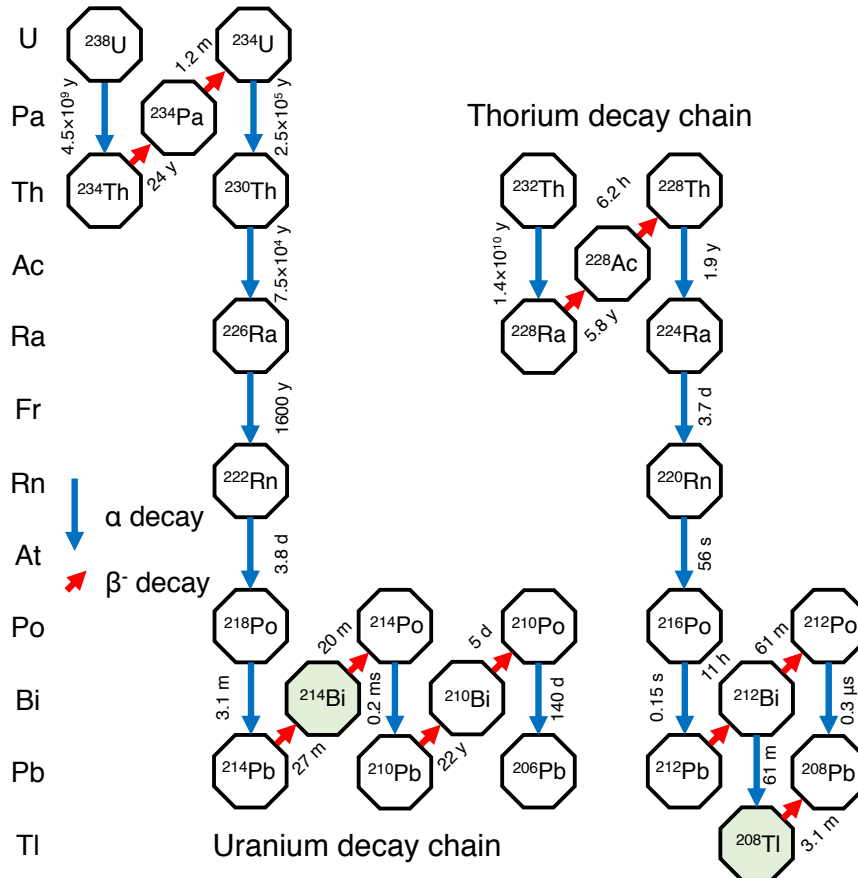
Figure 3.12: A schematic diagram of the Uranium and Thorium series decay chains.

cannot be released from rocks due to the short half-life of 1 minute. When snow is accumulated on the ground, gamma rays from the ground are shielded. Therefore, the line components of ^{40}K and ^{208}Tl, and their Compton component decrease during heavy snowing.

3.4 Detector Calibration and Responses

Energy calibration of detectors are performed with radioactive sources or environmental gamma-ray lines. In the case of BGO and NaIs, we extract the persistent background lines of 1.46 MeV (^{40}K) and 2.61 MeV (^{208}Tl) by fitting them with a gaussian function, and decide a calibration function. Because the light output of BGO crystals depends on temperature, this calibration procedure is performed every 30 minutes, while once a day for the NaI scintillator. The calibration accuracy is evaluated with the 0.609 MeV line of ^{214}B. As a result, we confirmed 1.1% accuracy at 0.609 MeV. Since GSO crystals have almost no temperature dependence of light output and are set to be sensitive to <1 MeV gamma rays, the calibration was performed with a ^{137}Cs source before deployment.

To obtain incident gamma-ray spectra, detector responses have to be removed from detector outputs. Instead of performing Monte-Carlo simulation every time, we prepare a response matrix of detectors calculated by the Monte-Carlo simulation framework `Geant4` [Agostinelli et al., 2003, Allison et al., 2006, 2016]. Assuming that gamma rays come from zenith, a mass model of scintillators was irradiated with photons of a flat energy spectrum in 0.04–41.0 MeV.
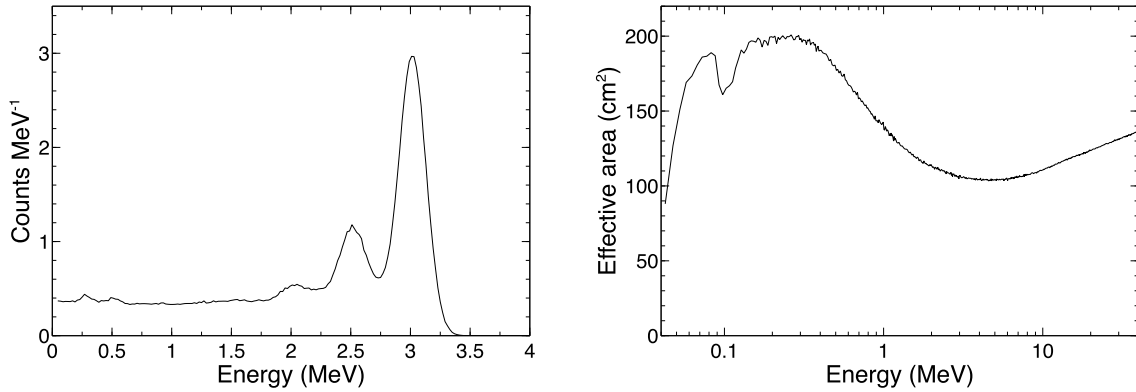
Figure 3.13: A simulation spectrum with incident gamma-ray energies of 3.00–3.04 MeV (left) and the effective area of BGO type 1 (right). In the left panel, there are the total absorption peak at 3 MeV and the single escape line at 2.5 MeV.

Then, a response matrix of incident photon energies versus detected energy spectra was constructed. The energy resolution of BGO scintillators is obtained in a function of photon energy E as $\Delta E = 0.15 \times (E/1 \text{ MeV})^{0.55}$ MeV (FWHM) This function was derived by extracting width of background emission lines such as ^{214}Bi (0.609 MeV), ^{40}K (1.46 MeV), and ^{208}Tl (2.61 MeV), and then fitting them with a power-law function. Figure 3.13 shows an example of the response matrix and the effective area of BGO type 1. This response matrix is stored in the Flexible Image Transporting System (FITS[10]) format, and can be utilized in the spectral analysis framework XSPEC [Arnaud, 1996]. XSPEC makes a response-included spectrum from a spectral model and the response matrix, compares with an observed spectrum by the χ^2-fitting method, and derives the best-fit model by changing model parameters and iterating the χ^2 fittings.

3.5 Monitoring Posts

Besides the compact and stationary gamma-ray detectors, radiation monitoring posts (MPs) are installed in Kashiwazaki-Kariwa Nuclear Power Station. They are operated by TEPCO to monitor radiation environment around the nuclear power station. Nine MPs surrounding the station are in operation, as seen in Figure 3.14. Each MP has two types of dosimeters for high and low dose rates. They monitor a total absorption dose for 30 seconds, convert it to an hourly dose rate (Gy h^{-1}), and record it every 30 seconds. Gray or Gy is a unit of ionizing radiation dose, absorbed energy per mass (J kg^{-1}).

A dosimeter for low dose rates (low-level dosimeter) consist of a $\phi 5.08$ cm $\times$ 5.08 cm cylindrical NaI scintillator, sensitive to 0.05-3.0 MeV gamma rays. The measurement range of low-level dosimeters is set to 10 nGy h^{-1}–10 μGy h^{-1} with a 10% accuracy. The dose rate is calculated based on count rates in the NaI crystal. Considering $1 \text{ MeV} = 1.602 \times 10^{-4}$ nJ and the NaI crystal weights 0.378 kg, a dose of 3 MeV in the crystal is 1.27×10^{-3} nGy. It is assumed that all counted events deposit 3 MeV in the crystal, and hence the conversion factor 4.57 nGy h^{-1} (counts s^{-1})$^{-1}$ is utilized for the dose calculation.

A dosimeter for high dose rate (high-level dosimeter) consist of an ionization chamber. The chamber is a sphere of a 29.9-cm diameter covered by 2-mm-thick stainless steel (14-L inner

---

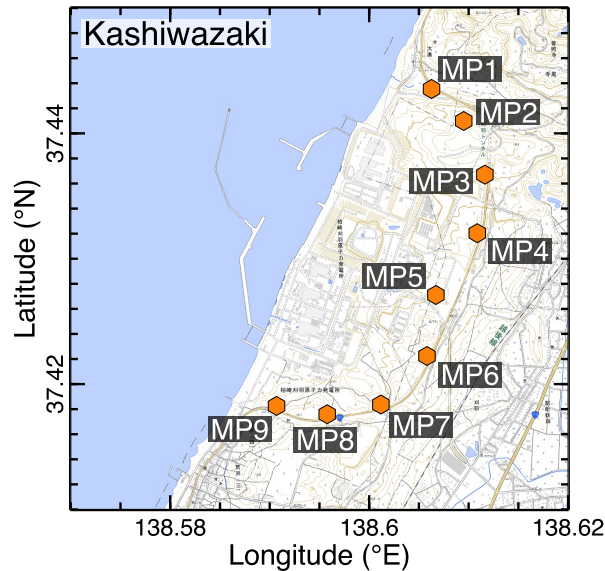[10]https://fits.gsfc.nasa.gov/

48

Figure 3.14: Distribution of monitoring posts installed in Kashiwazaki-Kariwa Nuclear Power Station.

capacity), and filled with argon gas at 4 atm. It is sensitive to ionizing particles of >0.05 MeV, and have a range of 10 nGy h^{-1}–100 mGy h^{-1} with a 15% accuracy, by measuring ionizing currents rather than photon counts.

3.6 Radio-frequency Measurement

We refer to commercial lightning information provided by Japanese Lightning Detection Network (JLDN) of Franklin Japan Co., Ltd. JLDN provides time, location, current, polarity, and type (CG or IC) of a lightning pulse. It monitors lightning flashes with 31 radio-frequency antennas installed in Japan, locates them by magnetic-detection-finder and time-of-arrival techniques, and classify their type (a cloud-to-ground or in-cloud discharge) by measuring the peak-to-zero time of current waveforms.[11] Negative polarity of lightning discharges is defined as negative downward currents or positive upward currents, and positive polarity as positive downward currents or negative upward currents.

---

[11]https://www.franklinjapan.jp/contents/observation/jldn/

Chapter 4

Photonuclear Reactions in Lightning

4.1   Overview of Short Bursts in Two Winter Seasons

In the GROWTH experiment, we searched observation data for gamma-ray bursts associated with lightning and thunderstorms after the observation period. We extract count-rate histories of each day, and visually search for significant enhancements of gamma-ray counts from a background level. A detailed analysis is then performed to determine the type of gamma-ray bursts, namely gamma-ray glows or short bursts. The appropriate bin width of count-rate histories for event surveys depends on typical duration of gamma-ray events. We employ 1-sec-binned histograms for the short-burst survey.

In the present analysis, two short bursts in the 2016–2017 winter season and three in the 2017–2018 winter season were detected. The observed five short bursts are listed in Table 4.1. Count-rate variations of representative detectors in the days when short bursts were detected are shown in Figure 4.1. Variation of background below 3 MeV is caused by radon washout (Subsection 3.3). The background variation depends on precipitation and half-lives of ^{214}Bi and its parent nuclide ^{214}Pb (27 and 20 minutes respectively), and hence has a time scale of tens of minutes to a few hours. On the other hand, short bursts and gamma-ray glows cause count-rate variations with a time scale of <1 second and a few minutes, respectively. If these events are bright enough, spike-like variations are seen in count-rate histories. In fact, significant increases in 1-second-binned count rates are found in Figure 4.1. These are candidates of short bursts.

Close-up views of count-rate histories of the gamma-ray events are shown in Figure 4.2. All the detected events share common features of count-rate variation: the count rates quickly

Table 4.1: Summary of short burst events.

Event No.	1	2	3	4	5
Area	Kashiwazaki	Kashiwazaki	Kashiwazaki	Kanazawa	Kanazawa
Season	2016–2017	2016–2017	2017–2018	2017–2018	2017–2018
Date (JST)	2017-01-16	2017-02-06	2017-11-24	2017-12-05	2018-01-10
Time (JST)	12:19:23	17:34:06	19:03:02	18:35:24	02:54:50
Date (UTC)	2017-01-16	2017-02-06	2017-11-24	2017-12-05	2018-01-09
Time (UTC)	03:19:23	08:34:06	10:03:02	09:35:24	17:54:50
Detector	Detector 1	Detector 1	Detector 1	Detector 9	Detector 7
	Detector 2	Detector 2	Detector 2		Detector 8
	Detector 3	Detector 3	Detector 3		
	Detector 4	Detector 4	Detector 4		
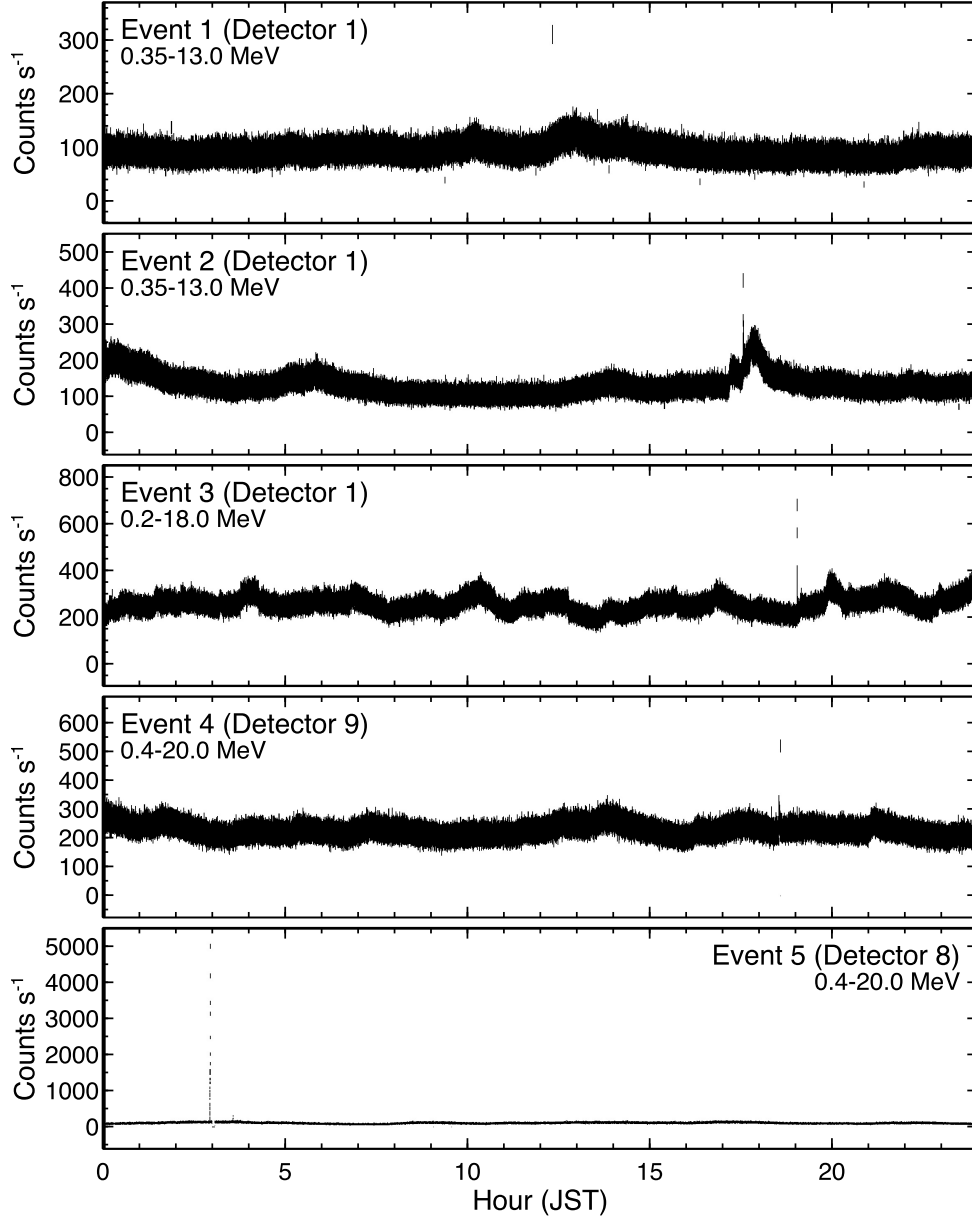
Figure 4.1: Count-rate histories of gamma rays for 24 hours when short bursts were detected. Histograms are 1-sec binned.

jumped coincident with lightning discharges, exponentially decayed with a 200–300-ms duration. Therefore, these events are categorized as short bursts. Exceptionally, the history of Detector 8 (Event 5) presents significant high count rates from background before the onset of the short burst. This count-rate enhancement is categorized as a gamma-ray glow because it lasted for ~1 minute until the short burst. A detail analysis of the gamma-ray glow is shown in Wada et al. [2019c]. For all the events, JLDN reported corresponding lightning discharges within 3 km from detectors (including cloud-to-ground and in-cloud discharges). Time differences between JLDN detection and short bursts are less than 1 sec for Events 1 and 2, and less than 1 ms for Events 3–5. Note that the absolute timing accuracy in the 2016-2017 season (Events 1 and 2) is limited to be only better than 1 sec due to failure in receiving GPS signals, while better than 1 μs in the 2017-2018 season (Events 3–5) calibrated with GPS signals.
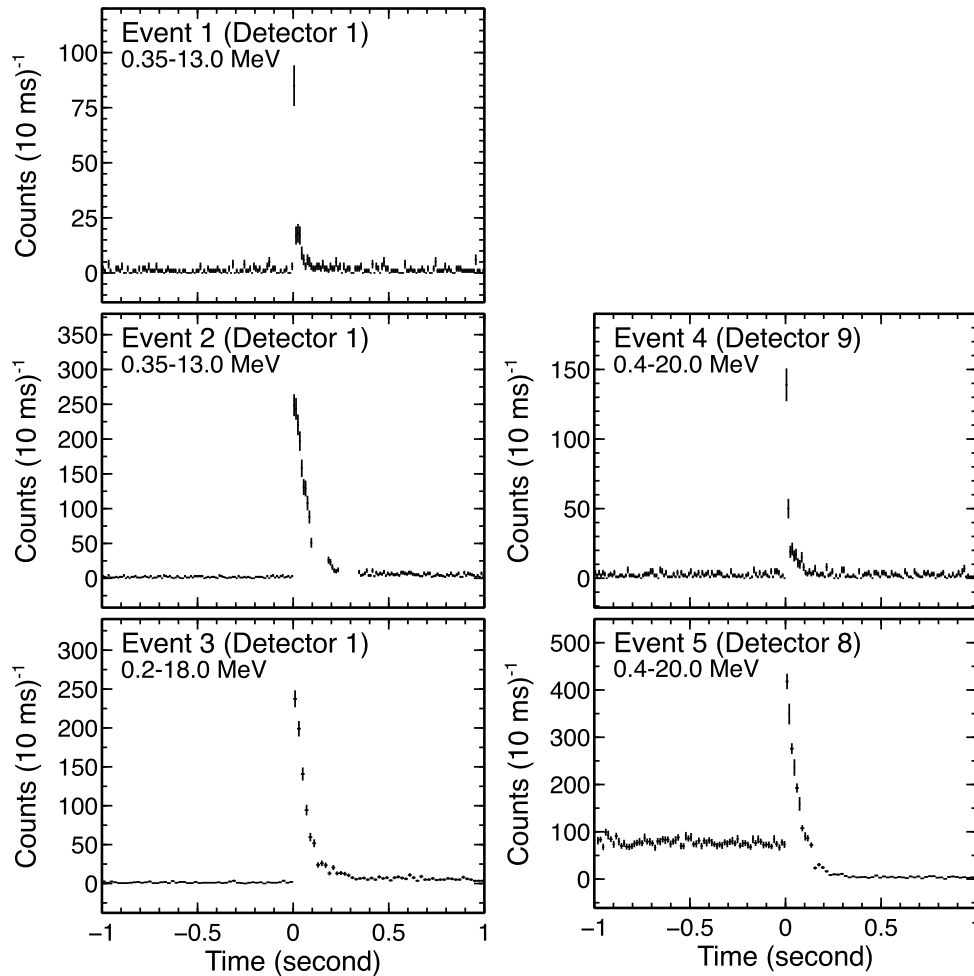
Figure 4.2: Count-rate histories of 5 short burst events during the 2016-2017 and 2017-2018 winter seasons. Histograms are 10-ms binned. Dead-time corrections are applied. Time origin of each histogram is set to the onset of a short burst.

4.2 Short-burst Event 2 on 2017 February 6th

4.2.1 Observational results

The short burst Event 2 was observed at 17:34:06, February 6th, 2017, in Kashiwazaki, Niigata Prefecture, simultaneously by four gamma-ray detectors (Detectors 1–4) installed at Kashiwazaki-Kariwa Nuclear Power Station. The stationary type Detector 4, different from the other detectors (see Table 3.2), was paralyzed at the short-burst detection. Therefore, we exclude data of Detector 4 within 500 ms from the lightning discharge for the analysis. Count-rate histories of Event 2 are presented in Figure 4.3. They show a quick rise within 10 ms, and a decay lasting for 200–300 ms. This decay is reproduced by an exponential function with a time constant of 56 ± 3, 55 ± 12, and 36 ± 4 ms for Detectors 1–3, respectively.

The pulse height and waveform baseline of photon events recorded by the GROWTH FPGA/ADC board during the short burst are plotted in Figure 4.4. During normal operations, the waveform baseline (i.e. red points in the figure) retains 0 V. However, Detectors 1–3 recorded significant negative baseline values of -4 V to -1 V at the beginning of the short burst. Then the waveform baseline gradually returned to $\sim$0 V; a baseline undershoot were recorded by Detectors 1–3 at
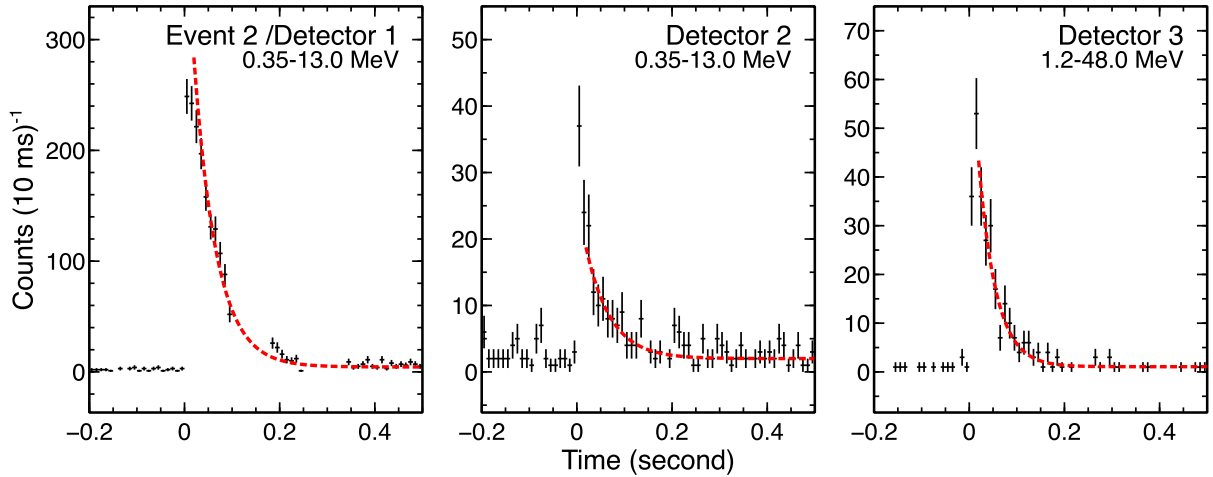
Figure 4.3: Count-rate histories of a short burst on February 6th, 2017 (10-ms binning). Time origin of each histogram is set to the onset of the short burst. The best-fit model of an exponential function is overlaid with red-dotted lines.
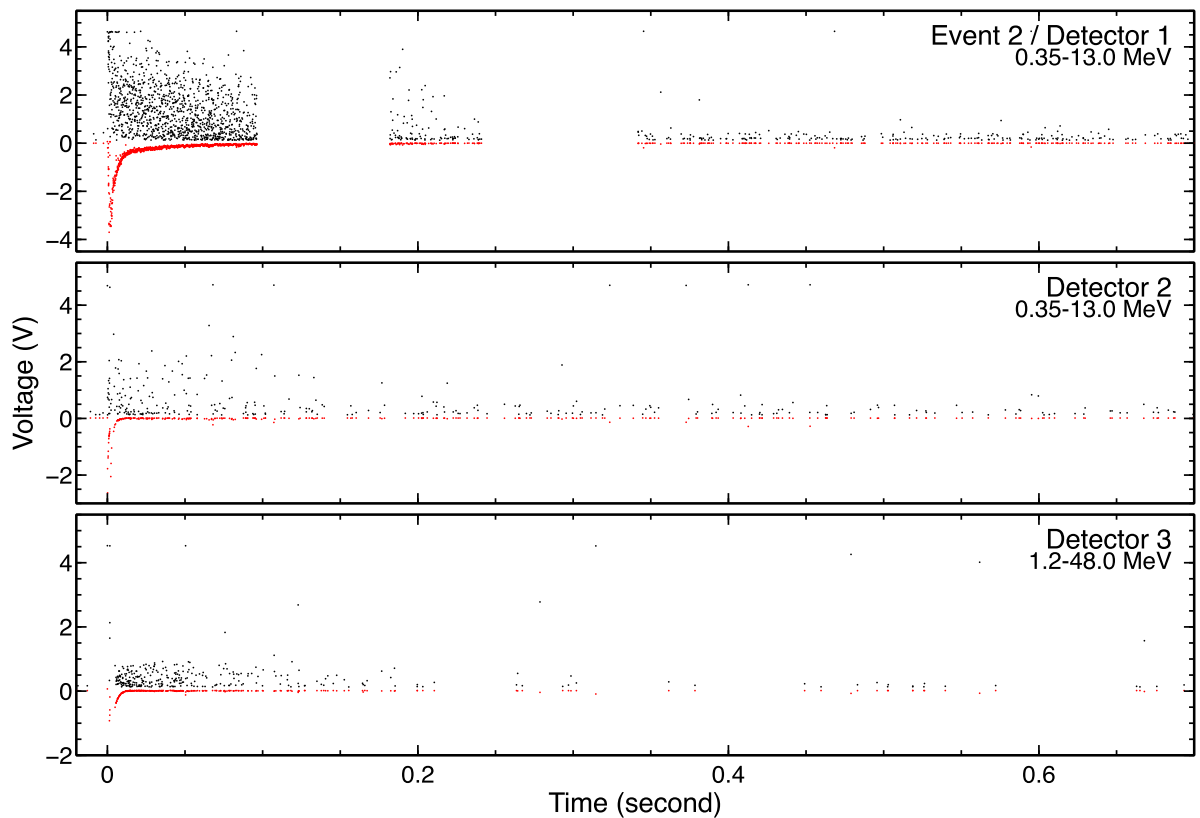
Figure 4.4: Time series of pulse height (black) and analog baseline (red) of each photon event in Event 2. A part of data of Detector 1 was not recorded due to buffer overflow.

the beginning of the short burst.

Energy spectra of the short burst extracted after the recovery of the undershoot are shown in Figure 4.5. Each spectrum consists of a continuum-like component extending up to 8–10 MeV, with a photon index of ∼0.5. They have a steep cutoff at 8–10 MeV, and almost no photons
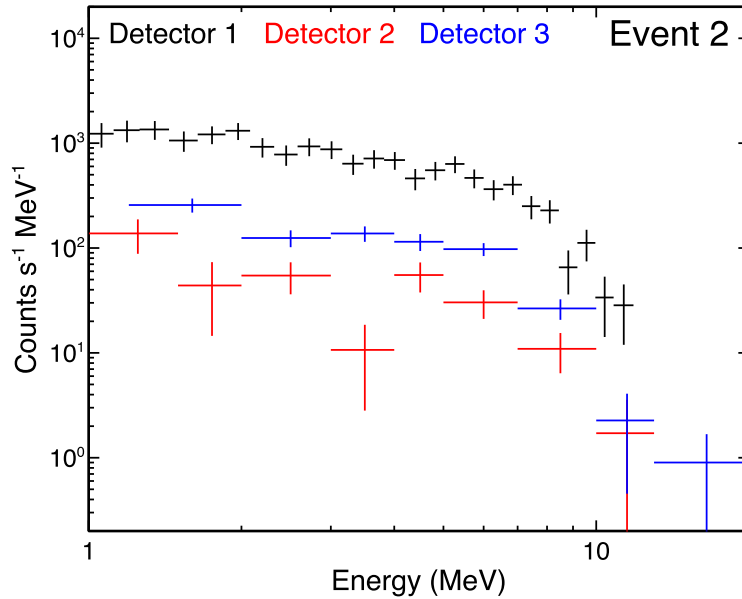
Figure 4.5: Background-subtracted energy spectra of the short burst Event 2. Spectra of the short burst are extracted from 50 ms$< t <$200 ms, 20 ms$< t <$200 ms and 50 ms$< t <$200 ms for Detectors 1 (black), 2 (red) and 3 (blue) respectively, due to baseline undershoots at the beginning of the short burst. Background spectra are extracted from -660 sec $< t < -60$ sec, where t is an elapsed time from the beginning of the short burst.

above 10 MeV. Energy spectra of gamma-ray glows and TGFs are typically a power-law continuum up to $>$20 MeV with a photon index of 1–2, and have an exponential cutoff [Smith et al., 2005, Tsuchiya et al., 2011, Wada et al., 2018]. Therefore, the spectra of the present short burst are apparently different from those of gamma-ray glows and TGFs, originating from bremsstrahlung of energetic electrons.

Furthermore, Detectors 1 and 4 recorded an afterglow lasting for tens of seconds after the short burst. Figure 4.6 shows count-rate histories below and above 0.7 MeV. No significant variations above 0.7 MeV except the short burst itself were recorded by any detectors. On the other hand, Detectors 1 and 4 observed count-rate enhancements below 0.7 MeV lasting for 70 and 30 sec, respectively. Scatter plots of photon energy and timing recorded by Detectors 1 and 4 are shown in Figure 4.7. The count-rate enhancement recorded by Detector 1 is divided into two components: a decaying component starting immediately after the lightning discharge and a delayed component peaked at 35 sec after the lightning. Detector 4 only recorded a decaying component.

Energy spectra during the enhancement below 0.7 MeV are extracted in Figure 4.8. Both Detectors 1 and 4 recorded a line emission peaked at $\sim$0.5 MeV, and a continuum component by Compton scattering below 0.5 MeV. Photon counts above 0.7 MeV are statistically consistent with zero counts. The energy spectra are reproduced by the sum of a Gaussian and a quadratic functions. The center energy of the line is 0.515$\pm$0.008 MeV and 0.501$\pm$0.007 MeV for Detectors 1 and 4, respectively. The line width (FWHM) is 0.120$\pm$0.009 MeV and 0.061$\pm$0.007 MeV, respectively. Detectors 1 and 4 are energy-calibrated with an accuracy of 1.1% at 0.609 MeV (Subsection 3.4). It corresponds to 0.006 MeV at 0.511 MeV. The energy center of the line emission is thus consistent with 0.511 MeV. The detected line width is consistent with the energy resolution of detectors (0.109$\pm$0.002 MeV and 0.055$\pm$0.001 MeV at 0.511 MeV for
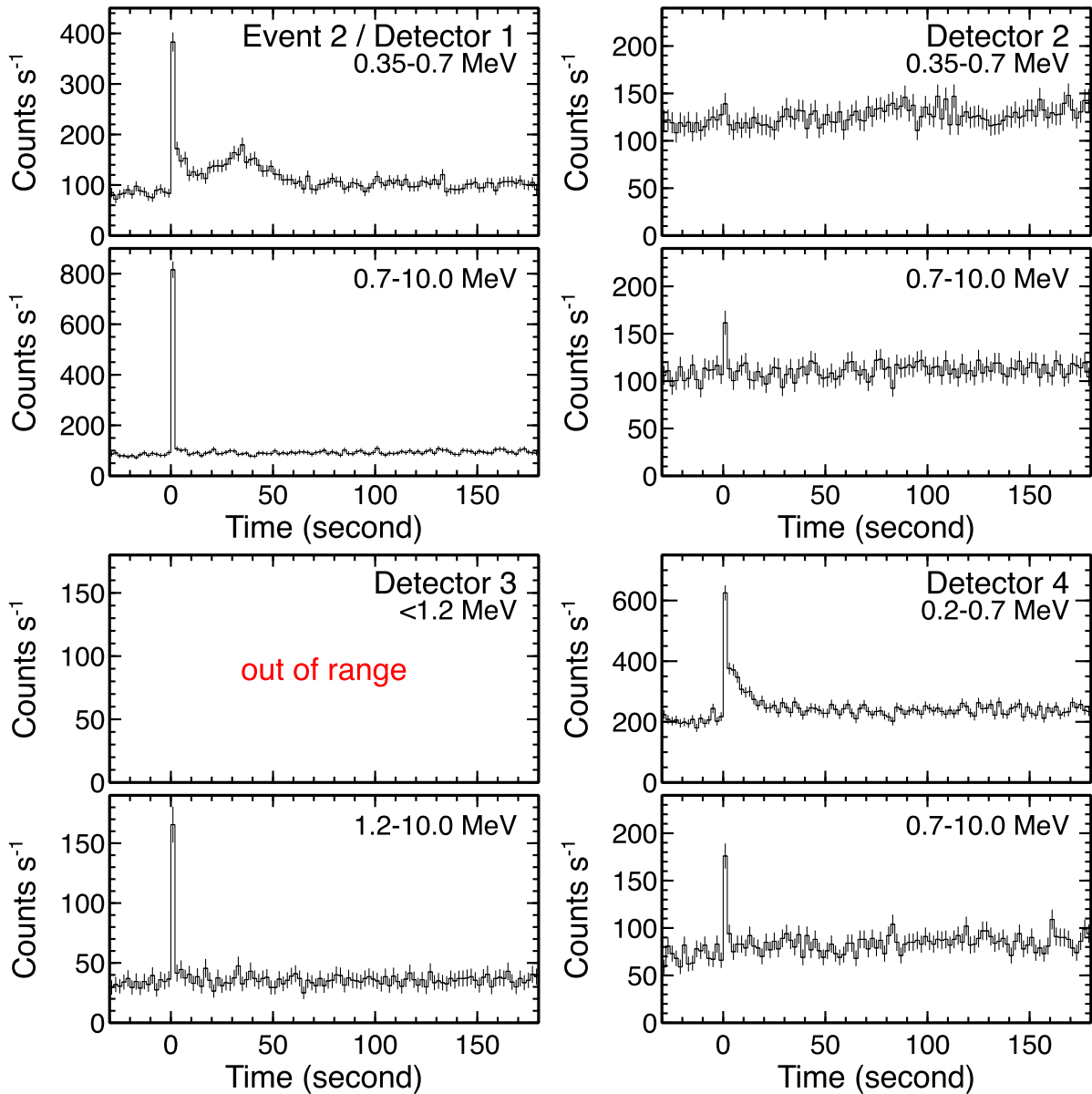
Figure 4.6: Count-rate histories after the short burst with two energy ranges with 2-sec binning.

Detectors 1 and 4 respectively). Therefore, the observed line emissions suggest that positrons were produced after the short burst and emitted 0.511-MeV gamma rays by annihilating with ambient electrons.

At the moment when the gamma-ray detectors recorded the short burst, JLDN detected two radio-frequency pulses associated with a lightning flash. Both pulses were located on the coast of Kashiwazaki-Kariwa Nuclear Power Station (Figure 4.9). The first one (JLDN1 in Figure 4.9) took place at 17:34:06.002716 JST, and was categorized as a cloud-to-ground current with a peak current of -33 kA. The second one was detected 23 μs after the first one, and also categorized as a cloud-to-ground current with a peak current of $+44$ kA. No other lightning pulses were detected within 10 km from the power station, within 1 minute from the short burst detection.

High-level dosimeters of MPs operated by TEPCO also recorded increases in dose rates at the moment of the short burst. Dosimeters of MPs measure doses integrated for every 30 sec,
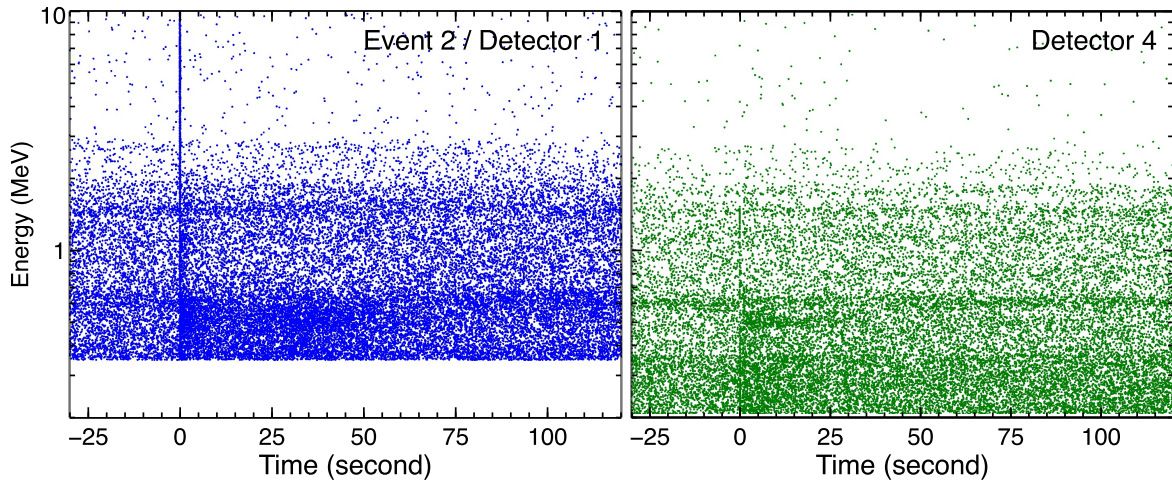
Figure 4.7: Time histories of photon energy recorded by Detectors 1 and 4.
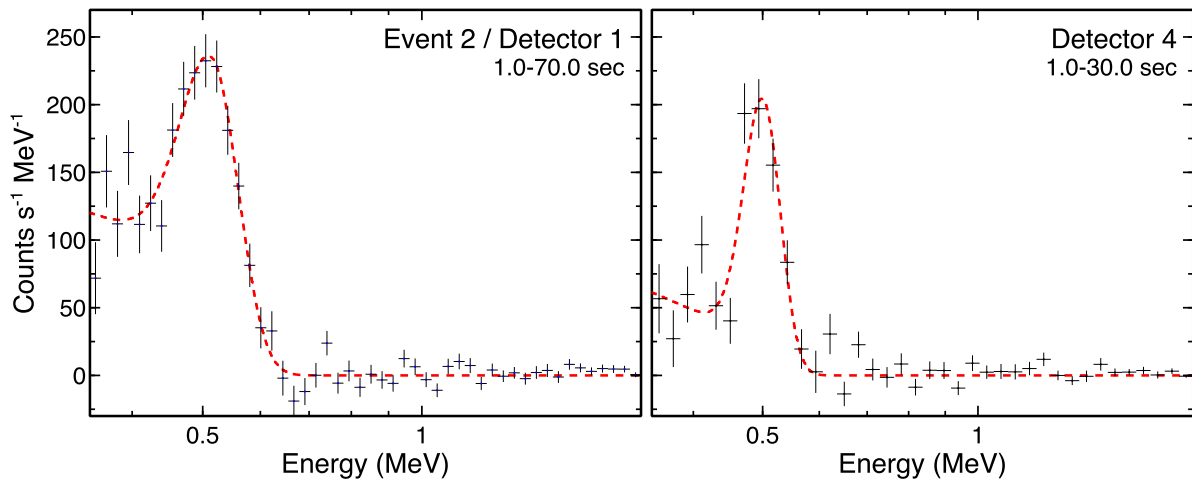
Figure 4.8: Background-subtracted spectra of a sub-minute afterglow in Event 2. Source spectra are extracted from 1 sec$< t <$70 sec and 1 sec$< t <$30 sec for Detectors 1 and 4 respectively, where t is an elapsed time from the beginning of the short burst. Background spectra are extracted from -660 sec $< t < -60$ sec and 120 sec $< t < 720$ sec. Best-fit models of a gaussian plus a quadratic function are overlaid with red-dotted lines.

and convert them to dose rates (Section 3.5). Therefore, the recorded doses of the event are converted into total doses by multiplying the integration time (30 sec=30/3600 hours) after background dose rates are subtracted. The total doses are presented in Figure 4.9. High total doses were recorded by the dosimeters installed in the south area of the power station. In particular, the maximum dose was 1.72 μGy, recorded by MP9.

The wind flow at the moment of the short burst was estimated with data of eXtended RAdar Information Network (XRAIN). By analyzing 11 sets of radar images observed from 17:30–17:40 (JST), the ambient wind flow was estimated to be north-westward, with a speed of 17.0 ± 1.5 m s^{-1} (see Appendix A). This estimation is consistent with an observation of a wind profiler operated by the power station, north-westward with a speed of 17.0 m s^{-1} at an 85-m altitude.
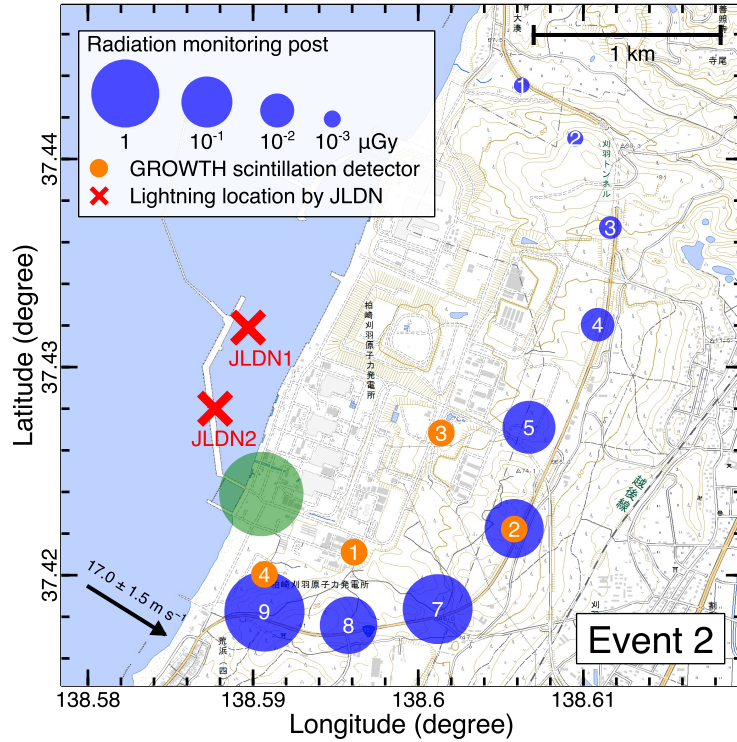
Figure 4.9: Lightning locations and radiation doses of Event 2 measured at Kashiwazaki-Kariwa Nuclear Power Station. Wind velocity and direction at the moment of the shot burst are indicated by the black arrow. Detector B and MP6 are located at the same position. The green circle shows the region filled with positron-emitting nuclei such as ^{13}N and ^{15}O at the moment of lightning.
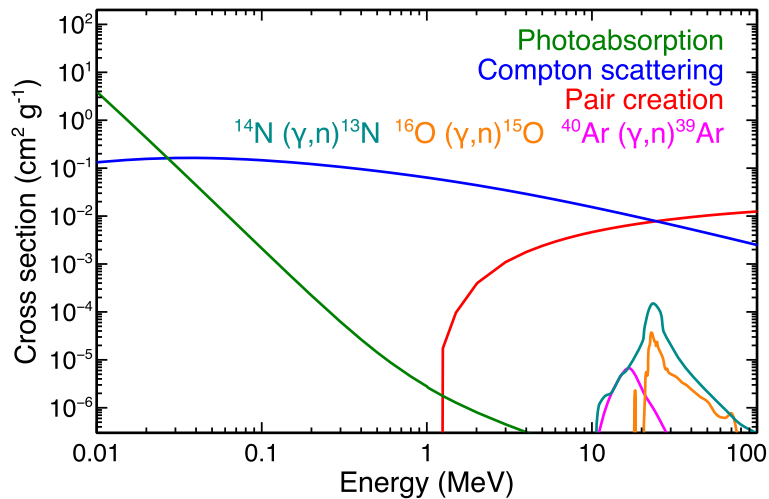
Figure 4.10: Cross sections of reactions with photons and atmospheric nuclides, extracted from NIST/XCOM and ENDF/B-VII.I [Chadwick et al., 2011]

.

58

4.2.2 Scenarios to produce positrons

The line emission at 0.511 MeV detected after the short burst can be interpreted that positrons were produced around the detectors and annihilated with ambient electrons. The simplest mechanism to produce positrons is the pair production. Photons above $\sim$1 MeV can trigger pair productions and produce positrons. Reaction cross sections of photons in the atmosphere are shown in Figure 4.10. In fact, pair creations are realistic with photons above several MeVs. However, photons above 1 MeV were hardly detected during the annihilation gamma-ray detection, and hence positrons cannot be produced by the pair-production scheme. The produced positrons annihilate with ambient electrons after they lose their kinetic energy by ionization and radiation losses. Assuming that the stopping power of positrons in the atmosphere is 0.2 MeV m^{-1}, a positron with a kinetic energy of 1 MeV annihilates after flying 5 m over 0.5 ms. Even though positrons were generated at the moment of the short burst, they cannot exist in the atmosphere for seconds. Therefore, the observed annihilation line cannot be explained by pair productions.

The other candidate to produce positrons is photonuclear reactions. For atmospheric photonuclear reactions such as ^{14}N + $\gamma \rightarrow$ ^{13}N + n and ^{16}O + $\gamma \rightarrow$ ^{15}O + n, each photon reacts with ^{14}N and ^{16}O, kicks a neutron off from them, and finally produces a proton-rich nucleus ^{13}N and ^{15}O [Babich, 2006, 2007, Carlson et al., 2010]. These proton-rich nuclei exhibit β^{+}-decay with half-lives of 10 and 2 minutes turning into ^{13}C and ^{15}N by emitting positrons, respectively. In these decay processes, other particles such as X-rays and gamma rays, except positrons and neutrinos, are not emitted. Cross sections of ^{14}N (γ,n) ^{13}N and ^{16}O (γ,n) ^{15}O in the atmosphere are also shown in Figure 4.10. The threshold energies of ^{14}N (γ,n) ^{13}N and ^{16}O (γ,n) ^{15}O are 10.55 and 15.7 MeV, and the cross sections reach their maximum at $\sim$23 and 22 MeV, respectively. Besides these reactions, photonuclear reactions with ^{40}Ar are also expected to take place, despite the product ^{39}Ar being a β^{-}-decay nuclide and emitting no positrons. The cross sections of photonuclear reactions are two orders of magnitude lower than those of pair creation. However, they are the most convincing mechanism to produce positrons when pair productions are not plausible. Therefore, we hypothesize that the short burst and the afterglow of annihilation gamma rays are caused by photonuclear reactions, triggered by gamma rays above 10 MeV in lightning.

The production rate of positrons emitted from ^{13}N and ^{15}O exponentially decays with their
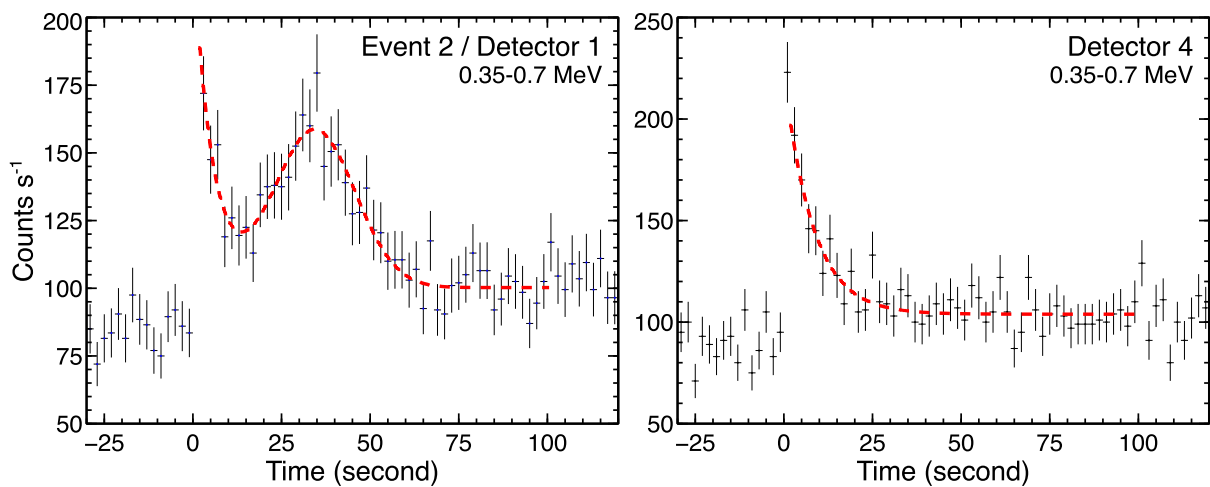

Figure 4.11: Count-rate histories of annihilation gamma rays. The overlaid red-dotted lines present the best-fit model (see text).

half-lives. Here we define the numbers of ^{13}N and ^{15}O produced by photonuclear reactions as $n_N(0)$ and $n_O(0)$ and cross sections of photonuclear reactions as σ_N and σ_O for ^{13}N and ^{15}O, respectively. Decay constants $\lambda_N \approx 1.16 \times 10^{-3}\,\mathrm{s}^{-1}$ and $\lambda_O \approx 5.67 \times 10^{-3}\,\mathrm{s}^{-1}$ are also utilized. Given that $n_O(0) = n_N(0) \times (\sigma_O/\sigma_N)$, the production rate of positrons is

$$
\begin{aligned}
\frac{dn_p}{dt} &= \lambda_N n_N(0) \exp(-\lambda_N t) + \lambda_O n_O(0) \exp(-\lambda_O t) \\
&= n_N(0) \left[\lambda_N \exp(-\lambda_N t) + \frac{\sigma_O}{\sigma_N} \lambda_O \exp(-\lambda_O t) \right],
\end{aligned}
\tag{4.1}
$$

where σ_O/σ_N is 0.054 and 0.154 for gamma rays of 20 MeV and 30 MeV, respectively. The rate decays with a half-life close to ^{15}O just after photonuclear reactions, and the half time becomes closer to that of ^{13}N as time passes.

Then the count-rate histories of annihilation gamma rays recorded by Detectors 1 and 4 were fitted with an exponential and Gaussian function. The fit results are shown in Figure 4.11. The decaying component recorded by Detector 4 is reproduced by an exponential function. The decaying and delayed components in Detector 1 are reproduced by an exponential and a Gaussian functions, respectively. The half-life of the decaying component is 3.7±1.2 sec and 7.2±1.1 sec for Detectors 1 and 4, respectively. The delayed component of Detector 1 peaked at 34.4±1.2 sec after the onset of the short burst with a width of 26.7±3.2 sec (FWHM). The half-lives of the decaying components are shorter than those of ^{13}N and ^{15}O. Also, the delayed component cannot be reproduced by a simple decay of a radioactive isotope. Therefore, these count-rate variations cannot be explained by a simple decay model of ^{13}N and ^{15}O.

The delayed annihilation emissions peaked at 34.4±1.2 sec after the short burst. Since the Gaussian-like variation of count rates resembles those of gamma-ray glows [Tsuchiya et al., 2007, 2011], which move with ambient wind flow, we hypothesize that a cloud of ^{13}N and ^{15}O was moving with ambient wind. Utilizing the estimated wind speed 17.0 m s^{-1}, these positron-emitting nuclei moved 590±20 m for 34.4±1.2 sec. Therefore, ^{13}N and ^{15}O should have been generated in an area whose center is located 590±20 m windward of Detector 1. Here it is assumed that ^{13}N and ^{15}O were distributed in a cylinder formed along the lightning path, and the center of the cylinder passed above Detector 1. The diameter of the cylinder is estimated to be 450±60 m (FWHM) by the wind speed and the Gaussian width of the count-rate history. The position and diameter of the cylinder under the assumption is shown in Figure 4.9. Since the cylinder is located close to the positions where JLDN detected lightning pulses, it is consistent that the JLDN-reported lightning currents produced ^{13}N and ^{15}O. Therefore, the delayed emission recorded by Detecter 1 is interpreted as a cloud of ^{13}N and ^{15}O passing above Detector 1 with ambient wind while emitting positrons.

Table 4.2: Summary of photonuclear reactions and β^+-decaying nuclei.[12,13]

Reaction	Reaction threshold [1,2]	Product	Half life	Average energy of positron
^{12}C (γ,n) ^{11}C	18.72 MeV	^{11}C	20.36 min	0.386 MeV
^{14}N (γ,n) ^{13}N	10.55 MeV	^{13}N	597.9 sec	0.492 MeV
^{16}O (γ,n) ^{15}O	15.66 MeV	^{15}O	122.2 sec	0.735 MeV
^{27}Al (γ,n) ^{26m}Al	13.06 MeV	^{26m}Al	6.35 sec	1.440 MeV
^{28}Si (γ,n) ^{27}Si	17.18 MeV	^{27}Si	4.15 sec	1.720 MeV
^{40}Ca (γ,n) ^{39}Ca	15.64 MeV	^{39}Ca	0.86 sec	2.558 MeV
^{40}Ar (γ,n) ^{39}Ar	9.87 MeV	^{39}Ar	268 year	N/A (β^- decay)

Detectors 1 and 4 also recorded the decaying component of annihilation gamma rays. As shown in Figure 4.12, both component consist of the annihilation line peaked at 0.511 MeV. There are two interpretations of the component. The first one is that ^{13}N and ^{15}O were produced in another area from the one which caused the delayed component, and the decay was caused by positional shift via wind. In this case, ^{13}N and ^{15}O should have been produced the leeward of Detector 1 because the decaying component decreased monotonously. The numbers of detected photons in the decaying component are 670±300 and 970±290 counts in 0.35–0.7 MeV for Detectors 1 and 4, respectively. Since the effective area at 0.511 MeV is 149.2 cm^2 and 28.3 cm^2 for Detectors 1 and 4 respectively, the gamma-ray fluences are estimated to be 4.5±2.0 photons cm^{-2} and 34±10 photons cm^{-2}, respectively. It is thus suggested that the area responsible for the decaying component should be produced closer to Detector 4 than Detector 1. However, this suggestion is inconsistent with the interpretation that the area should be located the leeward of Detector 1. Therefore the hypothesis that two areas containing ^{13}N and ^{15}O existed is not consistent with the observation data.

The other one is positron emissions from radioactive isotopes besides ^{13}N and ^{15}O. There are various nuclides around detectors such as ^{28}SI, ^{27}Al and ^{56}Fe in soil, ^{40}Ca, ^{28}SI and ^{27}Al in concrete, ^{27}Al and ^{12}C in components of detectors. These nuclides also react with photons and transform into proton-rich nuclei by photonuclear reactions such as ^{56}Fe (γ, n) ^{55}Fe, ^{40}Ca (γ, n) ^{39}Ca, ^{28}Si (γ, n) ^{27}Si, ^{27}Al (γ, n) ^{26m}Al and ^{12}C (γ, n) ^{11}C. Among these products, only ^{55}Fe is not a β^+-decay nuclide (undergoes electron capture), but the others emit positrons by β^+-decay. The half-lives of ^{39}Ca, ^{27}Si, ^{26m}Al and ^{11}C are 0.86 sec, 4.15 sec, 6.35 sec and 20.36 min, respectively. Since these nuclei are fixed in solid bodies around detectors, detectors could observe the variation of annihilation gamma rays associated with the half-lives. In fact, the time constants recorded by Detectors 1 and 4, 3.7±1.2 sec and 5.6±1.3 sec, are consistent with the half-lives of ^{27}Si and ^{26m}Al. Therefore, the decaying component observed by Detec-
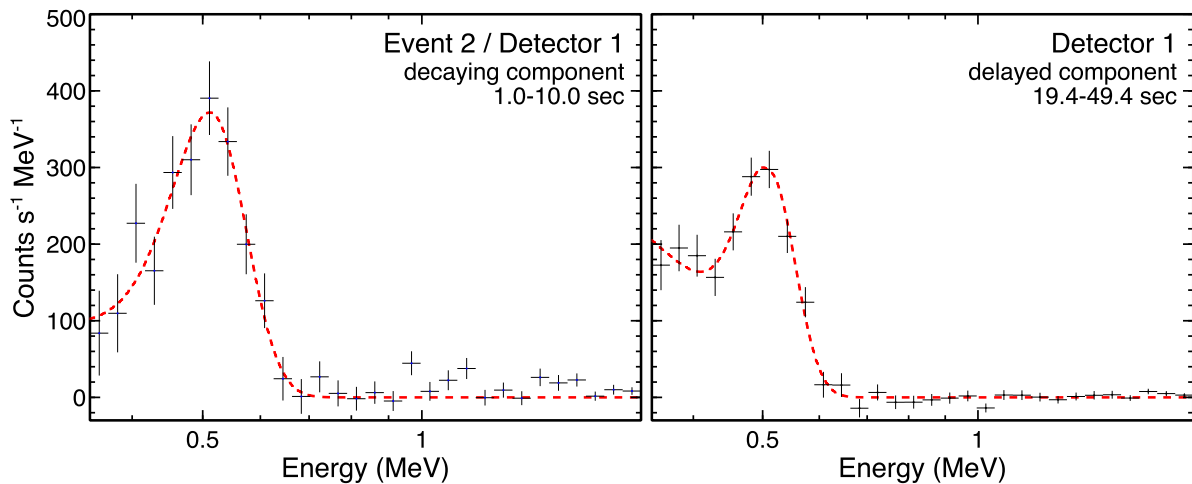
Figure 4.12: Background-subtracted spectra of the decaying and delayed components of the annihilation afterglow in Event 2 recorded by Detector 1. Source spectra are extracted from 1.0 sec< t <10.0 sec and 19.4 sec< t <49.4 sec for the decaying and delayed components, respectively. Best-fit models of a gaussian plus a quadratic function are overlaid with red-dotted lines.

---

[12]ENDF/B-VII.I [Chadwick et al., 2011]

[13]IAEA ENSDF https://www-nds.iaea.org/public/ensdf_pgm/

tors 1 and 4 is suggested to be caused by positron-emitting nuclei ^{27}Si and ^{26m}Al, produced by photonuclear reactions with ^{28}Si and ^{27}Al existing around detectors. Photonuclear reactions with ambient nuclei are summarized in Table 4.2.

4.2.3 Atmospheric interactions of neutrons

Photonuclear reactions produce fast neutrons as well as proton-rich nuclei. If lightning triggers photonuclear reactions, our detectors should also detect signatures of neutrons. Despite depending on incident gamma-ray energy, kinetic energies of photoneutrons are typically $\sim$10 MeV [Babich et al., 2010]. As introduced in Section 2.6, photoneutrons are elastic-scattered by atmospheric nuclei and lose their kinetic energy. When they become epithermal or thermal neutrons, they are gradually captured by ambient nuclei (Section 2.6). Figure 2.26 shows cross sections of atmospheric nuclei ^{14}N, ^{16}O and ^{40}Ar with neutrons. Elastic scatterings with ^{14}N and ^{16}O are dominant among neutrons with energies of larger than keV. For epithermal and thermal neutrons, whose kinetic energy is less than 1 eV, charge-exchange productions ^{14}N (n, p) ^{14}C and neutron captures ^{14}N (n, γ) ^{15}N become dominant. Although the charge-exchange productions generate protons, it is difficult to detect the reactions because the range of protons in the atmosphere is too short. On the other hand, neutron captures emit multiple gamma-ray lines, which can be detected by normal radiation monitors.

First of all, we consider a time scale of neutron thermalization by elastic scattering. Here mass attenuation coefficients of elastic scatterings with ^{14}N and ^{16}O, neutrons captures and charge-exchange productions with ^{14}N are expressed as Σ_{N}, Σ_{O}, $\Sigma_{n\gamma}$ and Σ_{np}, respectively. Effects by other nuclei and reactions are negligible. The mean free path of neutrons λ is defined as $\lambda = 1/(\Sigma_{\text{N}} + \Sigma_{\text{O}})$. For example, neutrons with a kinetic energy of 1 keV undergo an elastic scattering after moving 22 m on average in the standard atmosphere at 1 atm.

According to Subsection 2.6.1, the averaged ratio of kinetic energy of a neutron after the (n+1)-th elastic scattering to that after the n-th elastic scattering E_{n+1}/E_n is a constant as follows

$$\frac{E_{n+1}}{E_n} = \exp(\xi). \tag{4.2}$$

Here ξ, called lethargy, is defined as

$$\xi = \frac{2}{\text{A} + 2/3}, \tag{4.3}$$

where the mass number of scattering nuclei A is

$$\text{A} = 14 \times \frac{\Sigma_{\text{N}}}{\Sigma_{\text{N}} + \Sigma_{\text{O}}} + 16 \times \frac{\Sigma_{\text{O}}}{\Sigma_{\text{N}} + \Sigma_{\text{O}}} \approx 14.2. \tag{4.4}$$

Then a kinetic energy loss of a neutron by an elastic scattering ΔE is

$$\Delta E = E_n - E_{n+1} = E_n(1 - e^{-\xi}) \approx 0.125 E_n. \tag{4.5}$$

By solving the recurrence formula,

$$E_n = 0.125^n E_0 \tag{4.6}$$

is obtained. On average, photoneutrons with an initial kinetic energy of 10 MeV are elastic scattered 104 and 131 times to become epithermal (1 eV) and thermal (0.025 eV) neutrons, respectively.

The velocity of neutrons after n-times of scatterings v_n is

$$v_n = 3.0 \times 10^8 \text{ m/s}\sqrt{1 - \left(\frac{940 \text{ MeV}}{940 \text{ MeV} + E_n}\right)^2}. \quad (4.7)$$

It takes t_n to undergo n-times of elastic scatterings, where

$$t_n = \sum_{i=0}^{n-1} \frac{\lambda}{v_i}. \quad (4.8)$$

Temporal variations in kinetic energy of neutrons by elastic scatterings is shown in Figure 4.13. It takes 7.5 ms and 45.2 ms for neutrons with the 10 MeV initial kinetic energy to became epithermal and thermal neutrons, respectively.
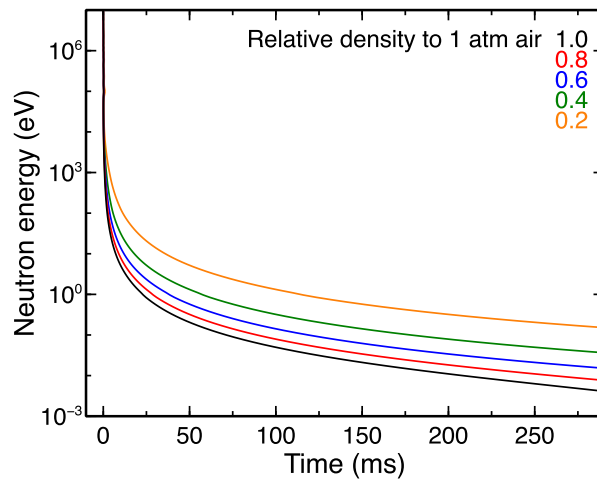
Figure 4.13: Time variations in kinetic energy of neutrons by elastic scatterings.
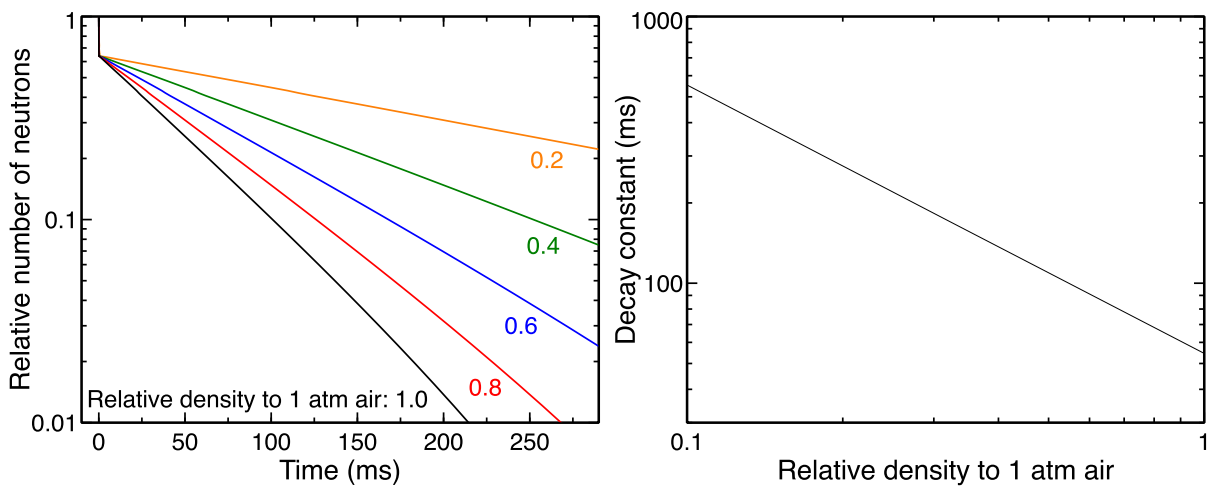
Figure 4.14: Time variations in the number of neutrons (left) and variation of time constants of the neutron number depending on air density (right). The initial number of neutrons is normalized to 1.

Then we consider the case that neutrons are absorbed by neutron captures and charge-exchange productions. The probability that neutron captures and charge-exchange productions occurs while a neutron moves the mean free path λ is expressed as

$$P = 1 - e^{-(\Sigma_{n\gamma} + \Sigma_{np})\lambda}. \tag{4.9}$$

Since $\lambda = 1/(\Sigma_N + \Sigma_O)$ is employed, the number of neutrons absorbed between n-th and (n+1)-th elastic scatterings is

$$\Delta N = N_n - N_{n+1} = N_n \left[1 - e^{-(\Sigma_{n\gamma} + \Sigma_{np})\lambda} \right] = N_n \left[1 - \exp\left(-\frac{\Sigma_{n\gamma} + \Sigma_{np}}{\Sigma_N + \Sigma_O} \right) \right]. \tag{4.10}$$

The left panel of Figure 4.14 presents variations in the number of neutrons with $E_0 = 10$ MeV. First, 30–40% of fast neutrons produced by photonuclear reactions are absorbed by ^{14}N within 1 ms, due to resonance of the charge-exchange production shown in the right-top panel of Figure 2.26. As the kinetic energy of neutrons gets lower by multiple elastic scatterings, resonance of the charge-exchange production disappears, then both the charge-exchange production and neutron capture become effective. These variations in the number of neutrons can be empirically reproduced by an exponential function

$$N(t) = N(0)e^{-t/\tau}, \tag{4.11}$$

where the decay constant is $\tau \approx 55$ ms in the 1-atm atmosphere. The constant τ depends on the atmosphere density ρ, and they have a relation $\tau \approx 55 \times (\rho/\rho_{1\ \text{atm}})^{-1}$ ms as shown in Figure 4.14 right. Since the rate of neutron absorption is the differential of the variations in the neutron number, the rate of neutron captures is

$$N_{n\gamma}(t) = \frac{\Sigma_{n\gamma}}{\Sigma_{n\gamma} + \Sigma_{np}} \frac{N(0)}{\tau} e^{-t/\tau} \propto e^{-t/\tau}. \tag{4.12}$$

Therefore, the rate of neutron captures as well as that of de-excitation gamma rays by neutron captures also exponentially decrease with the time constant τ.

In the actual observational results, the count-rate histories of the short burst exponentially decayed, and their time constants were obtained as 56±3, 55±12 and 36±4 ms for Detectors 1–3, respectively. This is consistent with $\tau \approx 55$ ms, obtained by the calculation above. Therefore, the time variation in gamma-ray count rates of the short burst can be interpreted as de-excitation gamma rays by neutron captures after neutrons undergo multiple elastic scatterings.

Then, can the energy spectra of the short burst be explained by de-excitation gamma rays of neutron captures? For neutron captures with ^{14}N, multiple de-excitation gamma-ray lines are emitted by the rest nuclei ^{15}N (Subsection 2.6.3). The de-excitation lines whose relative intensity to the brightest line is larger than 10% are shown in Table 2.1. The 5.269 MeV line has the maximum intensity, and the 10.829 MeV line has the maximum energy.

When these gamma-ray lines enter radiation monitors, observed energy spectra include detector responses. We thus fit the observed energy spectra of the short burst with a model of de-excitation gamma rays by utilizing a spectral analysis framework XSPEC to remove detector responses. The model of multiple de-excitation lines from ^{14}N are constructed based on the energies and intensities listed in Table 2.1. The fitting results are shown in Figure 4.15. The steep cutoff at ∼10 MeV seen in all the short burst spectra corresponds to the maximum energy 10.829 MeV of de-excitation lines of ^{14}N. Spectra of Detectors 2 and 3 can be reproduced by the de-excitation gamma-ray model, while that of Detector 1 is not consistent with gamma rays from ^{14}N only.
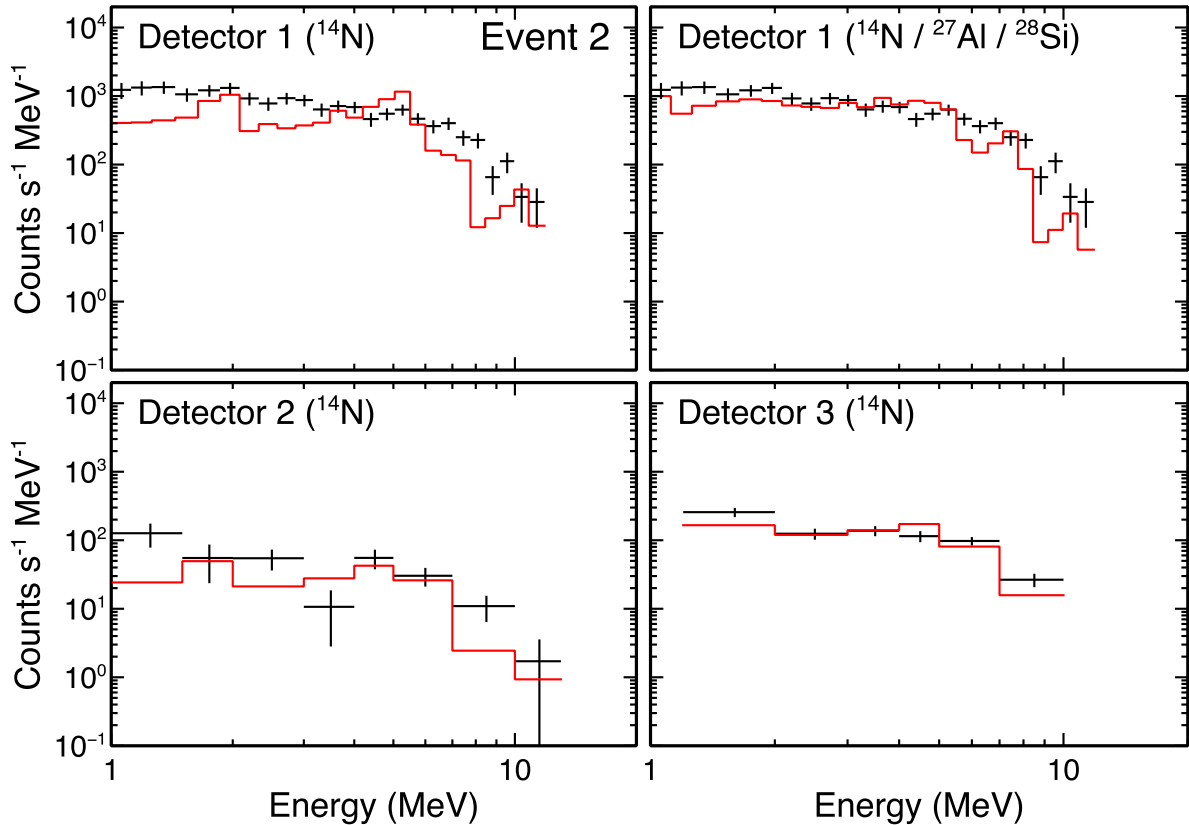
Figure 4.15: Fitting results of the short-burst spectra of Event 2 with de-excitation gamma-ray lines. The black cross markers and red lines show observation data and the best-fit models, respectively.

It is possible that neutrons can be captured by nuclei in soil or in materials of detectors when they reach the ground. Figure 2.26 also shows cross sections of neutron reactions with ^{27}Al and ^{28}Si, which are contained in soil and in detector's component. De-excitation gamma rays of neutron captures with ^{27}Al and ^{28}Si are also shown in Table 2.1. The maximum intensity of de-excitation lines from ^{27}Al and ^{28}Si is at 0.03 MeV and 1.27 MeV, and the maximum energy at 7.72 MeV and 7.20 MeV, respectively. The maximum energy of gamma rays from ^{27}Al and ^{28}Si is lower than that from ^{14}N. The fitting result considering the effects of ^{27}Al and ^{28}Si is shown in the right upper panel of Figure 4.15. Only the ^{14}N and ^{27}Al components, but not the ^{28}Si component are required to improve the fitting result. While atmospheric attenuation of de-excitation gamma rays should be considered for more precise discussions, it is suggested that energy spectra of the short burst consist of a superposition of de-excitation gamma rays that are emitted by neutron captures. Based on the temporal and spectral analysis above, it is confirmed that the short burst was caused by de-excitation gamma rays of neutron captures with ^{14}N and ^{27}Al after neutrons were thermalized by elastic scatterings in the atmosphere. In summary, neutrons were produced in the lightning.

4.2.4 Initial flash triggering photonuclear reactions

If photonuclear reactions occurred and produced neutrons and β^+-decay nuclei, seed photons of >10 MeV must have existed. Since the cross sections of photonuclear reactions are two orders

of magnitude lower than those of Compton scattering and pair creation, enormous number of photons should have produced and a part of them could have reached the ground. As reviewed in Chapter 2, X-ray emissions below a few MeV, and TGFs, whose energy spectra extending up to 40 MeV, have been discovered. Considering the threshold energy of photonuclear reactions, TGFs are potentially able to trigger them [Babich, 2006, 2007, Carlson et al., 2010, Tavani et al., 2013]. While most of detected TGFs are upward going observed from space, a few are going downward (called downward TGFs), and observed at ground-level [Abbasi et al., 2018, 2017, Colalillo, 2017, Dwyer et al., 2004, 2012a, Hare et al., 2016, Tran et al., 2015].

At the beginning of the short burst, waveform baseline of shaping amplifier output got significantly negative, and gradually recovered to the normal level, as shown in Figure 4.4. This situation is called "undershoot". The recovery of the baseline undershoot can be fitted by an exponential function as shown in Figure 4.16. The time constant of the exponential function is determined as 3.45 ± 0.05 ms, 1.17 ± 0.04 ms and 2.31 ± 0.04 ms for Detector 1–3, respectively. Since the undershoot took place only at the beginning of the short burst, it is likely that the undershoot was triggered by a phenomenon preceding the short burst, not the short burst itself.

We hypothesized that the undershoot is a signature of a downward TGF triggering the photonuclear reactions. We then performed a verification experiment. The detectors used in the observation have photomultiplier tubes coupled with a scintillation crystal, and their output signals are read by the data acquisition system (subsection 3.2). When photons enter scintillation crystals with a shorter interval than time constants of scintillation, preamplifier or shaping amplifier, a saturation called "pileup" should take place. Namely, accurate energy measurement and photon counting cannot be performed under such a condition. If an enormous number of photons reach the ground within a typical TGF duration of tens of microseconds to a few milliseconds, our detectors can easily experience pileups.

We performed an investigation to examine how output waveform of shaping amplifier is disturbed at the moment of pileup. The setup of the verification experiment is shown in Figure 4.17. To imitate a situation that a large number of gamma rays enter a scintillation crystal, optical photons produced by LEDs directly irradiated photomultiplier tubes. We employed LEDs emitting greens photons of 567 nm, and a pulse generator PB-5 (Berkeley Nucleonics
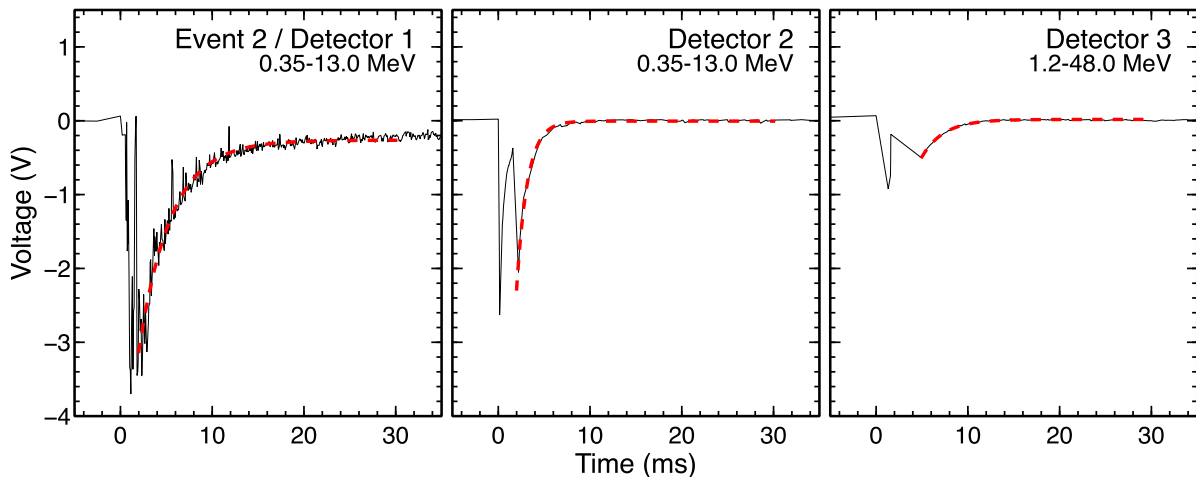
Figure 4.16: Undershoots detected at the beginning of Event 2. The best-fit model of an exponential function is overlaid with red-dashed lines.
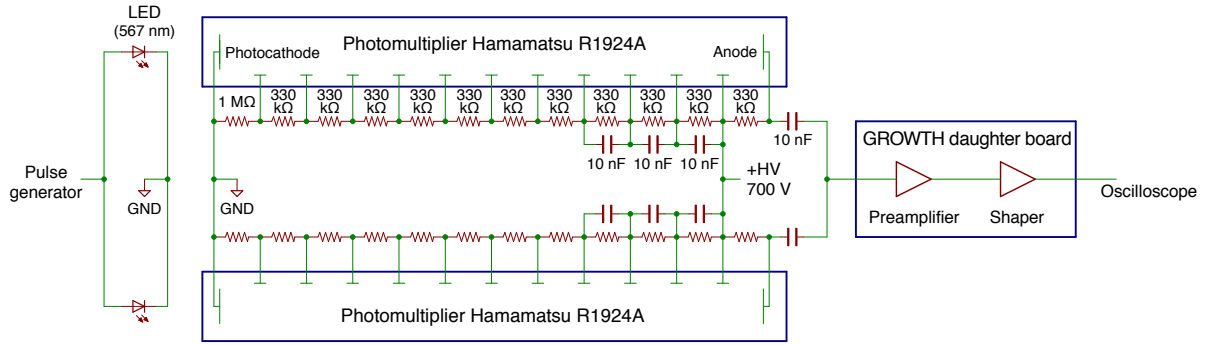
Figure 4.17: A schematic diagram of the setup for the verification experiment of undershoots.
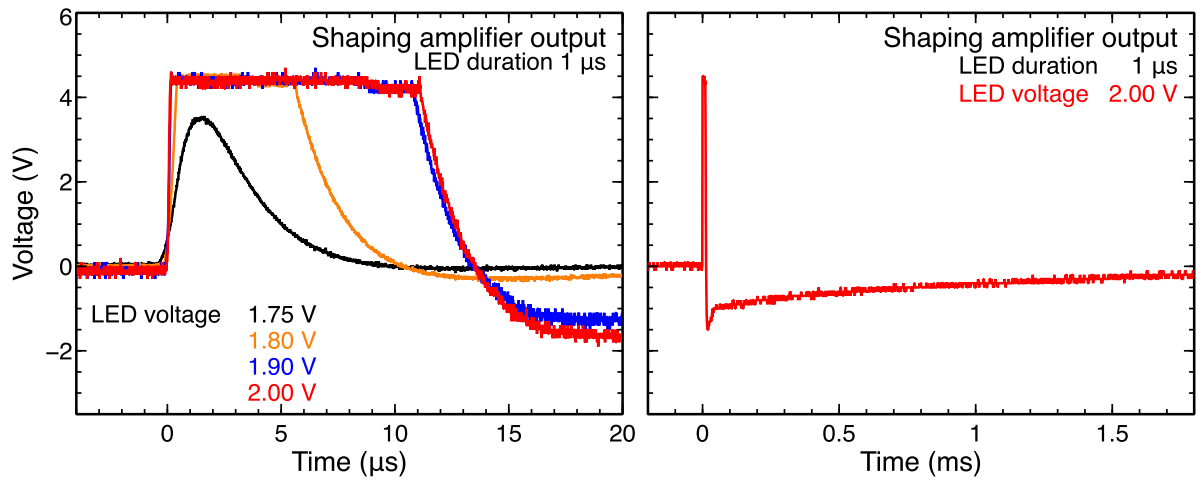
Figure 4.18: Analog outputs of shaping amplifier with various LED intensities (left) and an entire waveform of a reproduced undershoot (right).
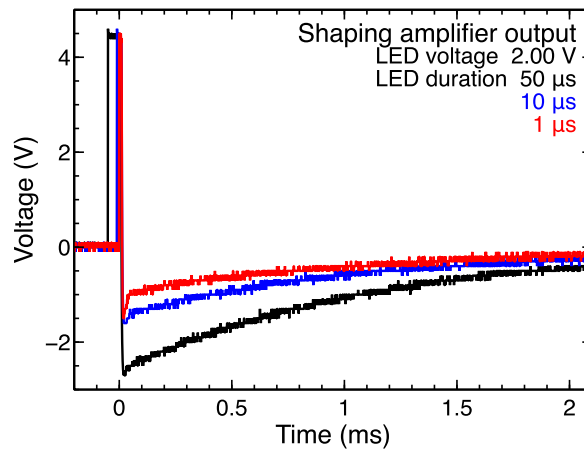
Figure 4.19: Reproduced baseline undershoots with various durations of LED pulses.

Corporation) to control LEDs. Pulses generated by PB-5 were set to be a square wave, whose onset and falling time constant were fixed to 0.05 μs and 0.5 μs respectively. A couple of photo-

multiplier tubes R1924A (Hamamatsu) were used to reproduce the same configuration of BGO type 1. Bias voltage was set to be +700 V, provided through a divider circuit which is the same as BGO type 1. Their output signals were input into the amplifier circuit of the DAQ system, and amplified signals were monitored by an oscilloscope.

First of all, saturation of amplifier outputs were monitored by changing pulse voltages supplied to LEDs. The output waveforms when pulse duration is fixed to 1 μs are shown in the left panel of Figure 4.18. While output signal was normal when 1.75 V was supplied to LEDs, it was saturated when 1.8 V was supplied. Moreover, as the supply voltage increased, baseline undershoots after the saturation became visible while the pulse height did not significantly change. The entire waveform when 2.00 V was supplied is presented in the right panel of 4.18. Just after the LED pulse, the waveform got negative and recovered to the normal level over a few milliseconds.

To investigate how the amount of charges from PMTs affects the depth of undershoots, we obtained waveforms by changing the pulse duration to 1.0 μs, 10.0 μs and 50.0 μs while the pulse voltage was fixed to 2.00 V. The result is shown in Figure 4.19. The depth of undershoots got larger as the pulse duration got longer, namely a larger amount of charges from PMTs were input.

The time constant of baseline recovery is 1.310 ± 0.050 ms, 0.947 ± 0.016 ms and 1.108 ± 0.012 ms for the pulse duration of 1.0 μs, 10.0 μs and 50.0 μs, respectively. These time constants of the reproduced undershoots are similar to those of the observed undershoots in the order of magnitude. Therefore, it is suggested that much larger amount of energy than the energy range of detectors was input within a few milliseconds, and the undershoots took place at the leading part of the short burst.

It is impossible to obtain photon count rates or energy spectra of gamma rays which triggered undershoots. Considering an extreme case, it is difficult to distinguish whether the undershoots were triggered by one photon of >100 MeV or by a hundred photons of 1 MeV. On the other hand, the latter scenario is more likely, given that the undershoots was recorded by three detectors simultaneously and the reaction cross section with scintillation crystals at >100 MeV is much lower. Therefore, we conclude that the undershoots are a signature of a downward TGF triggering photonuclear reactions.

As seen in Figure 4.16, Detectors 2 and 3 recorded undershoots twice with an interval of a few milliseconds. On the other hand, only one undershoot took place for one LED pulse in the verification experiment (Figure 4.19). Therefore, the repetition of the undershoots indicates that gamma-ray flashes occurred twice, rather than an instrumental response. In fact, TGFs containing multiple pulses called multi-pulse TGFs [Fishman et al., 1994, Foley et al., 2014] have been observed from space (Subsection 2.1.1). The correlations between the undershoots and radio-frequency waveforms are presented in Appendix E.

We consider that the capacitors in the final step of the PMT divider caused the undershoot. Since the present divider circuit is designed for positive bias voltage input, a decoupling capacitor is attached to the signal output line to cut bias voltage. In a normal operation, positive charges are accumulated at the side connected to the anode of the divider. However, abnormal currents from PMTs discharge the decoupling capacitors, and large current flows into the preamplifier. It causes baseline undershoots. The undershoots recover by recharging the decoupling capacitors via the preamplifiers. The recovery time constant is determined by the value of the decoupling capacitors and the feedback resister of the amplifier. Since two dividers are connected in parallel in the present case, the capacity of the decoupling capacitors is 20 nF, the synthesis of two 10 nF capacitors. The value of the feedback resister is 100 kΩ. Therefore, the recovery time constant is 2 ms, which is consistent with those of the observed and reproduced
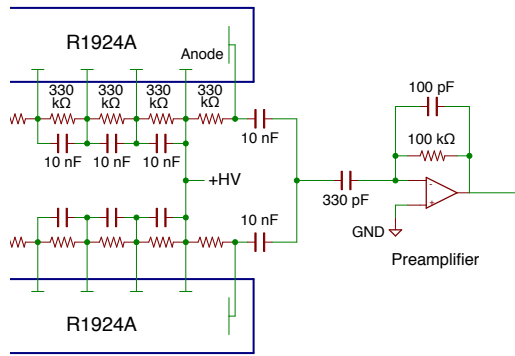
Figure 4.20: A setup to confirm an effect of capacity in the decoupling capacitors.
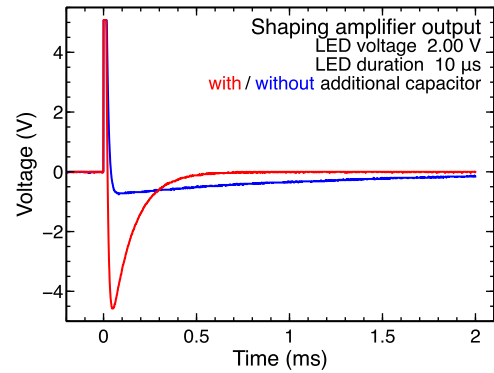

Figure 4.21: Comparison of recovery time scale from undershoots with and without and additional capacitor.

undershoots.

Considering the discussion above, the recovery time constant should be smaller as the capacity of the decoupling capacitor gets smaller. To confirm this hypothesis, a capacitor of 330 pF was inserted between the divider output and the preamplifier, as shown in Figure 4.20. The reproduced undershoot is presented in Figure 4.21. The recovery time constant is 0.1184 ± 0.0004 μs with the additional capacitor, faster than 0.947 ± 0.016 μs without it. In contrast, the depth of the undershoot became larger with it. Even though relatively moderate saturation could also disturb baseline, a smaller capacity of the decoupling capacitor recovers baseline undershoots faster and hence reduces dead time.

From the discussions above, the series of observed phenomena in Event 2 can be interpreted as:

- A lightning discharge produced an enormous number of gamma rays, called a downward TGF.
- Gamma rays reaching the ground saturated the detectors, and triggered an undershoot of analog outputs.
- Gamma-ray photons of >10 MeV triggered photonuclear reactions with ^{14}N and ^{16}O in the atmosphere and ^{27}Al and ^{28}Si surrounding the detectors, then produced fast neutrons and proton-rich nuclei such as ^{13}N, ^{15}O, ^{26m}Al and ^{27}Si.
- Fast neutrons were thermalized by multiple elastic scatterings with atmospheric nuclei, and disappeared by neutron captures or charge-exchange productions with ^{14}N.
- ^{15}N in an excited state by neutron captures emitted de-excitation gamma rays. These gamma rays were detected as the short burst.
- The duration of the short burst is characterized by neutron thermalization in the atmosphere.
- Proton-rich nuclei ^{13}N and ^{15}O emit positrons with half-lives of 10 and 2 minutes, respectively. Gamma-ray detectors recorded annihilation gamma rays when these nuclei were produced around the detectors, or passed over with ambient wind.
- Annihilation gamma rays of positrons from ^{26m}Al and ^{27}Si produced around the detectors are also detected.

4.3 Interpretation of All Detected Events

In this section, we survey whether all the short-burst events besides Event 2 originate from photonuclear reactions in lightning. Hereafter, we set the onset of a short burst as the origin of time t.

4.3.1 Event 1

In the Kashiwazaki site, two short bursts 20170116 (Event 1) and 20171124 (Event 3) were detected beside Event 2. Event 1 was detected at 12:19:23 JST, January 16th, 2017. Figure 4.22 shows count-rate histories recorded by Detectors 1–3. Despite successful operation of Detector 4, it was highly saturated at this moment like Event 2, thus excluded from the analysis. The count-rate histories of the short burst exhibited a steep onset associated with lightning, and an
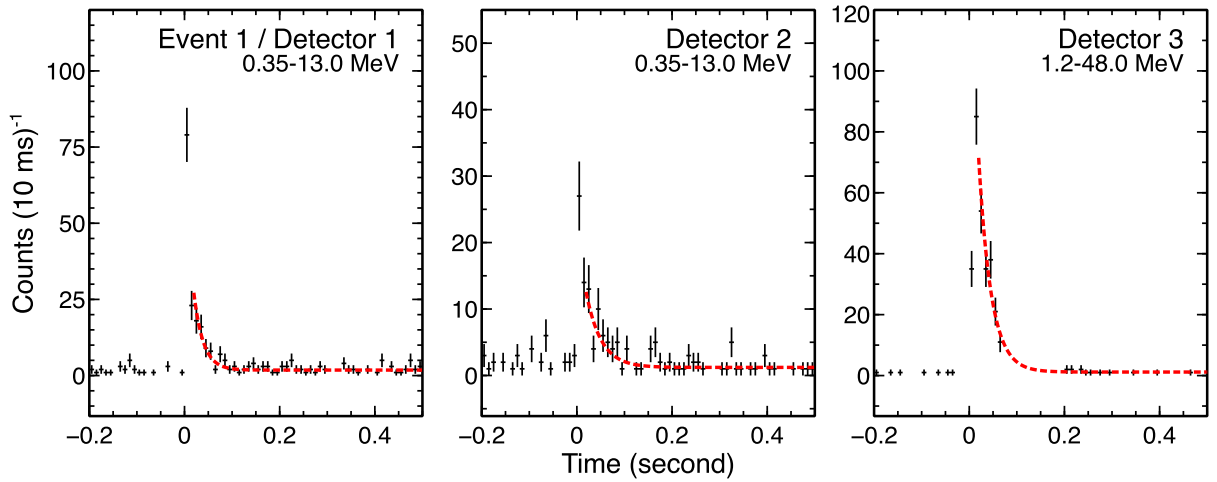
Figure 4.22: Count-rate histories of the short burst Event 1. Best-fit exponential functions are overlaid by red-dotted lines. A part of Detector 3 during 0.1–0.2 ms was lacked due to buffer overflow of the DAQ system.
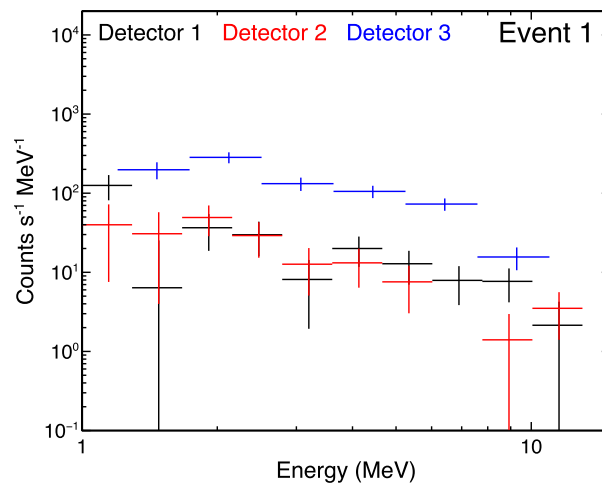
Figure 4.23: Energy spectra of the short burst Event 1. Photon events are extracted from 20 ms$<$ $t <$300 ms.

70
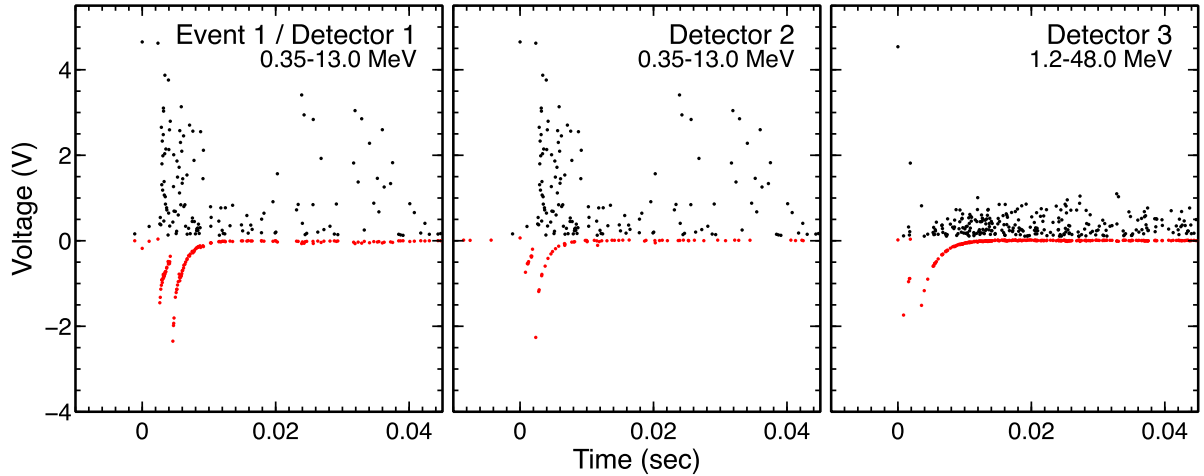
Figure 4.24: Time series of pulse height (black) and waveform baseline (red) of each photon event in Event 1.
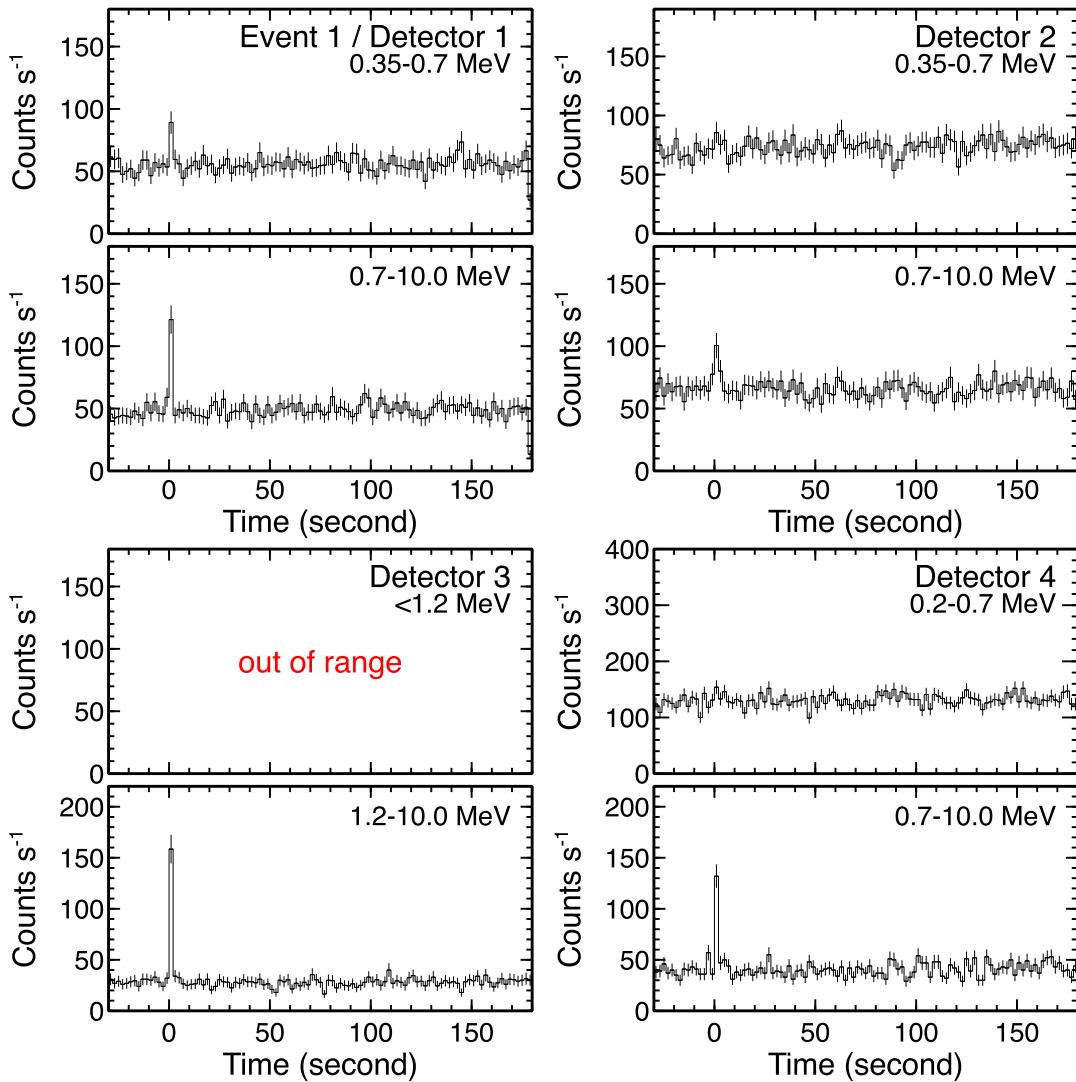
Figure 4.25: Count-rate histories of gamma rays below and above 0.7 MeV after the short burst Event 1.

71
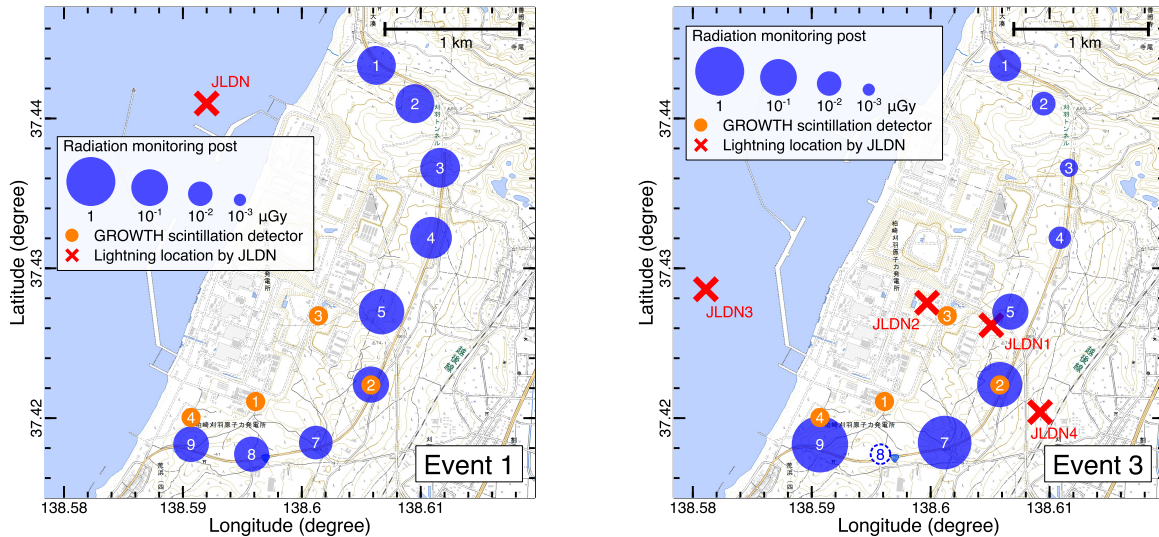
Figure 4.26: Maps of gamma-ray detectors and lightning locations at Kashiwazaki-Kariwa Nuclear Power Station with total doses recorded by MPs in Events 1 (left) and 3 (right). JLDN-reported lightning events are numbered by time. MP8 was unavailable in Event 3.

exponential decay. The decay constant is 21±5 ms, 32±14 ms and 26±7 ms for Detectors 1–3, respectively. The observed decay constants are the same order of magnitude as that in Event 2, although they are slightly shorter than the calculated one $\tau \approx 55$ ms. The energy spectra of the short burst are shown in Figure 4.23. Regardless of poorer photon statics than Event 2, a continuum-like component with a steep cutoff at 10 MeV are seen in the spectra.

Scatter plots of photon pulse height and analog baseline at the beginning of the short burst are shown in Figure 4.24. All the detectors recorded saturated pulses exceeding 4 V, and baseline undershoots twice, at least. The recovery time constant of Detectors 1–3 is 1.59±0.03 ms, 1.43±0.05 ms and 2.130±0.014 ms, respectively.

Figure 4.25 presents count-rate histories after the short burst. Since no detectors recorded significant enhancements below 0.7 MeV, annihilation gamma rays were not detected in this event. However, it is unclear whether positrons were not produced, because annihilation lines are out of range of Detector 3, which recorded the largest number of short-burst photons among the detectors.

At the moment of the short-burst detection, JLDN recorded lightning currents in the Kashiwazaki area. JLDN reported in total 10 discharges in a 20×20 km^2 area centered at the power station from 12:19:23.00 to 12:19:24.00JST. Only the first discharge took place within 3 km from the power station. Its estimated position is shown in the left panel of Figure 4.26. It was detected at 12:19:23.027064 JST, categorized as an in-cloud current of -25 kA. Total doses measured by high-level dosimeters of MPs are also shown in Figure 4.26 left. MP5 recorded 0.22 μGy, the highest dose among MPs. MPs located in the north of the power station recorded higher doses. Ambient wind flew at west-northwest with a speed of 11.8±1.3 m s^{-1}, estimated by XRAIN analysis.

Since annihilation signals were not detected in this event, it is insufficient to conclude that photonuclear reactions took place. On the other hand, the energy spectra and count-rate histories similar to Event 2 suggest neutron production. Furthermore, JLDN recorded a lightning discharge associated with the short burst, and signatures of downward TGFs such as analog baseline undershoots and dose enhancements in MPs were recorded. Therefore, a downward

TGF probably triggered photonuclear reactions. Because higher doses were recorded by MPs in the north area and the count rate was highest at Detector 3, the downward TGF is thought to have occurred in the north area of the power station. It is thus consistent that annihilation signals were not recorded by Detectors 1, 2 and 4 in the south area. If Detecter 3 had covered below 1.2 MeV, it might have detected annihilation gamma rays.

4.3.2 Event 3

Event 3 took place at 19:03:02 JST, November 24th, 2017. Count-rate histories of the short burst are shown in Figure 4.27. As well as Events 1 and 2, the short burst exhibited a steep onset and an exponential decay. The decay constant is 59 ± 2 ms, 47 ± 14 ms and 48 ± 6 ms for Detectors 1–3 respectively, which is consistent with the calculated time constant of neutron thermalization $\tau \approx 55$ ms. Energy spectra, shown in Figure 4.28, extend up to 10 MeV and have a steep cutoff at 10 MeV, similar characteristics to Events 1 and 2.

Scatter plots of photon pulse heights and analog baseline are shown in Figure 4.29. Each detector recorded several saturation signals exceeding 4 V at the beginning of the short burst. Detectors 1 and 3 also recorded significant multiple undershoots. The last undershoot has a recovery time constant of 1.99 ± 0.04 ms and 1.533 ± 0.006 ms for Detectors 1 and 3, respectively. Although Detector 2 did not record significant undershoots, its baseline was significantly negative at the beginning of the short burst. It might have missed baseline undershoots due to the small number of photon detection.

Count-rate histories after the short burst are shown in Figure 4.30. While any enhancements were not registered by Detectors 2 and 3, Detectors 1 and 4 recorded a significant afterglow below 0.7 MeV. The afterglow exponentially decayed, with a decay constant of 6.8 ± 1.3 sec and 10.0 ± 2.3 sec for Detectors 1 and 4, respectively.

Energy spectra of the afterglow observed with Detectors 1 and 4 are presented in Figure 4.31. Both detectors observed a line emission and its Compton-scattered component. The line component is reproduced by a Gaussian function, centered at 0.530 ± 0.004 MeV and 0.490 ± 0.003 MeV with a width (FWHM) of 0.130 ± 0.009 MeV and 0.057 ± 0.007 MeV for Detectors 1 and 4, respectively.

JLDN detected 8 discharge currents at the timing of the short burst (19:03:02 JST), in a 20×20 km^2 area centered at the power station. Among the 8 discharges, the first to forth ones took place within 3 km from the plant. Their locations are presented in the right panel of Figure 4.26. The first and third ones are categorized as cloud-to-ground currents, and the second and forth ones as in-cloud currents. At the same time as the short burst and lightning detection, high-level dosimeters also recorded a significant increase in radiation doses, as shown in Figure 4.26 right. The amounts of dose enhancements are larger in south area of the power station. The maximum dose was 1.37 μGy, measured at MP9. By an XRAIN analysis, ambient wind was estimated to be from west with a speed of 15.3 ± 1.4 m s^{-1}.

In the present case, detectors registered the annihilation line from positrons, signatures of neutrons and a downward TGF associated with a lightning discharge. Therefore, Event 3 also originates from photonuclear reactions triggered by a lightning discharge. For Event 3, a delayed component of the annihilation line was not detected, while the decaying component was detected by Detectors 1 and 4. We have two hypothesis to interpret this result. The first one is that most of the annihilation gamma rays originated from β^+ decay of ^{26m}Al and ^{27}Si, not from atmospheric nuclei such as ^{13}N and ^{15}O. The other is that ^{13}N and ^{15}O also contributed to the positron annihilation emissions in addition to ^{26m}Al and ^{27}Si. The latter case requires that the photonuclear reactions should have taken place right over the detectors or slightly downwind.
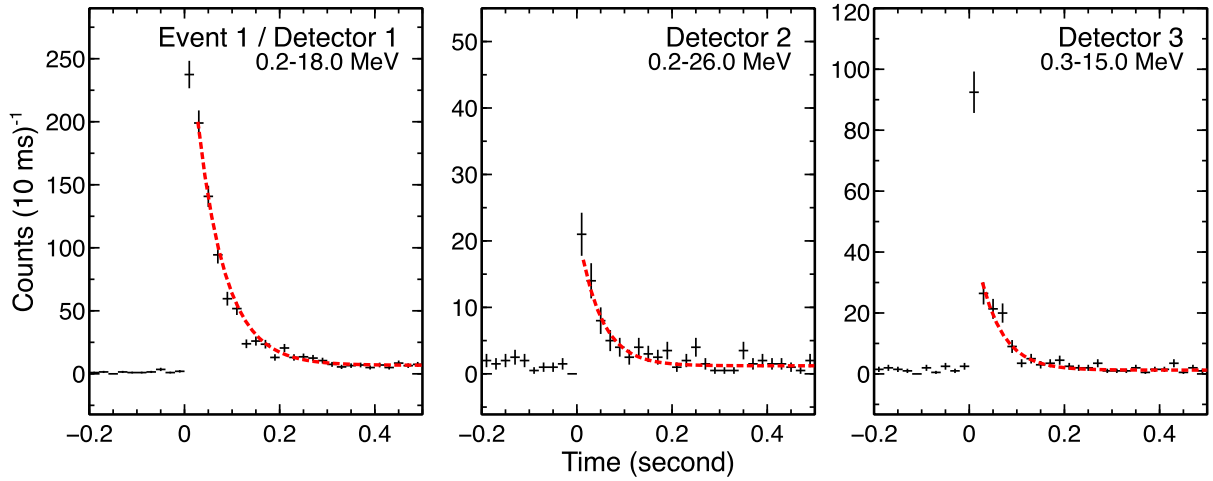
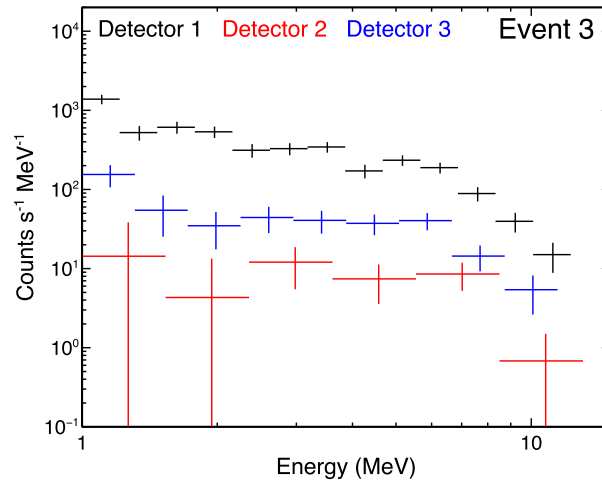Figure 4.27: Count-rate histories of the short burst Event 3.

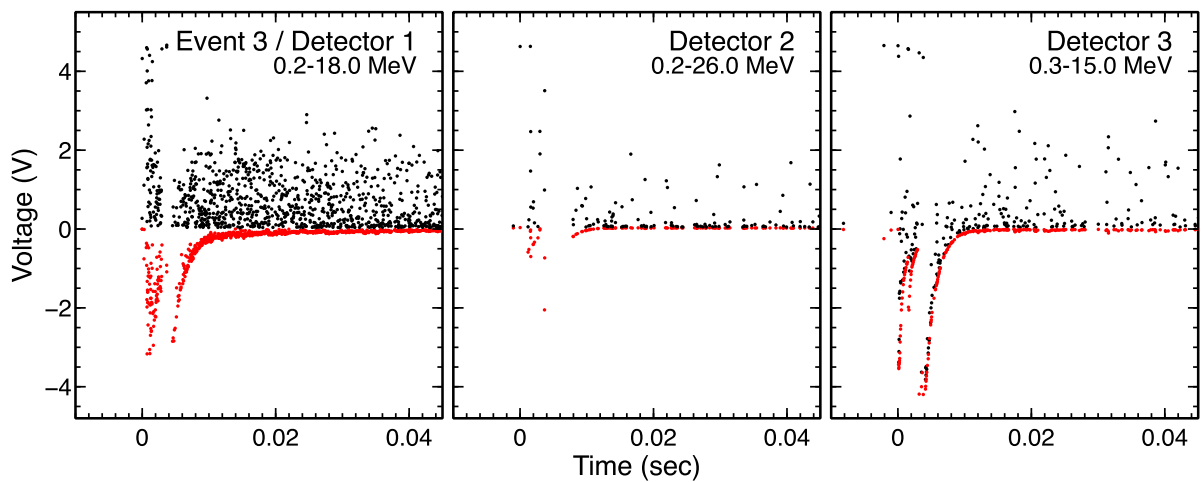Figure 4.28: Energy spectra of the short burst Event 3.

Figure 4.29: Time series of pulse height (black) and waveform baseline (red) of each photon event for Event 3. Detector 3 employs the differential threshold mode (Section 3.2).
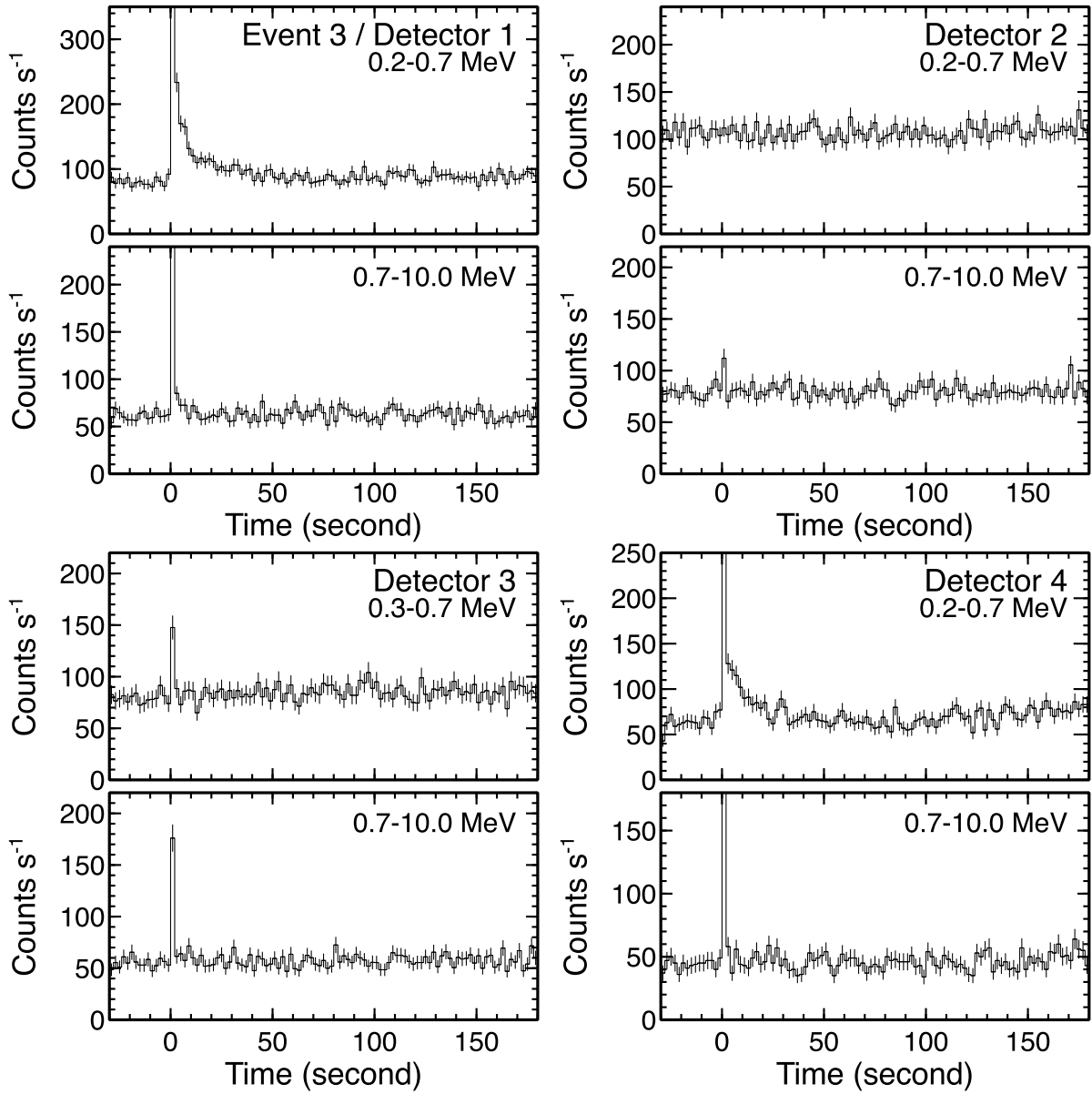
Figure 4.30: Count-rate histories of gamma rays below and above 0.7 MeV after the short burst Event 3.
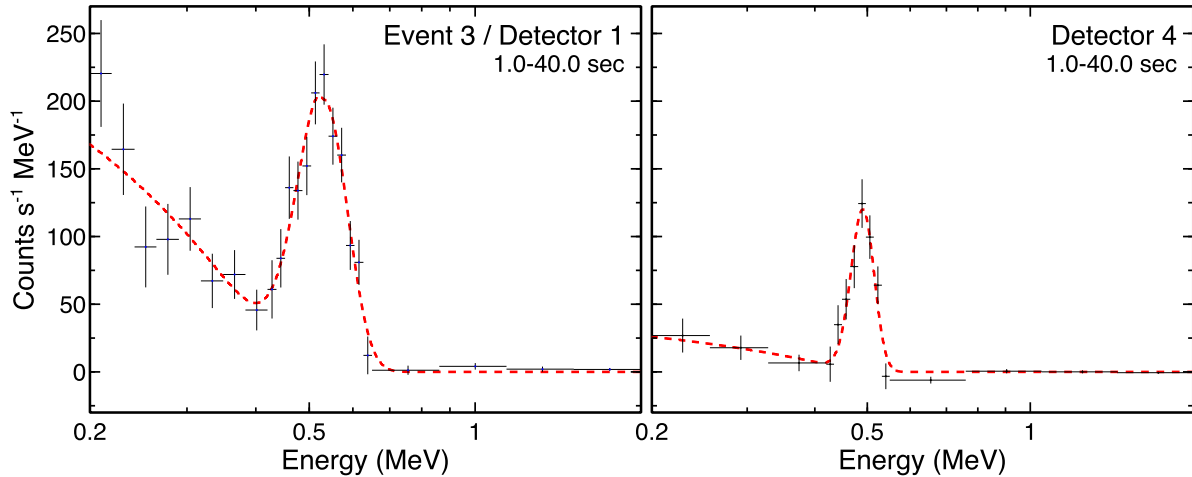
Figure 4.31: Energy spectra of annihilation gamma rays of Event 3. Photon events are extracted from 1.0 sec$< t <$40.0 sec.

4.3.3 Event summary

During the FY2016 and 2017 observation periods, three in Kashiwazaki, two in Kanazawa, in total five short-burst events were successfully detected. Events 4 and 5, detected in Kanazawa are analyzed in Appendix B. All the detected short bursts are consistent with gamma-ray signatures originating from neutron thermalization and capture in the atmosphere. At the beginning of the short bursts, intense gamma-ray flashes lasting for less than milliseconds, namely downward TGFs, were indicated. Furthermore, four short bursts are characterized by annihilation emissions of positrons. Based on these observational results and discussions, all the observed short bursts originated from photonuclear reactions with nuclei in the atmosphere and in ambient matters triggered by high-energy photons of downward TGFs. These reactions are interpreted to have created fast neutrons and β^+-decay nuclei. Major parameters of the short bursts are summarized in Tables 4.3 and 4.4.

Table 4.3: Summary of short bursts observed in Kashiwazaki.

Event 1 (20170116)				
Time (JST)	Coincidence with lightning		Observation area	
2017-01-16 12:19:23	Yes		Kashiwazaki	
Detector	1	2	3	4
Energy range	0.35–13.0 MeV	0.35–13.0 MeV	1.2–48.0 MeV	0.2–27.0 MeV
Undershoot	Yes (multiple)	Yes (multiple)	Yes (multiple)	Saturated
(Time Constant)	1.59±0.03 ms	1.43±0.05 ms	2.130±0.014 ms	N/A
Short burst	Yes	Yes	Yes	Saturated
(Decay constant)	21±5 ms	32±14 ms	26±7 ms	N/A
Annihilation gamma rays	No	No	Out of range	No
(Center energy)	N/A	N/A	N/A	N/A
Decaying emission	N/A	N/A	N/A	N/A
(Time constant)	N/A	N/A	N/A	N/A
Delayed emission	N/A	N/A	N/A	N/A

Event 2 (20170206)				
Time (JST)	Coincidence with lightning		Observation area	
2017-02-06 17:34:06	Yes		Kashiwazaki	
Detector	1	2	3	4
Energy range	0.35–13.0 MeV	0.35–13.0 MeV	1.2–48.0 MeV	0.2–27.0 MeV
Undershoot	Yes (multiple)	Yes (multiple)	Yes (multiple)	Saturated
(Time Constant)	3.45±0.05 ms	1.17±0.04 ms	2.31±0.04 ms	N/A
Short burst	Yes	Yes	Yes	Saturated
(Decay constant)	56±3 ms	55±12 ms	36±4 ms	N/A
Annihilation gamma rays	Yes	No	Out of range	Yes
(Center energy)	515±8 keV	N/A	N/A	501±7 keV
Decaying emission	Yes	N/A	N/A	Yes
(Time constant)	3.7±1.2 sec	N/A	N/A	7.2±1.1 sec
Delayed emission	Yes	N/A	N/A	No

Event 3 (20171124)				
Time (JST)	Coincidence with lightning		Observation area	
2017-11-24 19:03:02	Yes		Kashiwazaki	
Detector	1	2	3	4
Energy range	0.2–18.0 MeV	0.2–26.0 MeV	0.3–15.0 MeV	0.2–27.0 MeV
Undershoot	Yes (multiple)	Slightly	Yes (multiple)	Saturated
(Time Constant)	1.99±0.04 ms	N/A	1.533±0.006 ms	N/A
Short burst	Yes	Yes	Yes	Saturated
(Decay constant)	59±2 ms	47±14 ms	48±6 ms	N/A
Annihilation gamma rays	Yes	No	No	Yes
(Center energy)	530±4 keV	N/A	N/A	490±3 keV
Decaying emission	Yes	N/A	N/A	Yes
(Time constant)	6.8±1.3 sec	N/A	N/A	10.0±2.3 sec
Delayed emission	No	N/A	N/A	No

Table 4.4: Summary of short bursts observed in Kanazawa.

Event 4 (20171205)		
Time (JST)	Coincidence with lightning	Observation area
2017-12-05 18:35:24	Yes	Kanazawa
Detector	9	
Energy range	0.4–20.0 MeV	
Undershoot	Yes (single)	
(Time Constant)	1.58±0.04 ms	
Short burst	Yes	
(Decay constant)	49±7 ms	
Annihilation gamma rays	Slightly	
(Center energy)	460±20 keV	
Decaying emission	Slightly	
(Time constant)	$2.6^{+4.1}_{-2.6}$ sec	
Delayed emission	No	

Event 5 (20180110)		
Time (JST)	Coincidence with lightning	Observation area
2018-01-10 02:54:50	Yes	Kanazawa
Detector	7	8
Energy range	0.4–20.0 MeV	0.4–20.0 MeV
Undershoot	Yes (single)	Yes (buffer overflow)
(Time Constant)	1.87±0.03 ms	N/A
Short burst	Yes	Yes
(Decay constant)	52±5 ms	59±2 ms
Annihilation gamma rays	No	Slightly
(Center energy)	N/A	518±13 keV
Decaying emission	N/A	Slightly
(Time constant)	N/A	6.8±2.6 sec
Delayed emission	N/A	No

Chapter 5

Positrons from Proton-rich Radionuclides

In Chapters 5–7, Monte-Carlo simulations are performed to quantitatively interpret the observational data. Physical processes considered here are listed in Figure 5.1. This chapter considers photonuclear reactions in the atmosphere, and propagations of positrons produced by β^+-decay nuclei. Chapter 6 considers neutron propagation and reactions, and Chapter 7 propagation of electrons and gamma rays produced by downward TGFs. The simulation results are compared with our measurements.
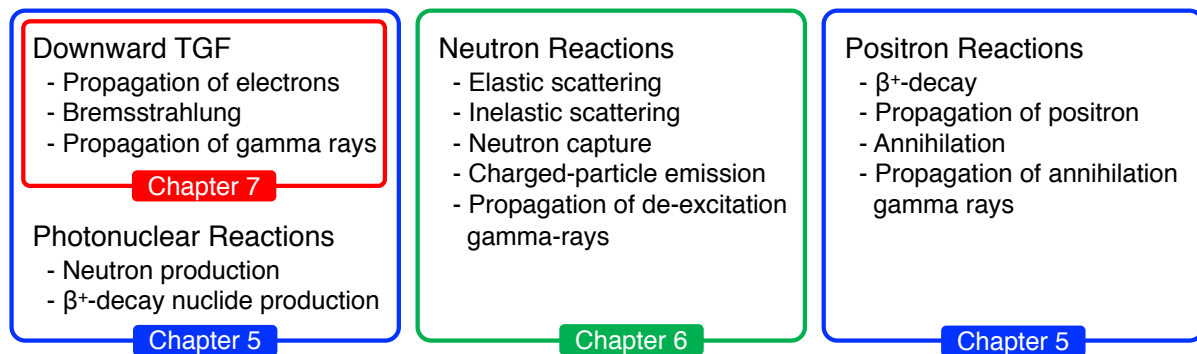
Figure 5.1: Instruction of physical processes considered in Chapters 5–7.

5.1 Channels of Photonuclear Reactions in the Atmosphere

In Section 4.2.2, only two primary channels, $^{14}\mathrm{N}(\gamma, n)^{13}\mathrm{N}$ and $^{16}\mathrm{O}(\gamma, n)^{15}\mathrm{O}$, are considered to produce β^+-decay nuclei. However, more reaction channels are listed in nuclear reaction libraries complied by atomic energy agencies. The present thesis refers to the nuclear reaction database ENDF/B-VII.1 [Chadwick et al., 2011] compiled and maintained by National Nuclear Data Center of Brookhaven National Laboratory. Data included in ENDF/B-VII.1 are theoretically calculated and verified by comparing with experimental data. ENDF/B-VII.1 contains production cross sections, energy spectrum, and ejection angle of secondary particles for photonuclear reactions with 163 nuclides in the ENDF-6 format.[14] Figure 5.2 presents cross sections of major products from photonuclear reactions with major atmospheric nuclides ($^{14}\mathrm{N}$, $^{15}\mathrm{N}$, $^{16}\mathrm{O}$, $^{17}\mathrm{O}$, $^{18}\mathrm{O}$, and $^{40}\mathrm{Ar}$). Considering reactions in the atmosphere, these reactions are weighted

---

[14]https://www.bnl.gov/isd/documents/70393.pdf

by nuclide compositions of the standard atmosphere, listed in Table 5.1. Composition-included cross sections (mass attenuation coefficients) are also presented in Figure 5.3. Major reactions in the atmosphere and their threshold energies are summarized in Table 5.2. Their threshold energies and peak energies of cross sections are determined by binding energy of neutrons in a nucleus and giant resonances, respectively.

Table 5.1: Number density of atmospheric nuclides.

molecule	ratio in the atmosphere by volume	nuclide	isotope ratio	number density in the atmosphere at 1 atm
N_2	78.08%	^{14}N	99.634%	4.18×10^{19} nuclei cm^{-3}
		^{15}N	0.366%	1.51×10^{17} nuclei cm^{-3}
O_2	20.95%	^{16}O	99.76%	1.12×10^{19} nuclei cm^{-3}
		^{17}O	0.039%	4.50×10^{15} nuclei cm^{-3}
		^{18}O	0.201%	2.36×10^{16} nuclei cm^{-3}
Ar	0.93%	^{40}Ar	99.600%	2.50×10^{17} nuclei cm^{-3}

Among products of the photonuclear reactions considered above, β^+-decay nuclides are only ^{13}N and ^{15}O. The production channels of them are one-neutron emitting reactions $^{14}N(\gamma, n)^{13}N$ and $^{16}O(\gamma, n)^{15}O$, and two-neutron emitting reactions $^{15}N(\gamma, 2n)^{13}N$ and $^{17}O(\gamma, 2n)^{15}O$. Their reaction thresholds are 10.55 MeV, 15.66 MeV, 21.39 MeV, and 19.81 MeV, respectively.

There are more photonuclear channels to produce neutrons than ones to produce β^+-decay nuclides. Reactions (γ, np), emitting a neutron and a proton simultaneously, are the most popular channels in photonuclear reactions with ^{14}N, ^{15}N, ^{16}O, and ^{17}O. Therefore, it is predicted that a larger number of neutrons are produced than β^+-decay nuclei by photonuclear reactions in the atmosphere. Nuclides produced by (γ, np) reactions, ^{12}C, ^{13}C, ^{14}N, and ^{15}N, are all stable isotopes. Neutron production channels with ^{18}O and ^{40}Ar are mainly $^{18}O(\gamma, n)^{17}O$, $^{18}O(\gamma, 2n)^{16}O$, $^{40}Ar(\gamma, n)^{39}Ar$, and $^{40}Ar(\gamma, 2n)^{38}Ar$. Only ^{39}Ar is a radioactive isotope. It exhibits β^--decay with a half-life of 269 years and emits an electron, but not a positron. In addition to these reactions, each atmospheric nuclide can be broken into multiple neutrons and protons by photons of > 40 MeV via nuclear spallation reactions.

In actual atmospheric reactions, the contributions of ^{15}N, ^{17}O, and ^{18}O are negligible due to the small fraction of atmospheric composition, as shown in Figure 5.3. Therefore, the present thesis considers contributions of ^{14}N and ^{16}O for β^+-decay nuclide productions, and ^{14}N, ^{15}N, ^{16}O, and ^{40}Ar for neutron productions. Reactions $^{15}N(\gamma, 2n)^{13}N$ and $^{17}O(\gamma, n)^{16}O$, and neutron productions with ^{17}O and ^{18}O are ignored.

---

[15]JAEA JENDL/PD-2016 [Iwamoto et al., 2016]
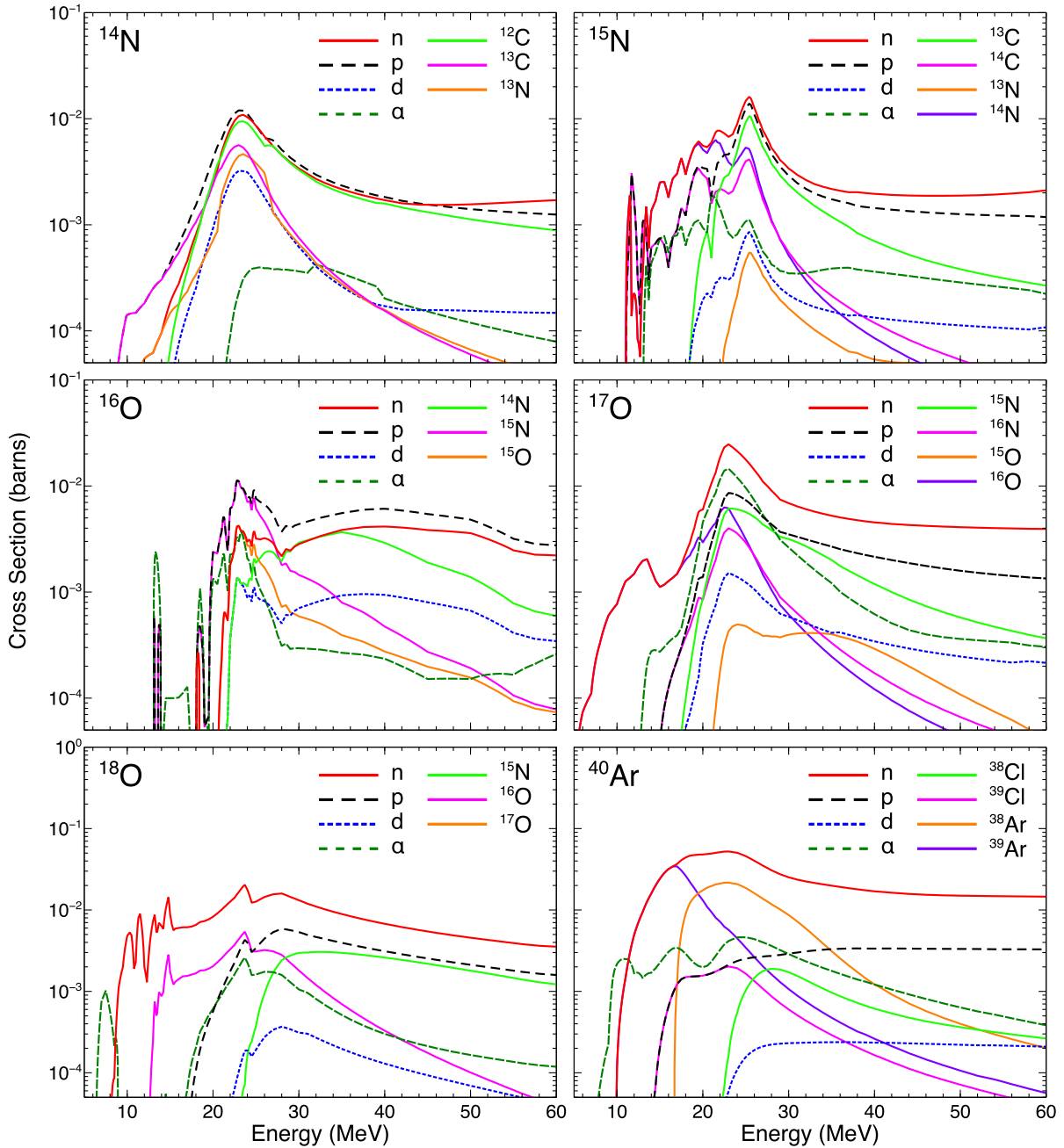
Figure 5.2: Cross sections of major products via photonuclear reactions with atmospheric nuclei as a function of incident gamma-ray energy. Data are extracted from ENDF/B-VII.1.
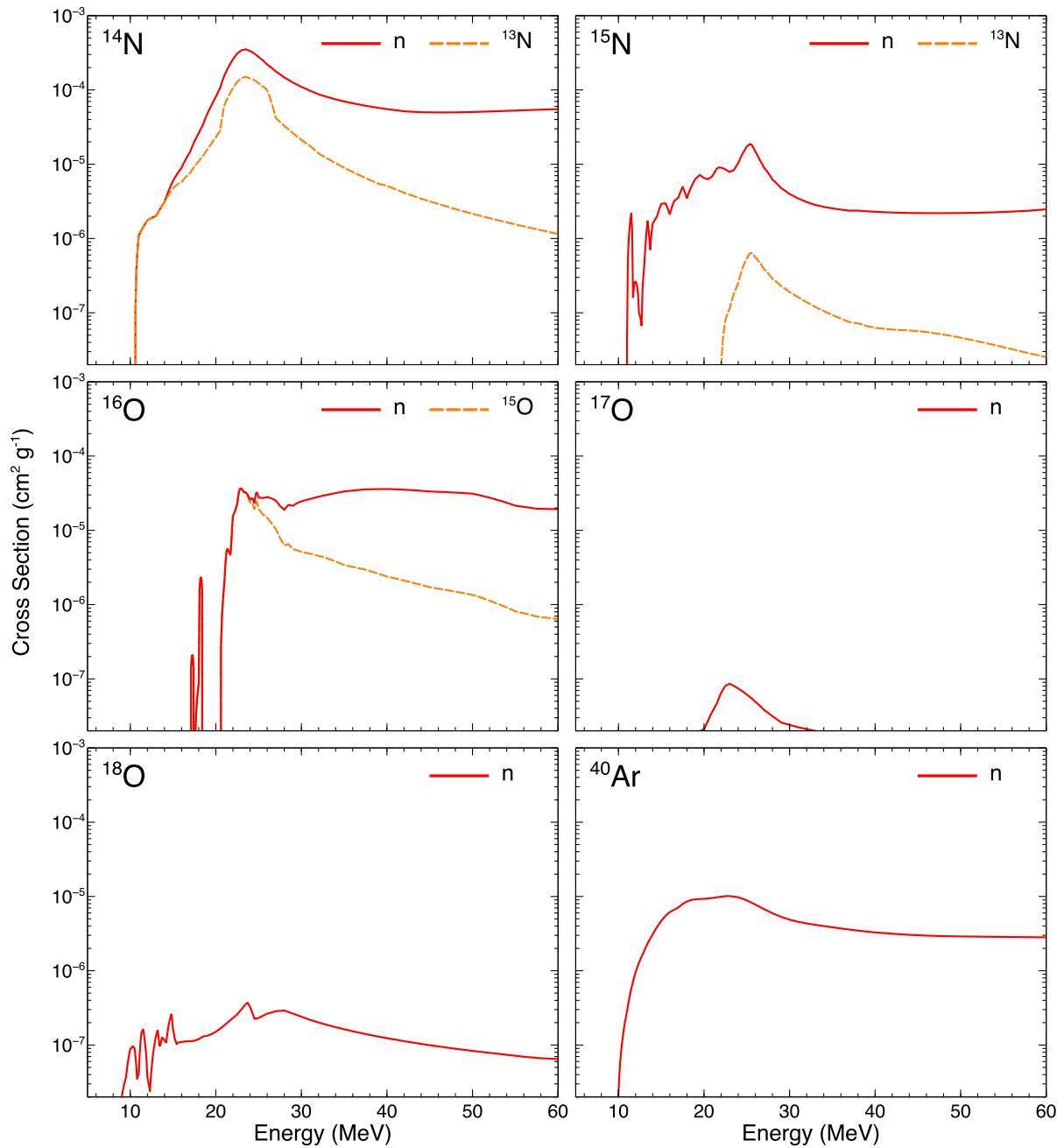
Figure 5.3: Cross sections of photonuclear reactions including nuclide compositions of the standard atmosphere, as a function of incident gamma-ray energy. Reactions producing ^{13}N and ^{15}O are ^{14}N$(\gamma, n)^{13}$N, ^{15}N$(\gamma, 2n)^{13}$N, and ^{16}O$(\gamma, n)^{15}$O. Cross sections of neutron productions consider all the photonuclear channels producing neutrons.

Table 5.2: Major channels of photonuclear reactions with atmospheric nuclei.[15]

Target: ^{14}N					
Reaction	Products	Threshold	Reaction	Products	Threshold
^{14}N$(\gamma, n)^{13}$N	^{13}N	10.55 MeV	^{14}N$(\gamma, d)^{12}$C	^{12}C	10.27 MeV
^{14}N$(\gamma, p)^{13}$C	^{13}C	7.55 MeV	^{14}N$(\gamma, \alpha)^{10}$B	^{10}B	11.61 MeV
^{14}N$(\gamma, np)^{12}$C	^{12}C	12.50 MeV	^{14}N$(\gamma, np\alpha)^{8}$Be	^{8}Be	17.64 MeV

Target: ^{15}N					
^{15}N$(\gamma, n)^{14}$N	^{14}N	10.83 MeV	^{15}N$(\gamma, np)^{13}$C	^{13}C	18.38 MeV
^{15}N$(\gamma, 2n)^{13}$N	^{13}N	21.39 MeV	^{15}N$(\gamma, d)^{13}$C	^{13}C	16.16 MeV
^{15}N$(\gamma, p)^{14}$C	^{14}C	10.21 MeV	^{15}N$(\gamma, \alpha)^{11}$B	^{11}B	10.99 MeV

Target: ^{16}O					
^{16}O$(\gamma, n)^{15}$O	^{15}O	15.66 MeV	^{16}O$(\gamma, np)^{14}$N	^{14}N	22.96 MeV
^{16}O$(\gamma, p)^{15}$N	^{15}N	12.13 MeV	^{16}O$(\gamma, \alpha)^{12}$C	^{12}C	7.16 MeV

Target: ^{17}O					
^{17}O$(\gamma, n)^{16}$O	^{16}O	4.14 MeV	^{17}O$(\gamma, np)^{15}$N	^{15}N	16.27 MeV
^{17}O$(\gamma, 2n)^{15}$O	^{15}O	19.81 MeV	^{17}O$(\gamma, \alpha)^{13}$C	^{13}C	6.36 MeV
^{17}O$(\gamma, p)^{16}$N	^{16}N	13.78 MeV			

Target: ^{18}N					
^{18}O$(\gamma, n)^{17}$O	^{17}O	8.04 MeV	^{18}O$(\gamma, \alpha 2n)^{12}$C	^{12}C	19.34 MeV
^{18}O$(\gamma, 2n)^{16}$O	^{16}O	12.12 MeV	^{18}O$(\gamma, n\alpha)^{13}$C	^{13}C	14.40 MeV
^{18}O$(\gamma, \alpha)^{14}$C	^{14}C	6.23 MeV	^{18}O$(\gamma, p2n)^{15}$N	^{15}N	15.83 MeV

Target: ^{40}Ar					
^{40}Ar$(\gamma, n)^{39}$Ar	^{39}Ar	9.87 MeV	^{40}Ar$(\gamma, np)^{38}$Cl	^{38}Cl	20.60 MeV
^{40}Ar$(\gamma, 2n)^{38}$Ar	^{38}Ar	16.47 MeV	^{40}Ar$(\gamma, \alpha)^{36}$S	^{36}S	6.80 MeV
^{40}Ar$(\gamma, p)^{39}$Cl	^{39}Cl	12.52 MeV			

5.2 Monte-Carlo Simulations with Geant4

5.2.1 Three-stage simulation

To obtain spatial distributions of β^+-decay nuclei and neutrons produced by photonuclear reactions in the atmosphere, Mote-Carlo simulations were performed. The present thesis employs the particle transportation framework `Geant4` Version 10.3 [Agostinelli et al., 2003, Allison et al., 2006, 2016]. Simulation processes from an initial TGF triggering photonuclear reactions to detector responses are divided into three stages. In the first stage, avalanche electrons of a downward TGF are injected into a mass model of atmosphere. Then, positions from β^+-decay nuclei and neutrons produced by photonuclear reactions with bremsstrahlung of the initial electrons are recorded. In the second stage, positrons are injected based on the spatial distribution of β^+-decay nuclei obtained in the first stage. When their annihilation gamma rays arrive at the ground, position, momentum vector, and energy of the annihilation photons are recorded. In the final stage, temporal variation and spectral models are obtained by injecting gamma rays obtained in the second stage into a mass model of our detector. In each stage, a linear relation between the number of input and output particles exists. Therefore, this multiple-stage method is useful to save computational resources by injecting more input particles than output particles of the previous step. Monte-Carlo simulations in the present thesis were performed on the high-performance computing system Hokusai BigWaterfall and GreatWave of RIKEN.

5.2.2 Distribution of β^+-decay nuclei

In the first stage, a mass model of the atmosphere is utilized. The mass model is vertically divided into 100-m thick layers, then atmospheric pressure of each layer is implemented based on the standard atmosphere [International Organization for Standardization, 1975]. The initial electrons of a downward TGF are assumed to be avalanche electrons of RREA. As expressed in Equation 2.19, avalanche electrons of the RREA model follows an energy spectrum proportional to $\exp(-E/7.3\,\text{MeV})$ [Dwyer et al., 2012b]. In the present simulation, a simple electron source is assumed: a downward narrow flow like a pencil beam, without no divergence nor tilt angle. The energy range of the initial electrons are set to 9.8–50.0 MeV to cover the energy threshold of $^{40}\text{Ar}(\gamma, n)^{39}\text{Ar}$, the lowest one among the reactions taken into account here (Table 5.2). Considering a typical structure of winter thunderclouds, altitude of the initial electrons are assumed to be in the 1–4 km range with a 0.5 km step (7 altitude patterns). At each altitude, 5×10^9 electrons are injected. Hereafter, the simulation results are normalized to 10^{18} initial electrons (1–50 MeV), which is typical in upward TGFs [Mailyan et al., 2016]. The normalization constant is

$$\frac{10^{18}}{5 \times 10^9} \times \frac{\int_{9.8}^{50} \exp(-E/7.3)dE}{\int_1^{50} \exp(-E/7.3)dE} = 5.97 \times 10^7. \tag{5.1}$$

The injected electrons are decelerated by ionization losses, or by emitting bremsstrahlung photons. In the present simulation, the bremsstrahlung photons are tracked until they cause photonuclear reactions, reach the ground, or reduce their energy lower than 9.8 MeV by Compton scatterings and pair productions. When photonuclear reactions considered in this analysis (see Section 5.1) take place, a type of the reaction, position, kinetic energy, and momentum vector of secondary particles are recorded, then tracking of the secondary particles is terminated. The recorded information is utilized in the second stage.

`Geant4` contains several physics lists which are suitable for simulations of low energy neutrons and related reactions. The present simulation employs the Shielding_LIV model[16] for calculations of photonuclear reactions and neutron propagations, and the FTFP_VERT_LIV model for calculations of only electromagnetic interactions with photons, electrons, and positrons. The physics list of electromagnetic interactions with the LIV option in `Geant4` was verified by comparing with other Monte-Carlo codes [Sarria et al., 2018]. Since cross sections employed in Shielding_LIV are slightly different from ENDF/B-VII.1, cross-section correction was applied (see Appendix C).

Spatial distributions of produced neutrons, and β^+-decay nuclei ^{13}N and ^{15}O are shown in Figure 5.4. There are not significant differences in spatial shape of the distributions. The total number of production is summarized in Table 5.3. When electrons are injected above 1.5 km, the total number of neutrons and β^+-decay nuclei is almost constant, not depending on injection altitude. In the case of the 2.0-km altitude injection, the numbers of neutrons, ^{13}N, and ^{15}O are 1.1×10^{-5}, 3.8×10^{-6}, and 4.6×10^{-7} times of the initial electrons (1–50 MeV), respectively. Also the numbers of ^{13}N and ^{15}O are 0.35 and 0.04 times of neutrons, respectively.

Table 5.3: The total number of neutrons and β^+-decay nuclei produced via photonuclear reactions calculated by Monte-Carlo simulations.

Altitude	1.0 km	1.5 km	2.0 km	2.5 km	3.0 km	3.5 km	4.0 km
	with 5×10^9 electrons in 9.8–50.0 MeV						
neutrons	1.60×10^5	1.8×10^5	1.8×10^5	1.8×10^5	1.9×10^5	1.9×10^5	1.9×10^5
^{13}N	5.7×10^4	6.3×10^4	6.3×10^4	6.4×10^4	6.7×10^4	6.4×10^4	6.4×10^4
^{15}O	6.5×10^3	7.3×10^3	7.6×10^3	7.5×10^3	7.7×10^3	7.7×10^3	7.7×10^3
	with 10^{18} electrons in 1.0–50.0 MeV						
neutrons	9.6×10^{12}	1.1×10^{13}	1.1×10^{13}	1.1×10^{13}	1.1×10^{13}	1.1×10^{13}	1.1×10^{13}
^{13}N	3.4×10^{12}	3.8×10^{12}	3.8×10^{12}	3.8×10^{12}	4.0×10^{12}	3.8×10^{12}	3.8×10^{12}
^{15}O	3.9×10^{11}	4.4×10^{11}	4.6×10^{11}	4.5×10^{11}	4.6×10^{11}	4.6×10^{11}	4.6×10^{11}

5.2.3 Spacial distribution and energy spectrum of annihilation emissions

In the second stage, positrons are injected based on the spatial distribution of β^+-decay nuclei, obtained in the first stage, then atmospheric propagation of positrons and their annihilation gamma rays are calculated. A positron-emitting rate dn/dt from β^+-decay nuclei is a function of the number of β^+-decay nuclei $n(t)$ and its decay constant λ as

$$\frac{dn}{dt} = \lambda n(t) = \lambda n(0) \exp(-\lambda t). \tag{5.2}$$

To compare the simulation model with the delayed annihilation component of Event 2 observed by Detector 1, positrons produced 34.4 ± 15 sec after the short burst, namely $t_1 = 19.4$ sec $< t < t_2 = 49.4$ sec, are considered here. The total number of electrons produced in this time domain N is expressed as

$$N = n(0) \int_{t_1}^{t_2} \lambda \exp(-\lambda t) dt. \tag{5.3}$$

---

[16]https://www.slac.stanford.edu/comp/physics/geant4/slac_physics_lists/shielding/shielding.html
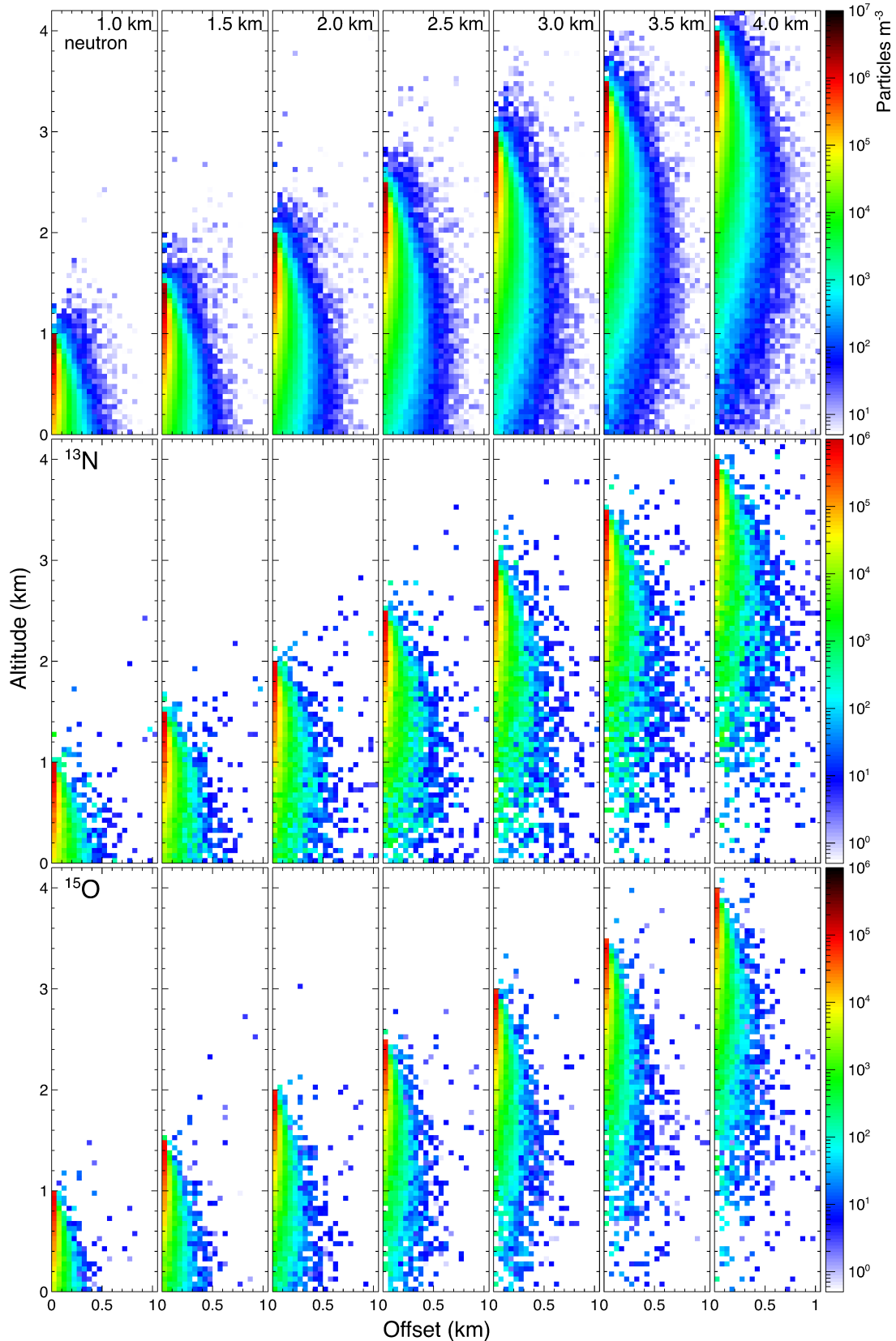
Figure 5.4: Spatial distributions of neutrons and β^+-decay nuclei productions by photonuclear reactions in a function of altitude and radius. The initial electrons are injected at altitude ranging from 1 to 4 km with a 0.5-km interval. Production densities of the distributions are normalized to the initial injected electron number of 10^{18} (1–50 MeV).

By utilizing decay constants of ^{13}N and ^{15}O ($\lambda_{N13} = 1.159 \times 10^{-3}$ sec^{-1} and $\lambda_{O15} = 5.67 \times 10^{-3}$ sec^{-1}), $N_{N13} = 0.0334\, n_{N13}(0)$ and $N_{O15} = 0.1402\, n_{O15}(0)$ are obtained. Namely, 3.34% of ^{13}N and 14% of ^{15}O produced by photonuclear reactions decay and emit positrons in $t_1 < t < t_2$. When the number density of ^{13}N and ^{15}O are expressed as ρ_{N13} and ρ_{O15}, the number of emitted positrons per unit volume in 19.4 sec $< t <$ 49.4 sec is $0.0334\, \rho_{N13} + 0.14\, \rho_{O15}$.
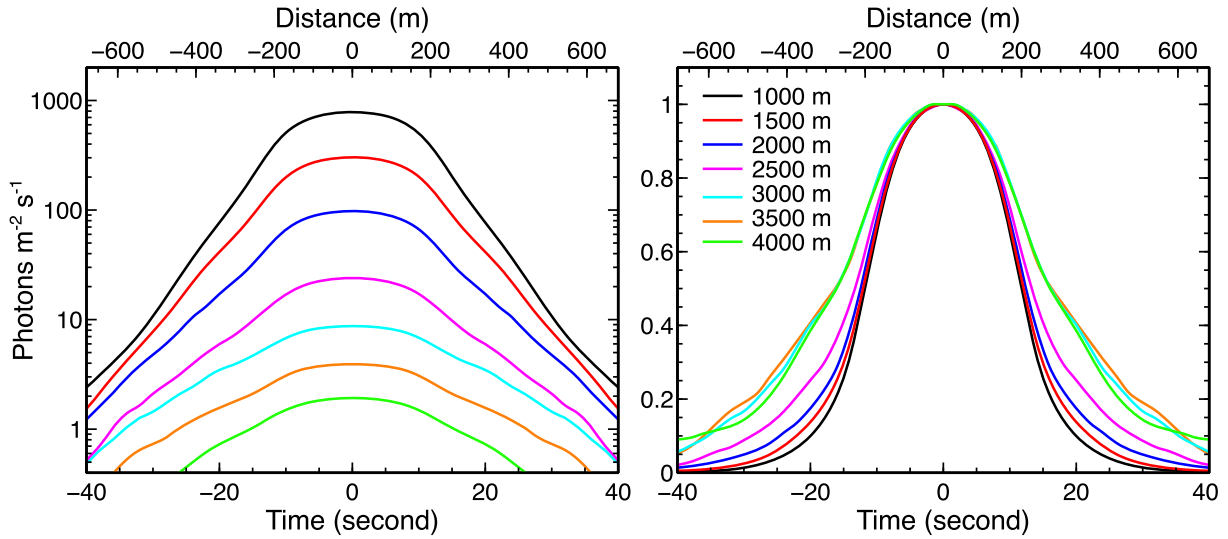
Figure 5.5: Simulations on temporal variations of gamma-ray fluxes by positron signals. Differences by altitude of the electron beam are displayed by colors. The peak of the variations is normalized to the initial injected electron number of 10^{18} (left), and to 1.0 for comparison purpose (right). Fluxes are first obtained as a function of horizontal distance from the initial electron beam, and are converted into those as a function of time by multiplying wind velocity. In this case, the velocity of Event 2, 17.0 m s^{-1}, is assumed for the conversion.
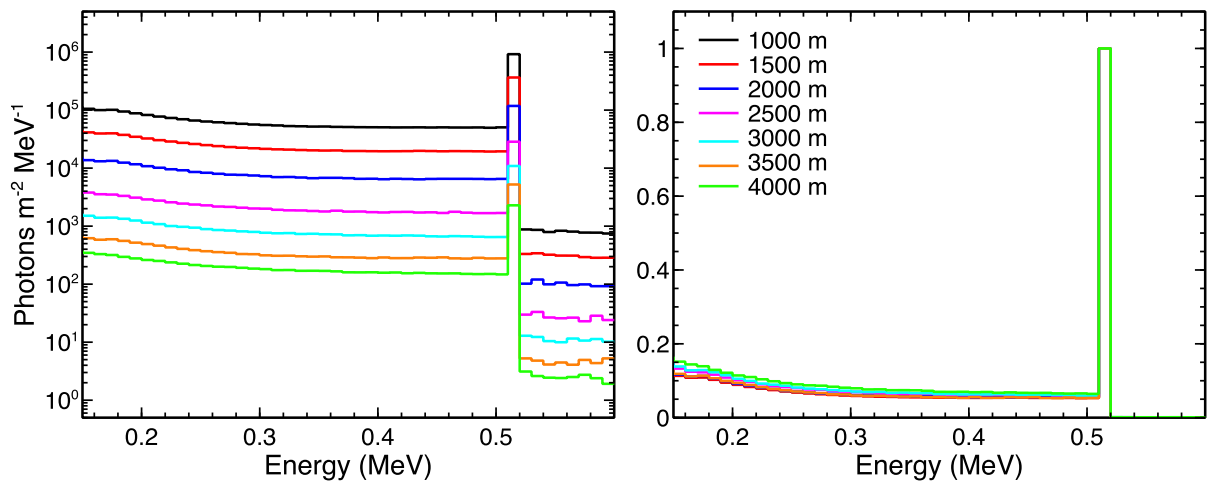
Figure 5.6: Simulations on energy spectra of annihilation signals for Event 2. The annihilation peak in the spectra is normalized to the initial injected electron number of 10^{18} (left), and to 1.0 for comparison purpose (right).

87

Positrons emitted from β^+-decay nuclei follow a continuous energy spectrum of

$$f(E, E_{\max}, Z) \propto \frac{(E + m_e c^2)^2 (E_{\max} - E)^2}{\exp\left[2\pi\alpha(Z+1)(E + m_e c^2)/\sqrt{E^2 + 2m_e c^2 E}\right] - 1}, \tag{5.4}$$

where E, $E_{\max}$, $m_e c^2$, Z, and $\alpha = 1/137$ are kinetic energy of positron, the maximum kinetic energy of the β^+-decay, the rest mass of electron, atomic number of the parent nuclide, and the fine structure constant, respectively [Levin and Hoffman, 1999]. Z and $E_{\max}$ are $Z_{\mathrm{N13}} = 7$ and $E_{\mathrm{N13}} = 1.19$ MeV for ^{13}N, $Z_{\mathrm{O15}} = 8$ and $E_{\mathrm{O15}} = 1.73$ MeV for ^{15}O, respectively. Therefore, a positron spectrum $g(E, \rho_{\mathrm{N13}}, \rho_{\mathrm{O15}})$ is

$$\begin{aligned}
g(E, \rho_{\mathrm{N13}}, \rho_{\mathrm{O15}}) \propto\ & 0.0334\, \rho_{\mathrm{N13}} \frac{f(E, E_{\mathrm{N13}}, Z_{\mathrm{N13}})}{\lim_{\epsilon \to 0} \int_\epsilon^{E_{\mathrm{N13}}} f(E', E_{\mathrm{N13}}, Z_{\mathrm{N13}}) dE'} \\
& + 0.1402\, \rho_{\mathrm{O15}} \frac{f(E, E_{\mathrm{O15}}, Z_{\mathrm{O15}})}{\lim_{\epsilon \to 0} \int_\epsilon^{E_{\mathrm{O15}}} f(E', E_{\mathrm{O15}}, Z_{\mathrm{O15}}) dE'}.
\end{aligned} \tag{5.5}$$

The simulation geometry in the second stage is divided into concentric rings of 200-m height and width. Then, in each region, densities of positrons emitted by ^{13}N and ^{15}O are configured based on the result of the first stage. The mean free path of 0.511-MeV annihilation gamma rays is 89 m in the 1-atm atmosphere, and hence the probability that emissions from positrons injected at >1-km altitude reach the ground is quite low. Therefore, initial particles only injected at <2 km altitude are considered here. The initial particles are isotropically-emitted positrons whose energy spectrum follows Equation 5.5. In total 10^9 positrons are injected at each altitude in this stage. To normalize gamma-ray distributions in this stage to 10^{18} initial electrons, the result should be multiplied by $r_e \times [0.0334 \times r_{\mathrm{N13}} n_{\mathrm{N13}}(0) + 0.1402 \times r_{\mathrm{O15}} n_{\mathrm{O15}}(0)]$ times, where $r_e = 5.97 \times 10^7$ is a factor to convert the number of initial electrons of 5×10^9 (9.8–50.0 MeV) to 10^{18} (1.0–50.0 MeV). Here r_{N13} and r_{O15} are the ratios of ^{13}N and ^{15}O produced at <2 km to all ^{13}N and ^{15}O produced in the first stage, respectively.

In this stage, energy, and position of annihilation gamma rays arriving at the ground are registered. Here the position of gamma rays are expressed as a coordinate (x, y). Its origin is set to be where the initial electrons are injected. This section considers gamma-ray photons of Event 2 detected in $19.4\,\mathrm{sec} < t < 49.4\,\mathrm{sec}$. This time domain is converted into $-15.0\,\mathrm{sec} < t' < 15.0\,\mathrm{sec}$, where $t' = t - 34.4\,\mathrm{sec}$ is time from when the delayed component gets its peak. Considering the wind velocity of Event 2, $17.0\,\mathrm{m\,s^{-1}}$, this time domain is converted to the distance range $-250\,\mathrm{m} < x < 250\,\mathrm{m}$. With the simulation photons extracted from $-250\,\mathrm{m} < x < 250\,\mathrm{m}$, models of energy spectra and spatial distributions of gamma-ray fluxes are constructed. The width of the extraction area is set to be 50 m, namely $-25\,\mathrm{m} < y < 25\,\mathrm{m}$, for enough photon statistics. The spatial distribution is again converted to a temporal distribution by multiplying the wind velocity of Event 2.

The simulation results on temporal variations of annihilation emissions are shown in Figure 5.5. Figure 5.6 shows energy spectra averaged in $19.4\,\mathrm{sec} < t < 49.4\,\mathrm{sec}$. For both temporal variations and energy spectra, gamma-ray fluxes are fainter as the altitude of initial electrons are higher. The widths (FWHM) of the temporal variations are 11.8 sec, 13.4 sec, and 16.1 sec for 1.0 km, 2.5 km, and 4.0 km altitude, respectively. The width becomes larger as the altitude of initial electrons are higher. The energy spectra consist of two component: an annihilation line whose photons are not scattered ever, and a continuum whose photons are scattered once or more in the atmosphere. While normalization of the spectra significantly depends on the altitude of initial electrons, the difference in spectral shapes is hardly seen above 0.3 MeV.

5.2.4 Comparison with observation

In the third stage, detector responses are convolved into the model spectra by injecting initial particles obtained in Section 5.2.3 to a mass model of the detector and ground. The initial particles are injected with a fluence of 1.27×10^4 photons cm^{-2} for response calculation.

The simulation models are then compared with the observed data here. The spectrum and count-rate history of Event 2 recorded by Detector 1 is utilized because it is the only one that the delayed component is clearly seen. The count-rate history to be compared with the model is the same as shown in Figure 4.11. The energy spectrum is extracted from $19.4\,\mathrm{sec} < t < 49.4\,\mathrm{sec}$, and background is subtracted.

The comparison of temporal variations are shown in Figure 5.7. The model reproduced the observed count-rate histories in $19.4\,\mathrm{sec} < t < 49.4\,\mathrm{sec}$. While the model difference in altitude is not clear in the present count statistics, each model is consistent with the observation. The spectral comparison is also shown in Figure 5.8. Both the line and continuum components are reproduced by the spectral model. Since the shape of temporal variation and spectrum hardly depend on altitude of initial electrons, it cannot determine altitude. On the other hand, the relation between altitude and the total number of initial electrons is obtained as in Figure 5.9. In an altitude range of 1.0–4.0 km, the number of initial electrons N (1–50 MeV) in Event 2 based on the annihilation emissions approximately follows an exponential function with an altitude h as

$$N = 6.5 \times 10^{17} \text{ electrons} \times \exp(h/0.5 \text{ km}). \tag{5.6}$$
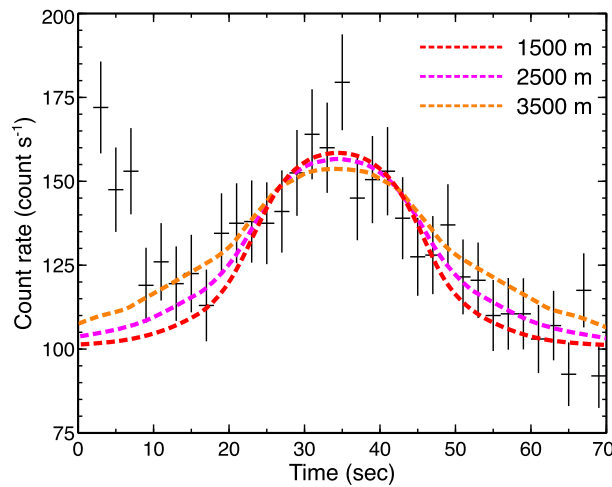
Figure 5.7: Comparison between observed and simulated count-rate histories of annihilation emissions (0.35–0.7 MeV). The observation data was recorded in Event 2 by Detector 1.
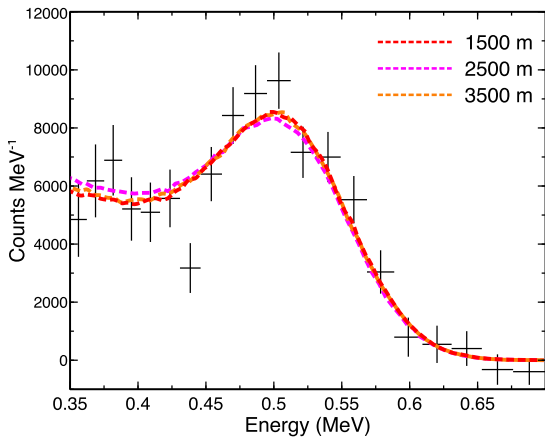
Figure 5.8: Comparison between observed and simulated energy spectra of annihilation emissions. The observation spectrum, background-subtracted, was recorded in Event 2 by Detector 1.
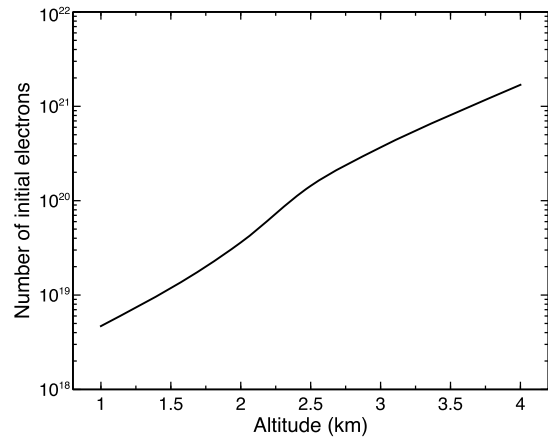
Figure 5.9: The relation between altitude and the number of avalanche electrons in the downward TGF of Event 2.

Chapter 6

Atmospheric Reactions of Photoneutrons

The present chapter performs Monte-Carlo simulations of neutron propagation in the atmosphere, around the ground, and in detectors, based on the initial spatial distribution of neutrons obtained in Chapter 5. The simulation includes neutron thermalization and capture in the atmosphere and ground, and gamma-ray lines from nuclei excited by neutron captures. Then the simulation results are compared with our measurements to derive altitude, position, and the number of the initial electrons.

6.1　Monte-Carlo Simulations of Neutron Propagation

6.1.1　Photoneutron spectrum by terrestrial gamma-ray flashes

Kinetic energy of neutrons produced by photonuclear reactions is determined by energy of incident gamma rays, binding energy of neutrons in target nuclei, and excitation energy of the rest nuclei. The database of photonuclear reactions ENDF/B-VII.1 [Chadwick et al., 2011] compiles neutron spectra by photonuclear reactions as a function of incident monochromatic gamma rays. Examples for atmospheric nuclei are shown in Figure 6.1. Neutron spectra consist of continuum and lines originating from resonance states. By convolving the neutron spectra with the TGF spectrum, a neutron spectrum by photonuclear reactions in the atmosphere can be obtained.

　　For the Monte-Carlo simulations in Subsection 5.2.2, it is assumed that the electron spectrum of TGFs follows an exponential function $\exp(-E/7.3 \text{ MeV})$ [Dwyer et al., 2012b]. A bremsstrahlung spectrum from such avalanche electrons is approximately proportional to $\exp(-E/7.3 \text{ MeV})/E$ (Subsection 2.5.1; Dwyer [2008]). Then, a calculated energy spectrum of photoneutrons in the atmosphere with TGF photons is shown in Figure 6.2. In this figure, weighting factors of the atmospheric composition are multiplied by each neutron spectrum of atmospheric nuclides such as ^{14}N, ^{15}N, ^{16}O, and ^{40}Ar. A resonance line at $\sim$3.5 MeV from ^{14}N, which is the main component of the convolved spectrum, is clearly seen. While this thesis primarily employs ENDF/B-VII.1, JENDL/PD-2016 [Iwamoto et al., 2016], a data base of photonuclear reactions compiled by Japan Atomic Energy Agency, is available. JENDL/PD-2016 includes cross sections theoretically calculated with a different code from ENDF/B-VII.1. For reference, a neutron spectrum by a TGF convolved with JENDL/PD-2016 is presented in Appendix D.
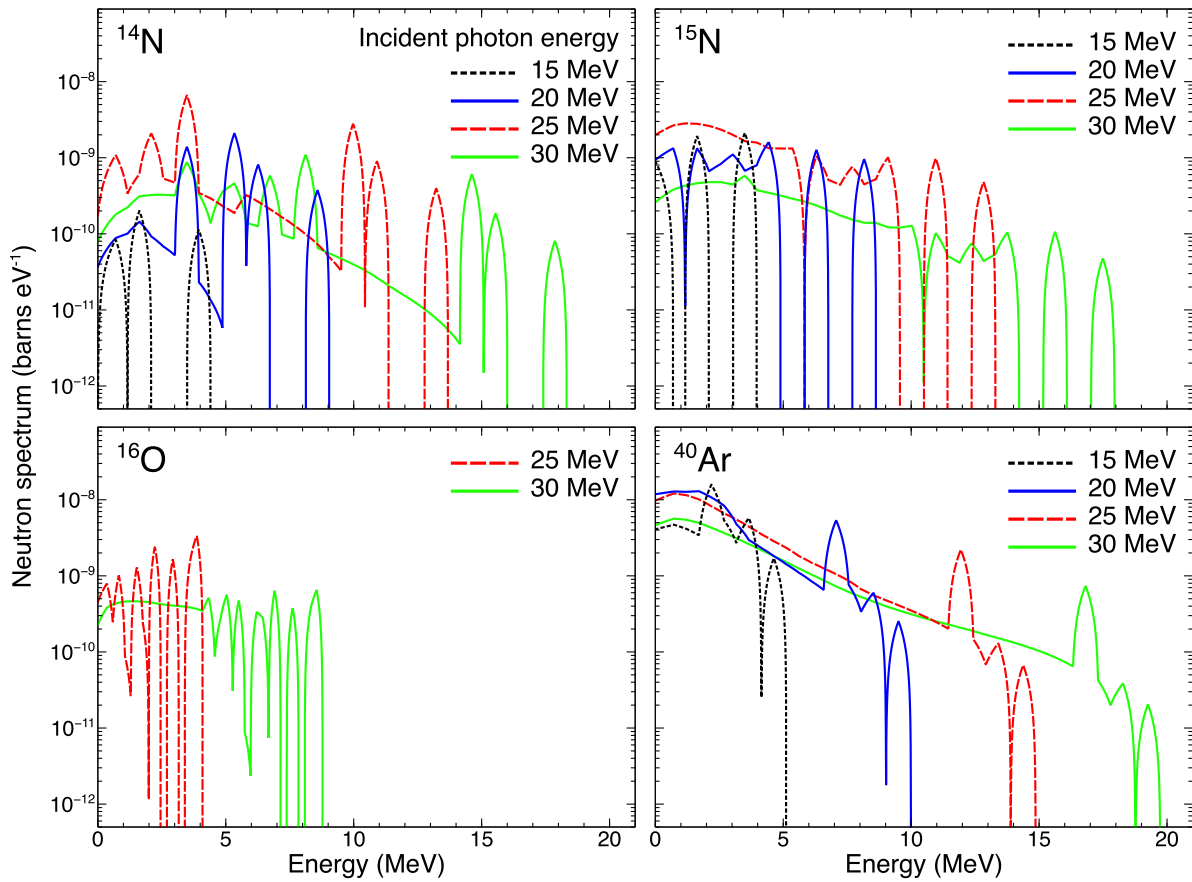
Figure 6.1: Neutron spectra produced by atmospheric photonuclear reactions with monochrome incident gamma rays. Calculated with ENDF/B-II.1.
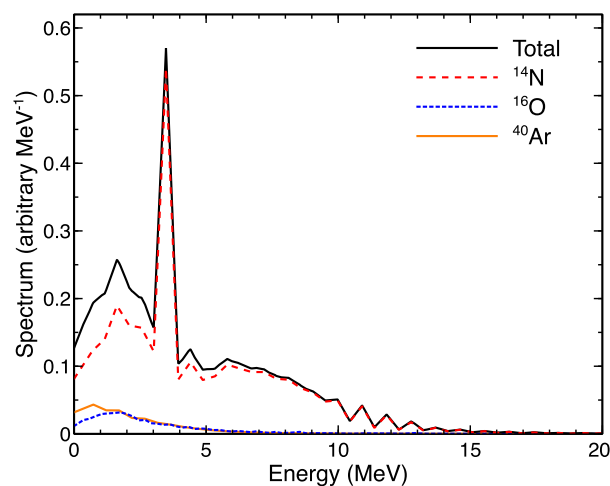
Figure 6.2: A neutron spectrum of photonuclear reactions convolved with the typical TGF spectrum. Components of ^{14}N, ^{16}O, and ^{40}Ar are overlaid by red, blue, and orange dashed lines, respectively. The contribution from ^{15}N is too small to be displayed.

6.1.2 Neutron thermalization in the ground

Fast neutrons produced near the ground plunge into the ground without being captured in the atmosphere. As pointed out by Yamashita et al. [1966] and Bowers et al. [2017], it is important to consider neutron thermalization by materials in the ground. As presented in Subsection 4.2.3, averaged kinetic energy of neutrons is determined by the number of elastic scatterings they experience. The time scale of thermalization is also determined by the interval of scatterings, namely velocity of neutrons and a mean free path of elastic scatterings. Since a mean free path in the atmosphere is longer than typical solid materials due to low density, it takes longer time to thermalize. On the other hand, it takes shorter time to thermalize in materials of the ground due to higher density. To confirm this phenomenon, the effect of ground thermalization is tested with `Geant4` before a full-scale simulation is performed.

For the simulation, the mass model of atmosphere used in Subsection 5.2.2 and 50-cm ground made of concrete which imitates the environment around Detector 1 were implemented. In total 10^9 monochromatic neutrons of 4 MeV were injected at each altitude in the geometry. The neutron source is point-like and isotropic. In the case that ground effects are ignored, time and kinetic energy of neutrons are registered and tracking is terminated when neutrons reach the ground. In the case that ground effects are considered, time and kinetic energy of neutrons are registered when they reach the ground, but tracking continues until they are captured. Therefore, neutrons can cross the ground surface multiple times in the latter case.

The simulation result is shown in Figure 6.3. When ground thermalization is ignored, kinetic energy of neutrons arriving at the ground and their arrival time are correlated. Namely, less-scattered neutrons keep their initial kinetic energy and reach the ground faster, and neutrons experiencing more scatterings get slower and reach the ground later. In contrast, when ground thermalization is considered, thermal and epithermal neutrons reach the ground even immediately after the injection. It is interpreted that fast neutrons entering the ground are thermalized quickly in the ground and go back to the atmosphere. Even though neutrons are injected at a higher altitude, the effect of ground thermalization is significant. The effect are seen even in the time domain of >10 ms, and hence it should affect the time scale of neutron captures. Therefore, ground effects are considered in the full-scale simulation.

6.1.3 Full simulation of photoneutrons in the atmosphere

Based on the results in Subsections 6.1.1 and 6.1.2, we performed a full simulation of neutron propagation produced by atmospheric photonuclear reactions. Initial particles, photoneutrons following the spectrum shown in Figure 6.2, are injected in the mass model, based on the spatial distribution of Figure 5.4. It is assumed that photoneutrons are isotropically ejected from nuclei. In the full simulation, neutrons and de-excitation gamma rays by neutron captures are tracked, and particle type, kinetic energy, momentum vector, time, and position of them are registered each time they cross the ground surface. While 10^9 neutrons are injected at each altitude of initial electrons, results displayed in the following discussions are normalized to 10^{18} initial electrons (1–50 MeV: see Table 5.3).

First, arriving time of gamma rays (>0.3 MeV) and neutrons (all energy band) to the ground surface are shown in Figures 6.4 and 6.5, respectively. Here an offset is defined as the horizontal distance between the initial electron beam and a detector or an observer. A jump at the first bin is seen in all the calculations. After this initial 10 ms, the arriving time approximately decays with the decay constant of 40-70 ms, which is consistent with the calculated value in Subsection 4.2.3 (55 ms). Figure 6.6 shows the decay constants evaluated by fitting in 30–200 ms with an exponential function. The difference of the constant by offsets is larger than
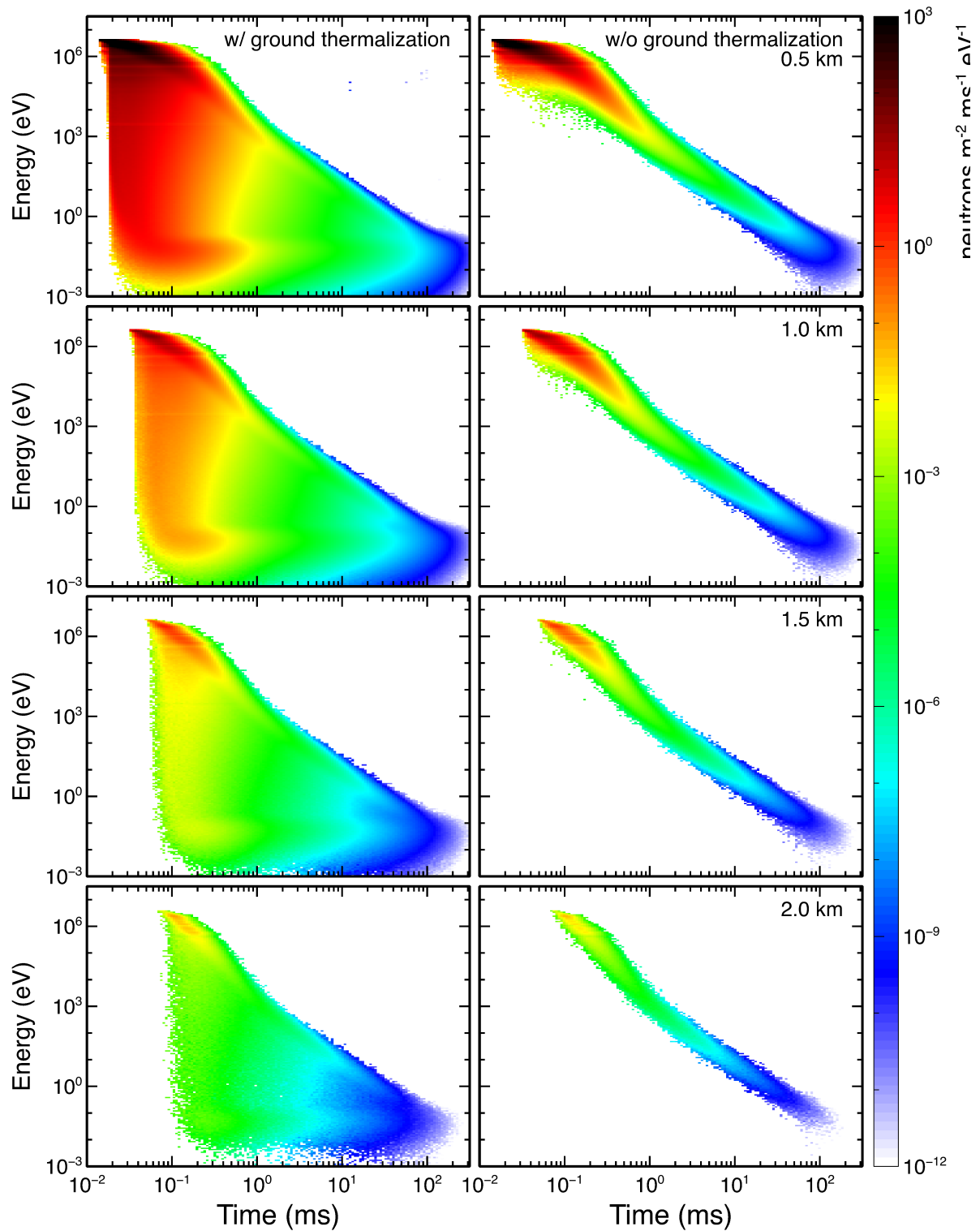
Figure 6.3: The relations between arrival time and kinetic energy of neutrons on the ground surface with and without ground thermalization. In total 10^9 monochromatic neutrons of 4 MeV are isotropically injected at 0.5-, 1.0-, 1.5-, and 2.0-km altitudes.

that by altitude of initial electrons. The ratio of gamma rays (>0.3 MeV) to neutrons is shown in Figure 6.7. The ratio becomes smaller as an offset gets larger; the number of gamma rays increases relatively to neutrons as an offset becomes larger.

Then energy spectra of particles arriving at the ground are extracted. Figure 6.8 shows energy spectra of gamma rays arriving later than 30 ms. The spectra is normalized to the 10.83 MeV line, which is the highest energy among de-excitation gamma rays from ^{15}N by ^{14}N (n, γ) ^{15}N. The spectra mostly consist of de-excitation gamma rays by neutron captures. Main contribution comes from neutron captures with ^{14}N (e.g. 5.269 MeV), ^{28}Si (e.g. 3.538 MeV), ^{27}Al (e.g. 7.724 MeV), ^{56}Fe (e.g. 7.631 MeV), ^{1}H (e.g. 2.223 MeV), etc. Table 6.1 summarizes energy and relative intensity of de-excitation lines from these nuclides. With a large offset, the contribution except ^{14}N becomes smaller. Because the number of neutrons becomes relatively smaller with a large offset as shown in Figure 6.7, gamma rays by atmospheric neutron captures become more significant than those by neutron captures in the ground. In addition, low-energy gamma-ray lines are more scattered and absorbed with higher altitude of initial electrons.

Comparison of gamma-ray spectra arriving at the ground earlier and later than 30 ms is presented in Figure 6.9. The spectra are normalized to the 10.83 MeV line as the same manner as Figure 6.8. In spectra arriving at the ground earlier than 30 ms, There are significant spectral features of de-excitation gamma rays from ^{14}N (e.g. 1.635, 2.313, 5.105 MeV: Ajzenberg-Selove [1991]), ^{16}O (e.g. 6.129 MeV: Tilley et al. [1993]), and ^{28}Si (e.g. 1.779 MeV: Shamsuzzoha Basunia [2013]). Their intensities are also much higher than those by neutron captures. These de-excitation gamma rays are produced by inelastic scatterings, rather than neutron captures. Cross sections of inelastic scatterings is comparable to those of elastic scatterings in sub-MeV range or higher (Figure 2.26). Therefore, a lot of de-excitation gamma rays by inelastic scatterings are emitted before the neutrons are thermalized. This seems to cause the jumps seen in Figure 6.4.

Table 6.1: Representative de-excitation gamma-ray lines from neutron captures.[16,17]

^{1}H	^{14}N	^{27}Al	^{28}Si	^{56}Fe
2.223 MeV / 100.0%	5.269 MeV / 29.9%	7.724 MeV / 26.8%	3.538 MeV / 70.2%	7.631 MeV / 29.0%
	5.297 MeV / 21.2%	3.033 MeV / 8.8%	4.933 MeV / 65.6%	7.645 MeV / 25.0%
	5.533 MeV / 19.6%	3.465 MeV / 7.0%	2.092 MeV / 19.5%	6.018 MeV / 9.9%
	1.884 MeV / 18.8%	4.133 MeV / 6.9%	1.273 MeV / 16.9%	5.920 MeV / 9.6%
	6.322 MeV / 18.2%	4.259 MeV / 6.8%	6.379 MeV / 11.3%	0.352 MeV / 9.5%
	4.508 MeV / 16.7%	4.733 MeV / 5.5%	7.199 MeV / 7.0%	4.217 MeV / 6.8%
	3.677 MeV / 14.5%			1.725 MeV / 6.3%
	10.829 MeV / 14.3%			7.278 MeV / 6.0%
	5.562 MeV / 10.7%			1.612 MeV / 5.4%

---

[16]Line energy / emission probability per one neutron capture reaction.

[17]CapGam https://www-nds.iaea.org/capgam/index.htmlx
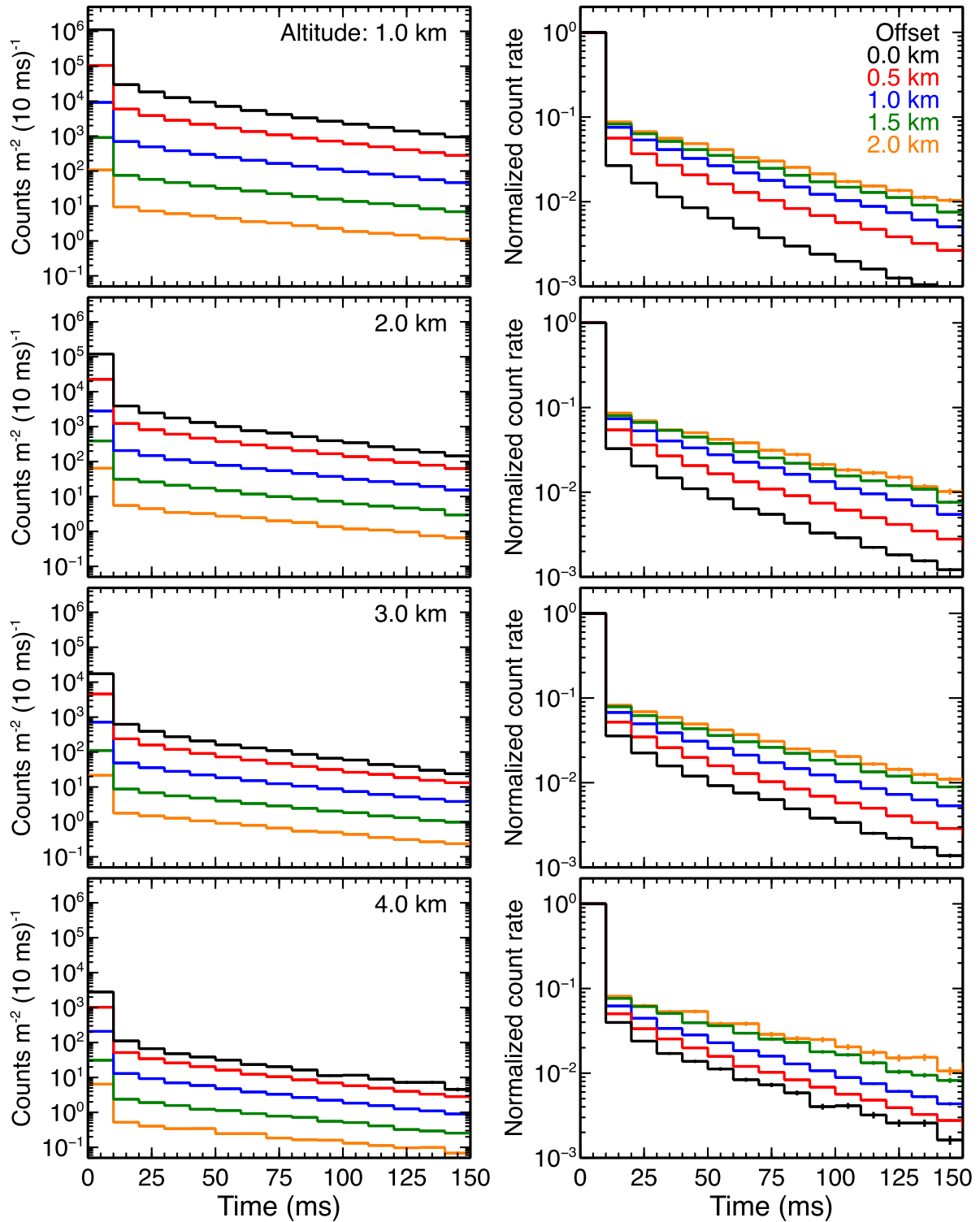
Figure 6.4: Simulation results on arriving time of gamma rays to the ground. The left plots are normalized to the number of the total injected avalanche electrons (10^{18}) and the right ones to the first bins.
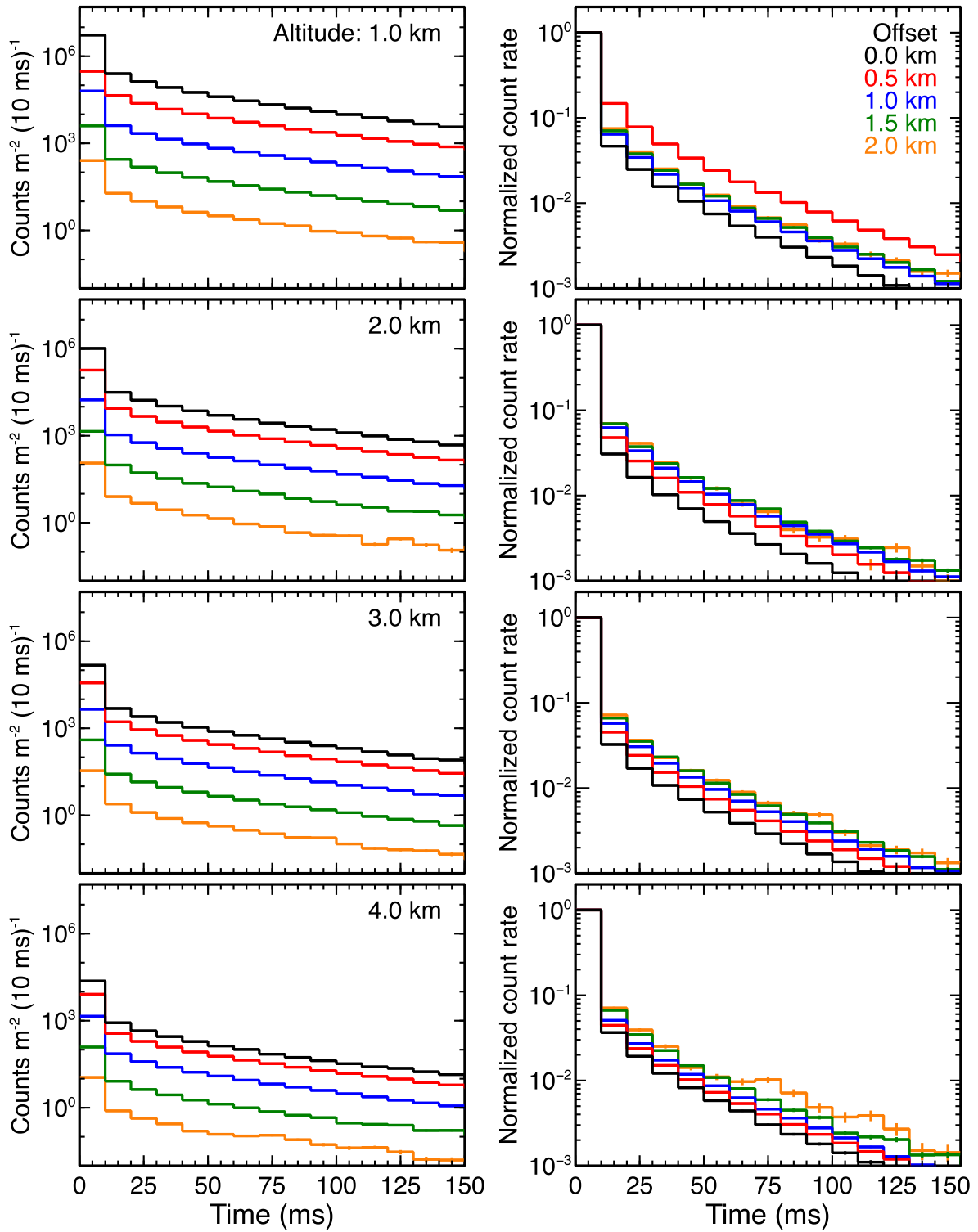
Figure 6.5: Simulation results on arriving time of neutrons displayed by the same format as Figure 6.4
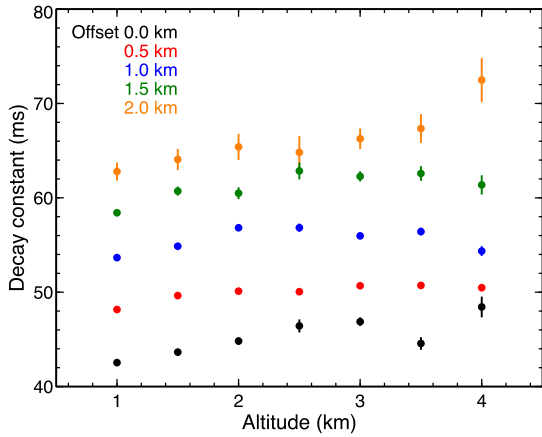
Figure 6.6: Decay constants of arriving time of gamma rays on the ground, obtained by fitting with an exponential function in 30–200 ms.
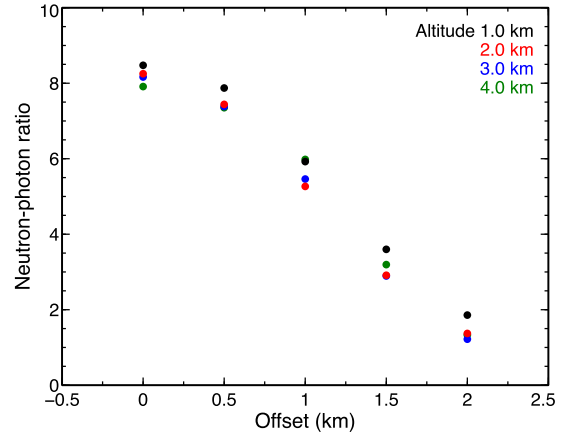
Figure 6.7: The number ratio of neutrons (all energy) to gamma rays (>0.3 MeV) arriving at the ground.
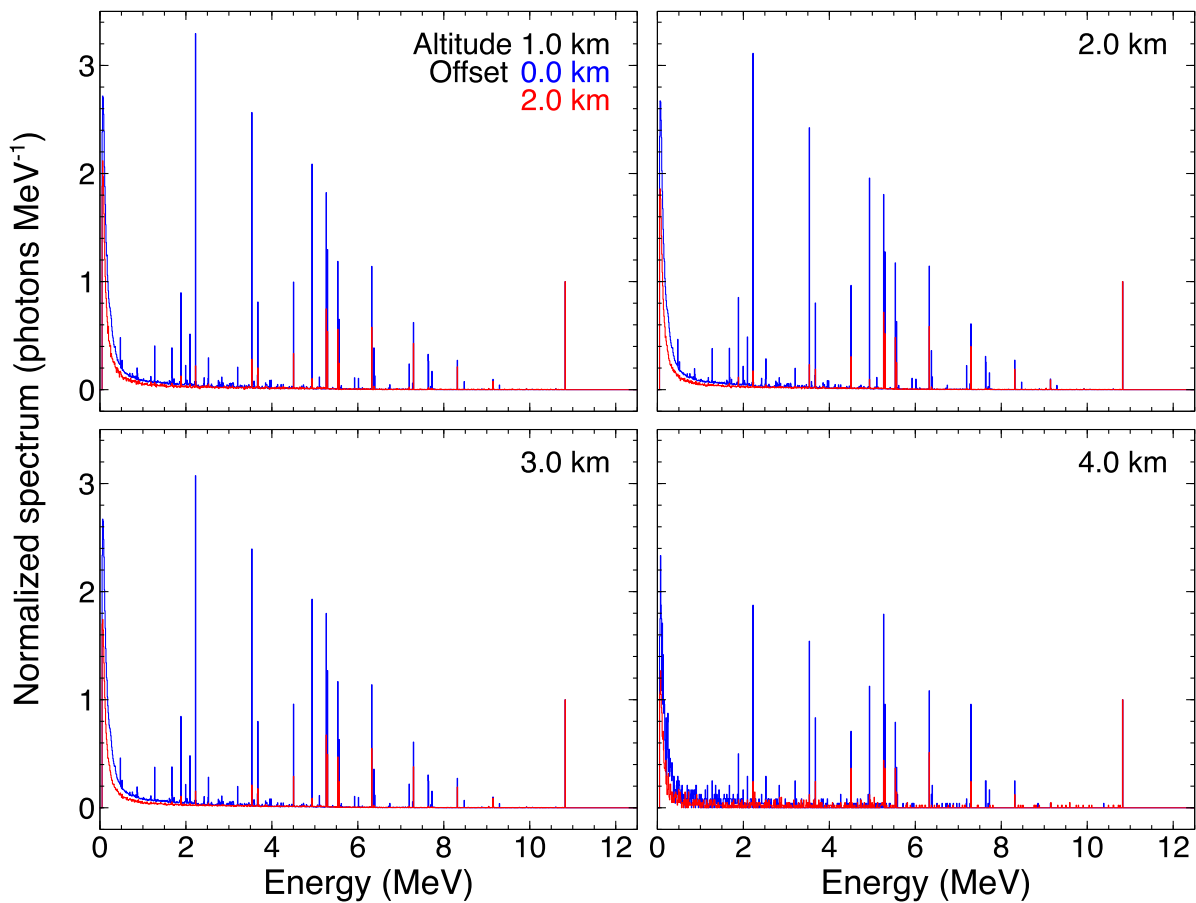
Figure 6.8: Energy spectra of gamma rays arriving on the ground with different altitudes and offsets, normalized to the 10.83-MeV de-excitation line from ^{15}N.
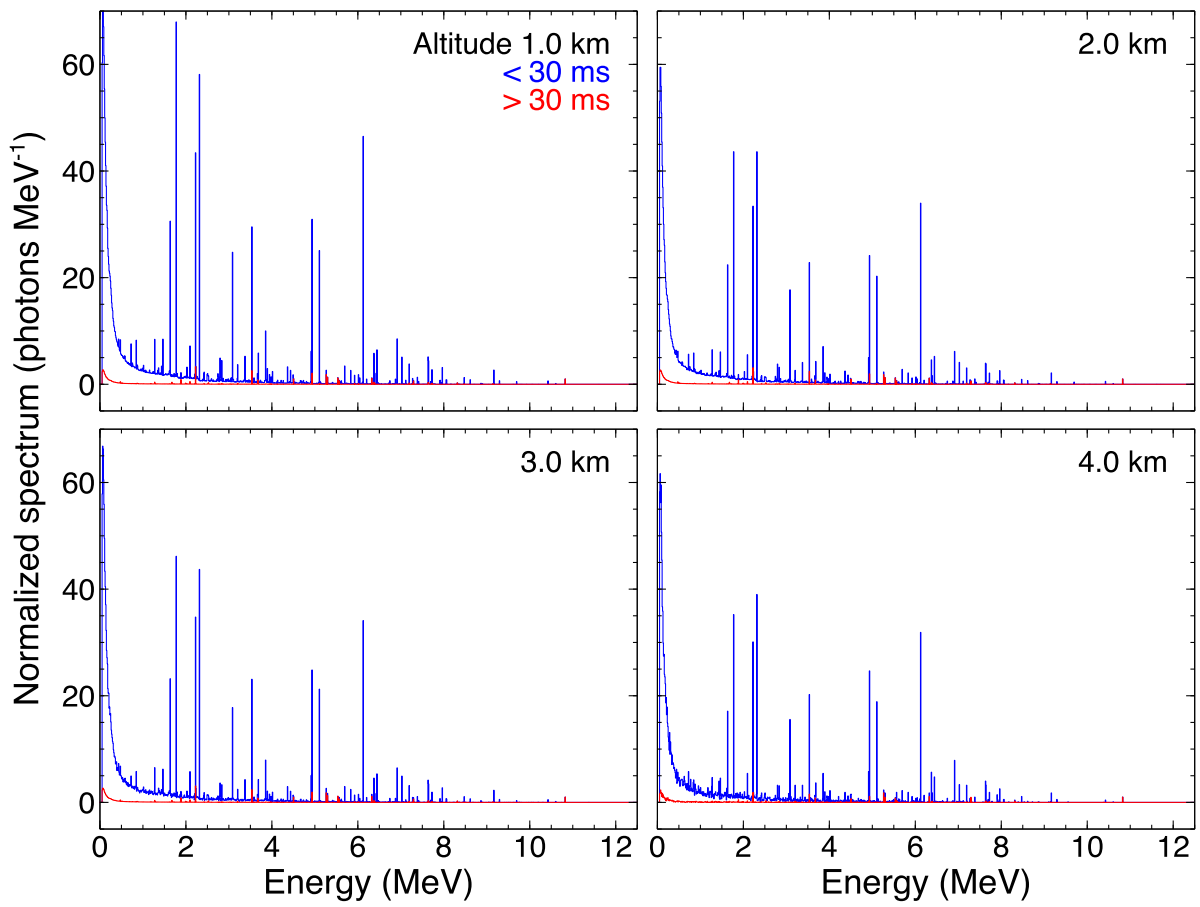
Figure 6.9: Energy spectra of gamma rays arriving on the ground with different time domain, normalized to the 10.83-MeV de-excitation line from [15]N. The offset of the observer is 0.0 km.

6.2 Neutron Detection with GSO Scintillators

In FY2017, GSO scintillators were equipped with Detectors 1–4 in Kashiwazaki-Kariwa Nuclear Power Station to monitor neutrons. GSO (Gd_2SiO_5) scintillators can directly detect de-excitation gamma rays of neutron captures by Gd contained in themselves. The Gd isotopes ^{155}Gd (14.8% in nature) and ^{157}Gd (15.7%) have significantly high cross sections of neutron captures to thermal neutrons (0.025 eV) such as 6.1×10^4 and 2.5×10^5 barns, respectively (Figure 3.6). The present section performs a calibration of GSO scintillators and present an observational result of Event 3.

6.2.1 Responses of GSO scintillators to thermal neutrons

This subsection confirms GSO responses to neutrons by an experiment and a simulation. First, a gamma-ray spectrum is obtained by irradiating neutrons to a GSO scintillator. A measurement setup is shown in Figure 6.10. The size of the GSO scintillator is $2.0 \times 2.0 \times 0.5$ cm^3, the same as utilized in the FY2017 observation. As a neutron source, ^{252}Cf is utilized, which exhibits spontaneous fissions with a half life of 2.645 years. On average, 0.117 neutrons are emitted per a decay. The energy spectrum of emitted neutrons follows $E^{0.5} \exp(-E/1.656 \text{ MeV})$, where E is the kinetic energy of neutrons [Meadows, 1967]. When the present calibration measurement was performed (June 20th, 2019), the ^{252}Cf source utilized here had a radioactivity of 30 kBq, calibrated by the manufacturer of this source; 3.5×10^3 neutrons were emitted per second. Note that 30% uncertainty should be taken into account because radioactivities measured by manufacturers generally have such uncertainty.

A lead block of 5-cm thickness, a tin plate of 3-mm thickness, and a paraffin block of 5-cm thickness are placed between the GSO scintillator and the neutron source. The lead block reduces background counts in GSO by screening gamma rays from ^{252}Cf. Neutrons penetrating the lead block are thermalized by the paraffin block, then enter GSO as thermal or epithermal neutrons. When the lead block absorbs gamma rays, the Kα X-ray line of 74.2 keV can be emitted from lead. This line can contaminate the energy spectrum in GSO and be mixed up with 89.0 keV and 79.5 keV gamma rays from ^{155}Gd and ^{157}Gd, respectively. Therefore, the
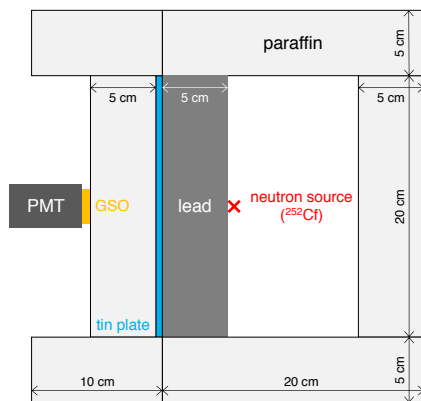
Figure 6.10: A schematic view of the experiment setup for the GSO calibration.
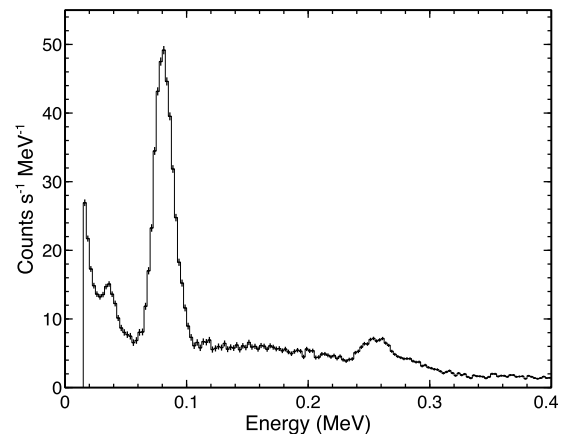
Figure 6.11: A background-subtracted spectrum of neutron captures in the GSO scintillator measured by the setup displayed in Figure 6.10.

tin plate is inserted to screen the Kα line from lead. The plate of 3-mm thickness cuts 99.8% of 80-keV photons, and X rays from tin (25.2 keV) are not mixed up with gamma rays from Gd. Energy calibration of GSO was performed with the 32- and 662-keV lines of ^{137}Cs, 81- and 356-keV lines of ^{133}Ba. The calibration accuracy is within 4%, and took into account as a systematic error.

Measurements with ^{252}Cf and background measurements were performed for 45.5 hours and 124 hours, respectively. Figure 6.11 presents the obtained energy spectrum. The most significant line is at $\sim$80 keV. In addition, lines around 35 keV and 260 keV are also found. This spectral feature is consistent with a previous work [Reeder, 1994]. By evaluating the primary line with a Gaussian and a continuum component, the center and count rate of the line is determined to be 81.08 ± 0.08 (stat.) ± 3.20 (sys.) keV and 0.794 ± 0.009 count s^{-1}, respectively. The line center is consistent with the 79.5 keV line from ^{157}Gd. Therefore, the line mainly originates from neutron captures by ^{157}Gd. It is thought that the contribution from ^{155}Gd, which emits a 89.0 keV line, is smaller than ^{157}Gd because its cross section to thermal neutrons is one forth of ^{157}Gd. In the same way, the center of the $\sim$260-keV line is determined to be 258.6 ± 1.1(stat.) ± 10.4(sys.) keV. This line is consistent with a simultaneous detection of 79.5-keV and 181.9-keV lines from ^{157}Gd as one line at 261.4 keV. In addition, ^{155}Gd and ^{157}Gd emit 38.7-keV and 29.3-keV electrons by internal conversions instead of 79.5-keV and 89.0-keV gamma rays [Reeder, 1994]. The line structure around 35 keV seems to originate from monochromatic electrons of the internal conversion.

Then a Monte-Carlo simulation was performed to test the number of neutrons captured in GSO in the geometry of the present experiment. A mass model of the geometry shown in Figure 6.10 is utilized. Neutrons with the spectrum from ^{252}Cf fissions were injected isotropically, then the number of the reactions ^{155}Gd(n,γ)^{156}Gd and ^{157}Gd(n,γ)^{158}Gd is registered. When neutrons are captured in GSO, tracking of their secondary products was terminated. For comparison, neutron cross sections of Nuclear Data Library (largely coming from ENDF/B-VI[18]; the standard library of `Geant4`) and JENDL-4.0 [Shibata et al., 2011] developed and distributed by Japan Atomic Energy Agency were utilized.

When 10^9 neutrons were injected, 1.60×10^5 for ^{155}Gd(n,γ)^{156}Gd and 5.54×10^5 for ^{157}Gd(n,γ)^{158}Gd with Nuclear Data Library, and 1.59×10^5 for ^{155}Gd(n,γ)^{156}Gd and 5.49×10^5 for ^{157}Gd(n,γ)^{158}Gd with JENDL-4.0 were registered. There are no significant difference between two database. For the present geometry, the ratios of reactions ^{155}Gd(n,γ)^{156}Gd and ^{157}Gd(n,γ)^{158}Gd to the injected neutrons are 0.016% and 0.055% respectively, and 0.071% in total.

At last, the simulation and the experiment are compared. The neutron source ^{252}Cf emitted $(3.5 \pm 1.1) \times 10^3$ neutrons s^{-1}. Combining the rate with the ratio 0.071% obtained by the simulation, an expected neutron-capture rate is 2.5 ± 0.8 neutrons s^{-1}. While, the calibration measurement derived that the main 80-keV peak in Figure 6.11 has an intensity of 0.794 ± 0.009 count s^{-1}. Therefore, one neutron-capture reaction inside GSO makes 0.32 ± 0.10 counts at 80-keV. This conversion factor 0.32 ± 0.10 counts per one neutron capture is utilized to estimate neutron fluxes.

6.2.2 Neutron flux in Event 3

Count-rate histories obtained by GSO scintillators in Event 3, detected on November 24th, 2017, are shown in Figure 6.12, and scatter plots of analog pulse height and baseline are in Figure 6.13.

---

[18]https://www.nndc.bnl.gov/endf/b6.8/

Each detector recorded an increase in counts coincident with the lightning discharge, and significant increases are observed by Detectors 1 and 4. Each detector also recorded undershoots coincident with the lightning (Figure 6.13), and hence the GSO scintillators also experienced extremely large gamma-ray fluxes of a downward TGF.

Since the analog baseline experienced an undershoot for 10 ms after the lightning, energy calibration is not reliable in this time domain. Therefore, this time domain was excluded for spectral analysis. Figure 6.14 shows extracted energy spectra of Detectors 1 and 4. Both spectra has a significant line feature at a low energy range around 80 keV. The center of the line was fitted by the Gaussian function at 83.1 ± 2.8 (stat.) ± 3.2 (sys.) keV and 80.7 ± 1.9 (stat.) ± 3.2 (sys.) keV for Detectors 1 and 4, respectively. This is consistent with the center energy obtained by the calibration experiments, and hence this is a successful detection of neutrons by GSO scintillators.

The photon counts at the line were evaluated to be 71 ± 18 counts and 116 ± 23 counts for Detectors 1 and 4, respectively. By utilizing the conversion factor 0.32 ± 0.10, in total $(2.3 \pm 0.9) \times 10^2$ and $(3.7 \pm 1.4) \times 10^2$ neutrons were captured in GSO of Detectors 1 and 4, respectively.
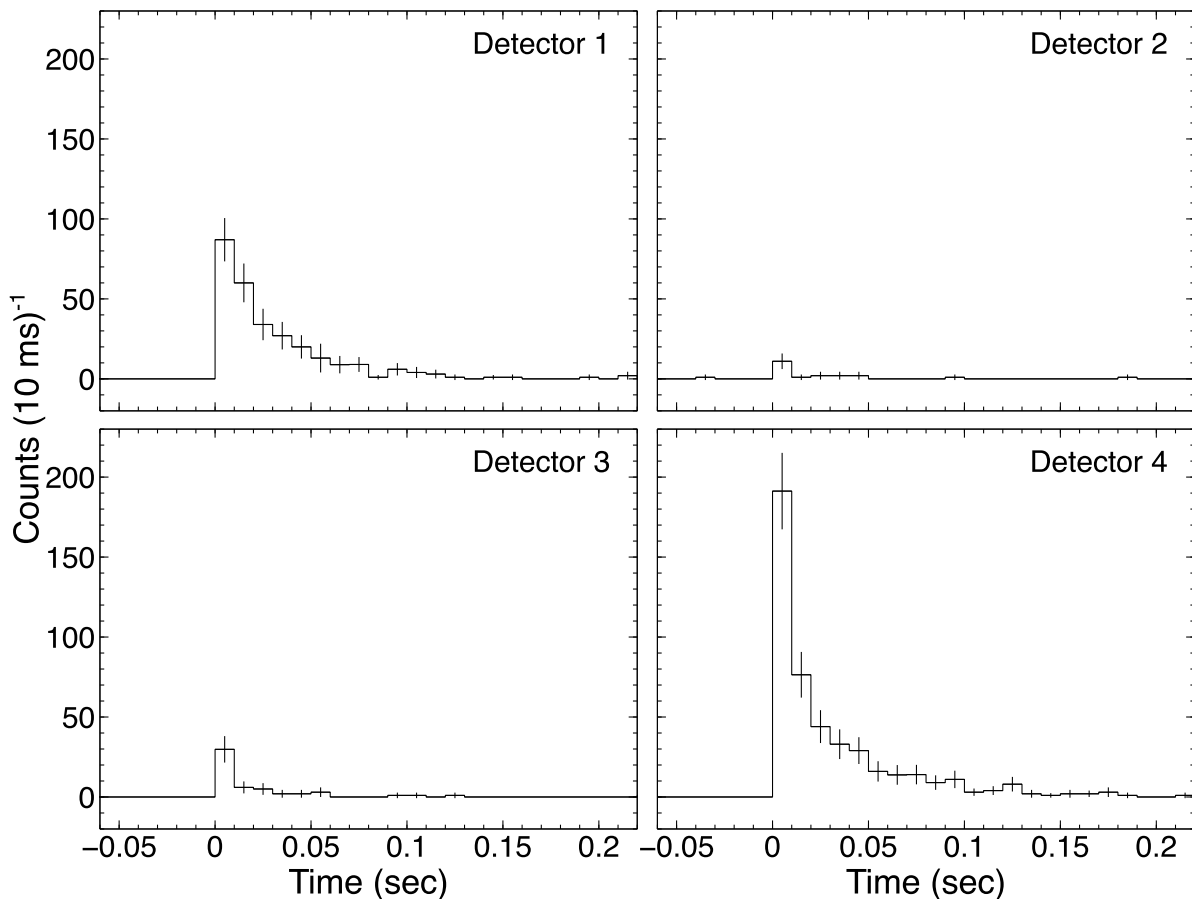
Figure 6.12: Count-rate histories of Event 3 in 0.04–1.0 MeV obtained with GSO scintillators. The origin of time is the beginning of the short-burst event, displayed by the same format as Figure 4.29.
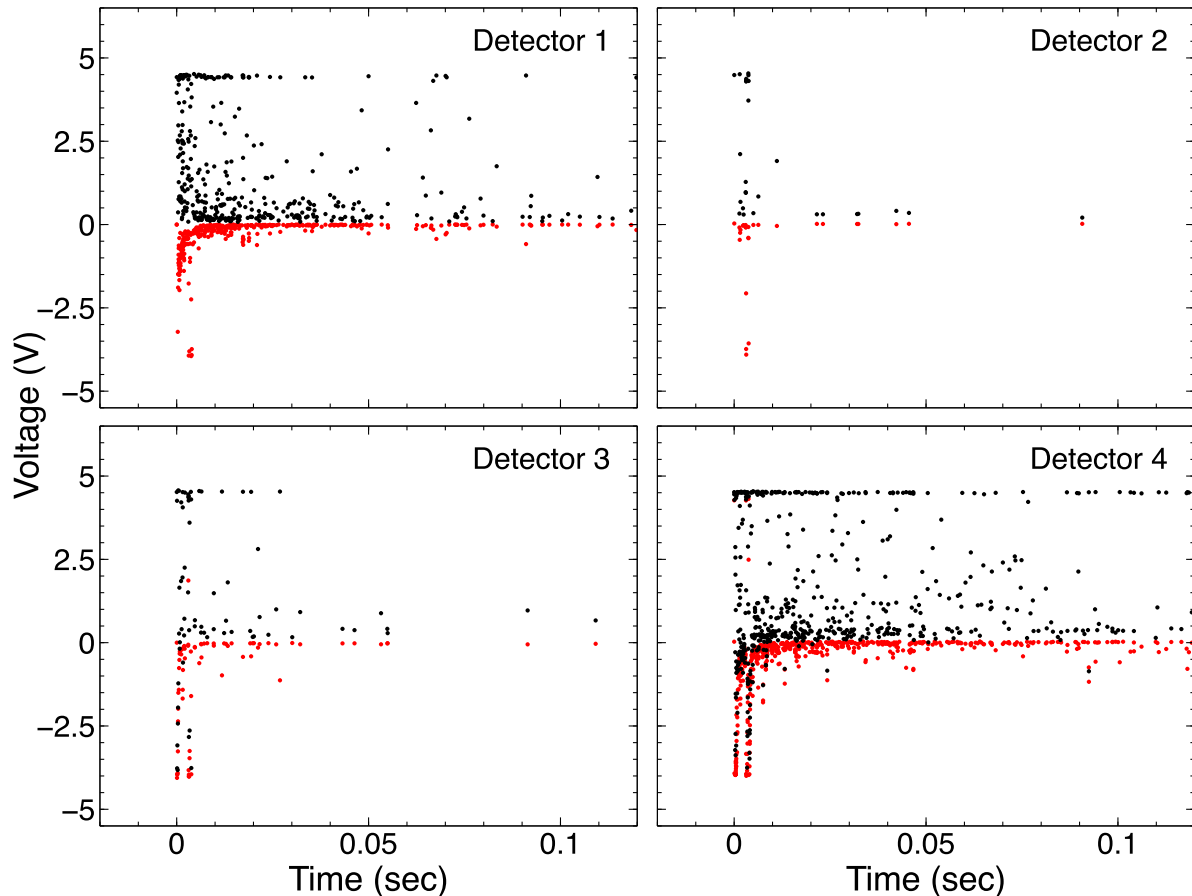
Figure 6.13: Scatter plots of analog pulse heights and baseline of GSO scintillators in Event 3. Detectors 3 and 4 employ the differential threshold mode (Section 3.2).

6.3 Comparison between Observations and Simulations

So far, two types of signals originating from neutrons are discussed. One is de-excitation gamma rays produced by neutron captures in the atmosphere or around detectors, recorded by BGO scintillators. The other is direct neutron detections by GSO scintillators. This section first constructs models corresponding to the two types of signatures, and then compares the models with our measurements to derive properties of downward TGFs.

6.3.1 Model construction

This subsection constructs models of de-excitation gamma rays and neutrons which can be directly compared with our measurements; detector responses are convolved into the simulation results obtained in Section 6.2. Observational data are the energy spectra obtained with BGO scintillators originating from de-excitation gamma rays by neutron captures in the atmosphere and ground, and the number of neutrons directly detected by GSO scintillators.

To construct a spectral model of BGO scintillators, de-excitation gamma rays from neutron captures by nuclei in detector materials are considered in addition to those by atmospheric nuclei. As shown in Figure 6.8, gamma rays and neutrons are classified by offsets from and altitude of initial electron injection. Based on the classified particle distribution, detector responses

103
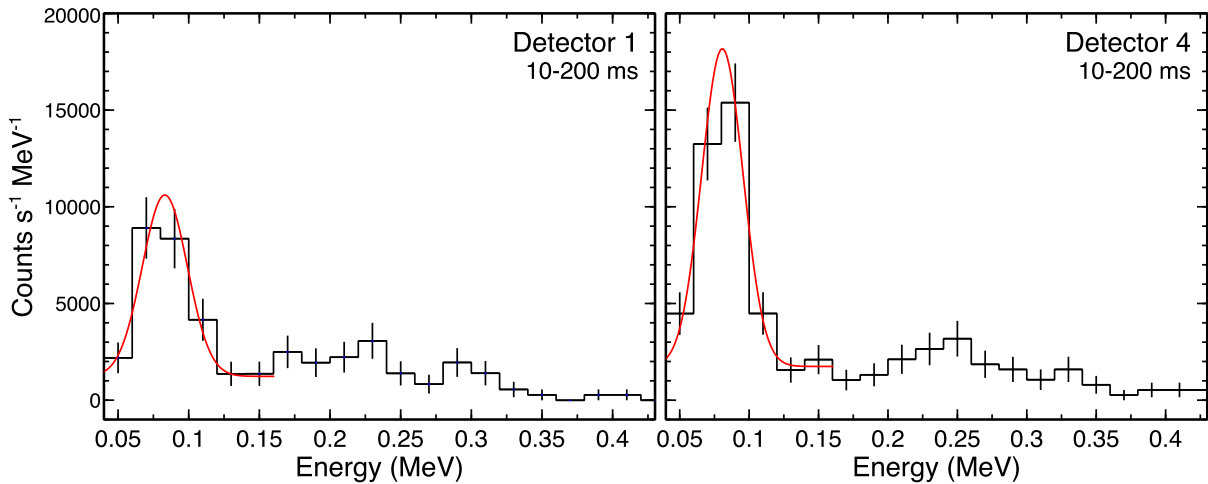
Figure 6.14: Background-subtracted spectra of GSO scintillators in Event 3. The overlaid red lines present the best-fit models of a line structure around 80 keV.

of BGO scintillators are calculated by injecting gamma rays and neutrons into a mass model of detectors. Particles arriving at the ground in 30–200 ms are considered for the response calculation because the observation data recoded in <30 ms are affected by the undershoots and hence excluded from spectral analysis. Then a response-included spectral model shown in Figure 6.15 is obtained by considering energy resolution of BGO scintillators. The spectral model in Figure 6.15 is normalized to 10^{18} initial electrons.

Although the spectra shown in Figure 6.15 consist of multiple lines, their shapes appear continuum due to moderate energy resolution of BGO scintillators. There is a steep cutoff at $\sim$10 MeV caused by the 10.7 MeV line from neutron captures with ^{14}N, and a line-like structure at 5.3 MeV. In addition, a line structure at 1.88 MeV becomes significant as an offset is smaller. The normalization of the spectral model depends on altitude of initial electrons and offset of detectors.

The spectral model is implemented in a table model used in XSPEC as a three-dimensional function of detector offset, injection altitude and the number of initial electrons. In a proper usage of XSPEC, detector responses are not included in table models, instead a detector response matrix should be separately loaded. In the present case, however, the table model includes detector responses, and a response matrix consisting of only diagonal components with 100% detection efficiency is prepared. This is because detector responses can be changed by model parameters such as altitude and offsets due to different arrival angles.

Likewise, the particles classified by offset and altitude are injected into a mass model of detectors to calculate a model with GSO scintillators. In this case, only the neutron component is considered. Also, neutrons arriving in 10–200 ms are considered because GSO scintillators were recovered from undershoots quicker than BGO scintillators. When neutrons enter the GSO mass model and experience neutron capture reactions, the reaction type is recorded and tracking of their byproducts are terminated in the same manner as Subsection 6.2.1. The obtained model of neutron number detected by GSO scintillators is shown in Figure 6.16. This model is also a three-dimensional function of detector offsets, injection altitude and the number of initial electrons.
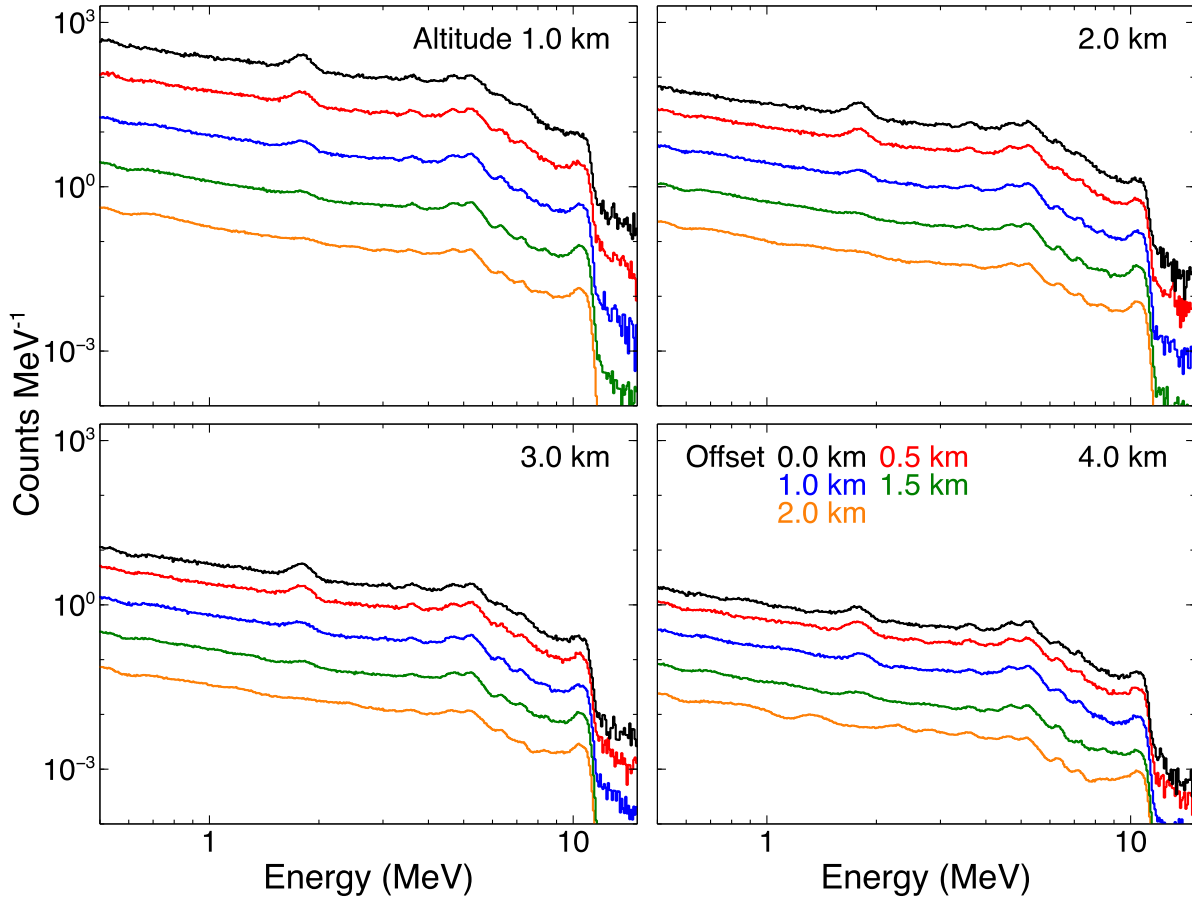
Figure 6.15: Simulated energy spectra of de-excitation gamma rays including BGO detector responses, normalized to 10^{18} initial electrons. The incident particles are extracted from 30–200 ms.

6.3.2 Fitting results

This subsection compares observations with the models obtained in Subsection 6.3.1. The models compared with BGO and GSO data are a function with three parameters (detector offset, source altitude and the number of initial electrons). On the other hand, BGO data were obtained from 3 detectors in Events 1–3, and GSO data were from 2 detectors in Event 3, It is difficult to determine the model parameters with only these data of neutron origin. Therefore, this subsection handles Event 2, whose TGF center is estimated by the positron emissions, and Event 3, which both BGO and GSO scintillators were in operation.

For Event 2, since Detector 1 recorded the delayed component of annihilation emissions, the TGF center was estimated based on the delay time and wind velocity in Subsection 6.3.1 (see Figure 4.9). Therefore, the TGF center is fixed to the result from annihilation emissions. The estimated TGF center is 0.59 km northwest from Detector 1, and offsets of Detectors 1–3 are 0.59, 1.37, and 1.02 km, respectively. The model fitting is performed by the χ^2 method with XSPEC. Spectra of different detectors are simultaneously fitted. Detector offsets are fixed, while altitude and electron number are set to be free parameters common to spectra of the other detectors. The spectrum of Detector 2 is excluded in the present analysis due to poor photon statistics for the χ^2 method. Figure 6.17 shows the best-fit spectral model. With 29 degrees of freedom, $\chi^2 = 52.3$ is obtained. The altitude of electron injection and the electron number are
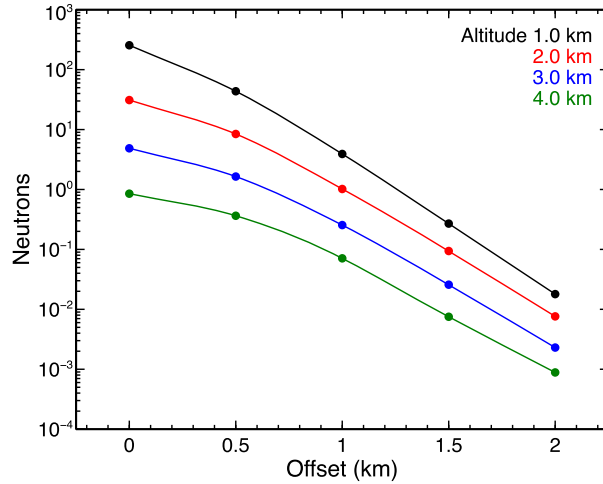
Figure 6.16: Simulated numbers of neutron detection with GSO scintillators as a function of offset, altitude, and the number of initial electrons, normalized with 10^{18} initial electrons.

estimated to be $1.6^{+0.3}_{-0.2}$ km and $16^{+9}_{-4} \times 10^{18}$ electrons, respectively. It is noted that the electron number and the altitude are not independent parameter. Namely, larger number of electrons are needed with higher altitude if considering constant on-ground fluxes. The possible region at 1σ confidence level in the altitude-electron number space is shown in Figure 6.18.

For Event 3, both BGO and GSO scintillators were in operation. In particular, Detector 1 recorded both the spectra of de-excitation gamma rays by BGO and the number of neutrons directly detected by GSO. The data of GSO and BGO recorded by Detector 1 are compared first to confirm the consistency between them. Data of GSO is then used to narrow possible area of the TGF position, and spectral analysis of BGO is performed to estimate altitude and electron
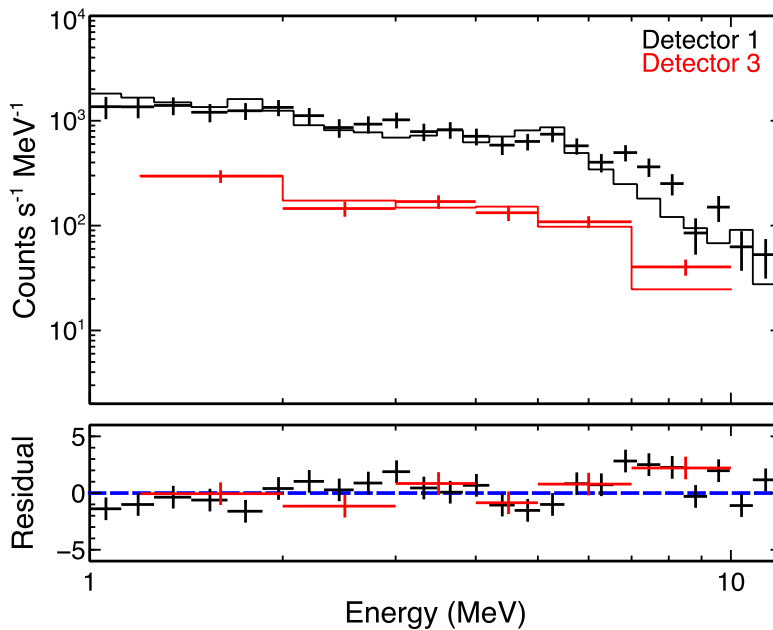
Figure 6.17: The best-fit spectra of de-excitation gamma rays obtained by BGO in Event 2 (top) and its fitting residuals (bottom). The residual at each bin is defined as (data-model)/(error).
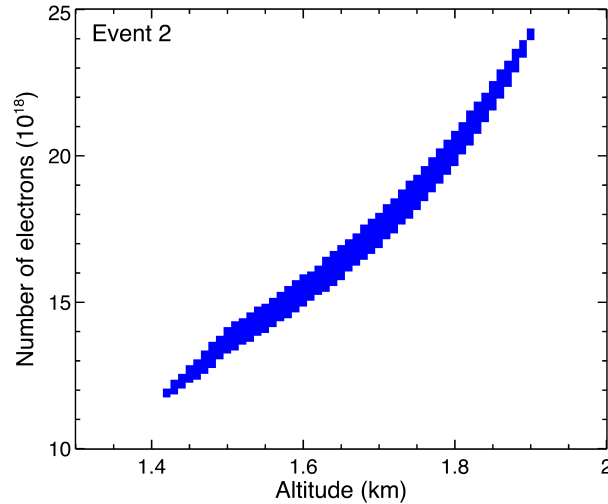
Figure 6.18: A contour of altitude-electron number space of Event 2 derived with BGO spectra. The blue-colored area presents 1σ confidence level.

number at last.

First, observation data of GSO and BGO are compared. The models constructed in Subsection 6.3.1 is a function of detector offsets, injection altitude and the number of initial electrons. By fitting the observation data with fixed altitude and offset, the number of injected electrons can be estimated. Therefore, altitude and offset are surveyed in the range of 1.0–4.0 km for a 1-km step and 0.0–1.0 km for a 0.1-km step, respectively. The electron number with each fixed altitude and offset is estimated from best-fit results with BGO and GSO of Detector 1. The result is shown in Figure 6.19. The numbers of electrons estimated by BGO and GSO data are consistent when detector offsets are small. In contrast, the numbers are inconsistent with larger detector offsets. In the case of the 1-km offset, for example, the estimated electron number by GSO is twice or three times larger than that by BGO at each electron-injection altitude. BGO scintillators are sensitive to gamma-ray signatures of neutron origin, and GSO scintillators to neutrons themselves. As shown in Figure 6.7, the ratio of gamma rays and neutrons arriving on the ground depends on detector offsets. In the present case, a smaller offset at Detector 1 is more favored than a larger offset. Therefore, a region within a 0.5-km radius from Detector 1 is surveyed to identify possible area of TGF center.

Then, the possible area of the TGF center is surveyed with GSO data. The neutron number detected by GSO scintillators on Detectors 1 and 4 are fitted with the model by the least-squares method with errors. The least-squares method with errors surveys parameters that minimize the dispersion s^2

$$s^2 = \Sigma_{i=1}^2 [(y_i - \text{model})/\Delta y_i]^2, \tag{6.1}$$

where y and Δy are the number of neutrons detected by GSO and its error. The region within a 0.5-km radius from Detector 1 is divided into 50 m × 50 m grids. At each grid, detector offsets are determined and model fitting is performed with the offsets. The distribution of s^2 is shown in Figure 6.20. In the east-half region which is not displayed in Figure 6.20, the best-fit model is not consistent with the data points within errors; one or more data points do not satisfy the condition $|y_i - \text{model}| < \Delta y_i$. In the next analysis with BGO data, the displayed region in Figure 6.20 is used for the survey of the TGF center. Around Detector 4, there are multiple survey points where $s^2 = 0$. A example of the best-fit model with $s^2 = 0$ is shown in Figure 6.21. For this example, the TGF center is 0.36 km from Detector 1, 0.2 km
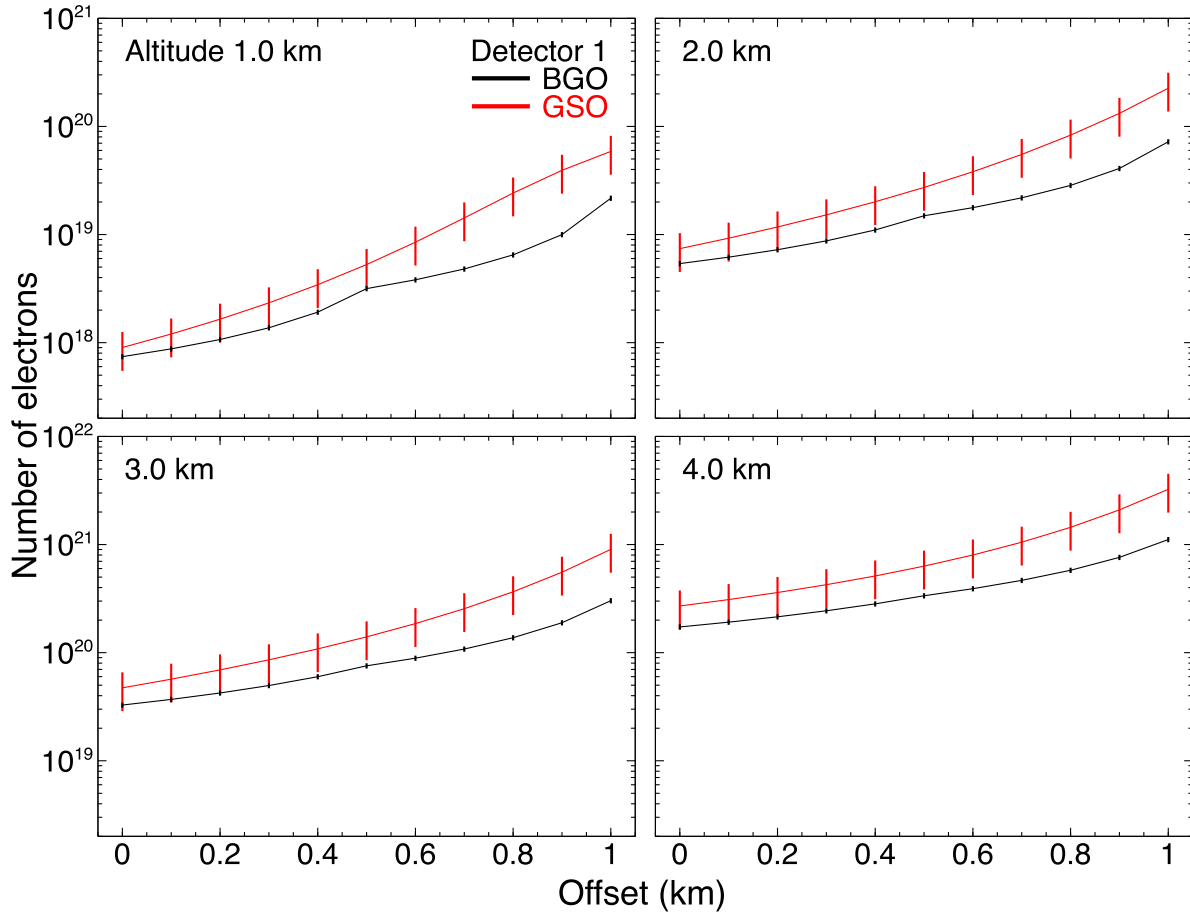
Figure 6.19: Best-fit numbers of electrons in Event 3 recorded by BGO and GSO scintillators on Detector 1 in the parameter space of offset and the number of initial electrons.
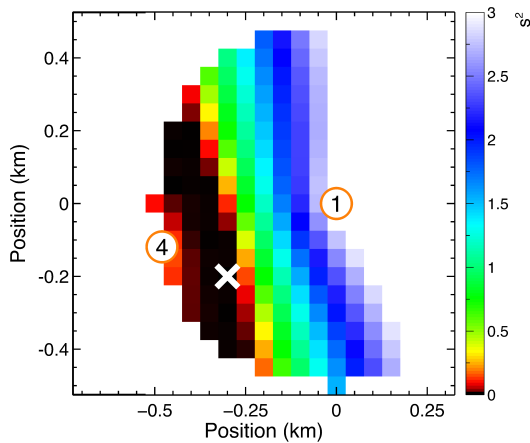
Figure 6.20: A survey result of s^2 with the detector numbers of neutrons by GSO scintillators in Event 3. The orange circles show Detectors 1 and 4. One of the best-fit position (namely $s^2 = 0$) is presented by a white cross marker. The axis origin is at Detector 1.
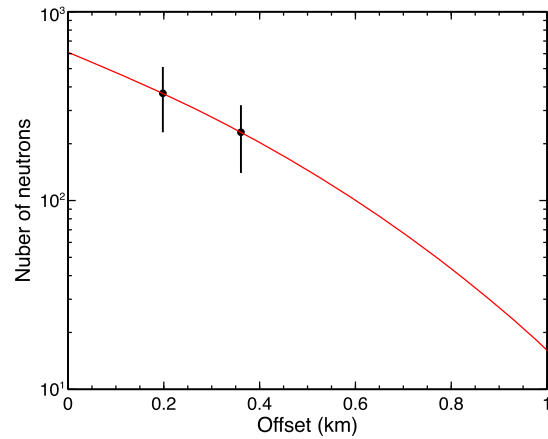
Figure 6.21: One of the best-fit results with two estimated number of neutrons by GSO scintillators. The best-fit model is overlaid by a red line. The TGF center of this best-fit solution is presented by a white cross marker in Figure 6.20.

from Detector 4, and the source altitude and the number of initial electrons are 1.6 km and 8.6×10^{18} m, respectively.

Based on the survey area obtained by the fitting of GSO data, spectra of BGO data are fitted with models. While spectra of BGO scintillators recorded by Detectors 1–3, data of Detector 2 is excluded due to poor photon statistics as well as Event 2. The best-fit result, $\chi^2 = 37.6$ with 17 degrees of freedom, is shown in Figure 6.22. The best-fit parameters of the source altitude and the number of initial electrons are estimated to be 1.0 km and 1.1×10^{18} electrons, respectively. The estimated TGF center, and a $\Delta\chi^2$ distribution from the best-fit model are shown in the left panel of Figure 6.23. Considering 1σ confidence level, namely a region where $\Delta\chi^2 < 1$, a possible region of TGF center is estimated as in Figure 6.23 right. In addition, error regions at 1σ confidence level in the altitude-electron number space are shown in Figure 6.24. There are two error regions. One indicates the altitude and the electron number as < 1.5 km and $< 2.7 \times 10^{18}$, and the other 1.9–2.2 km and $(5.6$–$10.2) \times 10^{18}$, respectively.
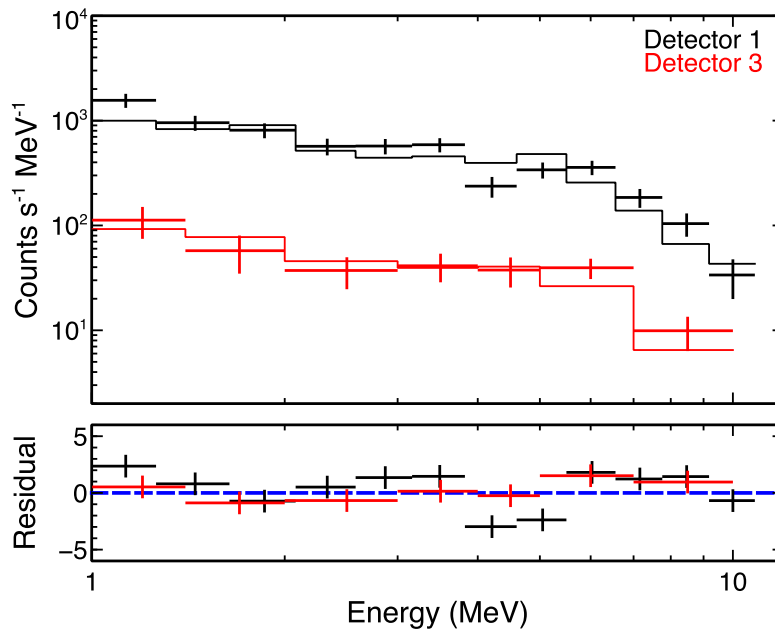
Figure 6.22: The best-fit spectra of de-excitation gamma rays in Event 3 obtained by BGO scintillators (top) and its fitting residuals (bottom).
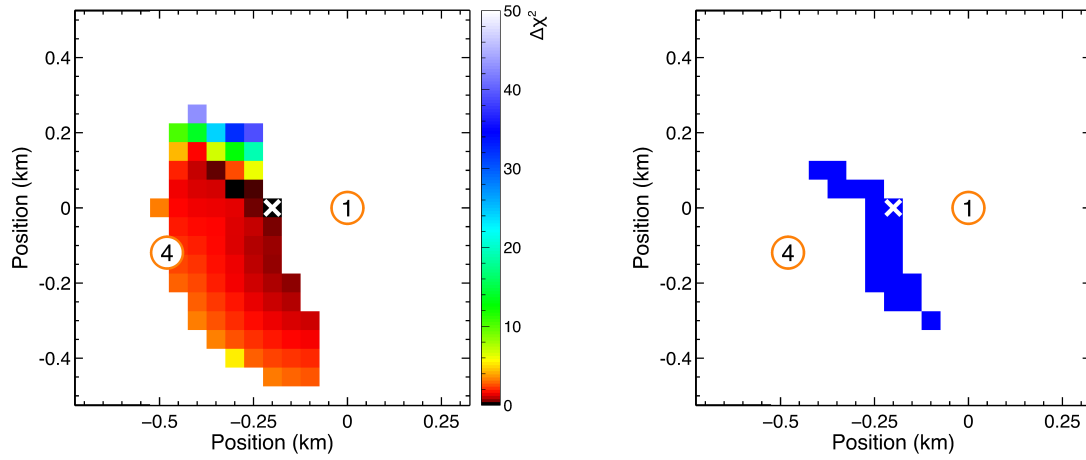
Figure 6.23: A $\Delta\chi^2$ distribution (left) and an error region (right) of a survey with spectra of BGO scintillators in Event 3. The axis origin is at Detector 1. The orange circles show the positions of Detectors 1 and 4. The best-fit position is presented by a white cross marker. The error region is the survey points where $\Delta\chi^2 < 1.0$.
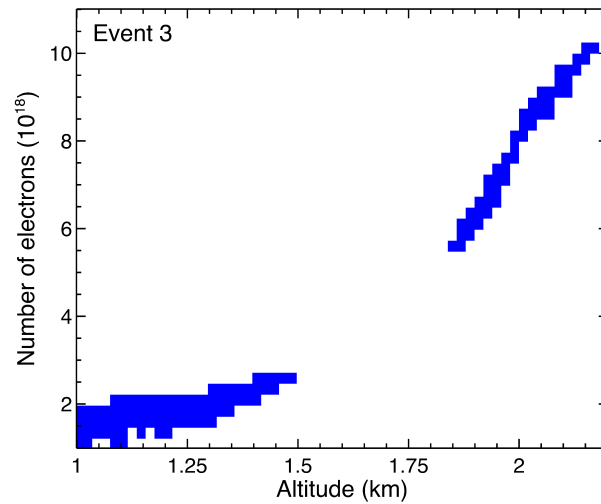
Figure 6.24: A contour in the parameter space of the source altitude and the electron number for Event 3, obtained by fitting of BGO spectra. The blue-colored area presents 1σ confidence level.

Chapter 7

Downward Terrestrial Gamma-ray Flash

The present chapter evaluates the number and source altitude of initial electrons via on-ground measurements of gamma-ray intensities during sub-millisecond-lasting downward TGFs. As described in Subsection 4.2.4, scintillation detectors are saturated by significantly high fluxes of downward TGFs. On the other hand, high-level dosimeters of MPs can measure total doses even in high-flux environment, instead of counting every photons. Here total doses of downward TGFs measured by multiple dosimeters and simulations are compared to directly evaluate properties of downward TGFs.

7.1 Verification of Dose Measurements with Monitoring Posts

Before performing a full simulation of downward TGFs from initial electrons, measurements of dosimeters (Section 3.5) are evaluated with a simple model. An energy spectrum of avalanche electrons produced by RREA has an energy cutoff as a form of $\exp(-E/7.3 \,\mathrm{MeV})$, as presented in Equation 2.19 [Dwyer et al., 2012b]. An energy spectrum of bremsstrahlung emissions from the avalanche electrons approximately follows $E^{-1}\exp(-E/7.3 \,\mathrm{MeV})$ [Dwyer, 2008]. As a preliminary attempt, let us assume the case that atmospheric attenuation is ignored. By utilizing `Geant 4`, the bremsstrahlung photons in 0.05–50.0 MeV are injected into a mass model of the high-level dosimeter. The specification of the dosimeters is summarized in Subsection 3.5. They are ionization chambers, consisting of a sphere of 2-mm thickness stainless and filled with 14-L argon gas at 4 atm. In this simulation, energy deposits in argon gas are recorded. Simulation doses are calculated with the energy deposits and the mass of argon gas. Then a relation between gamma-ray fluences and doses, 0.050 μGy per 10^4 photons cm^{-2}, is obtained under the condition of the bremsstrahlung spectrum in 0.05–50.0 MeV.

In the three short-burst events observed at Kashiwazaki-Kariwa Nuclear Power Station (Events 1–3), approximately 0.01–1.0 μGy doses were recorded by dosimeters at different locations (Figures 4.9 and 4.26).[19] With the conversion factor obtained by the simulation, a gamma-ray fluence in 0.05–50.0 MeV at each monitoring post ranges in 2.0×10^3–2.0×10^5 photons cm^{-2}. A typical duration of TGFs is hundreds of microseconds to several milliseconds [Briggs et al., 2013]. Since the timing resolution of the high-level dosimeter is 30 sec, the duration of the downward TGFs cannot be determined. Instead, conservatively considering the duration of the present downward TGFs is less than 10 ms, gamma-ray fluxes at monitoring posts seems to be larger than 2.0×10^5–2.0×10^7 photons cm^{-2} s^{-1}.

---

[19]The total doses of 0.01–1.0 μGy correspond to 6×10^3–6×10^5-MeV energy deposits in 14-L argon gas at 4 atm (100 g).

At MP6, installed at the identical position of Detector 2, 0.208 μGy was recorded by the dosimeter in Event 3. It is converted to a fluence of 4×10^4 photons cm^{-2}. The BGO scintillator onboard Detector 2 has a geometrical detection area of 200 cm^2, and their lower-energy threshold is set to be 0.2 MeV. Assuming a TGF duration of 0.1–10.0 ms and a $\sim$50% detection efficiency of BGO, count rates of BGO in Detector 2 are expected to be 3×10^8–3×10^{10} counts s^{-1}. This rates are $> 10^4$ times higher than the recorded count rates of short bursts ($<$1000 counts s^{-1}). The analog circuit onboard the compact detectors (including Detector 2) has a shaping time of 2 μs. Count rates of 5×10^5 counts s^{-1} or higher must saturate the detectors. Therefore, the on-ground flux estimated via the TGF dose is consistent with the saturation feature recorded by Detector 2

It is thought that doses of downward TGFs measured by high-level dosimeters could include contributions from de-excitation gamma rays of neutron captures because dosimeters record integrated amounts for 30 seconds. To evaluate this effect, doses measured by low-level dosimeters (Section 3.5) are analyzed. Low-level dosimeters consist of a cylindrical NaI scintillator of a 2-inch diameter and height, and register doses based on the number of counted photons. Therefore, low-level dosimeters should be completely saturated by downward TGFs and record almost nothing of TGF photons, while properly measure following de-excitation gamma rays as well as BGO scintillators. No significant enhancements were recorded in Event 1, and at maximum 3×10^{-4} μGy and 2×10^{-4} μGy were recorded in Events 2 and 3, respectively. The low-level dosimeters are sensitive to 0.05–3.0 MeV photons. Assuming the de-excitation emissions exhibit approximately a flat spectrum up to 10.8 MeV, based on the spectra obtained by BGO scintillators, total doses taking into account gamma rays of up to 10.8 MeV are as high as 4×10^{-3} μGy and 2×10^{-3} μGy for Events 2 and 3, respectively. Since the estimated doses are less than 1% of those recorded by high-level dosimeters, lower than the systematic uncertainty of high-level dosimeters, doses of de-excitation gamma rays are negligible comparing to those of downward TGFs.

7.2 Monte-Carlo Simulation of Radiation Doses at the Ground

In the present section, a full simulation starting from avalanche electrons are performed to construct dose models at the ground including atmospheric propagation and attenuation of electrons and gamma rays. The simulation is divided into two stages: the first stage calculates atmospheric interaction of particles, and the second stage detector responses. In the first stage, avalanche electrons are injected in the mass model of the atmosphere utilized in Section 5.2. At altitudes of 1–4 km with a 0.5-km interval, 10^9 in 1–50 MeV are injected. The condition of initial avalanche electrons is also same as the simulation in Section 5.2: a downward narrow beam without divergence, with an energy spectrum of $\exp(-E/7.3\,\mathrm{MeV})$. Since this simulation does not consider hadronic and neutron physics such as photonuclear reactions, the FTFP_BERT_LIV physics list is utilized (Subsection 5.2.2). The initial electrons are diffused by struggling, and emit bremsstrahlung photons. Then photons arrive at the ground as they experience Compton scatterings, photoabsorptions, and/or pair creations. When they or their byproducts (photons, electrons, positrons) reach the ground, their particle type, arrival position, momentum vector, and kinetic energy are registered. The simulation outputs are injected into the mass model of high-level dosimeters in the second stage to calculate doses.

Figure 7.1 shows gamma-ray spectra obtained in the first stage. Gamma-ray fluxes become lower due to the beaming effect of bremsstrahlung as offset gets larger. As well, there are differences in spectral shapes by altitude and offset, caused by the beaming effects and Compton scatterings of photons in the atmosphere. The annihilation line at 0.511 keV is significant with

small offsets.

Figure 7.2 is the model of total doses obtained by the two-stage full simulation. The displayed model is normalized to 10^{18} electrons, which is a typical number of TGF electrons. The dose model is also a three-dimensional function of detector offset, injection altitude and the number of initial electrons. At low altitude, doses are quickly attenuated as the detector offset becomes larger.

7.3 Fitting of Radiation Doses at Multiple Monitoring Posts

With the on-ground dose model of downward TGFs obtained by the full simulation, the three parameters (TGF position, altitude, and the number of avalanche electrons) are estimated by fitting doses measured by high-level dosimeters. Dose data obtained in Events 1–3, which were detected in Kashiwazaki-Kariwa Nuclear Power Station, are analyzed in the present thesis. The χ^2 method is utilized for the fitting. Areas around Kashiwazaki-Kariwa are divided into 25 m $\times$ 25 m grids. The offsets of monitoring posts are calculated at each grid, and measured doses are compared with the models, then best-fit parameters minimizing χ^2 are tested. The dose models
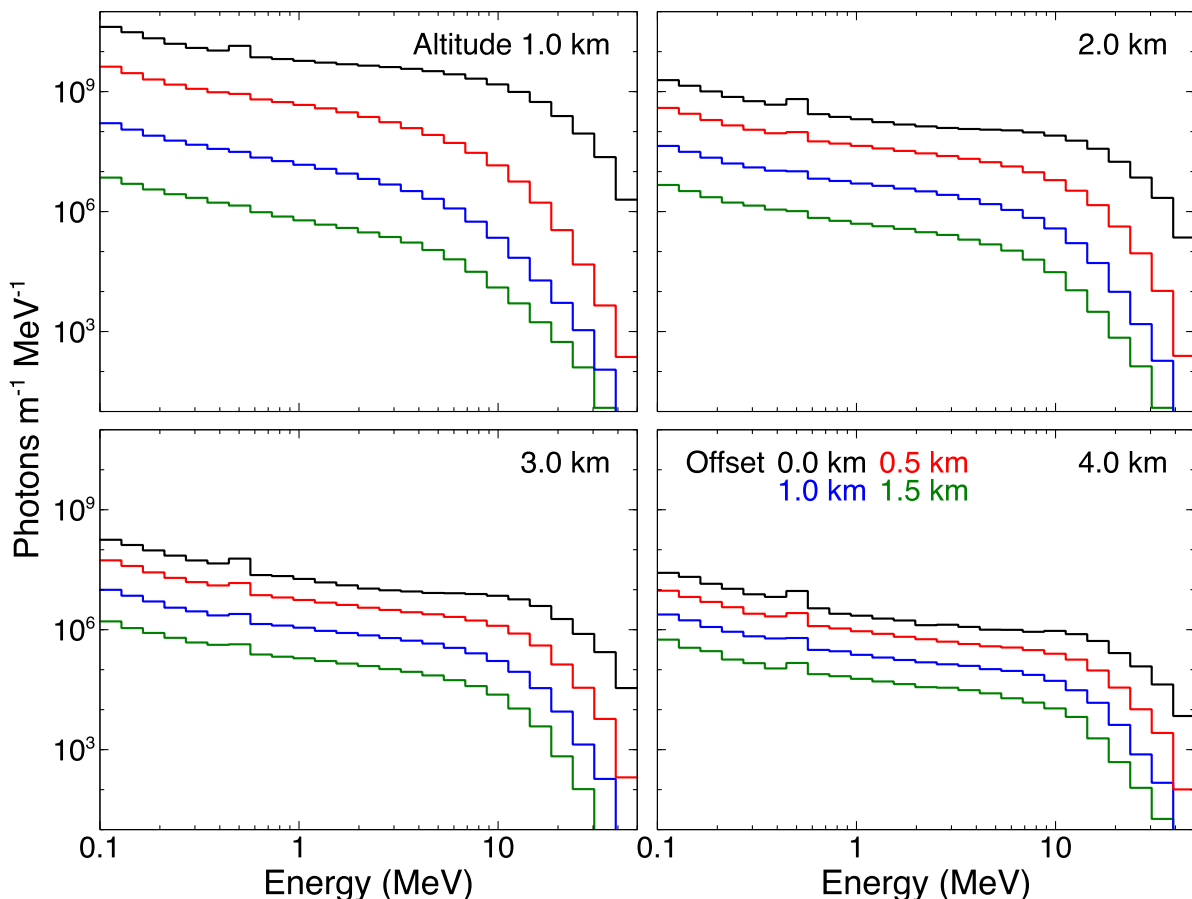
Figure 7.1: Simulated spectra of bremsstrahlung gamma rays at the ground emitted from avalanche electrons in the atmosphere. Four panels show different source altitude of avalanche electrons at 1.0 km, while different line colors corresponds to the offset of the observer from the source. Atmospheric attenuation is included.
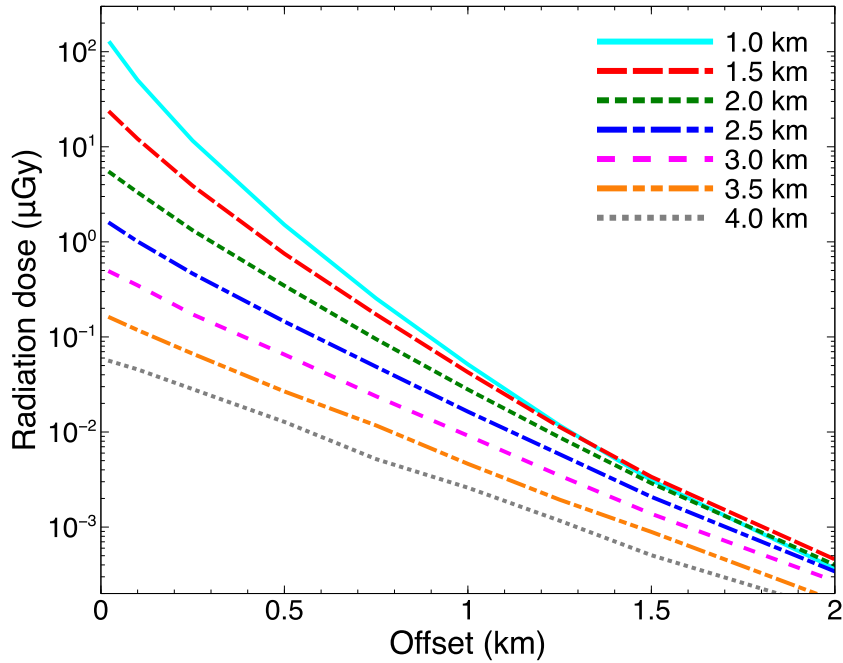
Figure 7.2: Simulation models of the relation between offsets from the TGF center and radiation doses measured by high-level dosimeters at various source altitudes of downward TGFs. The models are normalized to a typical number of electrons 10^{18} in 1–50 MeV for TGFs.
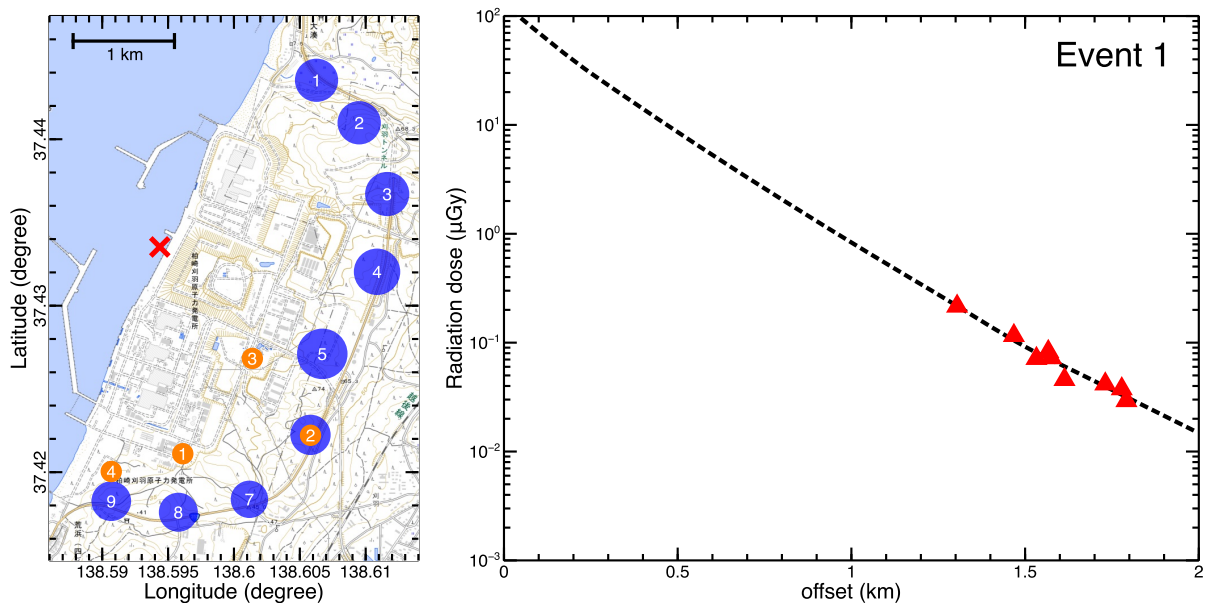
Figure 7.3: The fitting result of Event 1 with observations of high-level dosimeters. Left: the observed radiation doses (blue circles) and the estimate position of the TGF (red cross). The radiation doses are displayed in the same manner as Figure 4.26. Right: the best-fit result of the parameter survey. Each red triangle presents the dose recorded by each dosimeter. The best-fit model is overlaid by the black dotted line.
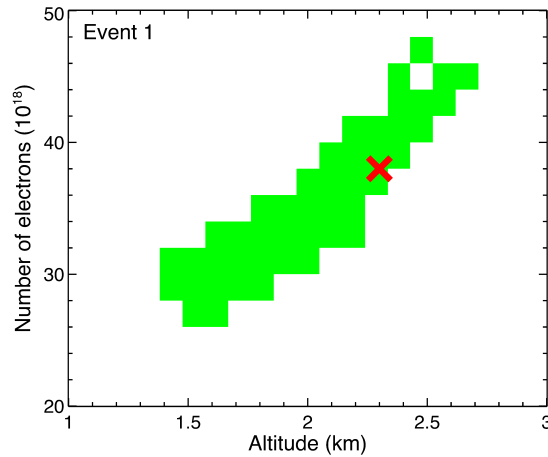
Figure 7.4: A 1σ-error region of Event 1 in the altitude-electron number space. The green-colored area and the red cross marker present 1σ confidence level and the best-fit solution, respectively.

(Figure 7.2) are only applicable when the detector offset is less than 2 km, and hence dose data of high-level dosimeters within 2 km from a survey grid are utilized for the fitting. When n of 9 high-level dosimeters are available for the fitting, $\chi^2 = \Sigma_{i=1}^{n}[(y_i - f(x_i, h, n))/\Delta y_i]^2$, where y_i and Δy_i are a dose and its error recorded by MPi respectively, and $f(x_i, h, N)$ is a value of the dose model with an offset at MPi, altitude h, and the electron number N. Here the uncertainty of radiation doses is 15%, the systematic uncertainty of high-level dosimeters (Section 3.5). The parameter errors at 1σ confidence level are also determined by surveying regions where $\Delta\chi^2$ from χ^2 of the best-fit model is less than 1.0.

Figure 7.3 left presents radiation doses measured in Event 1. Doses are higher in the north region of the power station, maximum at MP5. The best-fit result by the χ^2 method is shown in Figure 7.3 right. The estimated TGF position is 0.33 km east and 1.70 km north from MP9. The estimation uncertainty is a 80-m radius. The TGF altitude and the number of avalanche electrons are estimated to be $2.3^{+0.4}_{-0.9}$ km and $38^{+8}_{-11} \times 10^{18}$ electrons, respectively. This χ^2 fitting utilized doses of all the nine MPs, and $\chi^2 = 7.27$ for the best-fit model. The fitting has 5 degrees of freedom with 9 data points and 4 parameters (2-dimensional position, altitude, number of avalanche electrons), and reduced χ^2 is 1.45 for the best-fit model was obtained. It is noted that the TGF altitude and the number of avalanche electrons are not independent parameters. The error region at 1σ confidence level in the phase space of the source altitude and the electron number is shown in Figure 7.4.

As is the case with Event 1, measured doses and best-fit models of Events 2 and 3 are shown in Figure 7.5 and Figure 7.6, respectively. In both events, the highest dose was measured at MP9, and MPs in the south region recorded high doses. In Event 2, the dose measured at MP8 (0.11 μGy) is lower than those at adjacent MP9 (1.72 μGy) and MP7 (0.49 μGy). In fact, a χ^2 fitting with the dose at MP8 is not acceptable: $\chi^2 = 81.1$ with 3 degrees of freedom. In Event 3, MP8 went down by the lightning discharge, and it might also have gone down in Event 2 by the lightning discharge. Therefore, the measured dose at MP8 was excluded in the analysis for Events 2 and 3.

In Event 2, the estimated TGF position is 0.25 km east and 0.45 km north from MP9, with estimation error of 50 m for the west-east direction and 150 m for the north-south direction. The TGF altitude and the number of avalanche electrons are estimated to be $2.4^{+0.3}_{-0.8}$ km and

$11^{+3}_{-6} \times 10^{18}$ electrons, respectively. This χ^2 fitting utilized doses of five MPs, and $\chi^2 = 0.26$ with one degree of freedom was obtained. In Event 3, the estimated TGF position is 0.40 km east and 0.25 km north from MP9, with estimation error of 50 m for the west-east direction and 130 m for the north-south direction. The TGF altitude and the number of avalanche electrons are estimated to be $2.5^{+0.3}_{-0.4}$ km and $9^{+4}_{-2} \times 10^{18}$ electrons, respectively. This χ^2 fitting also utilized doses of five MPs, and $\chi^2 = 2.03$ with one degree of freedom. The error regions in the phase space of the source altitude and the electron number are presented in Figure 7.7.
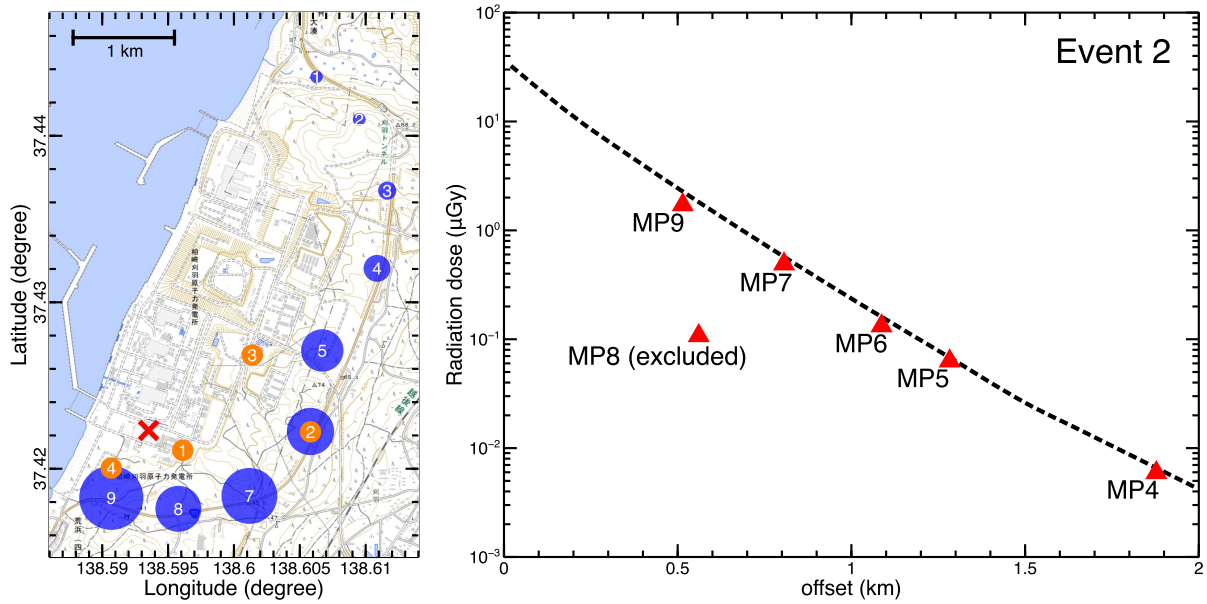
Figure 7.5: The fitting result of Event 2 with observations of high-level dosimeters, presented in the same manner as Figure 7.3. The dose recorded at MP8 was excluded in the actual analysis.
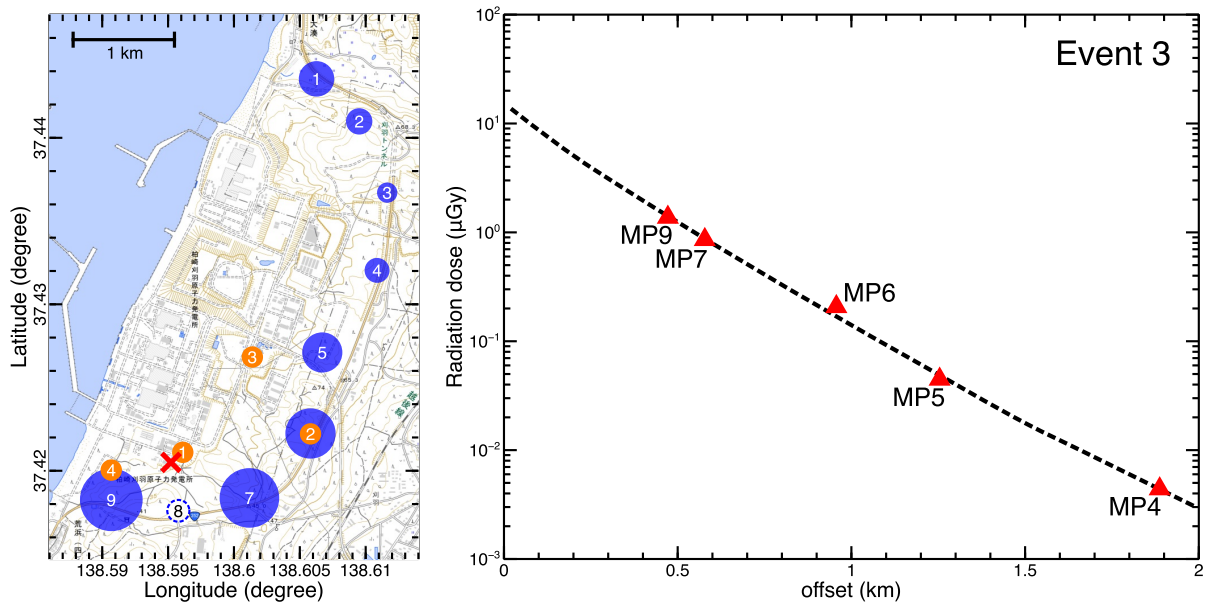
Figure 7.6: The fitting result of Event 3 with observations of high-level dosimeters, presented in the same manner as Figure 7.3.

116
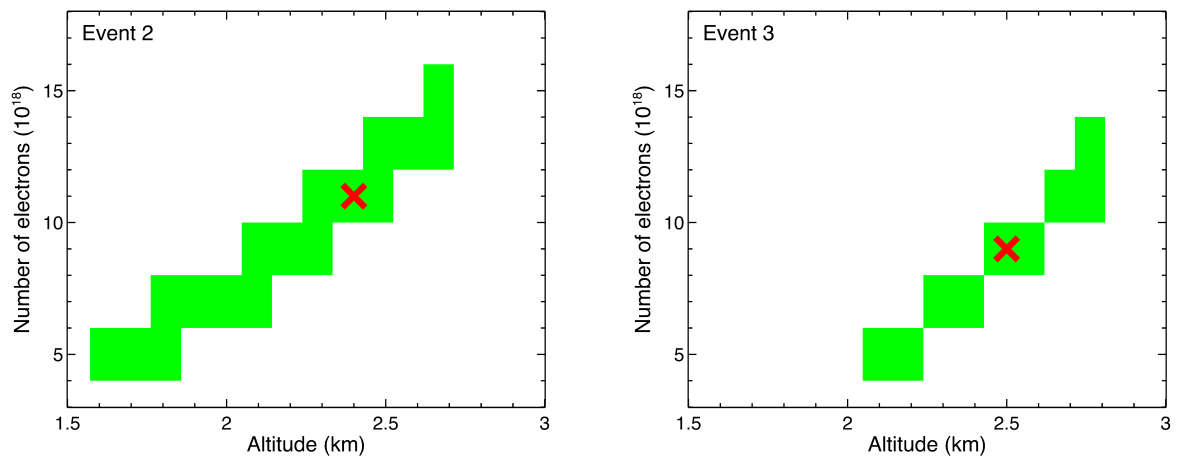
Figure 7.7: Error regions of Events 2 (left) and 3 (right) in the phase space of the source altitude and the electron number. The green-colored areas and red cross markers present 1σ confidence level region and the best-fit solutions, respectively.

Chapter 8

Discussions

8.1 Properties of Downward TGFs

In Chapters 5, 6, and 7, downward TGFs of Events 1–3 were quantitatively evaluated via positron and neutron signals, and doses of downward TGFs, respectively. The present section compares these results with each other. The results in Chapters 5–7 are summarized in Table 8.1.

Table 8.1: Summary of TGF properties.

	positrons		neutrons		TGF doses	
	altitude	num. electrons	altitude	num. electrons	altitude	num. electrons
Event 1	N/A	N/A	N/A	N/A	1.4–2.7 km	$(27\text{--}46) \times 10^{18}$
Event 2	h	$6.5 \times 10^{17} \exp(h/0.5\text{km})$	1.4–1.9 km	$(12\text{--}25) \times 10^{18}$	1.6–2.7 km	$(5\text{--}14) \times 10^{18}$
Event 3	N/A	N/A	<1.5 km	$< 2.7 \times 10^{18}$	2.1–2.8 km	$(7\text{--}13) \times 10^{18}$
			1.9–2.2 km	$(5.6\text{--}10.2) \times 10^{18}$		

8.1.1 Event 1

The downward TGF of Event 1 was evaluated only with the doses measured by high-level dosimeters. The TGF was estimated to have taken place at a 1.4–2.7 km altitude, with (27–46) $\times 10^{18}$ avalanche electrons (Section 7.3). For consistency, this result is compared with spectra of neutron origin obtained by BGO scintillators (the method employed in Section 6.3). The distance between the estimated TGF position and Detector 3, the nearest one from the position, is 0.97 ± 0.08 km. The energy spectrum obtained by Detector 3 is fitted, and the possible range of electron number is surveyed with the estimated altitude and detector offset of 1.4–2.7 km and 0.88–1.06 km, respectively. As a result, (1.4–23) $\times 10^{18}$ electrons are needed to explain the gamma-ray spectrum. This result is in the same order of magnitude as that with the dose analysis, and hence we conclude that avalanche electrons of the order of 10^{19} were produced at the TGF of Event 1.

8.1.2 Event 2

For Event 2, three observational data of positron (Subsection 5.2.4), neutron (Subsection 6.3.2), and TGF doses (Section 7.3) are utilized to estimate TGF parameters. The TGF position was

119

estimated by combining wind speed and the time profile analysis of annihilation signals, and by fitting TGF doses independently. As shown in Figure 8.1 left, the estimated positions by the two method match within 0.5 km.

The right panel of Figure 8.1 presents the estimation results of TGF altitude and the number of initial electrons. The relation derived from positron signals (the red region) crosses the error region derived from de-excitation gamma-ray spectra (the blue region) at a 1.5-km altitude, and the electron number of $\sim 1.5 \times 10^{19}$. On the other hand, the error region derived by radiation doses (the green region) shows the electron number of 5×10^{18} at a 1.6 km altitude, 3 times smaller than the estimations from positron and neutron signals. The differences between the two estimation method should be considered as systematic uncertainties. The analysis with positron and neutron signals shares the TGF position estimated by the count-rate history of annihilation signals and ambient wind speed, and both estimations of TGF parameters are consistent with each other. In contrast, the analysis of TGF doses independently derived the TGF positron. The slight gap between the two estimated positions by different approaches might cause systematic uncertainties in altitude and electron-number estimation, which are discussed in Section 8.2. Since the TGF position with the positron signal is a model-independent result, this is more reliable than that by the model-dependent dose analysis. Assuming the parameters obtained by analysis of neutron and positron signals, we conclude that 1.5×10^{19} avalanche electrons were produced at a 1.5-km altitude in Event 2.
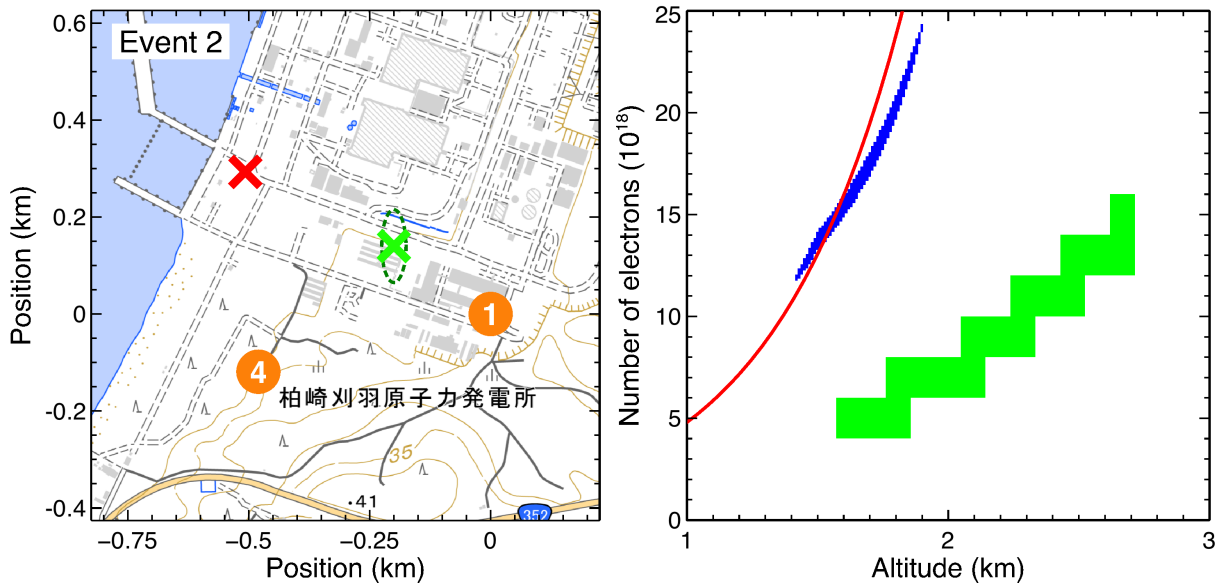
Figure 8.1: Comparison of TGF parameters for Event 2. Left: positions of the TGF estimated from radiation doses (position and its error displayed by the green cross and the green circle respectively) and from positron signals (the red cross). The positions of Detectors 1 and 4 are presented by the orange circles. The coordinate origin is at Detector 1. Right: Constraints in the phase space of source altitude and the number of electrons by positron (the red line), neutron (the blue region), and dose (the green region) measurements.

8.1.3 Event 3

The downward TGF of Event 3 was evaluated with the observation data of neutron origin (Subsection 6.3.2) and TGF doses (Section 7.3). The left panel of Figure 8.2 presents the TGF po-

sitions estimated with two data sets. The two estimations agree with each other within 200 m. The right panel of Figure 8.2 compares the estimation of altitude and electron numbers. The error region derived with neutron observation (the blue region) is divided into two regions. The region indicating lower altitude is inconsistent with that by TGF doses (the green region). On the other hand, the other region, indicating higher altitude, agrees with the green region within a 300-m altitude gap. The gap of the TGF position estimated by the two methods are smaller than that in Event 2, and hence the differences in estimations of altitude and electron numbers could be also smaller.
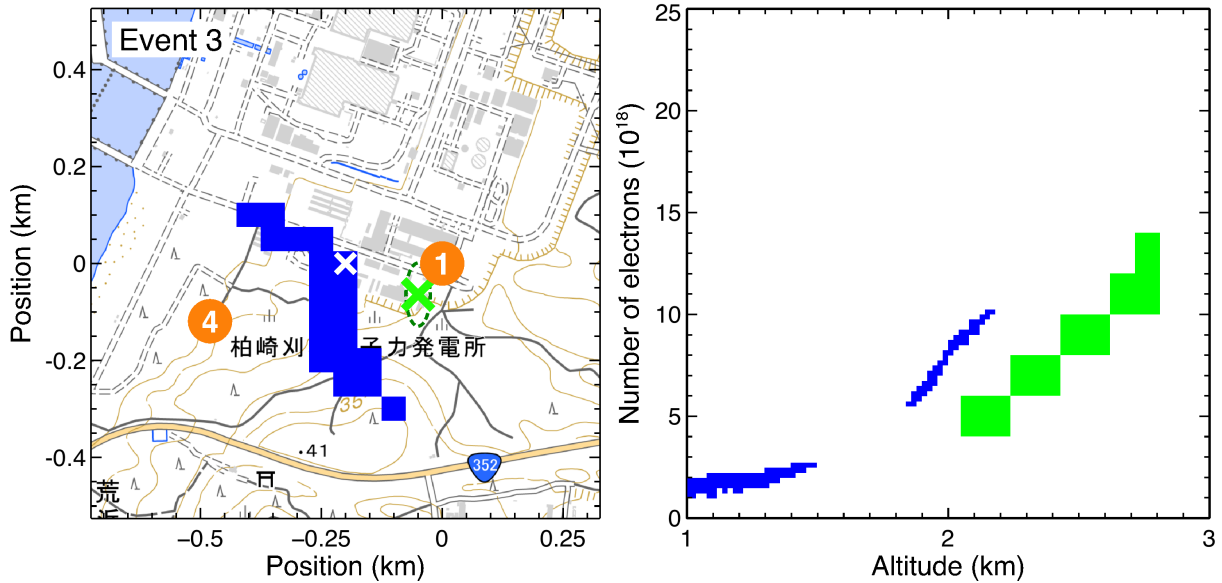
Figure 8.2: Comparison of TGF parameters for Event 3. Left: positions of the TGF estimated with radiation doses (the green cross and the green circle) and with neutron signals (the blue region with the white cross marker), displayed in the same way as Figure 8.1. Right: Constraints in the space of altitude and number of electrons by neutron (the blue region) and dose (the green region) measurements.

8.1.4   Summary of analysis

Among Events 1–3, which are intensively analyzed in the present thesis, TGF positions of Events 2 and 3 are estimated by two independent methods, with systematic uncertainties smaller than 500 m. This is the first result to estimate the source position of downward TGFs combining observations of TGF doses and products of photonuclear reactions.

The altitude of three events are estimated as 1.4–2.8 km. As shown in Figure 3.2, winter thunderclouds develop at lower altitude than summer thunderclouds, with a typical cloud base of <1 km and cloud top of 5–7 km. Therefore, each event is consistent to have occurred in lower to middle layers of typical winter thunderclouds. The number of initial electrons in 1.0–50.0 MeV is estimated to be 10^{18} and 10^{19}.

8.2 Origin of Possible Systematic Uncertainties

This section discusses systematic uncertainties that potentially affect the obtained results. There are two candidates which are not considered in the analysis and discussions. One is photonuclear reactions with nuclei in ground and detector materials. In Chapters 5 and 6, photonuclear reactions with atmospheric nuclei (^{14}N, ^{15}N, ^{16}O, ^{17}O, ^{18}O, and ^{40}Ar) are considered. As shown in Chapter 4.2.2, however, the decaying signals of annihilation gamma rays are thought to originate from photonuclear reactions with nuclei in the ground and detectors such as ^{40}Ca, ^{28}Si, ^{27}Al, and ^{12}C. These reactions also emit photoneutrons, and hence the present analysis might underestimate the total number of photoneutrons or overestimate the number of photoneutrons by atmospheric photonuclear reactions. Since TGF photons are attenuated in the atmosphere, the number of photoneutrons produced in the ground or in detectors should be less than that in the atmosphere. However, photoneutrons generated around the ground might affect the measurements because the reactions take place close to detectors. Therefore, considering such photonuclear reactions might lead better estimations of TGF parameters. At present, it is difficult to quantitatively evaluate this effect because one of the major photonuclear channels with nuclei in the ground and detectors ^{27}Al$(\gamma, n)^{26\mathrm{m}}$Al, which produces an isomer nuclide, is not included in databases of photonuclear reactions.

The other is the condition of initial electrons. The Monte-Carlo simulations in Chapters 5 and 7 employed a downward and narrow electron beam without opening angle as an initial electron source. However, this simple model might not be sufficient depending on the proposed models for TGF production. There are two major candidates under discussion: the relativistic feedback model and the thermal electron runaway model (see Subsections 2.5.2 and 2.5.3). The former considers positrons flowing upstream in a large electric-field structure and producing energetic seed electrons. Therefore, the model favors an extended electron source rather than a narrow or pencil beam. On the other hand, the latter model considers electrons gaining relativistic energies in streamers at the tip of lightning leaders, and accelerated to MeV energies by ambient electric fields. In this case, the electron beam should be narrow, and could be tilted depending on the direction of streamers and electric fields. In addition, structure of electric fields can cause an electron beam with non-negligible opening angle. In short, the electron beam can be geometrically large, tilted in angle, and/or diffusive in opening angle.

Figure 8.3 shows a simulation result of how on-ground distributions of gamma rays are affected by various beam conditions. Four cases, a narrow beam utilized in Chapters 5 and 7, an extended beam with a radius of 100 m, a 30°-tilted narrow beam, and a point-like beam with a half angle of 30° are presented. Each electron beam was injected at a 2.0-km altitude. The extended beam with a 100 m radius is not clearly different from the narrow beam. However, the tilted beam shows a significant movement of the flux peak position, and the beam with opening angle significantly extends the gamma-ray distribution. Therefore, initial conditions of electron beams affect gamma-ray distributions at the ground.

For the analysis in the present thesis, the TGF dose analyses in Chapter 7 are thought to be affected by the difference in geometrical beam conditions. On the other hand, the analyses in Chapters 5 and 6 are less affected. As presented by the simulations of photonuclear reactions in Chapters 5 and 6 (Figure 5.4), most part of photoneutrons and β^+-decay nuclei are produced near the region where the initial electrons are injected. Photoneutrons also lose their directivity by multiple elastic scatterings and are diffused isotropically. Therefore, photoneutrons and β^+-decay nuclei are less subject to the initial condition of electrons. These differences between TGF photons and products of photonuclear reactions might cause systematic uncertainties such as the gap of estimated TGF positions in Event 2.

Figure 8.4 shows distributions of TGF fluences along x-axis extracted from Figure 8.3. The on-ground distribution of gamma rays produced by an electron beam with opening angle is more diffused than that by a narrow electron beam, shown in the left panel. In general, an electron beam at a lower altitude produces a narrower on-ground distribution, and a beam at a higher altitude produces a wider distribution, as shown in the right panel. Therefore, the electron beam with opening angle requires a lower altitude to reproduce a similar on-ground distribution to the narrow beam. Also, an electron beams at a lower altitude requires less initial electrons to reproduce similar on-ground fluxes. Combining these two factors, the electron beam with opening angle requires a lower altitude and a smaller number of initial electrons than the narrow electron beam. However, this beam model cannot explain the difference between the estimations in Event 2 because the model expands the difference.

In the case of the tilted electron beam, the offset of the TGF position from the position where the gamma-ray flux becomes maximum could be several hundreds of meters to ~ 1 km, depending on the tilt angle. For example, the beam with opening angle of $30°$ at a 2 km altitude make the offset of 2 km $\times \tan 30° = 1.15$ km. Therefore, the TGF position estimated with the
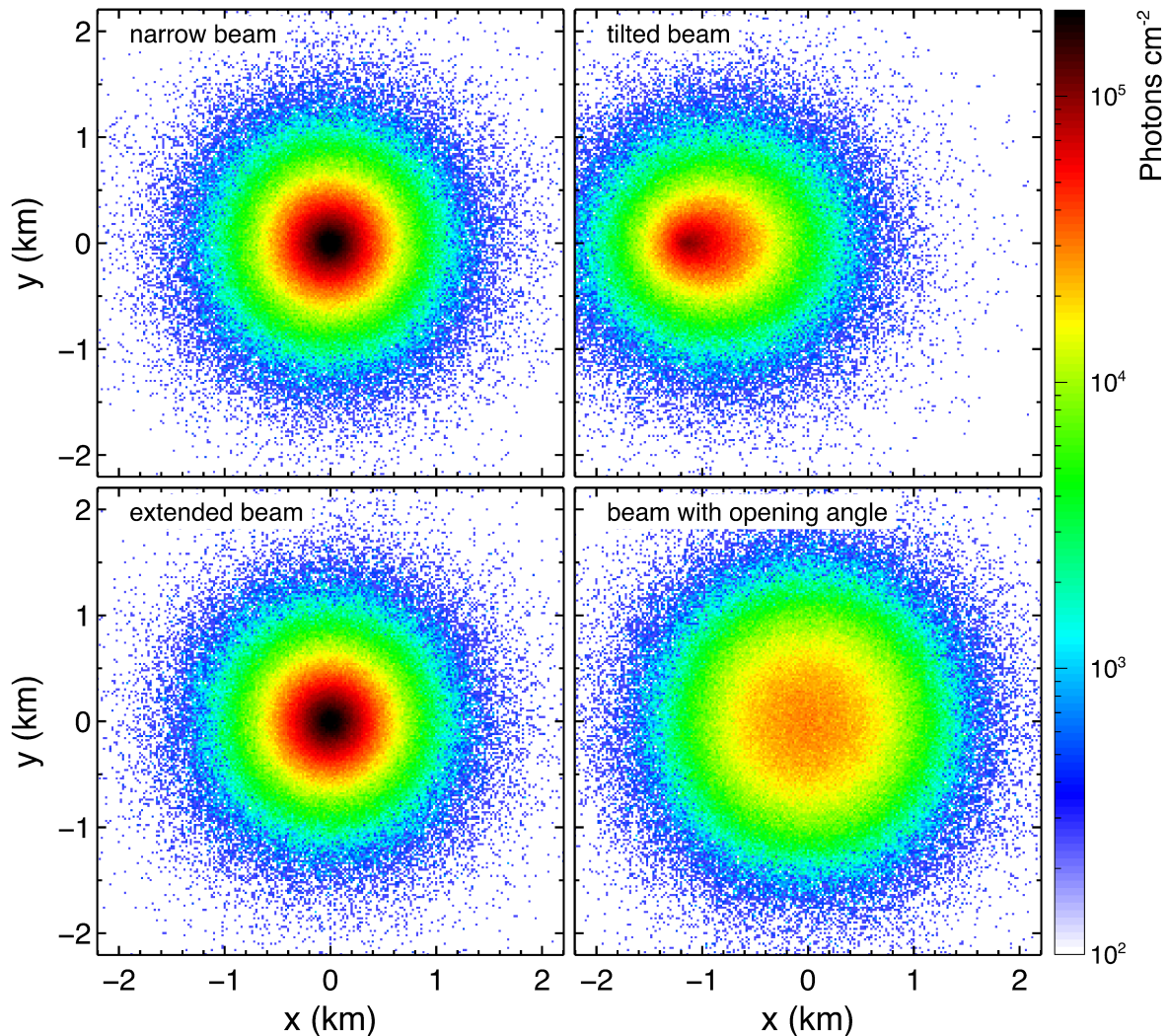
Figure 8.3: On-ground gamma-ray distribution models above 1 MeV with various electron-beam conditions. Initial electrons are injected at a 2.0-km altitude. The distributions are normalized to 10^{18} initial electrons (1–50 MeV).
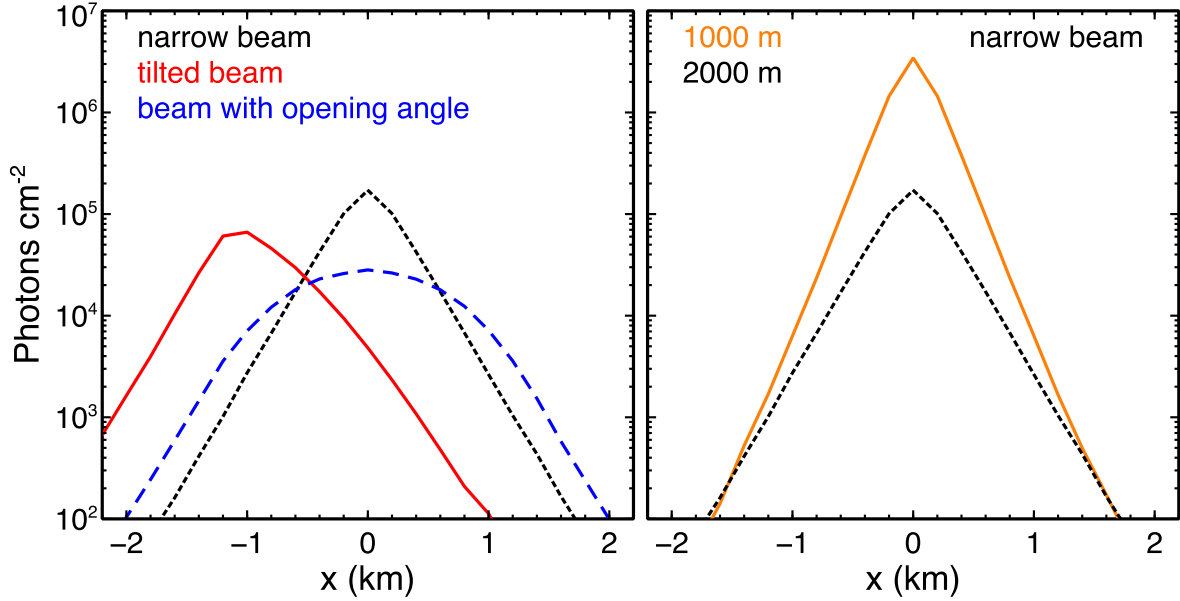
Figure 8.4: On-ground gamma-ray distribution models along x-axis of Figure 8.3. Left: comparison between narrow, tilted beams and a beam with opening angle at a 2000-m altitude. Right: comparison between narrow beams at different altitudes. The distributions are normalized to 10^{18} initial electrons.

tilted beam could be different from that with the narrow beam. For Event 2, the offset between the two estimated positions is 0.34 km. Assuming the source altitude at 1.5 km, estimated from the neutron and positron signals (Subsection 8.1.2), the tilt angle would be 13°. Since the offsets of monitoring posts are changed in this case, the number of initial electrons could be also changed. Among the four beam models, the tilt-beam model is a better candidate to explain the differences between estimations by neutron/positron signals and by dose measurements, while further modeling is required.

8.3 Comparison with Previous Upward and Downward TGFs

Most of detected TGFs are upward ones going from thunderstorms into space, and observed by in-orbit gamma-ray satellites. Upward TGFs observed from space typically take place at an altitude of 11–21 km [Cummer et al., 2014, Dwyer and Smith, 2005]. While this estimation is higher than the results in the present thesis (1.4–2.8 km), the difference is thought to originate from the difference between summer and winter thunderstorms. Dwyer and Smith [2005] estimated the TGF altitude with an accumulated TGF spectrum recorded by RHESSI [Smith et al., 2005], which did not include winter periods.[20] Also Cummer et al. [2014] analyzed TGFs took place during summer. Both estimations are based on TGFs during summer thunderstorms. The cloud top of a summer thundercloud can be higher than 10 km while 5–7 km for winter thunderclouds, as shown in Figure 3.2. Therefore, upward TGFs in summer thunderclouds and downward TGFs in winter thunderclouds can take place at different altitudes.

In addition, observation biases should be considered. Upward TGFs at a lower altitude are attenuated by the atmosphere, and hence cannot reach the satellite altitude. For example,

---

[20]Among successive gamma-ray astronomy satellites, only RHESSI was passing over Japan. CGRO, AGILE, and Fermi did not due to small inclination angle.

the column density of the atmosphere from a 11.6-km altitude (an example of upward TGF altitudes) to the satellite altitude is 2.3×10^2 g cm^{-2}. If an upward TGF takes place at a 5.0-km altitude, the column density is 5.7×10^2 g cm^{-2}. Considering an attenuation coefficient of 1-MeV photons in the atmosphere from NIST/XCOM, 6.4×10^{-2} cm^2 g^{-1}, TGFs at the 5.0-km altitude are $\sim 4 \times 10^{-10}$ times attenuated than at the 11.6 km altitude. Given that space-borne detectors only record tens of photons for individual TGFs at a 10-km altitude of higher, TGFs at the 5.0-km altitude are thought not to be detected by them. Likewise, downward TGFs at a higher altitude should be more attenuated than those at low altitudes, and fainter or not detected at ground level. Downward TGFs at the 5-km altitude, with the column density of 4.8×10^2 g cm^{-2}, are $\sim 4 \times 10^{-5}$ times attenuated than those at the 3-km altitude, with the column density of 3.2×10^2 g cm^{-2}.

Dwyer and Smith [2005] estimated the averaged number of initial electrons above 1 MeV as 1×10^{16}–2×10^{17} with the accumulated spectrum recorded by RHESSI. Mailyan et al. [2019] also analyzed individual spectra of TGFs recorded by Fermi, and estimated the number of avalanche electrons ranging between 6×10^{15} and 9×10^{18}. Figure 8.5 compares these previous estimations with the present results. The present thesis derives the number of avalanche electrons as 10^{18}–10^{19} by analyzing three downward TGFs. The present result is consistent with the estimation by Mailyan et al. [2019]. Therefore, the downward TGFs presented in this thesis is as powerful as upward TGFs observed from space. The present downward TGFs are suggested to be intrinsically the same as upward TGFs, despite the differences in summer and winter thunderstorms, altitude, and direction.
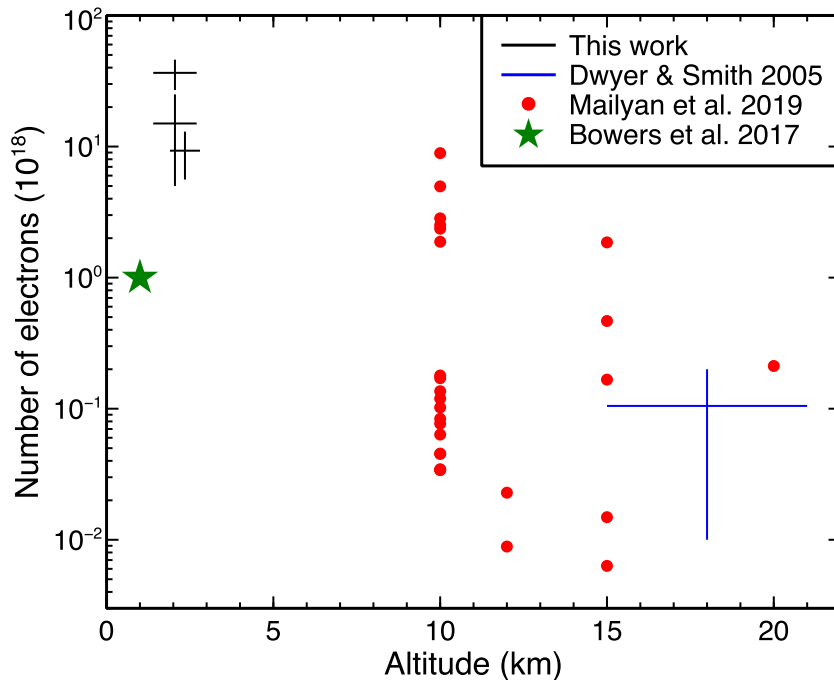
Figure 8.5: Comparison of upward and downward TGFs in the phase space of source altitude and electron number. Points from Dwyer and Smith [2005] and Mailyan et al. [2019] are results for upward TGFs, and Bowers et al. [2017] and this work for downward TGFs in winter thunderstorms. Mailyan et al. [2019] derived the source altitudes with four calculation points of 10, 12, 15, and 20 km.

Even upward TGFs are expected to trigger atmospheric photonuclear reactions because

their spectra extend up to >10 MeV [Babich, 2006, 2007, Carlson et al., 2010, Tavani et al., 2011]. However, it is difficult to detect neutrons by space-borne detectors because the number of photoneutrons are 10^{-5} fewer than initial avalanche electrons (see Subsection 5.2.2), and the number of TGF photons detected are typically a few dozens for a single TGF. Then, are photoneutrons produced by upward TGFs observable at ground level? As shown in Figure 5.4, neutrons and β^+-decay nuclei are hardly produced above the altitude of electron injection, and therefore photonuclear reactions from upward TGFs are also undetectable from the ground, at least for summer thunderclouds at a high altitude. If upward TGFs occur at lower altitude in such as winter thunderstorms, neutrons might be detectable at ground level. In those cases, bremsstrahlung of positrons accelerating downward could be detected [Bowers et al., 2018].

In addition to satellite observations, TGFs have been observed by on-ground apparatus [Abbasi et al., 2018, 2017, Bowers et al., 2017, Colalillo, 2017, Dwyer et al., 2004, 2012a, Hare et al., 2016, Pleshinger et al., 2019, Ringuette et al., 2013, Smith et al., 2018, Tran et al., 2015]. Except Bowers et al. [2017] and Smith et al. [2018], the observations were performed during summer thunderstorms. Abbasi et al. [2018] observed downward TGFs by the cosmic-ray observatory Telescope Array, and estimated the number of total gamma rays above 0.1 MeV as 10^{12}–10^{14}. Our Monte-Carlo simulation derives a relation that 10^{12}–10^{14} gamma rays of RREA origin are produced by 3×10^{13}–3×10^{15} avalanche electrons above 1 MeV. Therefore, Telescope Array's result can be interpreted as the initial electron number of 3×10^{13}–3×10^{15}, but this is still 10^{-5}–10^{-4} times smaller than the present result.

Dwyer et al. [2012a] concluded that $\sim 10^9$ avalanche electrons for downward acceleration or $\sim 10^{11}$ for upward acceleration at an 400-m altitude are required to explain the ground-level detection of a TGF in 2014. This case also requires much smaller number of avalanche electrons than the present result. The on-ground TGF observation TETRA-I/II (TGF and Energetic Thunderstorm Rooftop Array) reported 46 downward TGFs in total [Pleshinger et al., 2019, Ringuette et al., 2013]. Gamma-ray counts of TETRA-II BGO ($25.4 \times 2.5 \times 2.5$ cm^3) range from 19 to 203. As discussed in Section 7.1, the present downward TGFs was estimated to have had on-ground fluences of 10^3–10^5 photons cm^{-2}. Therefore, on-ground fluences of the TETRA-II cases are also much smaller than the present cases. Also, none of them reported photonuclear reaction.

Besides the present events, only one downward TGF during winter thunderstorms was reported by Bowers et al. [2017] (Smith et al. [2018] also analyzed the same event). In the case of Bowers et al. [2017], their scintillation detector was heavily saturated by a downward TGF, like the present observations. By assuming photoneutron productions by the downward TGF, they concluded that 10^{17} gamma rays were emitted. This number corresponds to 10^{18} avalanche electrons above 1 MeV. Therefore, the same order of avalanche electrons as the present cases were produced in their event.

Based on the discussions above, downward TGFs during winter thunderstorms apparently have larger number of avalanche electrons and on-ground fluences than those during summer thunderstorms reported so far. This might be caused by observational biases. Since downward TGFs in winter have beed identified by their photonuclear reactions so far, TGFs which are too faint to produce observable number of photoneutrons have never been reported. In fact, Østgaard et al. [2012] speculated that there are potentially faint-class TGFs with 10^{12} avalanche electrons which have never detected by satellites due to detector sensitivities. This observational bias might make the differences between summer and winter. On the other hand, no TGF or TGF-related photonuclear reactions were detected at Mt. Aragats, where TGEs (similar to gamma-ray glows) have been frequently observed [Chilingarian et al., 2019]. Therefore, it is still possible that characteristics of thunderstorms itself, such as seasonal conditions or ground

altitude, make intrinsic differences of occurrence, brightness, and production mechanisms of downward TGFs. Whether faint downward TGFs are discovered during winter or bright ones during summer is the key to solve this issue.

As the downward TGFs we observed are now found to be intrinsically same as upward ones observed from space, they are also a clue to reveal a mechanism of electron acceleration and multiplication in lightning. From space, two spacecraft AGILE and Fermi are in operation as TGF detectors. In 2018, ASIM (Atmosphere-Space Interactions Monitor: Neubert et al. [2019]) was launched, attached to the International Space Station, and joined the detection network. In addition, the French satellite mission Taranis (Tool for the Analysis of RAdiation from lightNIng and Sprites: Lefeuvre et al. [2008]) will be launched in 2020. Then, some of TGFs are expected to be detected by three satellites.[21] Even in such a golden age of TGF studies, downward TGFs in winter thunderstorms are fascinating because they are bright enough for spectroscopies, and can be observed by multiple on-ground detectors. Although an accurate measurement of such high fluxes is challenging, they should be excellent targets to study electron acceleration in the dense atmosphere.

8.4   Suggestions for Future Observations

This section discusses future observations of downward TGFs and photonuclear reactions in lightning, based on the results obtained in the present thesis. The scintillation detectors utilized in the present work were originally developed for gamma-ray glow observations. While de-excitation gamma rays were normally recorded, TGFs completely saturated them. Therefore, detectors more sharply aimed at downward TGF observations should be developed. Here three new approaches are proposed: spectroscopies of de-excitation gamma rays with high energy-resolution scintillators, spectroscopies of downward TGFs with fast scintillators, and three-dimensional observations of lightning discharges in the radio-frequency band.

The first one is spectroscopies of de-excitation gamma rays. The GROWTH experiment mainly employs BGO scintillators, whose stopping power is relatively large among typical inorganic scintillators. However, BGO has poor light yields, thus poor energy resolution. The energy resolution of BGO scintillators used in the present work is 18% (FWHM) at 662 keV, significantly lower resolution than NaI scintillators (typically better than 10%). The poor resolution made de-excitation gamma-ray lines detected as a continuum-like spectrum (Figure 4.5).

An ideal apparatus with high energy resolution is absolutely high-purity germanium detectors. However, germanium detectors are expensive, needs continuous cooling, and hence they are not suitable for long-duration stand-alone operations required in this field. Employing scintillators with high energy-resolution such as $LaBr_3$ and $CeBr_3$ is a realistic solution. These crystals are utilized at normal temperature, and their energy resolutions are 2.6%[22] and 4.0%[23] at 0.662 MeV for $LaBr_3$ and $CeBr_3$, respectively. Therefore, main lines of de-excitation gamma rays are expected to be resolved by them. The simulation results suggest that TGF parameters such as altitude and detector offsets make differences in line intensities (Figure 6.8), and hence spectroscopies of de-excitation gamma rays could be an important tool.

The second approach is developing dedicated high-speed detectors for TGF observations. As discussed in Section 7.1, on-ground fluences of downward TGFs reach 10^3–10^5 photons cm^{-2}. Assuming a TGF duration of $100 \, \mu$s, gamma-ray fluxes become 10^7–10^9 photons cm^{-2} s^{-1}. The

---

[21]AGILE and Fermi circle at the same altitude with the same period. Therefore, they do not reach each other and cannot detect identical TGFs.

[22]https://www.crystals.saint-gobain.com/products/standard-and-enhanced-lanthanum-bromide

[23]https://www.sii.co.jp/jp/segg/files/2019/07/CeBr_CatalogV1.3.pdf

maximum count rates of scintillation detectors are determined by the decay constant of scintillation light, shaping time constant of analog processors, and readout buffers of data acquisition system. The decay constant of plastic scintillators is 2 ns, the fastest among normal scintillators. If an analog amplifier processes the light output from scintillators into a 10-ns pulse, the maximum count rate reaches 10^8 counts s^{-1}. Considering a 1 cm^3 cubic plastic scintillator, whose detection efficiency is 7% at 1 MeV, the countable flux is as high as 10^9 photons cm^{-2} s^{-1}. Therefore, detectors with a small plastic scintillator is suitable for fast photon counting of TGFs. It is noted that, however, plastic scintillators are not suitable for spectroscopies because the main interaction is Compton scatterings. For spectroscopy purpose , inorganic scintillators with short decay constants such as $LaBr_3$ (26 ns), $CeBr_3$ (17 ns), and GSO (56 ns) should be employed.

The third one is lightning observations in the radio-frequency band. Recent progress of radio-frequency observations allows us to three-dimensionally locate VHF pulses by interferometry and/or the time-of-arrival method [Krehbiel et al., 2000, Mardiana et al., 2002, Morimoto et al., 2004, 2016, Rison et al., 1999]. VHF pulses are emitted not only at the moment of return strokes, but also at all stages in lightning such as leader progressions. Also the VHF band has a temporal resolution of 100 ns, and hence the accuracy of pulse locating is tens of meters in principle. Comparing the timing of TGF photons with VHF pulses can lead to independently estimate TGF positions, and examine in which stage of lightning TGFs are initiated. While simultaneous observations of TGFs in gamma rays and the VHF band have been performed [Hare et al., 2016, Lu et al., 2010, Mailyan et al., 2018], they have never been performed in winter thunderstorms. In particular, on-ground observations of gamma rays and VHF are promising because the absolute timing accuracy provided by GPS signals are better than satellite observations.

8.5 Radiation Exposures to Downward TGFs

In Section 7.2, on-ground radiation doses by downward TGFs were calculated. Assuming a downward TGF takes place with 10^{19} electrons at 2.0 km, similar to those analyzed in the present thesis, an on-ground dose is 60 μGy right under the TGF, and 0.3 μGy at 1 km offset. It corresponds to 5 times as high as a dose of a chest X-ray (20 μSv: e.g. Gargani and Picano [2015]) when approximating as 1 Sv=1 Gy. If a TGF with the same magnitude occurs at lower altitude, at 1.0-km for example, the radiation doses are expected to be 1 mGy right under the TGF, and 0.5 μGy at 1 km offset. Even in this case, doses by a single downward TGF are negligible, given that the threshold of deterministic effects of radiation hazards is at 0.1 Gy, and doses of computerized tomography and an international flight between Japan and the east coast in the US are 10 mGy and 0.1 mGy,[24] respectively

On the other hand, it could be better to avoid flying nearby and inside thunderstorms. Dwyer et al. [2010] estimated that radiation doses of passengers might reach 0.1 Gy when a TGF takes place nearby an aircraft. Since winter thunderstorms develop at lower altitude, aircrafts flying at a cruise altitude (typically 10 km) are hardly affected by TGFs from winter thunderstorms. However, aircrafts sometimes have to enter winter thunderclouds inevitably during take off and landing. In fact, Komatsu Air Base of Japan Air Self-Defense Force, in Ishikawa Prefecture, continues thunderstorm observations for lightning protection [Michimoto, 1993]. The possibility of radiation exposures to downward TGFs is a matter that should be seriously considered in the future.

---

[24]https://www.nirs.qst.go.jp/data/pdf/hayamizu/j/20180516.pdf

8.6 Isotope Production by Photonuclear Reactions

Besides neutrons and β^+-decay nuclei, photonuclear reactions produce various isotopes. This section estimates the number of rare isotope production in the atmosphere. In Section 5.1, major reactions in the atmosphere are considered, as listed below.

$$^{14}\text{N} + \gamma \rightarrow {}^{13}\text{N} + n$$
$$^{14}\text{N} + \gamma \rightarrow {}^{12}\text{C} + n + p$$
$$^{15}\text{N} + \gamma \rightarrow {}^{14}\text{N} + n$$
$$^{16}\text{O} + \gamma \rightarrow {}^{15}\text{O} + n$$
$$^{16}\text{O} + \gamma \rightarrow {}^{14}\text{N} + n + p$$
$$^{40}\text{Ar} + \gamma \rightarrow {}^{39}\text{Ar} + n$$
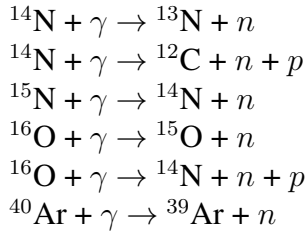
Among them, ^{13}N and ^{15}O exhibit β^+-decay and transform into ^{13}C and ^{15}N with half-lives of 10 and 2 minutes, respectively. While ^{39}Ar decays into ^{39}K, it is a long-lived isotope with a half life of 270 years. In addition, photoneutrons are captured by ^{14}N and experience neutron captures or charged-particle productions:

$$^{14}\text{N} + n \rightarrow {}^{14}\text{C} + p$$
$$^{14}\text{N} + n \rightarrow {}^{15}\text{N} + \gamma$$
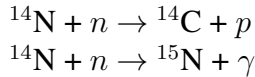
where either of ^{14}C or ^{15}N is produced. In summary, major products of atmospheric photonuclear reactions are stable isotopes of ^{12}C, ^{13}C, ^{14}N, ^{15}N, and long-lived isotopes of ^{14}C and ^{39}Ar. The present thesis focuses on ^{13}C, ^{14}C, and ^{15}N.

^{13}C is produced via β^+-decays of ^{13}N, which is a product of $^{14}\text{N}(\gamma,n)^{13}\text{N}$. Almost 100% of ^{13}N exhibit β^+-decay into ^{13}C. The numbers of ^{13}N, ^{15}O, and neutrons produced by photonuclear reactions are summarized in Table 5.3. When 10^{18} initial electrons are injected at an altitude of >1.5 km, 4×10^{12} nuclei of ^{13}N, and then 4×10^{12} of ^{13}C are produced. ^{15}N is produced via two channels: β^+ decays of ^{15}O produced via $^{16}\text{O} + \gamma \rightarrow {}^{15}\text{O} + n$, and neutron captures $^{14}\text{N} + n \rightarrow {}^{15}\text{N} + \gamma$. According to Table 5.3, 5×10^{11} nuclei of ^{15}O and 1.1×10^{13} photoneutrons are generated by 10^{18} initial electrons. Since almost 100% of ^{15}O exhibit β^+ decay, the former channel produces 5×10^{12} nuclei of ^{15}N. In the latter case, 96.3% of photoneutrons exhibit charged-particle productions, and the rest experiences neutron captures. The number of ^{15}N produced via neutron captures is thus 4×10^{11}. Therefore, in total 9×10^{11} nuclei of ^{15}O are produced by 10^{18} initial electrons. ^{14}C is produced by charged-particle productions $^{14}\text{N} + n \rightarrow {}^{14}\text{C} + p$. Since 96.3% of photoneutrons generate ^{14}C, the number of ^{14}C generated by 10^{18} initial electrons is 1×10^{13}. The numbers of produced isotopes are listed in Table 8.2.

Table 8.2: The number of produced isotopes by photonuclear reactions.

products	reaction	number with 10^{18} initial electrons
^{13}N	$^{14}\text{N} + \gamma \rightarrow {}^{13}\text{N} + n$	4×10^{12}
^{13}C	$^{13}\text{N} \rightarrow {}^{13}\text{C} + e^+ + \nu_e$	4×10^{12}
^{15}O	$^{16}\text{O} + \gamma \rightarrow {}^{15}\text{O} + n$	5×10^{11}
^{15}N	$^{15}\text{O} \rightarrow {}^{15}\text{N} + e^+ + \nu_e$	5×10^{11}
	$^{14}\text{N} + n \rightarrow {}^{15}\text{N} + \gamma$	4×10^{11}
	total	9×10^{11}
^{14}C	$^{14}\text{N} + n \rightarrow {}^{14}\text{C} + p$	1×10^{13}

^{14}C is an important isotope for radiocarbon dating because it decays with an intermediate half life of 5700 years. So far, ^{14}C is thought to be mainly produced via charged-particle productions with neutrons of cosmic-ray origin. However, photonuclear reactions in lightning are predicted to be another channel of ^{14}C production on Earth [Babich, 2017]. The present thesis proves the prediction by demonstrating photonuclear reactions in lightning.

Is the amount of ^{14}C production in lightning comparable to that by cosmic rays? The radiocarbon production rate by cosmic rays is estimated as $1.6 \, \mathrm{cm}^{-2} \, \mathrm{s}^{-1}$ [Poluianov et al., 2016], namely $4.2 \times 10^{18} \, \mathrm{s}^{-1}$ on the globe. Past cosmic-ray environments are known to have varied this value by 1.1% [Miyake et al., 2012]. The global lightning rate is measured as 44 ± 5 per second [Christian, 2003]. Even if all lightning discharges were related to TGFs and triggered photonuclear reactions, 4×10^{14}–4×10^{15} nuclei of ^{14}C would be produced per second. This is less than 0.1% of ^{14}C production rate originating from cosmic rays. Therefore, the contribution of lightning for ^{14}C production is negligible comparing to the global production rate, at least with the current lightning occurrence rate.

Then, do lightning contribute to the local distribution of ^{14}C? Considering a cylinder of a 3-km height and a 2-km, 10^{13}–10^{14} nuclei of ^{14}C are assumed to be produced in this region. Based on Standard Atmosphere [International Organization for Standardization, 1975], the region contains 4×10^{10} kg atmosphere. In the atmosphere, most carbon atoms are in carbon dioxide molecules. Assuming a CO_2 density of 400 ppm, the cylinder contains 2.4×10^7 kg CO_2, namely 3.3×10^{32} carbon atoms. Since the ^{14}C/^{12}C ratio is 1.2×10^{-12} in the atmosphere [Roberts and Southon, 2007], the cylindrical region contains 4×10^{20} nuclei of ^{14}C nuclei of cosmic-ray origin. Therefore, the number of ^{14}C produced by one downward TGF, 10^{13}–10^{14}, is 5 orders of magnitude smaller than those existing in such a local region, and hence photonuclear reactions by downward TGFs are thought not to affect local ratios of ^{14}C/^{12}C.

Chapter 9

Conclusion

Recent radiation observations in the atmosphere have proven the fact that lightning discharges and thunderclouds can behave as natural particle accelerators and produce relativistic electrons. Bremsstrahlung photons from electrons accelerated and multiplied in the atmosphere have been detected by space-borne, airborne, and on-ground experiments. These findings have been establishing a new academic field "high-energy atmospheric physics".

Since such energetic photons can exceed 10 MeV, they are thought to trigger photonuclear reactions with atmospheric nuclei such as $^{14}\text{N} + \gamma \rightarrow {}^{13}\text{N} + n$. In fact, separate detections of positrons from β^+-decay nuclei and neutrons during thunderstorms have been gradually accumulated. However, it is insufficient to prove the occurrence of photonuclear reactions in lightning because no simultaneous detection of neutrons and positrons has ever been reported.

In the present thesis, gamma-ray observations with compact detectors in coastal areas of the Sea of Japan were performed to detect high-energy phenomena during winter thunderstorms. As a result, we succeeded in detecting 5 short bursts coincident with lightning discharges during the observations in two years (FY2016 and 2017), and revealed their features listed below.

1. Count-rate histories of short bursts decay with a time constant of $\sim$50 ms, and their energy spectra exhibit a continuum component steeply cutting off at 10 MeV. These spectral and temporal features originate from de-excitation gamma rays by neutron captures in the atmosphere.

2. The leading part of short bursts shows saturated detector responses, which are interpreted as extremely high-flux gamma-ray showers.

3. Four of the five detected short bursts were followed by annihilation gamma rays lasting for several to tens of seconds. This is clear evidence of positron production.

4. Three short bursts detected in Kashiwazaki-Kariwa Nuclear Power Station coincided with significant increases in radiation doses by as high as 1.7 μGy, recorded by multiple high-level dosimeters of monitoring posts.

Based on these features, we observationally demonstrated, for the first time, that powerful gamma-ray bursts called downward TGFs coincident with lightning discharges triggered atmospheric photonuclear reactions,

$$^{14}\text{N} + \gamma \rightarrow {}^{13}\text{N} + n$$

$$^{16}\text{O} + \gamma \rightarrow {}^{15}\text{O} + n$$
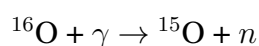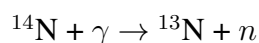
and produced neutrons, ^{13}N, ^{15}O, and even positrons via β^+ decays of ^{13}N and ^{15}O.

Furthermore, we considered all the major photonuclear channels in the atmosphere besides the ^{13}N and ^{15}O production, and performed Monte-Carlo simulations to derive the production amount of photoneutrons and other photonuclear products. We then quantitatively evaluated the detected photonuclear reactions and downward TGFs by comparing the present observations with the simulations, and obtained interpretations listed below.

1. 10^{18}–10^{19} avalanche electrons were produced at a 1.4–2.7-km altitude for each downward TGF. Then, 10^{13}–10^{14} photoneutrons and 10^{12}–10^{13} β^+-decay nuclei (^{13}N and ^{15}O) was generated by photonuclear reactions.

2. The present downward TGFs triggering photonuclear reactions contain a similar number of initial avalanche electrons to upward TGF observed from space. Therefore, they are intrinsically the same phenomena.

3. Downward TGFs in winter thunderstorms are suitable objects to examine mechanisms of electron acceleration and multiplication in TGFs because they provide high gamma-ray fluxes at the ground, and can be observed with multiple on-ground apparatus.

4. Radiation exposures on the present downward TGFs are less than 60 μGy, which is comparable with doses of a medical chest X-ray, but does not affect human beings.

5. Photonuclear reactions produce stable and long-lived isotopes such as ^{13}C, ^{14}C, and ^{15}N. In particular, ^{14}C is an important isotope for archeology. One TGF generate 10^{13}–10^{14} nuclei of ^{14}C, which is negligible for the global production rate of ^{14}C and local ratios of ^{14}C/^{12}C.

This thesis has demonstrated the existence of downward TGFs and atmospheric photonuclear reactions, and performed systematic studies of them with Monte-Carlo simulations. However, the mechanism of electron acceleration and multiplication in the atmosphere, exactly the origin of TGFs, is still an enigma. So far, TGFs have been observed from space. In addition to AGILE and Fermi, ASIM joined the fleet of TGF hunters, and soon Taranis will join in 2020. In contrast, on-ground observations of downward TGFs are also important despite fewer detections than upward TGFs from space. While high gamma-ray fluxes saturate typical scintillation detectors, dedicated high-speed detectors will observe downward TGFs closely, and obtain on-ground distributions of gamma-ray fluxes and spectra with high photon statistics. In addition, radio-frequency observations of lightning discharges will give us great insights into downward TGFs by combining with gamma-ray observations. Merging expertises in TGF observations from space and the ground will symbolize a golden age of high-energy atmospheric physics.

Appendix A

Wind Estimation with XRAIN

Wind velocity at the moment of short-burst events is estimated with precipitation data obtained by eXtended RAdar Information Network (XRAIN). XRAIN is a radar network in the X-band operated by Ministry of Land, Infrastructure, Transport and Tourism of Japan. It covers urban areas in Japan with a spatial resolution of 280 m (east-west) and 230 m (north-south) with a 1-minute interval.

Figure A.1 presents precipitation maps at the moment of Event 2. By overlaying and shifting the precipitation maps, wind velocity is surveyed [Wada et al., 2019c]. Eleven data sets with a 1-minute interval (10-minute duration) are extracted for each events. For the short bursts
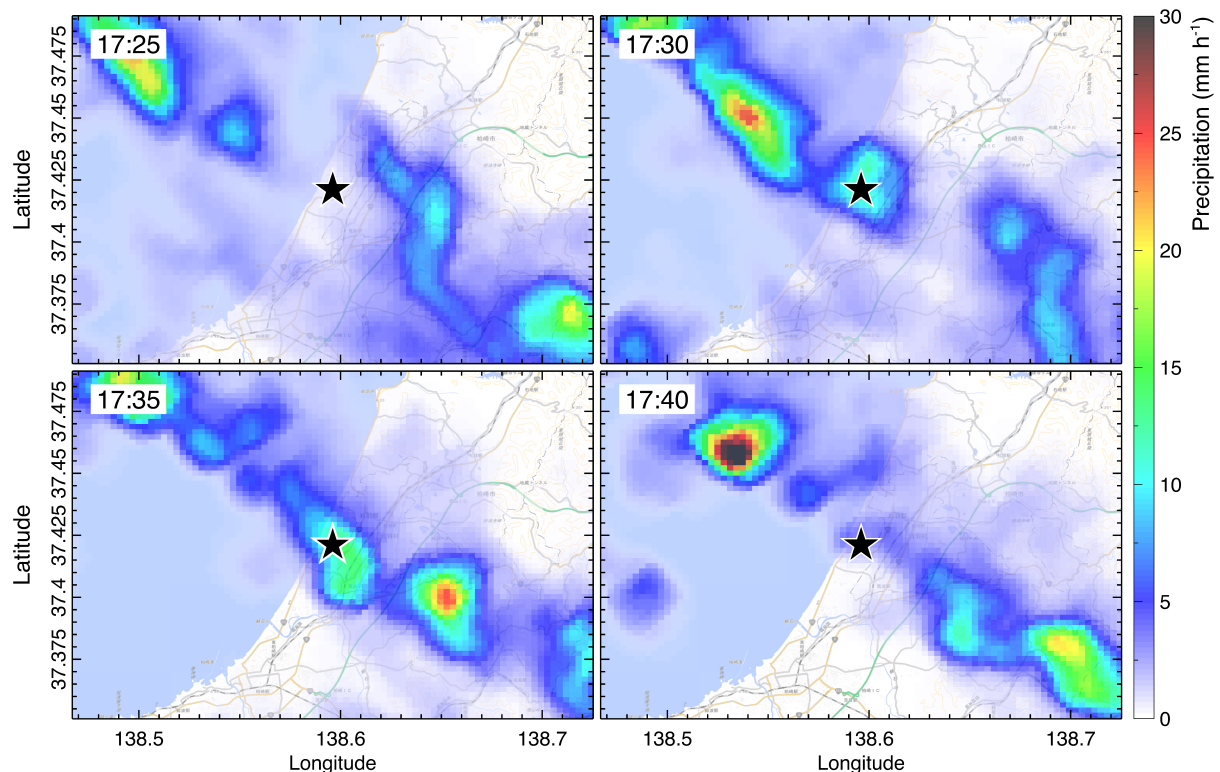
Figure A.1: Contours of precipitation in Event 2 measured by XRAIN. The black-star markers point Kashiwazaki-Kariwa Nuclear Power Station. XRAIN data are retrieved via Data Integration and Analysis System and extracted by the author. The background map is provided by Geospatial Information Authority of Japan.

in Kashiwazaki (Events 1–3), data in the range of 37.3°N–37.5°N and 138.4°E–138.8°E were retrieved. Then we took a pair of maps with a 5-minute interval (6 pairs in total), and calculated the sum of precipitation residual at each mesh, given by $\Sigma_{i,j}(P_{ij}^1 - P_{ij}^2)^2$, where P_{ij}^1 and P_{ij}^2 are precipitation at each mesh on each map, and i and j are mesh indexes. With trial shifting of one map with several steps of the spatial resolution for four directions, we searched for the position which takes the minimum residual sum. The distance and direction for which the cloud moved in 5 minutes can be estimated from the amount of the map shift at the point of the minimum residual sum, shown in Figure A.2.
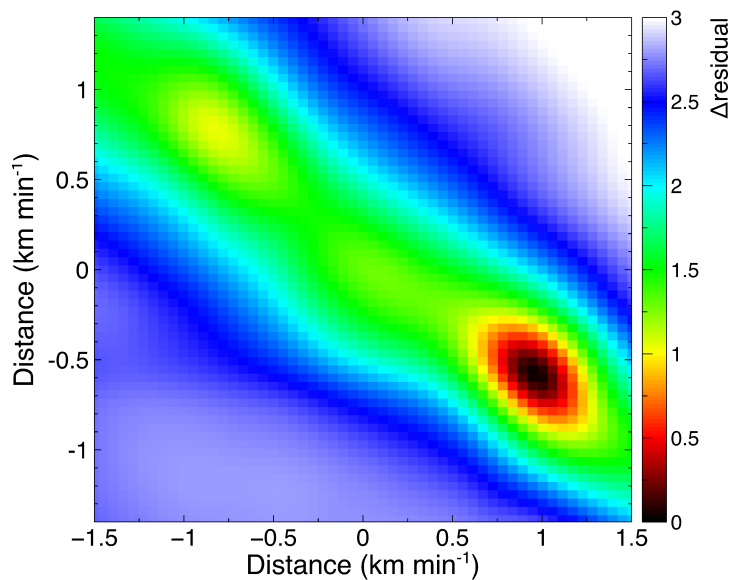
Figure A.2: A contour of Δresidual from the minimum residual for wind estimation of Event 2, calculated with precipitation maps at 17:30 and 17:35.

Appendix B

Short-burst Events in Kanazawa

In the Kanazawa site, two short bursts were detected in FY2017. Event 4 on December 5th, 2017, was registered by only Detector 9, installed at Kanazawa University. Event 5 on January 10th, 2018, was recorded by Detector 7 at Kanazawa Izumigaoka High School and by Detector 8 Kanazawa University High School simultaneously. Count-rate histories of these short-burst events are shown in Figure B.1. Each count-rate variation can be reproduced by an exponential function. The decay constant is 49±7 ms for Detector 9 (Event 4), 52±5 ms and 59±2 ms for Detectors 7 and 8 (Event 5), respectively. These time constants are consistent with that of neutron thermalization in the atmosphere (55 ms). Detector 9 recorded an extremely high count rates just before the short burst, which is a gamma-ray glow.

Energy spectra of both short-burst events are shown in Figure B.2. They consist of a continuum component extending up to 10 MeV, and photons above 10 MeV were barely detected due to a steep cutoff at 10 MeV. These features are similar to the short bursts observed in Kashiwazaki.

Figure B.3 presents scatter plots of photon pulse heights and analog baseline values. Each detector recorded saturation signals at the beginning of the short bursts. Detectors 9 (Event 4) and 7 (Event 5) also registered a significant undershoot. Detector 8 failed to obtain photon events just after the saturation signals due to buffer overflow. Despite the lack of photon events,
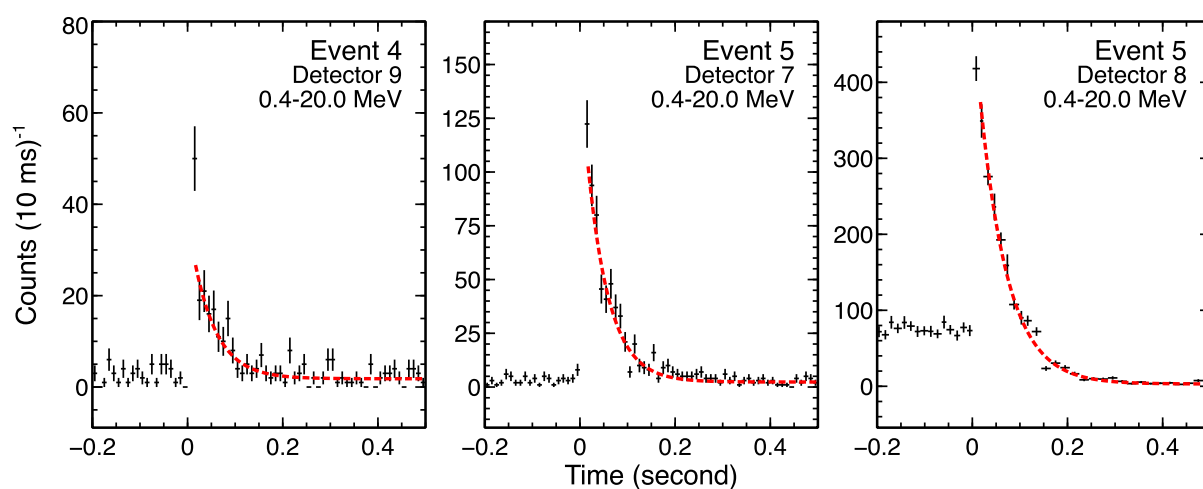
Figure B.1: Count-rate histories of the short bursts Event 4 (left) and Event 5 (center and right) detected in Kanazawa with 10-ms binning. Best-fit exponential functions are overlaid by the red lines.
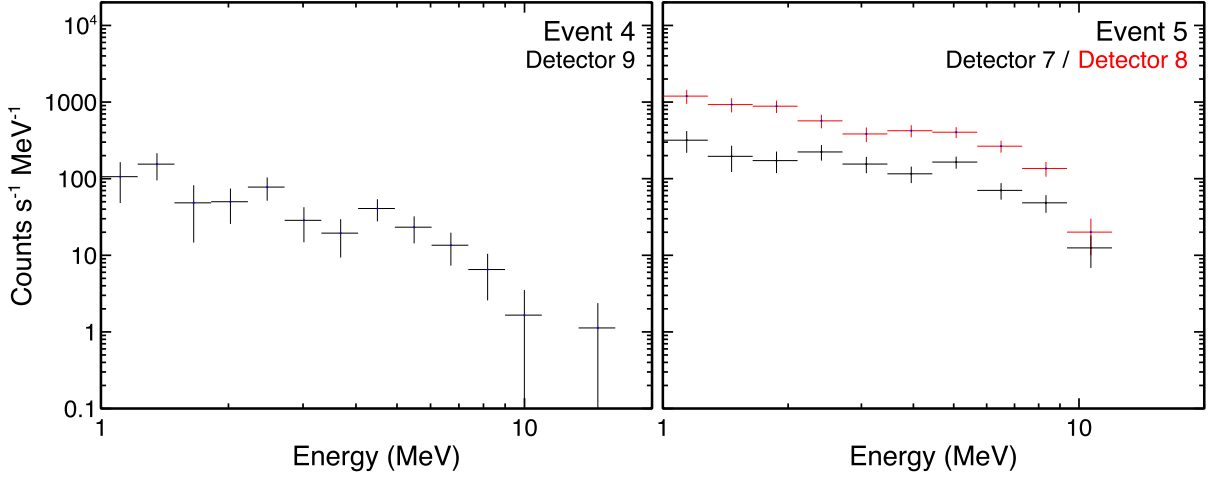
Figure B.2: Energy spectra of short bursts on Event 4 (left) and Event 5 (right). Photon events are extracted from 30 ms $< t <$ 300 ms.
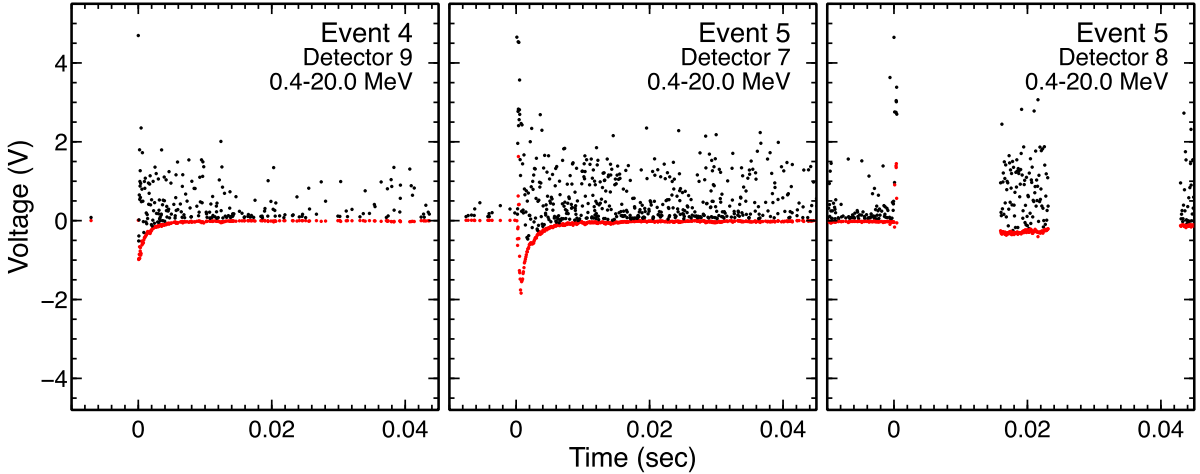
Figure B.3: Pulse height (black) and waveform baseline (red) of photon events at the beginning of short bursts Event 4 (left) and Event 5 (center and right).

however, Detector 8 is also thought to have experienced an undershoot because analog baseline was still negative even after it recovered from the buffer overflow. Being different form the short bursts in Kashiwazaki, only one undershoot was recorded in Events 4 (Detector 9) and 5 (Detector 7). The recovery time constants of the undershoots were 1.58±0.04 ms and 1.87±0.03 ms, respectively.

Figures B.4 and B.5 present count-rate variations after Events 4 and 5, respectively. For Event 4, a very slight afterglow lasting for ∼10 sec was recorded in the energy range below 0.7 MeV. The half-live of the afterglow is $2.6^{+4.1}_{-2.6}$ sec, not statistically significant. An energy spectrum extracted from 1.0 sec $< t <$ 10.0 sec is shown in Figure B.6 left. A hump is seen below 0.5 MeV. When it is evaluated by a Gaussian function, the hump is centered at 0.46±0.02 MeV with a width (FWHM) of 0.10±0.06 MeV. Considering systematic uncertainties due to calibration and background subtraction, the hump structure might originate from positron annihilation.

136
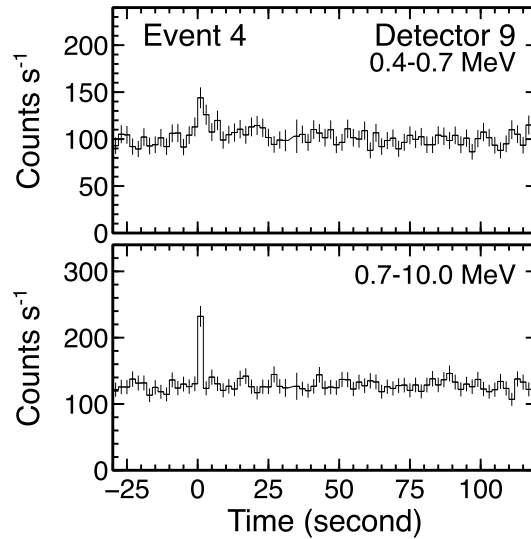
Figure B.4: Count-rate histories blow and above 0.7 MeV after the short burst Event 4 recorded by Detector 9.
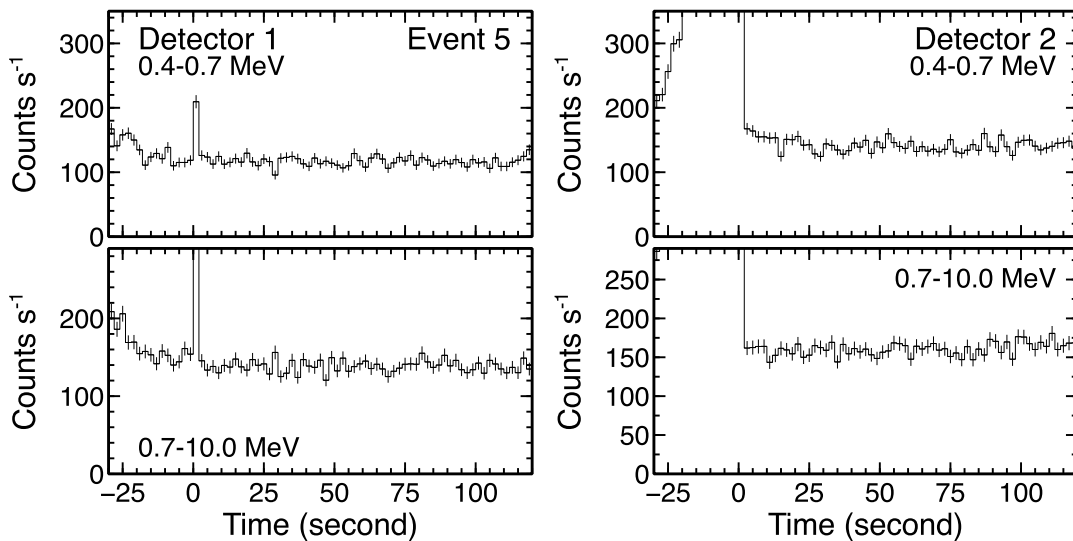
Figure B.5: Count-rate histories blow and above 0.7 MeV after the short burst Event 5 recorded by Detectors 7 and 8.
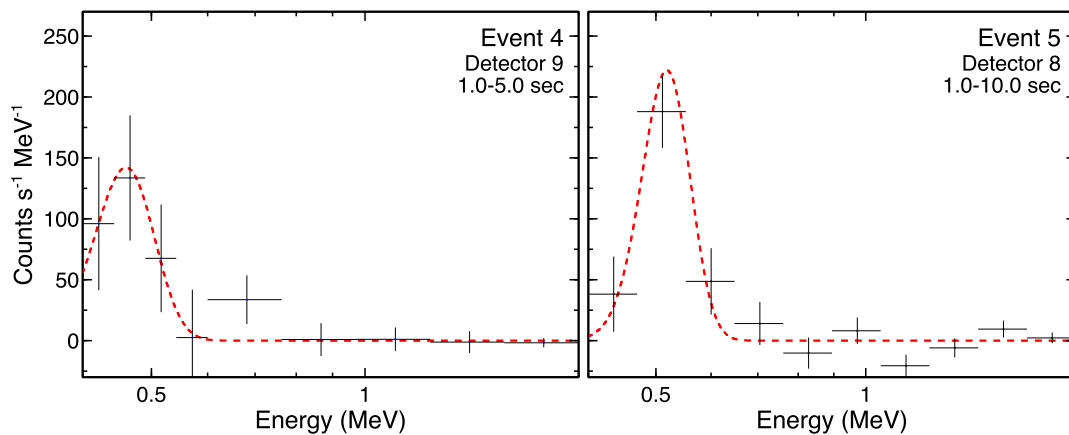
Figure B.6: Energy spectra of annihilation gamma rays recorded by Detectors 9 (left) and 8 (right).

For Event 5, only Detector 8 recorded an afterglow below 0.7 MeV lasting for 10 sec. Its half-life is 6.8±2.6 sec. An energy spectrum extracted from 1.0 sec $< t <$ 10.0 sec is shown in Figure B.6 right. A line structure can be detected at ∼0.5 MeV. The line is centered at 0.518±0.013 MeV with a width (FWHM) of 0.097±0.023 MeV estimated by fitting with a Gaussian function. Therefore it is consistent to originate from positrons.

JLDN detected lightning pulses associated with both events. The locations of the detectors and the JLDN-reported lightning pulses are shown in Figure B.7. For Event 4, two in-cloud lightning currents were observed 1-km northwest from Detector 9. The first one occurred at 18:35:24:908009, and the second one 128 μs after the first one. For Event 5, three discharge currents were detected in a 20×20 km^2 area centered at Detector 7. The first one took place 0.6 km east-southeast from Detector 7 at 02:54:50.308877, and the second and third ones 19 ms and 229 ms after the first one, respectively.

The two short-burst events observed in Kanazawa are also characterized by coincidence with the lightning discharges, the baseline undershoots at the beginning of the short bursts, the signatures of neutron captures, and the annihilation afterglows despite being faint. Therefore, they are interpreted as photonuclear reactions triggered by lightning. For Event 5, Detector 8 recorded a bright gamma-ray glow just before the short burst. Figure B.8 presents count-rate
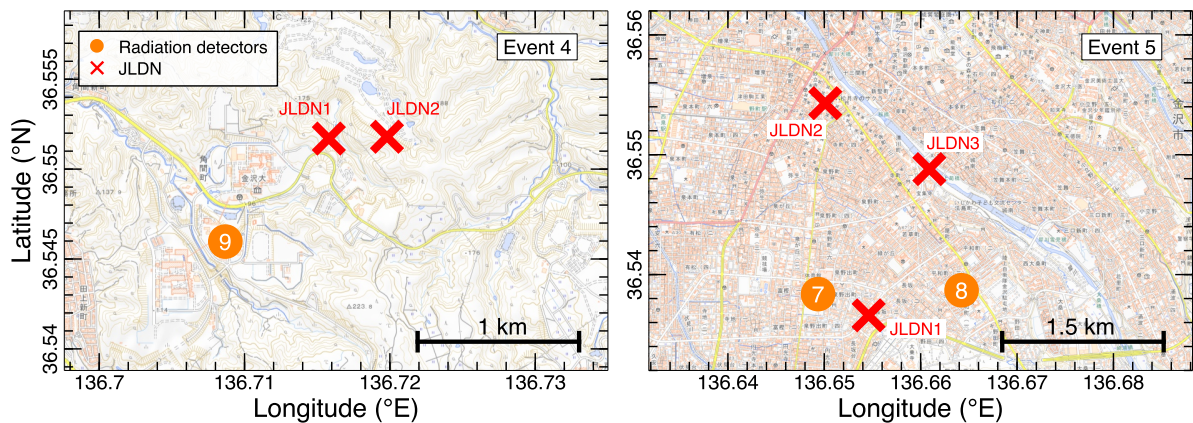
Figure B.7: Positions of gamma-ray detectors and lightning pulses reported by JLDN in Kanazawa for Events 4 (left) and 5 (right).
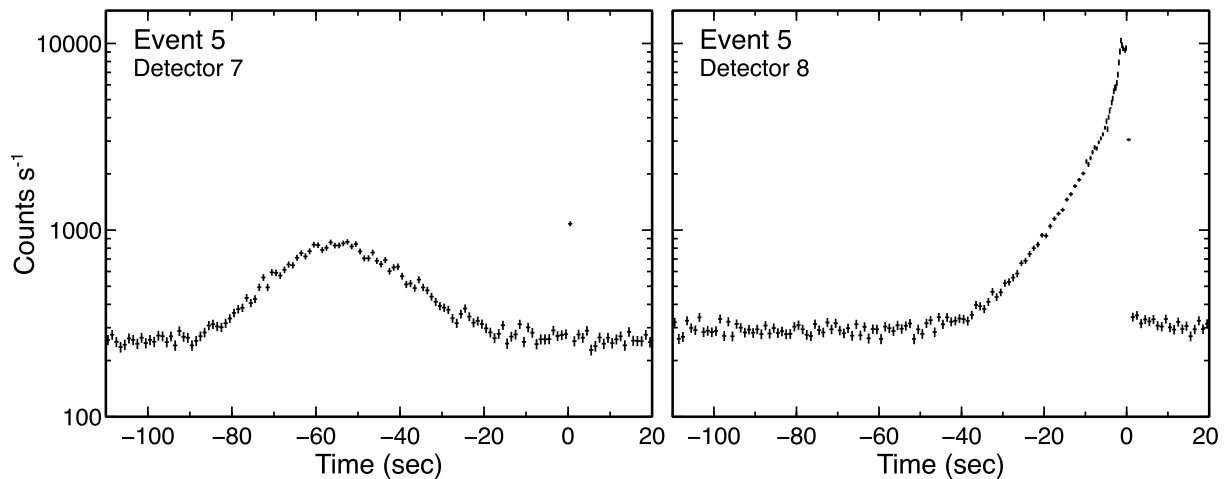
Figure B.8: Count-rate histories of a gamma-ray glow before the short burst 20180110.

histories of the gamma-ray glow. First, Detector 7 registered a gamma-ray glow, and then Detector 8 did. During the glow detection, the lightning discharge and the short burst took place, and the glow seems to have ceased. An XRAIN analysis estimated wind flow at the moment, from west-southwest to east-northeast with a speed of 19.3 ± 1.4 m s^{-1}. Therefore, it is consistent that an identical gamma-ray glow first passed over Detector 7, moved over Detector 8, then disappeared with the short burst. This is the first simultaneous detection of a glow termination and a short burst/downward TGF. Results and discussions of Event 5 from a point of view of gamma-ray glows are described in Wada et al. [2019c].

Appendix C

Cross Section Correction of Geant4

In Section 5.2, `Geant4` is utilized to simulate photonuclear reactions in the atmosphere. Cross sections of photonuclear reactions compiled in the Shielding_LIV physics list are slightly different from ENDF/B-VII.1 (NNDC). Figure C.1 compares two cross-section databases for reactions considered in the present thesis. The ratios of cross sections are utilized for cross-section corrections by weighting the number of products with them.
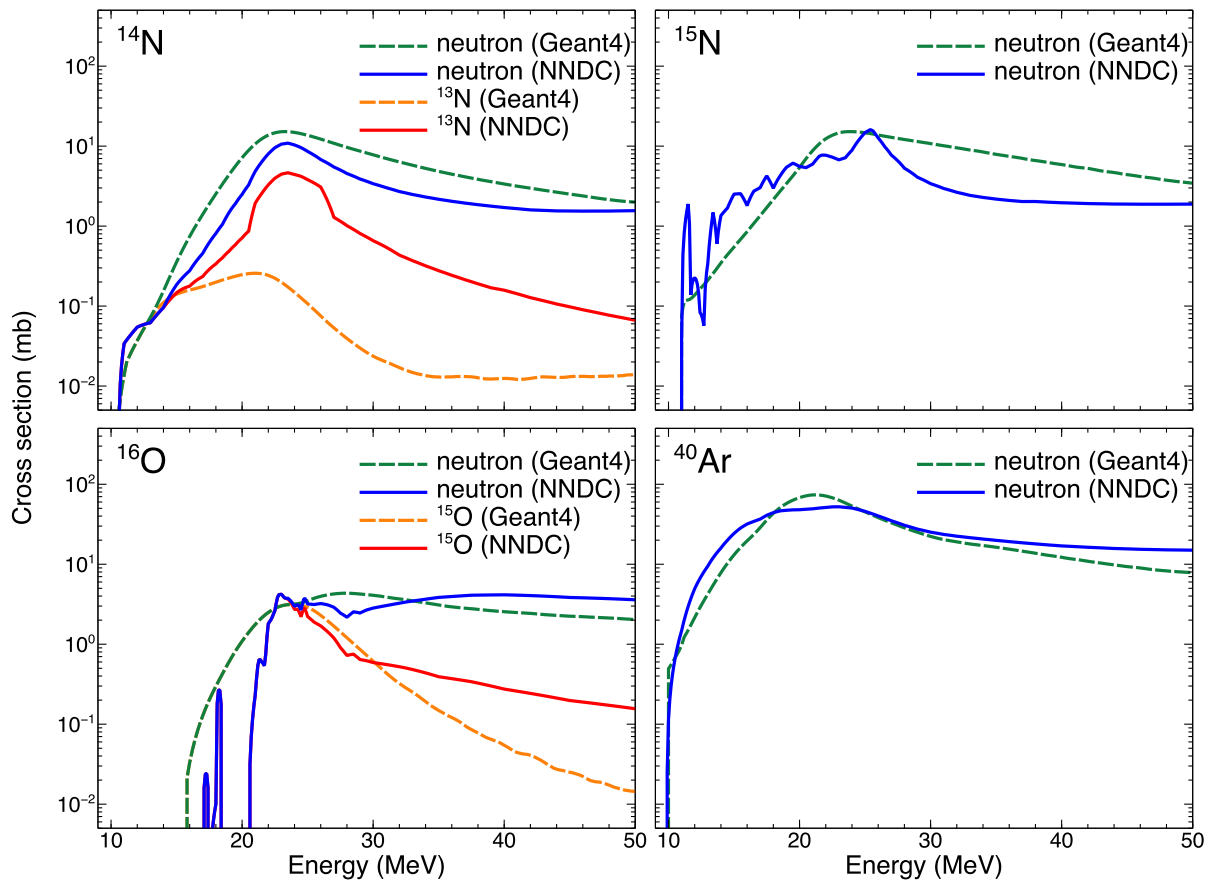
Figure C.1: Comparisons between cross sections of NNDC and Geant4 for atmospheric photonuclear reactions.

Appendix D

Neutron Spectrum with JENDL/PD-2016

In Subsection 6.1.1, a photoneutron spectrum was calculated with ENDF/B-VII.I (Chadwick et al. [2011]; Figure 6.2). This chapter also presents a photoneutron spectrum by TGF photons with the JENDL/PD-2016 database [Iwamoto et al., 2016] for reference purposes. Figure D.1 shows photoneutron spectra by monochromatic photons, and Figure D.2 a convolved spectrum with TGF photons following $E^{-1} \exp(-E/7.3 \text{ MeV})$, where E is a photon energy.
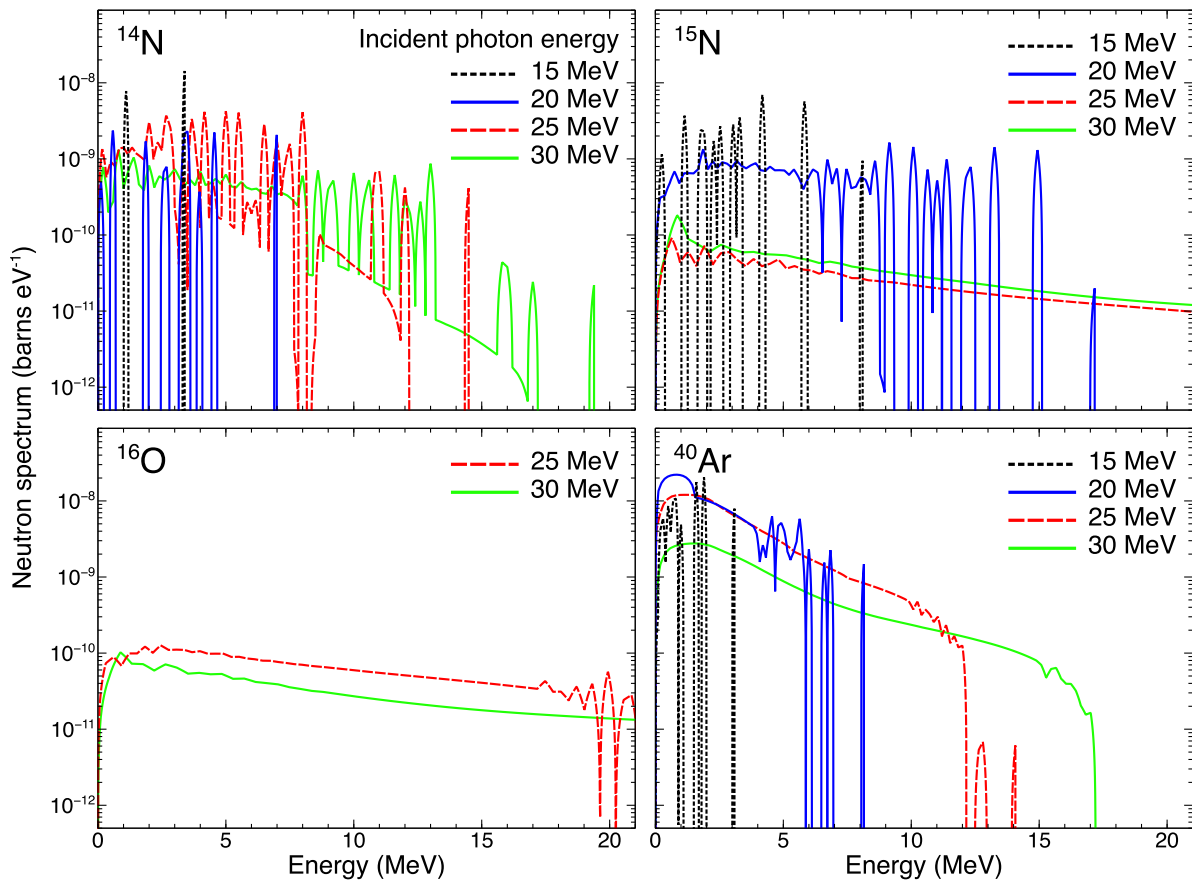
Figure D.1: Neutron spectra produced by photonuclear reactions with monochromatic photons, calculated with JENDL/PD-2016.
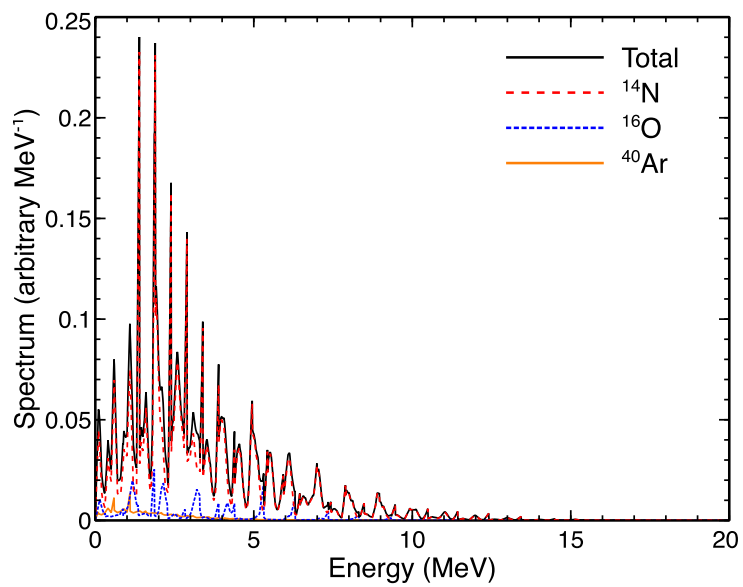
Figure D.2: A photoneutron spectrum produced by TGF photons calculated with JENDL/PD-2016. Components of ^{14}N, ^{16}O, and ^{40}Ar are overlaid by red, blue, and orange dashed lines, respectively. The contribution from ^{15}N is too small to be displayed.

Appendix E

Correlation between TGFs and LF pulses

Lightning discharges taking place in our observation area were also monitored by a broadband low-frequency lightning detection network (LF network) operated by Kindai University and Kobe City College of Technology. The LF network consist of 5 (FY2016) or 6 (FY2017) LF antennas, as in Figure E.1. The LF antenna is a flat-plate type, sensitive to 0.8–500 kHz. Signals from the antenna is digitized by a 4-MHz ADC, and their absolute timing is conditioned by GPS signals. Around the Kanazawa and Suzu observation sites, the LF network locates LF pulses two-dimensionally by the time-of-arrival method, while only waveforms are available for lightning discharges in Komatsu and Kashiwazaki sites by the present antenna distribution.

Figures E.2–E.6 compare gamma-ray signals and LF waveforms recorded by the Nyuzen station (NYZL: 36.954°N, 137.4980°E). The propagation delay between the Nyuzen station and the lightning locations reported by JLDN is corrected. Since GPS signals were not properly obtained by the gamma-ray detectors in FY2016, absolute time of detectors for Events 1 and 2 was adjusted so that their first saturated signals coincided with the timing of lightning reported by JLDN. For Events 3–5, absolute timing of each detector is conditioned by GPS signals with an accuracy of better than 1 μs, except Detector 7 in Event 5. Absolute timing of Detector 7 is adjusted with Detector 8.

All the short-burst events were correlated to LF pulses associated with lightning discharges. Among 5 short-burst events, Events 1–3 exhibit multiple analog undershoots. This is an evidence of multiple flashes in a TGF, similar to multi-pulse TGFs [Fishman et al., 1994, Foley et al., 2014]. Each saturated signal preceding undershoots of Events 1–3 coincided with LF pulses. Events 4 and 5 exhibited a single undershoot.
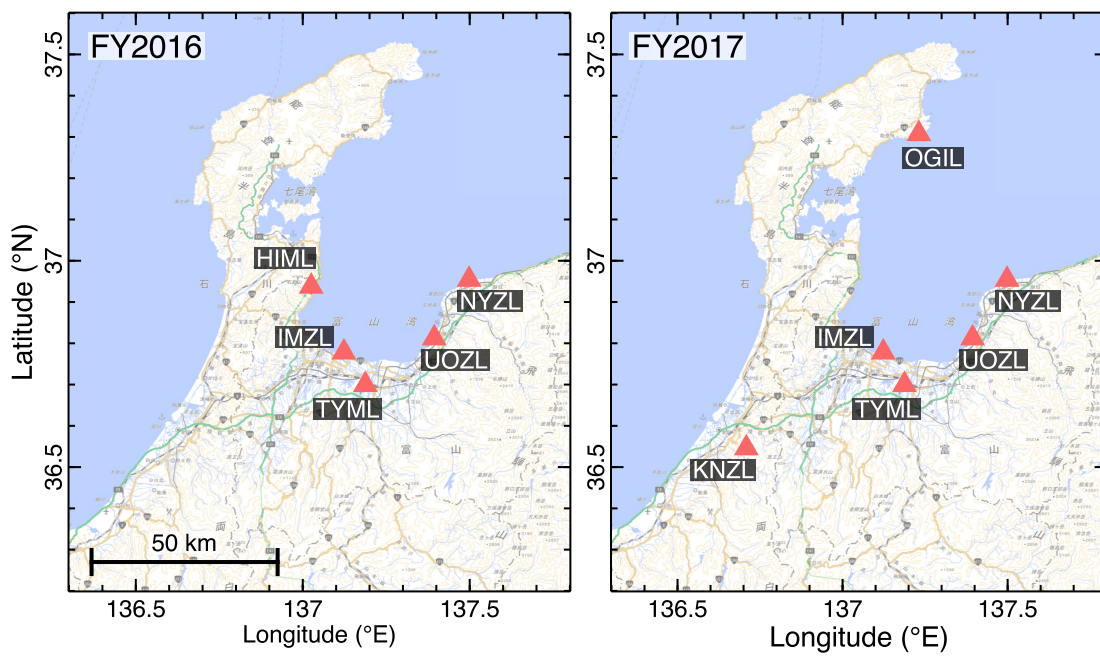
Figure E.1: Distribution of LF antennas in the Hokuriku area.
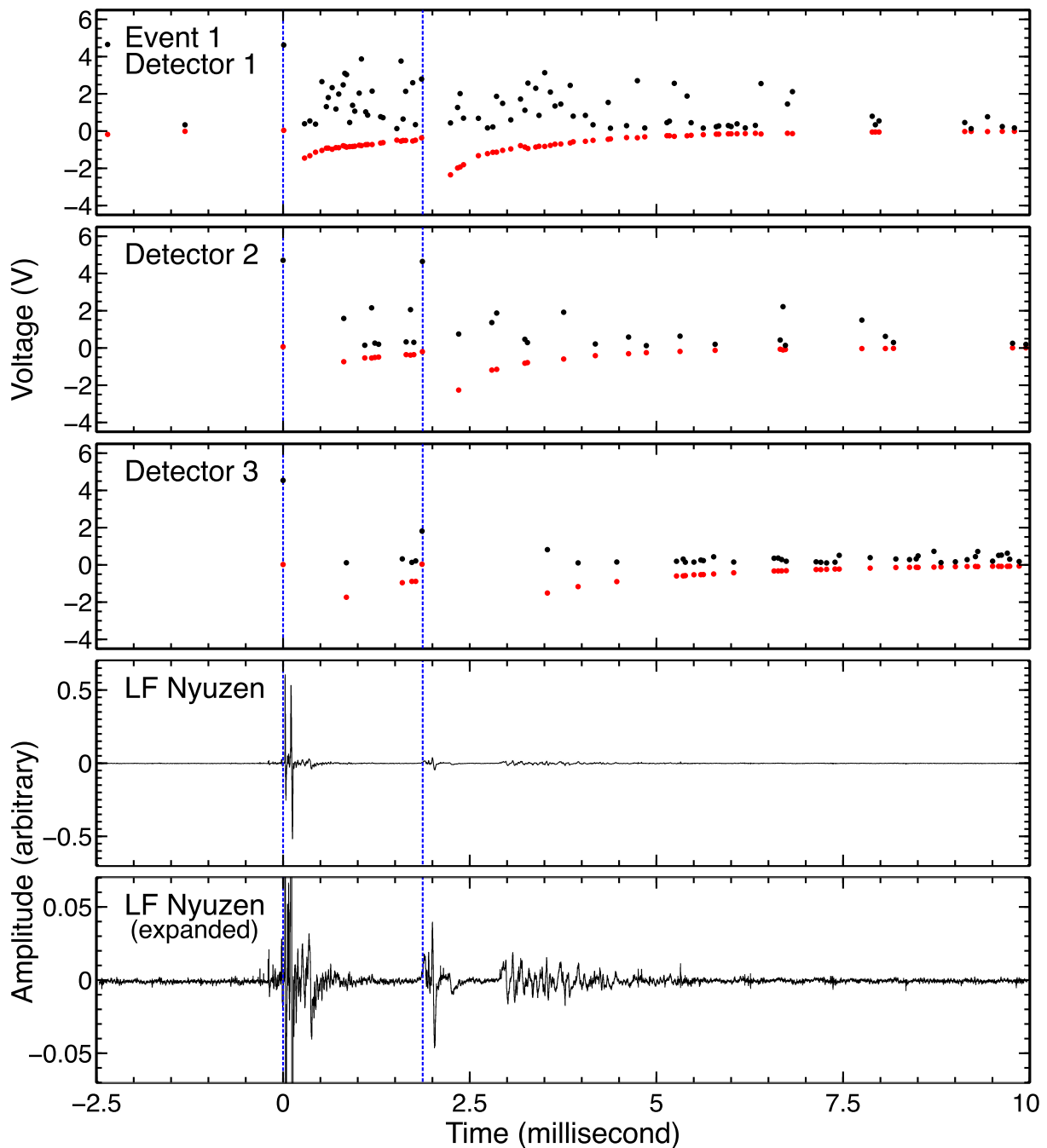
Figure E.2: A comparison between photon events and LF waveforms of Event 1. a–c: Scatter plots of analog pulse heights (black) and baseline (red) recorded by Detectors 1–3. Absolute timing of the gamma-ray detectors are adjusted due to lack of GPS signals. The timing of saturations is shown by blue-dotted lines. d–e: LF waveform and its expansion recorded by the Nyuzen station. The propagation delay between the receiver is the TGF is corrected.
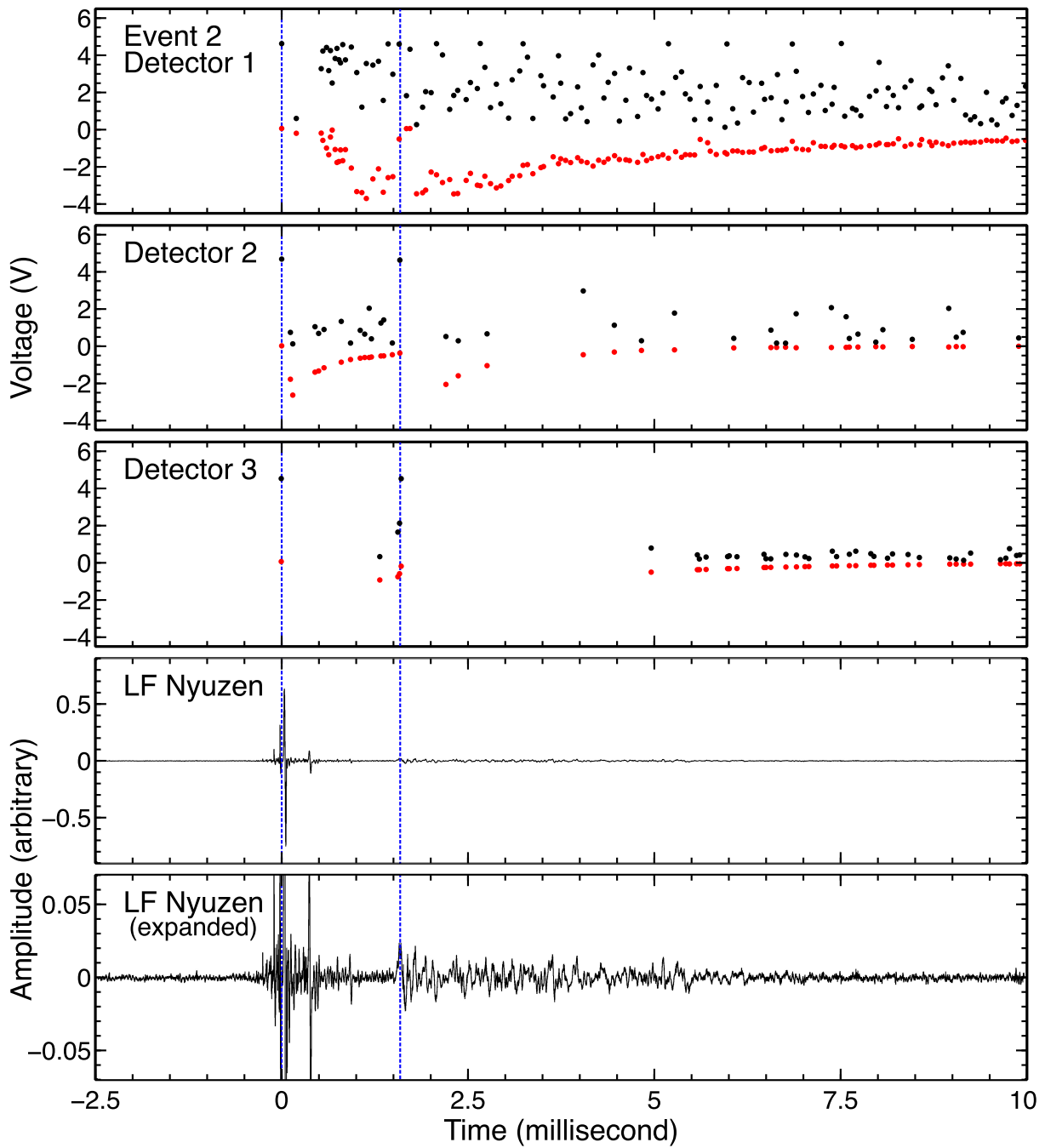
Figure E.3: A comparison between photon events and LF waveforms of Event 2, displayed in the same manner as Figure E.2. Absolute timing of the gamma-ray detectors is adjusted due to lack of GPS signals.
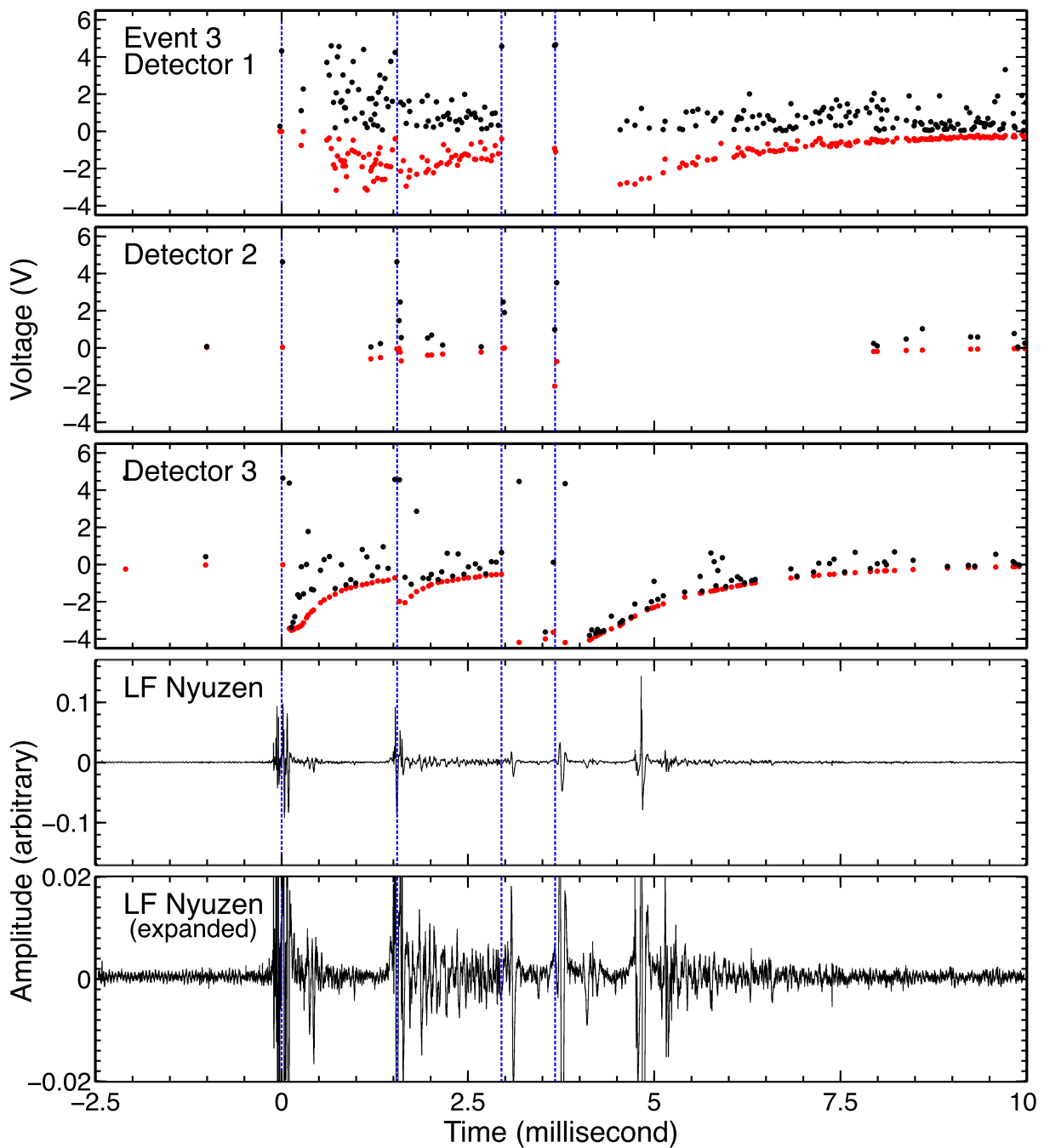
Figure E.4: A comparison between photon events and LF waveforms of Event 3, displayed in the same manner as Figure E.2. Absolute timing of gamma-ray detectors is conditioned by GPS signals with an accuracy of better than 1 μs.
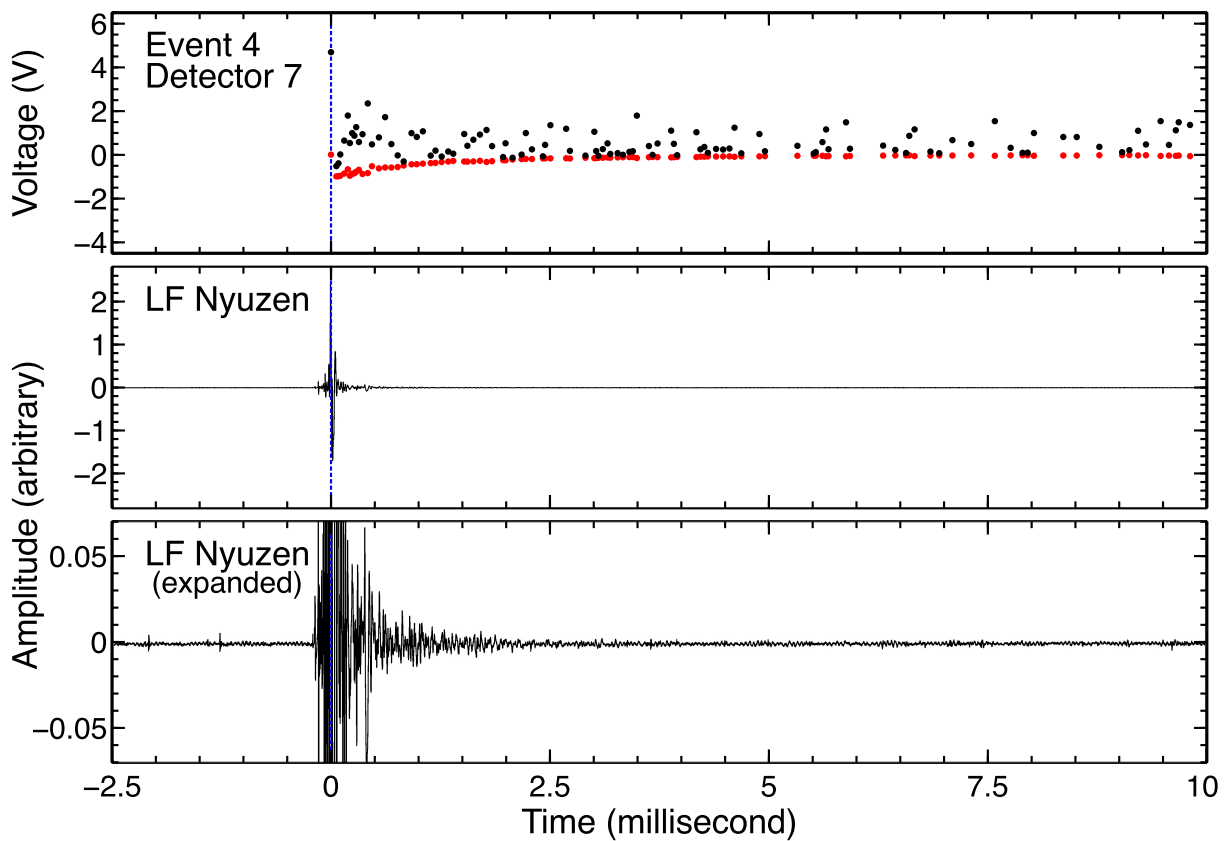
Figure E.5: A comparison between photon events and LF waveforms of Event 4, displayed in the same manner as Figure E.2. Absolute timing of Detector 9 is conditioned by GPS signals with an accuracy of better than 1 μs.
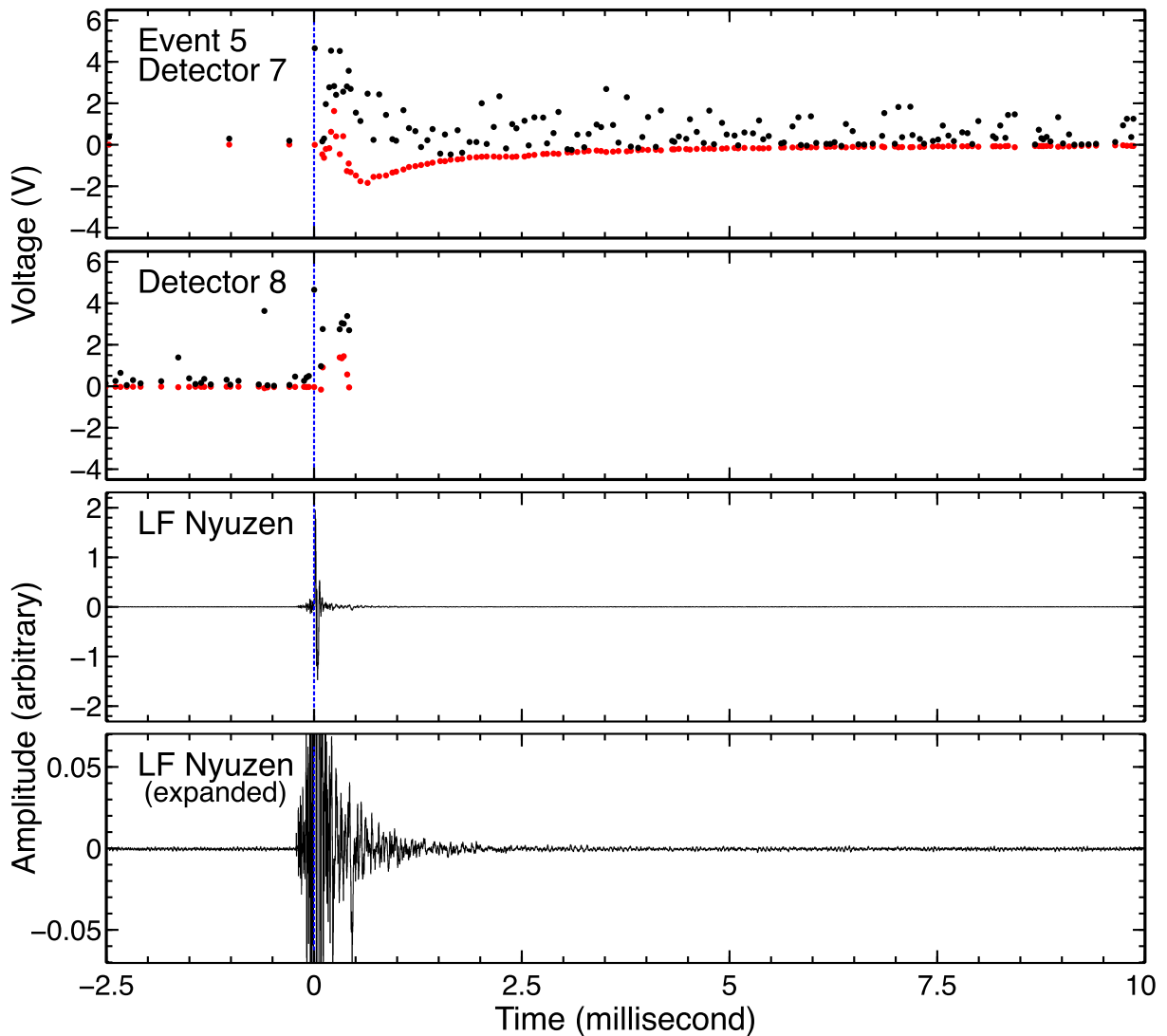
Figure E.6: A comparison between photon events and LF waveforms of Event 5 displayed in the same manner as Figure E.2. Absolute timing of Detector 8 is conditioned by GPS signals with an accuracy of better than 1 μs.

List of Figures

List of Tables

Reference

R. U. Abbasi, T. Abu-Zayyad, M. Allen, E. Barcikowski, J. W. Belz, D. R. Bergman, S. A. Blake, M. Byrne, R. Cady, B.G. Cheon, and et al. Gamma ray showers observed at ground level in coincidence with downward lightning leaders. *Journal of Geophysical Research: Atmospheres*, 123(13):6864–6879, Jul 2018. ISSN 2169-897X. doi: 10.1029/2017jd027931. URL http://dx.doi.org/10.1029/2017JD027931.

R.U. Abbasi, M. Abe, T. Abu-Zayyad, M. Allen, R. Anderson, R. Azuma, E. Barcikowski, J.W. Belz, D.R. Bergman, S.A. Blake, and et al. The bursts of high energy events observed by the telescope array surface detector. *Physics Letters A*, 381(32):2565–2572, Aug 2017. ISSN 0375-9601. doi: 10.1016/j.physleta.2017.06.022. URL http://dx.doi.org/10.1016/j.physleta.2017.06.022.

T. Abu-Zayyad, R. Aida, M. Allen, R. Anderson, R. Azuma, E. Barcikowski, J. W. Belz, D. R. Bergman, S. A. Blake, R. Cady, and et al. The cosmic-ray energy spectrum observed with the surface detector of the telescope array experiment. *The Astrophysical Journal*, 768(1):L1, Apr 2013. ISSN 2041-8213. doi: 10.1088/2041-8205/768/1/l1. URL http://dx.doi.org/10.1088/2041-8205/768/1/L1.

S. Agostinelli, J. Allison, K. Amako, J. Apostolakis, H. Araujo, P. Arce, M. Asai, D. Axen, S. Banerjee, G. Barrand, and et al. Geant4—a simulation toolkit. *Nuclear Instruments and Methods in Physics Research Section A: Accelerators, Spectrometers, Detectors and Associated Equipment*, 506(3):250–303, Jul 2003. ISSN 0168-9002. doi: 10.1016/s0168-9002(03)01368-8. URL http://dx.doi.org/10.1016/S0168-9002(03)01368-8.

F. Ajzenberg-Selove. Energy levels of light nuclei a = 13–15. *Nuclear Physics A*, 523(1): 1–196, Feb 1991. ISSN 0375-9474. doi: 10.1016/0375-9474(91)90446-d. URL http://dx.doi.org/10.1016/0375-9474(91)90446-D.

V.V. Alexeenko, N.S. Khaerdinov, A.S. Lidvansky, and V.B. Petkov. Transient variations of secondary cosmic rays due to atmospheric electric field and evidence for pre-lightning particle acceleration. *Physics Letters A*, 301(3-4):299–306, Aug 2002. ISSN 0375-9601. doi: 10.1016/s0375-9601(02)00981-7. URL http://dx.doi.org/10.1016/S0375-9601(02)00981-7.

J. Allison, K. Amako, J. Apostolakis, H. Araujo, P. Arce Dubois, M. Asai, G. Barrand, R. Capra, S. Chauvie, R. Chytracek, and et al. Geant4 developments and applications. *IEEE Transactions on Nuclear Science*, 53(1):270–278, Feb 2006. ISSN 0018-9499. doi: 10.1109/tns.2006.869826. URL http://dx.doi.org/10.1109/TNS.2006.869826.

J. Allison, K. Amako, J. Apostolakis, P. Arce, M. Asai, T. Aso, E. Bagli, A. Bagulya, S. Banerjee, G. Barrand, and et al. Recent developments in geant4. *Nuclear Instruments and Methods in Physics Research Section A: Accelerators, Spectrometers, Detectors and Associated*

Equipment, 835:186–225, Nov 2016. ISSN 0168-9002. doi: 10.1016/j.nima.2016.06.125. URL http://dx.doi.org/10.1016/j.nima.2016.06.125.

K. A. Arnaud. XSPEC: The First Ten Years. In G. H. Jacoby and J. Barnes, editors, *Astronomical Data Analysis Software and Systems V*, volume 101 of *Astronomical Society of the Pacific Conference Series*, page 17, 1996.

L. P. Babich. Generation of neutrons in giant upward atmospheric discharges. *JETP Letters*, 84(6):285–288, Nov 2006. ISSN 1090-6487. doi: 10.1134/s0021364006180020. URL http://dx.doi.org/10.1134/S0021364006180020.

L. P. Babich. Neutron generation mechanism correlated with lightning discharges. *Geomagnetism and Aeronomy*, 47(5):664–670, Oct 2007. ISSN 1555-645X. doi: 10.1134/s0016793207050155. URL http://dx.doi.org/10.1134/S0016793207050155.

L. P. Babich. Radiocarbon production by thunderstorms. *Geophysical Research Letters*, 44(21): 11,191–11,200, Nov 2017. ISSN 0094-8276. doi: 10.1002/2017gl075131. URL http://dx.doi.org/10.1002/2017GL075131.

L. P. Babich, E. N. Donskoy, R. I. Il'kaev, I. M. Kutsyk, and R. A. Roussel-Dupre. Fundamental parameters of a relativistic runaway electron avalanche in air. *Plasma Physics Reports*, 30(7): 616–624, Jul 2004. ISSN 1562-6938. doi: 10.1134/1.1778437. URL http://dx.doi.org/10.1134/1.1778437.

Leonid P. Babich, Evgenii I. Bochkov, Evgenii N. Donskoi, and Igor M. Kutsyk. Source of prolonged bursts of high-energy gamma rays detected in thunderstorm atmosphere in japan at the coastal area of the sea of japan and on high mountaintop. *Journal of Geophysical Research: Space Physics*, 115(A9), Sep 2010. ISSN 0148-0227. doi: 10.1029/2009ja015017. URL http://dx.doi.org/10.1029/2009JA015017.

G. S. Bowers, D. M. Smith, G. F. Martinez-McKinney, M. Kamogawa, S. A. Cummer, J. R. Dwyer, D. Wang, M. Stock, and Z. Kawasaki. Gamma ray signatures of neutrons from a terrestrial gamma ray flash. *Geophysical Research Letters*, 44(19):10,063–10,070, Oct 2017. ISSN 0094-8276. doi: 10.1002/2017gl075071. URL http://dx.doi.org/10.1002/2017GL075071.

G. S. Bowers, D. M. Smith, N. A. Kelley, G. F. Martinez-McKinney, S. A. Cummer, J. R. Dwyer, S. Heckman, R. H. Holzworth, F. Marks, P. Reasor, and et al. A terrestrial gamma-ray flash inside the eyewall of hurricane patricia. *Journal of Geophysical Research: Atmospheres*, 123 (10):4977–4987, May 2018. ISSN 2169-897X. doi: 10.1029/2017jd027771. URL http://dx.doi.org/10.1029/2017JD027771.

M. S. Briggs, G. J. Fishman, V. Connaughton, P. N. Bhat, W. S. Paciesas, R. D. Preece, C. Wilson-Hodge, V. L. Chaplin, R. M. Kippen, A. von Kienlin, and et al. First results on terrestrial gamma ray flashes from the fermi gamma-ray burst monitor. *Journal of Geophysical Research: Space Physics*, 115(A7), Jul 2010. ISSN 0148-0227. doi: 10.1029/2009ja015242. URL http://dx.doi.org/10.1029/2009JA015242.

Michael S. Briggs, Valerie Connaughton, Colleen Wilson-Hodge, Robert D. Preece, Gerald J. Fishman, R. Marc Kippen, P. N. Bhat, William S. Paciesas, Vandiver L. Chaplin, Charles A. Meegan, and et al. Electron-positron beams from terrestrial lightning observed with fermi

gbm. *Geophysical Research Letters*, 38(2), Jan 2011. ISSN 0094-8276. doi: 10.1029/ 2010gl046259. URL http://dx.doi.org/10.1029/2010GL046259.

Michael S. Briggs, Shaolin Xiong, Valerie Connaughton, Dave Tierney, Gerard Fitzpatrick, Suzanne Foley, J. Eric Grove, Alexandre Chekhtman, Melissa Gibby, Gerald J. Fishman, and et al. Terrestrial gamma-ray flashes in the fermi era: Improvedobservations and analysis methods. *Journal of Geophysical Research: Space Physics*, 118(6):3805–3830, Jun 2013. ISSN 2169-9380. doi: 10.1002/jgra.50205. URL http://dx.doi.org/10.1002/ jgra.50205.

B. E. Carlson, N. G. Lehtinen, and U. S. Inan. Neutron production in terrestrial gamma ray flashes. *Journal of Geophysical Research: Space Physics*, 115(A4), Apr 2010. ISSN 0148-0227. doi: 10.1029/2009ja014696. URL http://dx.doi.org/10.1029/ 2009JA014696.

Sebastien Celestin and Victor P. Pasko. Energy and fluxes of thermal runaway electrons produced by exponential growth of streamers during the stepping of lightning leaders and in transient luminous events. *Journal of Geophysical Research: Space Physics*, 116(A3), Mar 2011. ISSN 0148-0227. doi: 10.1029/2010ja016260. URL http://dx.doi.org/10. 1029/2010JA016260.

Sebastien Celestin, Wei Xu, and Victor P. Pasko. Variability in fluence and spectrum of high-energy photon bursts produced by lightning leaders. *Journal of Geophysical Research: Space Physics*, 120(12):10,712–10,723, Dec 2015. ISSN 2169-9380. doi: 10.1002/2015ja021410. URL http://dx.doi.org/10.1002/2015JA021410.

M.B. Chadwick, M. Herman, P. Obložinský, M.E. Dunn, Y. Danon, A.C. Kahler, D.L. Smith, B. Pritychenko, G. Arbanas, R. Arcilla, R. Brewer, D.A. Brown, R. Capote, A.D. Carlson, Y.S. Cho, H. Derrien, K. Guber, G.M. Hale, S. Hoblit, S. Holloway, T.D. Johnson, T. Kawano, B.C. Kiedrowski, H. Kim, S. Kunieda, N.M. Larson, L. Leal, J.P. Lestone, R.C. Little, E.A. McCutchan, R.E. MacFarlane, M. MacInnes, C.M. Mattoon, R.D. McKnight, S.F. Mughabghab, G.P.A. Nobre, G. Palmiotti, A. Palumbo, M.T. Pigni, V.G. Pronyaev, R.O. Sayer, A.A. Sonzogni, N.C. Summers, P. Talou, I.J. Thompson, A. Trkov, R.L. Vogt, S.C. van der Marck, A. Wallner, M.C. White, D. Wiarda, and P.G. Young. ENDF/B-VII.1 nuclear data for science and technology: Cross sections, covariances, fission product yields and decay data. *Nuclear Data Sheets*, 112(12):2887 – 2996, 2011. ISSN 0090-3752. doi: 10.1016/j.nds.2011.11.002. URL http://www.sciencedirect.com/ science/article/pii/S009037521100113X. Special Issue on ENDF/B-VII.1 Library.

A. Chilingarian and H. Mkrtchyan. Role of the lower positive charge region (lpcr) in initiation of the thunderstorm ground enhancements (tges). *Physical Review D*, 86(7), Oct 2012. ISSN 1550-2368. doi: 10.1103/physrevd.86.072003. URL http://dx.doi.org/10.1103/ PhysRevD.86.072003.

A. Chilingarian, A. Daryan, K. Arakelyan, A. Hovhannisyan, B. Mailyan, L. Melkumyan, G. Hovsepyan, S. Chilingaryan, A. Reymers, and L. Vanyan. Ground-based observations of thunderstorm-correlated fluxes of high-energy electrons, gamma rays, and neutrons. *Physical Review D*, 82(4), Aug 2010. ISSN 1550-2368. doi: 10.1103/physrevd.82.043009. URL http://dx.doi.org/10.1103/PhysRevD.82.043009.

A. Chilingarian, G. Hovsepyan, and L. Vanyan. On the origin of the particle fluxes from the thunderclouds: Energy spectra analysis. *EPL (Europhysics Letters)*, 106(5):59001, May 2014. ISSN 1286-4854. doi: 10.1209/0295-5075/106/59001. URL http://dx.doi.org/10.1209/0295-5075/106/59001.

A. Chilingarian, G. Hovsepyan, G. Khanikyanc, A. Reymers, and S. Soghomonyan. Lightning origination and thunderstorm ground enhancements terminated by the lightning flash. *EPL (Europhysics Letters)*, 110(4):49001, May 2015. ISSN 1286-4854. doi: 10.1209/0295-5075/110/49001. URL http://dx.doi.org/10.1209/0295-5075/110/49001.

A. Chilingarian, Y. Khanikyants, E. Mareev, D. Pokhsraryan, V. A. Rakov, and S. Soghomonyan. Types of lightning discharges that abruptly terminate enhanced fluxes of energetic radiation and particles observed at ground level. *Journal of Geophysical Research: Atmospheres*, 122(14):7582–7599, Jul 2017. ISSN 2169-897X. doi: 10.1002/2017jd026744. URL http://dx.doi.org/10.1002/2017JD026744.

A. Chilingarian, S. Soghomonyan, Y. Khanikyanc, and D. Pokhsraryan. On the origin of particle fluxes from thunderclouds. *Astroparticle Physics*, 105:54–62, Feb 2019. ISSN 0927-6505. doi: 10.1016/j.astropartphys.2018.10.004. URL http://dx.doi.org/10.1016/j.astropartphys.2018.10.004.

Ashot Chilingarian, Gagik Hovsepyan, and Armen Hovhannisyan. Particle bursts from thunderclouds: Natural particle accelerators above our heads. *Physical Review D*, 83(6), Mar 2011. ISSN 1550-2368. doi: 10.1103/physrevd.83.062001. URL http://dx.doi.org/10.1103/PhysRevD.83.062001.

Ashot Chilingarian, Bagrat Mailyan, and Levon Vanyan. Recovering of the energy spectra of electrons and gamma rays coming from the thunderclouds. *Atmospheric Research*, 114-115:1 – 16, 2012. ISSN 0169-8095. doi: https://doi.org/10.1016/j.atmosres.2012.05.008. URL http://www.sciencedirect.com/science/article/pii/S0169809512001378.

Hugh J. Christian. Global frequency and distribution of lightning as observed from space by the optical transient detector. *Journal of Geophysical Research*, 108(D1), 2003. ISSN 0148-0227. doi: 10.1029/2002jd002347. URL http://dx.doi.org/10.1029/2002JD002347.

A.P. Chubenko, V.P. Antonova, S.Yu. Kryukov, V.V. Piskal, M.O. Ptitsyn, A.L. Shepetov, L.I. Vildanova, K.P. Zybin, and A.V. Gurevich. Intensive x-ray emission bursts during thunderstorms. *Physics Letters A*, 275(1-2):90–100, Oct 2000. ISSN 0375-9601. doi: 10.1016/s0375-9601(00)00502-8. URL http://dx.doi.org/10.1016/S0375-9601(00)00502-8.

Roberta Colalillo. Peculiar lightning-related events observed by the surface detector of the pierre auger observatory. *Proceedings of 35th International Cosmic Ray Conference — PoS(ICRC2017)*, Aug 2017. doi: 10.22323/1.301.0314. URL http://dx.doi.org/10.22323/1.301.0314.

L. M. Coleman and J. R. Dwyer. Propagation speed of runaway electron avalanches. *Geophysical Research Letters*, 33(11), 2006. ISSN 0094-8276. doi: 10.1029/2006gl025863. URL http://dx.doi.org/10.1029/2006GL025863.

V. Connaughton, M. S. Briggs, R. H. Holzworth, M. L. Hutchins, G. J. Fishman, C. A. Wilson-Hodge, V. L. Chaplin, P. N. Bhat, J. Greiner, A. von Kienlin, and et al. Associations between fermi gamma-ray burst monitor terrestrial gamma ray flashes and sferics from the world wide lightning location network. *Journal of Geophysical Research: Space Physics*, 115 (A12):n/a–n/a, Dec 2010. ISSN 0148-0227. doi: 10.1029/2010ja015681. URL `http://dx.doi.org/10.1029/2010JA015681`.

E. S. Cramer, B. G. Mailyan, S. Celestin, and J. R. Dwyer. A simulation study on the electric field spectral dependence of thunderstorm ground enhancements and gamma ray glows. *Journal of Geophysical Research: Atmospheres*, 122(9):4763–4772, May 2017. ISSN 2169-897X. doi: 10.1002/2016jd026422. URL `http://dx.doi.org/10.1002/2016JD026422`.

Steven A. Cummer, Michael S. Briggs, Joseph R. Dwyer, Shaolin Xiong, Valerie Connaughton, Gerald J. Fishman, Gaopeng Lu, Fanchao Lyu, and Rahulkumar Solanki. The source altitude, electric current, and intrinsic brightness of terrestrial gamma ray flashes. *Geophysical Research Letters*, 41(23):8586–8593, Dec 2014. ISSN 0094-8276. doi: 10.1002/2014gl062196. URL `http://dx.doi.org/10.1002/2014GL062196`.

Steven A. Cummer, Fanchao Lyu, Michael S. Briggs, Gerard Fitzpatrick, Oliver J. Roberts, and Joseph R. Dwyer. Lightning leader altitude progression in terrestrial gamma-ray flashes. *Geophysical Research Letters*, 42(18):7792–7798, Sep 2015. ISSN 0094-8276. doi: 10.1002/2015gl065228. URL `http://dx.doi.org/10.1002/2015GL065228`.

Lev I. Dorman and Irena V. Dorman. Possible influence of cosmic rays on climate through thunderstorm clouds. *Advances in Space Research*, 35(3):476–483, Jan 2005. ISSN 0273-1177. doi: 10.1016/j.asr.2005.01.013. URL `http://dx.doi.org/10.1016/j.asr.2005.01.013`.

J. R. Dwyer. A fundamental limit on electric fields in air. *Geophysical Research Letters*, 30 (20), Oct 2003. ISSN 0094-8276. doi: 10.1029/2003gl017781. URL `http://dx.doi.org/10.1029/2003GL017781`.

J. R. Dwyer. Implications of x-ray emission from lightning. *Geophysical Research Letters*, 31 (12), Jun 2004. ISSN 0094-8276. doi: 10.1029/2004gl019795. URL `http://dx.doi.org/10.1029/2004GL019795`.

J. R. Dwyer. Relativistic breakdown in planetary atmospheres. *Physics of Plasmas*, 14(4): 042901, Apr 2007. ISSN 1089-7674. doi: 10.1063/1.2709652. URL `http://dx.doi.org/10.1063/1.2709652`.

J. R. Dwyer. Source mechanisms of terrestrial gamma-ray flashes. *Journal of Geophysical Research*, 113(D10), May 2008. ISSN 0148-0227. doi: 10.1029/2007jd009248. URL `http://dx.doi.org/10.1029/2007JD009248`.

J. R. Dwyer and D. M. Smith. A comparison between monte carlo simulations of runaway breakdown and terrestrial gamma-ray flash observations. *Geophysical Research Letters*, 32 (22), Nov 2005. ISSN 0094-8276. doi: 10.1029/2005gl023848. URL `http://dx.doi.org/10.1029/2005GL023848`.

J. R. Dwyer, H. K. Rassoul, M. Al-Dayeh, L. Caraway, B. Wright, A. Chrest, M. A. Uman, V. A. Rakov, K. J. Rambo, D. M. Jordan, and et al. A ground level gamma-ray burst observed in association with rocket-triggered lightning. *Geophysical Research Letters*, 31(5), Mar 2004. ISSN 0094-8276. doi: 10.1029/2003gl018771. URL `http://dx.doi.org/10.1029/2003GL018771`.

J. R. Dwyer, H. K. Rassoul, M. Al-Dayeh, L. Caraway, A. Chrest, B. Wright, E. Kozak, J. Jerauld, M. A. Uman, V. A. Rakov, D. M. Jordan, and K. J. Rambo. X-ray bursts associated with leader steps in cloud-to-ground lightning. *Geophysical Research Letters*, 32(1), 2005. ISSN 0094-8276. doi: 10.1029/2004gl021782. URL `http://dx.doi.org/10.1029/2004GL021782`.

J. R. Dwyer, D. M. Smith, M. A. Uman, Z. Saleh, B. Grefenstette, B. Hazelton, and H. K. Rassoul. Estimation of the fluence of high-energy electron bursts produced by thunderclouds and the resulting radiation doses received in aircraft. *Journal of Geophysical Research*, 115 (D9), May 2010. ISSN 0148-0227. doi: 10.1029/2009jd012039. URL `http://dx.doi.org/10.1029/2009JD012039`.

J. R. Dwyer, M. M. Schaal, E. Cramer, S. Arabshahi, N. Liu, H. K. Rassoul, J. D. Hill, D. M. Jordan, and M. A. Uman. Observation of a gamma-ray flash at ground level in association with a cloud-to-ground lightning return stroke. *Journal of Geophysical Research: Space Physics*, 117(A10), Oct 2012a. ISSN 0148-0227. doi: 10.1029/2012ja017810. URL `http://dx.doi.org/10.1029/2012JA017810`.

Joseph R. Dwyer, Martin A. Uman, Hamid K. Rassoul, Maher Al-Dayeh, Lee Caraway, Jason Jerauld, Vladimir A. Rakov, Douglas M. Jordan, Keith J. Rambo, Vincent Corbin, and Brian Wright. Energetic radiation produced during rocket-triggered lightning. *Science*, 299(5607):694–697, 2003. ISSN 0036-8075. doi: 10.1126/science.1078940. URL `http://science.sciencemag.org/content/299/5607/694`.

Joseph R. Dwyer, David M. Smith, and Steven A. Cummer. High-energy atmospheric physics: Terrestrial gamma-ray flashes and related phenomena. *Space Science Reviews*, 173(1-4): 133–196, Jun 2012b. ISSN 1572-9672. doi: 10.1007/s11214-012-9894-0. URL `http://dx.doi.org/10.1007/s11214-012-9894-0`.

Joseph R. Dwyer, David M. Smith, Bryna J. Hazelton, Brian W. Grefenstette, Nicole A. Kelley, Alexander W. Lowell, Meagan M. Schaal, and Hamid K. Rassoul. Positron clouds within thunderstorms. *Journal of Plasma Physics*, 81(4), Jun 2015. ISSN 1469-7807. doi: 10.1017/s0022377815000549. URL `http://dx.doi.org/10.1017/S0022377815000549`.

Kenneth B. Eack, William H. Beasley, W. David Rust, Thomas C. Marshall, and Maribeth Stolzenburg. Initial results from simultaneous observation of x-rays and electric fields in a thunderstorm. *Journal of Geophysical Research: Atmospheres*, 101(D23):29637–29640, Dec 1996. ISSN 0148-0227. doi: 10.1029/96jd01705. URL `http://dx.doi.org/10.1029/96JD01705`.

T. Enoto, Y. Wada, Y. Furuta, K. Nakazawa, T. Yuasa, K. Okuda, K. Makisshima, M. Sato, Y. Sato, T. Nakano, D. Umemoto, H. Tsuchiya, M. Kamogawa, G. S. Bowers, D. Smith, Morimoto T., Y. Nakamura, and D. Wang. Multi-point measurement campaigns of gamma rays from thunderclouds and lightning in japan. In *Proceedings of XVI International Conference on Atmospheric Electricity*, 06 2018.

Teruaki Enoto, Yuuki Wada, Yoshihiro Furuta, Kazuhiro Nakazawa, Takayuki Yuasa, Kazufumi Okuda, Kazuo Makishima, Mitsuteru Sato, Yousuke Sato, Toshio Nakano, and et al. Photonuclear reactions triggered by lightning discharge. *Nature*, 551(7681):481–484, Nov 2017. ISSN 1476-4687. doi: 10.1038/nature24630. URL http://dx.doi.org/10.1038/nature24630.

G. J. Fishman, P. N. Bhat, R. Mallozzi, J. M. Horack, T. Koshut, C. Kouveliotou, G. N. Pendleton, C. A. Meegan, R. B. Wilson, W. S. Paciesas, and et al. Discovery of intense gamma-ray flashes of atmospheric origin. *Science*, 264(5163):1313–1316, May 1994. ISSN 1095-9203. doi: 10.1126/science.264.5163.1313. URL http://dx.doi.org/10.1126/science.264.5163.1313.

S. Foley, G. Fitzpatrick, M. S. Briggs, V. Connaughton, D. Tierney, S. McBreen, J. R. Dwyer, V. L. Chaplin, P. N. Bhat, D. Byrne, and et al. Pulse properties of terrestrial gamma-ray flashes detected by the fermi gamma-ray burst monitor. *Journal of Geophysical Research: Space Physics*, 119(7):5931–5942, Jul 2014. ISSN 2169-9380. doi: 10.1002/2014ja019805. URL http://dx.doi.org/10.1002/2014JA019805.

Luna Gargani and Eugenio Picano. The risk of cumulative radiation exposure in chest imaging and the advantage of bedside ultrasound. *Critical Ultrasound Journal*, 7(1), Mar 2015. ISSN 2036-7902. doi: 10.1186/s13089-015-0020-x. URL http://dx.doi.org/10.1186/s13089-015-0020-x.

Y. Goto and K. Narita. Observations of winter lightning to an isolate tower. *Res. Lett. Atmos. Electr.*, 12:57–60, 1992.

A. V. Gurevich, V. P. Antonova, A. P. Chubenko, A. N. Karashtin, G. G. Mitko, M. O. Ptitsyn, V. A. Ryabov, A. L. Shepetov, Yu. V. Shlyugaev, L. I. Vildanova, and et al. Strong flux of low-energy neutrons produced by thunderstorms. *Physical Review Letters*, 108(12), Mar 2012. ISSN 1079-7114. doi: 10.1103/physrevlett.108.125001. URL http://dx.doi.org/10.1103/PhysRevLett.108.125001.

A.V. Gurevich. On the theory of runaway electrons. *Journal of Experimental and Theoretical Physics*, 12(5):904–912, May 1961.

A.V. Gurevich, G.M. Milikh, and R. Roussel-Dupre. Runaway electron mechanism of air breakdown and preconditioning during a thunderstorm. *Physics Letters A*, 165(5-6):463–468, Jun 1992. ISSN 0375-9601. doi: 10.1016/0375-9601(92)90348-p. URL http://dx.doi.org/10.1016/0375-9601(92)90348-P.

B. M. Hare, M. A. Uman, J. R. Dwyer, D. M. Jordan, M. I. Biggerstaff, J. A. Caicedo, F. L. Carvalho, R. A. Wilkes, D. A. Kotovsky, W. R. Gamerota, and et al. Ground-level observation of a terrestrial gamma ray flash initiated by a triggered lightning. *Journal of Geophysical Research: Atmospheres*, 121(11):6511–6533, Jun 2016. ISSN 2169-897X. doi: 10.1002/2015jd024426. URL http://dx.doi.org/10.1002/2015JD024426.

B. Hariharan, A. Chandra, S. R. Dugad, S. K. Gupta, P. Jagadeesan, A. Jain, P. K. Mohanty, S. D. Morris, P. K. Nayak, P. S. Rakshe, K. Ramesh, B. S. Rao, L. V. Reddy, M. Zuberi, Y. Hayashi, S. Kawakami, S. Ahmad, H. Kojima, A. Oshima, S. Shibata, Y. Muraki, and K. Tanaka. Measurement of the electrical properties of a thundercloud through muon imaging by the grapes-3 experiment. *Phys. Rev. Lett.*, 122:105101, Mar 2019. doi: 10.1103/PhysRevLett.

122.105101. URL `https://link.aps.org/doi/10.1103/PhysRevLett.122.105101`.

Ronald L. Holle, Kenneth L. Cummins, and William A. Brooks. Seasonal, monthly, and weekly distributions of nldn and gld360 cloud-to-ground lightning. *Monthly Weather Review*, 144 (8):2855–2870, Aug 2016. ISSN 1520-0493. doi: 10.1175/mwr-d-16-0051.1. URL `http://dx.doi.org/10.1175/MWR-D-16-0051.1`.

U. S. Inan and N. G. Lehtinen. Production of terrestrial gamma-ray flashes by an electromagnetic pulse from a lightning return stroke. *Geophysical Research Letters*, 32(19):n/a–n/a, Oct 2005. ISSN 0094-8276. doi: 10.1029/2005gl023702. URL `http://dx.doi.org/10.1029/2005GL023702`.

Umran S. Inan, Steven C. Reising, Gerald J. Fishman, and John M. Horack. On the association of terrestrial gamma-ray bursts with lightning and implications for sprites. *Geophysical Research Letters*, 23(9):1017–1020, May 1996. ISSN 0094-8276. doi: 10.1029/96gl00746. URL `http://dx.doi.org/10.1029/96GL00746`.

Masaru Ishii, Fumiyuki Fujii, Mikihisa Saito, Daisuke Natsuno, and Akiko Sugita. Detection of lightning return strokes hitting wind turbines in winter by jldn. *IEEJ Transactions on Power and Energy*, 133(12):1009–1010, 2013. ISSN 1348-8147. doi: 10.1541/ieejpes.133.1009. URL `http://dx.doi.org/10.1541/ieejpes.133.1009`.

Nobuyuki Iwamoto, Kazuaki Kosako, and Toru Murata. Photonuclear data file. In Osamu Iwamoto, Toshiya Sanami, Satoshi Kunieda, Hiroyuki Koura, and Shoji Nakamura, editors, *Proceedings of the 2015 Symposium on Nuclear Data*, pages 53–58. Japan Atomic Energy Agency, Japan Atomic Energy Agency, 2016.

Nicole A. Kelley, David M. Smith, Joseph R. Dwyer, Michael Splitt, Steven Lazarus, Forest Martinez-McKinney, Bryna Hazelton, Brian Grefenstette, Alexander Lowell, and Hamid K. Rassoul. Relativistic electron avalanches as a thunderstorm discharge competing with lightning. *Nature Communications*, 6:7845, Aug 2015. ISSN 2041-1723. doi: 10.1038/ncomms8845. URL `http://dx.doi.org/10.1038/ncomms8845`.

N. Kitagawa. Charge distribution of winter thunderclouds. *Res. Lett. Atmos. Electr.*, 12:143–153, 1992.

N. Kitagawa and K. Michimoto. Meteorological and electrical aspects of winter thunderclouds. *Journal of Geophysical Research*, 99(D5):10713, 1994. ISSN 0148-0227. doi: 10.1029/94jd00288. URL `http://dx.doi.org/10.1029/94JD00288`.

Glenn F Knoll. *Radiation Detection and Measurement; 3rd ed.* Wiley, New York, NY, 2000. URL `https://cds.cern.ch/record/441925`.

Pavlo Kochkin, A. P. J. van Deursen, M. Marisaldi, A. Ursi, A. I. de Boer, M. Bardet, C. Allasia, J.-F. Boissin, F. Flourens, and N. Østgaard. In-flight observation of gamma ray glows by ildas. *Journal of Geophysical Research: Atmospheres*, Dec 2017. ISSN 2169-897X. doi: 10.1002/2017jd027405. URL `http://dx.doi.org/10.1002/2017JD027405`.

Jun'ichi Kotoku, Kazuo Makishima, Yukari Matsumoto, Mitsuhiro Kohama, Yukikatsu Terada, and Toru Tamagawa. Effects of compton scattering on the gamma-ray spectra of solar flares.

Publications of the Astronomical Society of Japan, 59(6):1161–1174, Dec 2007. ISSN 2053-051X. doi: 10.1093/pasj/59.6.1161. URL `http://dx.doi.org/10.1093/pasj/59.6.1161`.

Paul R. Krehbiel, Ronald J. Thomas, William Rison, Timothy Hamlin, Jeremiah Harlin, and Michael Davis. Gps-based mapping system reveals lightning inside storms. *Eos, Transactions American Geophysical Union*, 81(3):21, 2000. ISSN 0096-3941. doi: 10.1029/00eo00014. URL `http://dx.doi.org/10.1029/00EO00014`.

Y. Kuroda, S. Oguri, Y. Kato, R. Nakata, Y. Inoue, C. Ito, and M. Minowa. A mobile antineutrino detector with plastic scintillators. *Nuclear Instruments and Methods in Physics Research Section A: Accelerators, Spectrometers, Detectors and Associated Equipment*, 690:41–47, Oct 2012. ISSN 0168-9002. doi: 10.1016/j.nima.2012.06.040. URL `http://dx.doi.org/10.1016/j.nima.2012.06.040`.

Y. Kuroda, S. Oguri, Y. Kato, R. Nakata, Y. Inoue, C. Ito, and M. Minowa. Observation of gamma ray bursts at ground level under the thunderclouds. *Physics Letters B*, 758:286–291, Jul 2016. ISSN 0370-2693. doi: 10.1016/j.physletb.2016.05.029. URL `http://dx.doi.org/10.1016/j.physletb.2016.05.029`.

J. R. Lamarsh and A. J. Baratta. *Introduction to Nuclear Engineering, 3rd Edition*. Pearson, 2001.

Lev Davidovich Landau, Evgenii Mikhailovich Lifshitz, and Lev Petrovich Pitaevskii. *Electrodynamics of continuous media; 2nd ed.* Course of theoretical physics. Butterworth, Oxford, 1984. URL `https://cds.cern.ch/record/712712`.

Francois Lefeuvre, Elisabeth Blanc, Jean-Louis Pinçon, Robert Roussel-Dupré, David Lawrence, Jean-André Sauvaud, Jean-Louis Rauch, Hervé de Feraudy, and Dominique Lagoutte. Taranis—a satellite project dedicated to the physics of tles and tgfs. *Space Science Reviews*, 137(1-4):301–315, Jun 2008. ISSN 1572-9672. doi: 10.1007/s11214-008-9414-4. URL `http://dx.doi.org/10.1007/s11214-008-9414-4`.

N. G. Lehtinen, T. F. Bell, and U. S. Inan. Monte carlo simulation of runaway mev electron breakdown with application to red sprites and terrestrial gamma ray flashes. *Journal of Geophysical Research: Space Physics*, 104(A11):24699–24712, Nov 1999. ISSN 0148-0227. doi: 10.1029/1999ja900335. URL `http://dx.doi.org/10.1029/1999JA900335`.

Craig S Levin and Edward J Hoffman. Calculation of positron range and its effect on the fundamental limit of positron emission tomography system spatial resolution. *Physics in Medicine and Biology*, 44(3):781–799, Jan 1999. ISSN 1361-6560. doi: 10.1088/0031-9155/44/3/019. URL `http://dx.doi.org/10.1088/0031-9155/44/3/019`.

L. M. Libby and H. R. Lukens. Production of radiocarbon in tree rings by lightning bolts. *Journal of Geophysical Research*, 78(26):5902–5903, Oct 1973. ISSN 0148-0227. doi: 10.1029/jb078i026p05902. URL `http://dx.doi.org/10.1029/JB078i026p05902`.

Gaopeng Lu, Richard J. Blakeslee, Jingbo Li, David M. Smith, Xuan-Min Shao, Eugene W. McCaul, Dennis E. Buechler, Hugh J. Christian, John M. Hall, and Steven A. Cummer. Lightning mapping observation of a terrestrial gamma-ray flash. *Geophysical Research Letters*, 37(11), Jun 2010. ISSN 0094-8276. doi: 10.1029/2010gl043494. URL `http://dx.doi.org/10.1029/2010GL043494`.

A. Luque. Relativistic runaway ionization fronts. *Physical Review Letters*, 112(4), Jan 2014. ISSN 1079-7114. doi: 10.1103/physrevlett.112.045003. URL http://dx.doi.org/10.1103/PhysRevLett.112.045003.

Fanchao Lyu, Steven A. Cummer, and Lindsay McTague. Insights into high peak current in-cloud lightning events during thunderstorms. *Geophysical Research Letters*, 42(16):6836–6843, Aug 2015. ISSN 0094-8276. doi: 10.1002/2015gl065047. URL http://dx.doi.org/10.1002/2015GL065047.

Fanchao Lyu, Steven A. Cummer, Michael Briggs, Martino Marisaldi, Richard J. Blakeslee, Eric Bruning, Jennifer G. Wilson, William Rison, Paul Krehbiel, Gaopeng Lu, and et al. Ground detection of terrestrial gamma ray flashes from distant radio signals. *Geophysical Research Letters*, 43(16):8728–8734, Aug 2016. ISSN 0094-8276. doi: 10.1002/2016gl070154. URL http://dx.doi.org/10.1002/2016GL070154.

B. G. Mailyan, M. S. Briggs, E. S. Cramer, G. Fitzpatrick, O. J. Roberts, M. Stanbro, V. Connaughton, S. McBreen, P. N. Bhat, and J. R. Dwyer. The spectroscopy of individual terrestrial gamma-ray flashes: Constraining the source properties. *Journal of Geophysical Research: Space Physics*, 121(11):11,346–11,363, Nov 2016. ISSN 2169-9380. doi: 10.1002/2016ja022702. URL http://dx.doi.org/10.1002/2016JA022702.

B. G. Mailyan, A. Nag, M. J. Murphy, M. S. Briggs, J. R. Dwyer, W. Rison, P. R. Krehbiel, L. Boggs, A. Bozarth, E. S. Cramer, and et al. Characteristics of radio emissions associated with terrestrial gamma-ray flashes. *Journal of Geophysical Research: Space Physics*, 123 (7):5933–5948, Jul 2018. ISSN 2169-9380. doi: 10.1029/2018ja025450. URL http://dx.doi.org/10.1029/2018JA025450.

B. G. Mailyan, W. Xu, S. Celestin, M. S. Briggs, J. R. Dwyer, E. S. Cramer, O. J. Roberts, and M. Stanbro. Analysis of individual terrestrial gamma‐ray flashes with lightning leader models and fermi gamma‐ray burst monitor data. *Journal of Geophysical Research: Space Physics*, 124(8):7170–7183, Aug 2019. ISSN 2169-9402. doi: 10.1029/2019ja026912. URL http://dx.doi.org/10.1029/2019JA026912.

R Mardiana, Z.-I Kawasaki, and T Morimoto. Three-dimensional lightning observations of cloud-to-ground flashes using broadband interferometers. *Journal of Atmospheric and Solar-Terrestrial Physics*, 64(1):91–103, Jan 2002. ISSN 1364-6826. doi: 10.1016/s1364-6826(01) 00099-2. URL http://dx.doi.org/10.1016/S1364-6826(01)00099-2.

M. Marisaldi, F. Fuschino, C. Labanti, M. Galli, F. Longo, E. Del Monte, G. Barbiellini, M. Tavani, A. Giuliani, E. Moretti, and et al. Detection of terrestrial gamma ray flashes up to 40 mev by the agile satellite. *Journal of Geophysical Research: Space Physics*, 115(A3), Mar 2010. ISSN 0148-0227. doi: 10.1029/2009ja014502. URL http://dx.doi.org/10.1029/2009JA014502.

L. Marti-Magro and Super-Kamiokande Collaboration. SuperK-Gd. *International Cosmic Ray Conference*, 301:1043, Jan 2017.

Michihiro Matsui, Koji Michishita, and Satoshi Kurihara. Accuracies of location and estimated peak current for negative downward return-strokes to wind turbine observed by jldn. *IEEJ Transactions on Power and Energy*, 135(10):644–645, 2015. ISSN 1348-8147. doi: 10.1541/ieejpes.135.644. URL http://dx.doi.org/10.1541/ieejpes.135.644.

M. McCarthy and G. K. Parks. Further observations of x-rays inside thunderstorms. *Geophysical Research Letters*, 12(6):393–396, Jun 1985. ISSN 0094-8276. doi: 10.1029/gl012i006p00393. URL `http://dx.doi.org/10.1029/GL012i006p00393`.

J. W. Meadows. Cf252fission neutron spectrum from 0.003 to 15.0 mev. *Physical Review*, 157(4):1076–1082, May 1967. ISSN 0031-899X. doi: 10.1103/physrev.157.1076. URL `http://dx.doi.org/10.1103/PhysRev.157.1076`.

Koichiro Michimoto. A study of radar echoes and their relation to lightning discharges of thunderclouds in the hokuriku district. *Journal of the Meteorological Society of Japan. Ser. II*, 71(2):195–204, 1993. doi: 10.2151/jmsj1965.71.2_195.

Gennady Milikh and Robert Roussel-Dupré. Runaway breakdown and electrical discharges in thunderstorms. *Journal of Geophysical Research: Space Physics*, 115(A12):n/a–n/a, Dec 2010. ISSN 0148-0227. doi: 10.1029/2009ja014818. URL `http://dx.doi.org/10.1029/2009JA014818`.

Fusa Miyake, Kentaro Nagaya, Kimiaki Masuda, and Toshio Nakamura. A signature of cosmic-ray increase in ad 774–775 from tree rings in japan. *Nature*, 486(7402):240–242, Jun 2012. ISSN 1476-4687. doi: 10.1038/nature11123. URL `http://dx.doi.org/10.1038/nature11123`.

K. Miyake, T. Suzuki, M. Takashima, M. Takuma, and T. Tada. Winter lightning on japan sea coast-lightning striking frequency to tall structures. *IEEE Transactions on Power Delivery*, 5(3):1370–1376, July 1990. ISSN 0885-8977. doi: 10.1109/61.57979.

K. Miyake, T. Suzuki, and K. Shinjou. Characteristics of winter lightning current on japan sea coast. *IEEE Transactions on Power Delivery*, 7(3):1450–1457, July 1992. doi: 10.1109/61.141864. URL `https://doi.org/10.1109/61.141864`.

Joan Montanyà, Ferran Fabró, Oscar van der Velde, David Romero, Gloria Solà, Juan Ramon Hermoso, Serge Soula, Earle R. Williams, and Nicolau Pineda. Registration of x-rays at 2500m altitude in association with lightning flashes and thunderstorms. *Journal of Geophysical Research: Atmospheres*, 119(3):1492–1503, Feb 2014. ISSN 2169-897X. doi: 10.1002/2013jd021011. URL `http://dx.doi.org/10.1002/2013JD021011`.

C. B. Moore, K. B. Eack, G. D. Aulich, and W. Rison. Energetic radiation associated with lightning stepped-leaders. *Geophysical Research Letters*, 28(11):2141–2144, Jun 2001. ISSN 0094-8276. doi: 10.1029/2001gl013140. URL `http://dx.doi.org/10.1029/2001GL013140`.

Takeshi Morimoto, Akimasa Hirata, Zen Kawasaki, Tomoo Ushio, Akinori Matsumoto, and Lee Jong Ho. An operational vhf broadband digital interferometer for lightning monitoring. *IEEJ Transactions on Fundamentals and Materials*, 124(12):1232–1238, 2004. ISSN 1347-5533. doi: 10.1541/ieejfms.124.1232. URL `http://dx.doi.org/10.1541/ieejfms.124.1232`.

Takeshi Morimoto, Hiroshi Kikuchi, Mitsuteru Sato, Tomoo Ushio, Atsushi Yamazaki, Makoto Suzuki, Ryohei Ishida, Yuji Sakamoto, Kazuya Yoshida, Yasuhide Hobara, and et al. An overview of vhf lightning observations by digital interferometry from iss/jem-glims. *Earth, Planets and Space*, 68(1), Aug 2016. ISSN 1880-5981. doi: 10.1186/s40623-016-0522-1. URL `http://dx.doi.org/10.1186/s40623-016-0522-1`.

Gregory D. Moss, Victor P. Pasko, Ningyu Liu, and Georgios Veronis. Monte carlo model for analysis of thermal runaway electrons in streamer tips in transient luminous events and streamer zones of lightning leaders. *Journal of Geophysical Research*, 111(A2), 2006. ISSN 0148-0227. doi: 10.1029/2005ja011350. URL `http://dx.doi.org/10.1029/2005JA011350`.

Yasushi Muraki, Wiliam Ian Axford, Yutaka Matsubara, Kimiaki Masuda, Yoichi Miyamoto, Hiroaki Menjyou, Shizuko Sakakibara, Takashi Sako, Takashi Takami, Takami Yamada, Shoichi Shibata, Yoshinori Munakata, Kazuoki Munakata, Shinnichi Yasue, Takasuke Sakai, Kiyomi Mitsui, Kazuhiko Fujimoto, and Erwin Flückiger. Effects of atmospheric electric fields on cosmic rays. *Phys. Rev. D*, 69:123010, Jun 2004. doi: 10.1103/PhysRevD.69.123010. URL `https://link.aps.org/doi/10.1103/PhysRevD.69.123010`.

A. Nag, S. Mallick, V. A. Rakov, J. S. Howard, C. J. Biagi, J. D. Hill, M. A. Uman, D. M. Jordan, K. J. Rambo, J. E. Jerauld, and et al. Evaluation of u.s. national lightning detection network performance characteristics using rocket-triggered lightning data acquired in 2004–2009. *Journal of Geophysical Research*, 116(D2), Jan 2011. ISSN 0148-0227. doi: 10.1029/2010jd014929. URL `http://dx.doi.org/10.1029/2010JD014929`.

Torsten Neubert, Nikolai Østgaard, Victor Reglero, Elisabeth Blanc, Olivier Chanrion, Carol Anne Oxborrow, Astrid Orr, Matteo Tacconi, Ole Hartnack, and Dan D. V. Bhanderi. The asim mission on the international space station. *Space Science Reviews*, 215(2), Mar 2019. ISSN 1572-9672. doi: 10.1007/s11214-019-0592-z. URL `http://dx.doi.org/10.1007/s11214-019-0592-z`.

S. Oguri, Y. Kuroda, Y. Kato, R. Nakata, Y. Inoue, C. Ito, and M. Minowa. Reactor antineutrino monitoring with a plastic scintillator array as a new safeguards method. *Nuclear Instruments and Methods in Physics Research Section A: Accelerators, Spectrometers, Detectors and Associated Equipment*, 757:33–39, Sep 2014. ISSN 0168-9002. doi: 10.1016/j.nima.2014.04.065. URL `http://dx.doi.org/10.1016/j.nima.2014.04.065`.

N. Østgaard, T. Gjesteland, R. S. Hansen, A. B. Collier, and B. Carlson. The true fluence distribution of terrestrial gamma flashes at satellite altitude. *Journal of Geophysical Research: Space Physics*, 117(A3):n/a–n/a, Mar 2012. ISSN 0148-0227. doi: 10.1029/2011ja017365. URL `http://dx.doi.org/10.1029/2011JA017365`.

N. Østgaard, H.J. Christian, J.E. Grove, D. Sarria, A. Mezentsev, P. Kochkin, N. Lehtinen, M. Quick, S. Al‐Nussirat, E. Wulf, and et al. Gamma‐ray glow observations at 20 km altitude. *Journal of Geophysical Research: Atmospheres*, May 2019. ISSN 2169-8996. doi: 10.1029/2019jd030312. URL `http://dx.doi.org/10.1029/2019JD030312`.

G. K. Parks, B. H. Mauk, R. Spiger, and J. Chin. X-ray enhancements detected during thunderstorm and lightning activities. *Geophysical Research Letters*, 8(11):1176–1179, Nov 1981. ISSN 0094-8276. doi: 10.1029/gl008i011p01176. URL `http://dx.doi.org/10.1029/GL008i011p01176`.

D. J. Pleshinger, S. T. Alnussirat, J. Arias, S. Bai, Y. Banadaki, M. L. Cherry, J. H. Hoffman, E. Khosravi, M. D. Legault, R. Rodriguez, and et al. Gamma ray flashes produced by lightning observed at ground level by tetra‐ii. *Journal of Geophysical Research: Space Physics*, Nov 2019. ISSN 2169-9402. doi: 10.1029/2019ja026820. URL `http://dx.doi.org/10.1029/2019JA026820`.

S. V. Poluianov, G. A. Kovaltsov, A. L. Mishev, and I. G. Usoskin. Production of cosmogenic isotopes7be,10be,14c,22na, and36cl in the atmosphere: Altitudinal profiles of yield functions. *Journal of Geophysical Research: Atmospheres*, 121(13):8125–8136, Jul 2016. ISSN 2169-897X. doi: 10.1002/2016jd025034. URL `http://dx.doi.org/10.1002/2016JD025034`.

V. A. Rakov and M. A. Uman. *Lightning: Physics and Effects*. Cambridge University Press, 2003. ISBN 9780521035415. URL `https://books.google.co.jp/books?id=TuMa5lAa3RAC`.

P.L. Reeder. Thin gso scintillator for neutron detection. *Nuclear Instruments and Methods in Physics Research Section A: Accelerators, Spectrometers, Detectors and Associated Equipment*, 353(1-3):134–136, Dec 1994. ISSN 0168-9002. doi: 10.1016/0168-9002(94)91619-5. URL `http://dx.doi.org/10.1016/0168-9002(94)91619-5`.

Rebecca Ringuette, Gary L. Case, Michael L. Cherry, Douglas Granger, T. Gregory Guzik, Michael Stewart, and John P. Wefel. Tetra observation of gamma-rays at ground level associated with nearby thunderstorms. *Journal of Geophysical Research: Space Physics*, 118(12):7841–7849, Dec 2013. ISSN 2169-9380. doi: 10.1002/2013ja019112. URL `http://dx.doi.org/10.1002/2013JA019112`.

W. Rison, R. J. Thomas, P. R. Krehbiel, T. Hamlin, and J. Harlin. A gps-based three-dimensional lightning mapping system: Initial observations in central new mexico. *Geophysical Research Letters*, 26(23):3573–3576, Dec 1999. ISSN 0094-8276. doi: 10.1029/1999gl010856. URL `http://dx.doi.org/10.1029/1999GL010856`.

M L Roberts and J R Southon. A preliminary determination of the absolute 14c/12c ratio of oxi. *Radiocarbon*, 49(2):441–445, 2007. ISSN 1945-5755. doi: 10.1017/s0033822200042363. URL `http://dx.doi.org/10.1017/S0033822200042363`.

C. J. Rodger, J. B. Brundell, R. H. Holzworth, E. H. Lay, Norma B. Crosby, Tai-Yin Huang, and Michael J. Rycroft. Growing detection efficiency of the world wide lightning location network. *AIP Conference Proceedings*, 2009. doi: 10.1063/1.3137706. URL `http://dx.doi.org/10.1063/1.3137706`.

R. Roussel-Dupré, J. J. Colman, E. Symbalisty, D. Sentman, and V. P. Pasko. Physical processes related to discharges in planetary atmospheres. *Space Science Reviews*, 137(1-4):51–82, Jun 2008. ISSN 1572-9672. doi: 10.1007/s11214-008-9385-5. URL `http://dx.doi.org/10.1007/s11214-008-9385-5`.

Z. Saleh, J. Dwyer, J. Howard, M. Uman, M. Bakhtiari, D. Concha, M. Stapleton, D. Hill, C. Biagi, and H. Rassoul. Properties of the x-ray emission from rocket-triggered lightning as measured by the thunderstorm energetic radiation array (tera). *Journal of Geophysical Research*, 114(D17), Sep 2009. ISSN 0148-0227. doi: 10.1029/2008jd011618. URL `http://dx.doi.org/10.1029/2008JD011618`.

David Sarria, Francois Lebrun, Pierre-Louis Blelly, Remi Chipaux, Philippe Laurent, Jean-Andre Sauvaud, Lubomir Prech, Pierre Devoto, Damien Pailot, Jean-Pierre Baronick, and et al. Taranis xgre and idee detection capability of terrestrial gamma-ray flashes and associated electron beams. *Geoscientific Instrumentation, Methods and Data Systems*, 6 (2):239–256, Jul 2017. ISSN 2193-0864. doi: 10.5194/gi-6-239-2017. URL `http://dx.doi.org/10.5194/gi-6-239-2017`.

David Sarria, Casper Rutjes, Gabriel Diniz, Alejandro Luque, Kevin M. A. Ihaddadene, Joseph R. Dwyer, Nikolai Østgaard, Alexander B. Skeltved, Ivan S. Ferreira, and Ute Ebert. Evaluation of monte carlo tools for high-energy atmospheric physics ii: relativistic runaway electron avalanches. *Geoscientific Model Development*, 11(11):4515–4535, Nov 2018. ISSN 1991-9603. doi: 10.5194/gmd-11-4515-2018. URL http://dx.doi.org/10.5194/gmd-11-4515-2018.

Tatsuhiko Sato. Analytical model for estimating terrestrial cosmic ray fluxes nearly anytime and anywhere in the world: Extension of parma/expacs. *PLOS ONE*, 10(12):e0144679, Dec 2015. ISSN 1932-6203. doi: 10.1371/journal.pone.0144679. URL http://dx.doi.org/10.1371/journal.pone.0144679.

Tatsuhiko Sato. Analytical model for estimating the zenith angle dependence of terrestrial cosmic ray fluxes. *PLOS ONE*, 11(8):e0160390, Aug 2016. ISSN 1932-6203. doi: 10.1371/journal.pone.0160390. URL http://dx.doi.org/10.1371/journal.pone.0160390.

M. M. Schaal, J. R. Dwyer, Z. H. Saleh, H. K. Rassoul, J. D. Hill, D. M. Jordan, and M. A. Uman. Spatial and energy distributions of x-ray emissions from leaders in natural and rocket triggered lightning. *Journal of Geophysical Research: Atmospheres*, 117(D15):n/a–n/a, Aug 2012. ISSN 0148-0227. doi: 10.1029/2012jd017897. URL http://dx.doi.org/10.1029/2012JD017897.

G. N. Shah, H. Razdan, C. L. Bhat, and Q. M. Ali. Neutron generation in lightning bolts. *Nature*, 313(6005):773–775, Feb 1985. ISSN 1476-4687. doi: 10.1038/313773a0. URL http://dx.doi.org/10.1038/313773a0.

M. Shamsuzzoha Basunia. Nuclear data sheets for a = 28. *Nuclear Data Sheets*, 114(10):1189–1291, Oct 2013. ISSN 0090-3752. doi: 10.1016/j.nds.2013.10.001. URL http://dx.doi.org/10.1016/j.nds.2013.10.001.

Keiichi Shibata, Osamu Iwamoto, Tsuneo Nakagawa, Nobuyuki Iwamoto, Akira Ichihara, Satoshi Kunieda, Satoshi Chiba, Kazuyoshi Furutaka, Naohiko Otuka, Takaaki Ohsawa, and et al. Jendl-4.0: A new library for nuclear science and engineering. *Journal of Nuclear Science and Technology*, 48(1):1–30, Jan 2011. ISSN 1881-1248. doi: 10.1080/18811248.2011.9711675. URL http://dx.doi.org/10.1080/18811248.2011.9711675.

D. A. Smith, M. J. Heavner, A. R. Jacobson, X. M. Shao, R. S. Massey, R. J. Sheldon, and K. C. Wiens. A method for determining intracloud lightning and ionospheric heights from vlf/lf electric field records. *Radio Science*, 39(1):n/a–n/a, Feb 2004. ISSN 0048-6604. doi: 10.1029/2002rs002790. URL http://dx.doi.org/10.1029/2002RS002790.

D. M. Smith, G. S. Bowers, M. Kamogawa, D. Wang, T. Ushio, J. Ortberg, J. R. Dwyer, and M. Stock. Characterizing upward lightning with and without a terrestrial gamma-ray flash. *Journal of Geophysical Research: Atmospheres*, Sep 2018. ISSN 2169-897X. doi: 10.1029/2018jd029105. URL http://dx.doi.org/10.1029/2018jd029105.

David M. Smith, Liliana I. Lopez, R. P. Lin, and Christopher P. Barrington-Leigh. Terrestrial gamma-ray flashes observed up to 20 mev. *Science*, 307(5712):1085–1088, 2005. ISSN 0036-8075. doi: 10.1126/science.1107466. URL http://science.sciencemag.org/content/307/5712/1085.

Tsutomu Takahashi. Riming electrification as a charge generation mechanism in thunderstorms. *Journal of the Atmospheric Sciences*, 35(8):1536–1548, Aug 1978. ISSN 1520-0469. doi: 10.1175/1520-0469(1978)035⟨1536:reaacg⟩2.0.co;2. URL http://dx.doi.org/10.1175/1520-0469(1978)035<1536:REAACG>2.0.CO;2.

M. Tavani, M. Marisaldi, C. Labanti, F. Fuschino, A. Argan, A. Trois, P. Giommi, S. Colafrancesco, C. Pittori, F. Palma, and et al. Terrestrial gamma-ray flashes as powerful particle accelerators. *Physical Review Letters*, 106(1), Jan 2011. ISSN 1079-7114. doi: 10.1103/physrevlett.106.018501. URL http://dx.doi.org/10.1103/PhysRevLett.106.018501.

M. Tavani, A. Argan, A. Paccagnella, A. Pesoli, F. Palma, S. Gerardin, M. Bagatin, A. Trois, P. Picozza, P. Benvenuti, and et al. Possible effects on avionics induced by terrestrial gamma-ray flashes. *Natural Hazards and Earth System Sciences*, 13(4):1127–1133, Apr 2013. ISSN 1684-9981. doi: 10.5194/nhess-13-1127-2013. URL http://dx.doi.org/10.5194/nhess-13-1127-2013.

The Institute of Electrical Engineers of Japan. *Radiation Engineering*. Ohm Publishing, 1982.

D.R. Tilley, H.R. Weller, and C.M. Cheves. Energy levels of light nuclei a = 16–17. *Nuclear Physics A*, 564(1):1–183, Nov 1993. ISSN 0375-9474. doi: 10.1016/0375-9474(93)90073-7. URL http://dx.doi.org/10.1016/0375-9474(93)90073-7.

Tatsuo Torii, Minoru Takeishi, and Teruo Hosono. Observation of gamma-ray dose increase associated with winter thunderstorm and lightning activity. *Journal of Geophysical Research: Atmospheres*, 107(D17):ACL 2–1–ACL 2–13, Sep 2002. ISSN 0148-0227. doi: 10.1029/2001jd000938. URL http://dx.doi.org/10.1029/2001JD000938.

Tatsuo Torii, Takeshi Nishijima, Zen-Ichiro Kawasaki, and Takeshi Sugita. Downward emission of runaway electrons and bremsstrahlung photons in thunderstorm electric fields. *Geophysical Research Letters*, 31(5), 2004. doi: 10.1029/2003GL019067. URL https://agupubs.onlinelibrary.wiley.com/doi/abs/10.1029/2003GL019067.

Tatsuo Torii, Takeshi Sugita, Sachiko Tanabe, Yoshihisa Kimura, Masashi Kamogawa, Kazuaki Yajima, and Hiroshi Yasuda. Gradual increase of energetic radiation associated with thunderstorm activity at the top of mt. fuji. *Geophysical Research Letters*, 36(13), Jul 2009. ISSN 0094-8276. doi: 10.1029/2008gl037105. URL http://dx.doi.org/10.1029/2008GL037105.

Tatsuo Torii, Takeshi Sugita, Masashi Kamogawa, Yasuyuki Watanabe, and Kenichi Kusunoki. Migrating source of energetic radiation generated by thunderstorm activity. *Geophysical Research Letters*, 38(24), Dec 2011. ISSN 0094-8276. doi: 10.1029/2011gl049731. URL http://dx.doi.org/10.1029/2011GL049731.

M.D. Tran, V.A. Rakov, S. Mallick, J.R. Dwyer, A. Nag, and S. Heckman. A terrestrial gamma-ray flash recorded at the lightning observatory in gainesville, florida. *Journal of Atmospheric and Solar-Terrestrial Physics*, 136:86–93, Dec 2015. ISSN 1364-6826. doi: 10.1016/j.jastp.2015.10.010. URL http://dx.doi.org/10.1016/j.jastp.2015.10.010.

H. Tsuchiya, T. Enoto, S. Yamada, T. Yuasa, M. Kawaharada, T. Kitaguchi, M. Kokubun, H. Kato, M. Okano, S. Nakamura, and et al. Detection of high-energy gamma rays

from winter thunderclouds. *Physical Review Letters*, 99(16), Oct 2007. ISSN 1079-7114. doi: 10.1103/physrevlett.99.165002. URL http://dx.doi.org/10.1103/PhysRevLett.99.165002.

H. Tsuchiya, T. Enoto, T. Torii, K. Nakazawa, T. Yuasa, S. Torii, T. Fukuyama, T. Yamaguchi, H. Kato, M. Okano, and et al. Observation of an energetic radiation burst from mountain-top thunderclouds. *Physical Review Letters*, 102(25), Jun 2009. ISSN 1079-7114. doi: 10.1103/physrevlett.102.255003. URL http://dx.doi.org/10.1103/PhysRevLett.102.255003.

H. Tsuchiya, T. Enoto, S. Yamada, T. Yuasa, K. Nakazawa, T. Kitaguchi, M. Kawaharada, M. Kokubun, H. Kato, M. Okano, and et al. Long-duration γ ray emissions from 2007 and 2008 winter thunderstorms. *Journal of Geophysical Research*, 116(D9), May 2011. ISSN 0148-0227. doi: 10.1029/2010jd015161. URL http://dx.doi.org/10.1029/2010JD015161.

H. Tsuchiya, K. Hibino, K. Kawata, N. Hotta, N. Tateyama, M. Ohnishi, M. Takita, D. Chen, J. Huang, M. Miyasaka, and et al. Observation of thundercloud-related gamma rays and neutrons in tibet. *Physical Review D*, 85(9), May 2012. ISSN 1550-2368. doi: 10.1103/physrevd.85.092006. URL http://dx.doi.org/10.1103/PhysRevD.85.092006.

H. Tsuchiya, T. Enoto, K. Iwata, S. Yamada, T. Yuasa, T. Kitaguchi, M. Kawaharada, K. Nakazawa, M. Kokubun, H. Kato, and et al. Hardening and termination of long-duration γ rays detected prior to lightning. *Physical Review Letters*, 111(1), Jul 2013. ISSN 1079-7114. doi: 10.1103/physrevlett.111.015001. URL http://dx.doi.org/10.1103/PhysRevLett.111.015001.

D. Umemoto, H. Tsuchiya, T. Enoto, S. Yamada, T. Yuasa, M. Kawaharada, T. Kitaguchi, K. Nakazawa, M. Kokubun, H. Kato, and et al. On-ground detection of an electron-positron annihilation line from thunderclouds. *Physical Review E*, 93(2), Feb 2016. ISSN 2470-0053. doi: 10.1103/physreve.93.021201. URL http://dx.doi.org/10.1103/PhysRevE.93.021201.

Y. Wada, G. S. Bowers, T. Enoto, M. Kamogawa, Y. Nakamura, T. Morimoto, D. M. Smith, Y. Furuta, K. Nakazawa, T. Yuasa, and et al. Termination of electron acceleration in thundercloud by intracloud/intercloud discharge. *Geophysical Research Letters*, 45(11): 5700–5707, Jun 2018. ISSN 0094-8276. doi: 10.1029/2018gl077784. URL http://dx.doi.org/10.1029/2018GL077784.

Y. Wada, T. Enoto, Y. Furuta, K. Nakazawa, T. Yuasa, T. Matsumoto, D. Umemoto, K. Makishima, and H. Tsuchiya. Mapping Observation Project of High-Energy Phenomena during Winter Thunderstorms in Japan. In *Proceedings of International Symposium TEPA 2018: Thunderstorms and Elementary Particle Acceleration*, pages 85–92, Mar 2019a.

Y. Wada, T. Enoto, K. Nakazawa, Y. Furuta, T. Yuasa, Y. Nakamura, T. Morimoto, T. Matsumoto, K. Makishima, and H. Tsuchiya. Downward terrestrial gamma-ray flash observed in a winter thunderstorm. *Physical Review Letters*, 123(6), Aug 2019b. ISSN 1079-7114. doi: 10.1103/physrevlett.123.061103. URL http://dx.doi.org/10.1103/PhysRevLett.123.061103.

Yuuki Wada, Teruaki Enoto, Yoshitaka Nakamura, Yoshihiro Furuta, Takayuki Yuasa, Kazuhiro Nakazawa, Takeshi Morimoto, Mitsuteru Sato, Takahiro Matsumoto, Daisuke Yonetoku, Tatsuya Sawano, Hideo Sakai, Masashi Kamogawa, Tomoo Ushio, Kazuo Makishima, and Harufumi Tsuchiya. Gamma-ray glow preceding downward terrestrial gamma-ray flash. *Communications Physics*, 2(1):67, 2019c. doi: 10.1038/s42005-019-0168-y. URL `https://doi.org/10.1038/s42005-019-0168-y`.

C. T. R. Wilson. The acceleration of β-particles in strong electric fields such as those of thunderclouds. *Mathematical Proceedings of the Cambridge Philosophical Society*, 22(04): 534, Mar 1925. ISSN 1469-8064. doi: 10.1017/s0305004100003236. URL `http://dx.doi.org/10.1017/S0305004100003236`.

Mikio Yamashita, Lloyd D. Stephens, and H. Wade Patterson. Cosmic-ray-produced neutrons at ground level: Neutron production rate and flux distribution. *Journal of Geophysical Research*, 71(16):3817–3834, Aug 1966. ISSN 0148-0227. doi: 10.1029/jz071i016p03817. URL `http://dx.doi.org/10.1029/JZ071i016p03817`.

S. Yoshida, T. Morimoto, T. Ushio, Z.-I. Kawasaki, T. Torii, D. Wang, N. Takagi, and T. Watanabe. High energy photon and electron bursts associated with upward lightning strokes. *Geophysical Research Letters*, 35(10), May 2008. ISSN 0094-8276. doi: 10.1029/2007gl032438. URL `http://dx.doi.org/10.1029/2007gl032438`.

Acknowledgement

Finally, I would like to appreciate dedicated supports from my parents, Yoshimi and Tetsuo, my sister Mari, and my lovely wife Shiho.

Tous les chemins ménent à Rome...

December 2019,
Yuuki Wada

Reference Paper
参考論文

Gamma-ray Glow Preceding
Downward Terrestrial Gamma-ray Flash

A Dissertation Submitted for the Degree of Doctor of Philosophy

December 2019

令和元年12月 博士 (理学) 申請

Department of Physics, Graduate School of Science,
The University of Tokyo
東京大学大学院理学系研究科
物理学専攻

Yuuki Wada
和田 有希

ARTICLE

Gamma-ray glow preceding downward terrestrial gamma-ray flash

Yuuki Wada [1,2,3], Teruaki Enoto [2,4], Yoshitaka Nakamura[5], Yoshihiro Furuta[6], Takayuki Yuasa [7], Kazuhiro Nakazawa [8], Takeshi Morimoto [9], Mitsuteru Sato[10], Takahiro Matsumoto[1], Daisuke Yonetoku[11], Tatsuya Sawano[11], Hideo Sakai[12], Masashi Kamogawa[13], Tomoo Ushio[14], Kazuo Makishima[1,2,15] & Harufumi Tsuchiya[16]

Two types of high-energy events have been detected from thunderstorms. One is "terrestrial gamma-ray flashes" (TGFs), sub-millisecond emissions coinciding with lightning discharges. The other is minute-lasting "gamma-ray glows". Although both phenomena are thought to originate from relativistic runaway electron avalanches in strong electric fields, the connection between them is not well understood. Here we report unequivocal simultaneous detection of a gamma-ray glow termination and a downward TGF, observed from the ground. During a winter thunderstorm in Japan on 9 January 2018, our detectors caught a gamma-ray glow, which moved for ~100 s with ambient wind, and then abruptly ceased with a lightning discharge. Simultaneously, the detectors observed photonuclear reactions triggered by a downward TGF, whose radio pulse was located within ~1 km from where the glow ceased. It is suggested that the highly-electrified region producing the glow was related to the initiation of the downward TGF.

---

[1] Department of Physics, Graduate School of Science, The University of Tokyo, 7-3-1, Hongo, Bunkyo-ku, Tokyo 113-8654, Japan. [2] High Energy Astrophysics Laboratory, RIKEN Nishina Center, 2-1, Hirosawa, Wako, Saitama 351-0198, Japan. [3] Laboratoire AstroParticule et Cosmologie, Université Paris Diderot, CNRS/IN2P3, CEA/DRF/IRFU, Observatoire de Paris, 10, rue Alice Domon et Léonie Duquet, 75013 Paris, France. [4] The Hakubi Center for Advanced Research and Department of Astronomy, Kyoto University, Kitashirakawa Oiwake-cho, Sakyo-ku, Kyoto 606-8302, Japan. [5] Department of Electrical Engineering, Kobe City College of Technology, 8-3, Gakuen-Higashimachi, Nishi-ku, Kobe, Hyogo 651-2194, Japan. [6] Collaborative Laboratories for Advanced Decommissioning Science, Japan Atomic Energy Agency, 2-4 Shirakata, Tokai-mura, Naka-gun, Ibaraki 319-1195, Japan. [7] Block 4B, Boon Tiong Road, Singapore 165004, Singapore. [8] Kobayashi-Maskawa Institute for the Origin of Particles and the Universe, Nagoya University, Furo-cho, Chikusa-ku, Nagoya, Aichi 464-8601, Japan. [9] Faculty of Science and Engineering, Kindai University, 3-4-1 Kowakae, Higashiosaka, Osaka 577-8502, Japan. [10] Graduate School of Science, Hokkaido University, Kita 8, Nishi 5, Kita-ku, Sapporo, Hokkaido 060-0808, Japan. [11] School of Mathematics and Physics, Kanazawa University, Kakuma, Kanazawa, Ishikawa 920-1192, Japan. [12] University of Toyama, 3190 Gofuku, Toyama, Toyama 930-0887, Japan. [13] Global Center for Asian and Regional Research, University of Shizuoka, 3-6-1, Takajo, Aoi-ku, Shizuoka, Shizuoka 420-0839, Japan. [14] Faculty of Systems Design, Tokyo Metropolitan University, 6-6 Asahigaoka, Hino, Tokyo 191-0065, Japan. [15] Kavli Institute for the Physics and Mathematics of the Universe, The University of Tokyo, 5-1-5 Kashiwa-no-ha, Kashiwa, Chiba 277-8683, Japan. [16] Nuclear Science and Engineering Center, Japan Atomic Energy Agency, 2-4 Shirakata, Tokai-mura, Naka-gun, Ibaraki 319-1195, Japan. Correspondence and requests for materials should be addressed to Y.W. (email: wada@juno.phys.s.u-tokyo.ac.jp)

Since McCarthy and Parks[1] found radiation-dose enhancements inside thunderclouds with an airborne detector in 1980s, high-energy phenomena associated with thunderstorms have been detected inside the Earth's atmosphere and from space. Terrestrial gamma-ray flashes (TGFs) are burst-like emission with their photon energy extending up to 20 MeV that last for several hundred microseconds, coincident with lightning discharges. They were first detected from space by Compton Gamma-Ray Observatory[2], and since then have been reported by many other satellites[3–8]. Similar phenomena but going downward have been found in recent years at ground level[9–17]. They, now called "downward TGFs", share several features with TGFs observed from space, such as coincidence with lightning, sub-millisecond durations, and energy spectra extending to >10 MeV. Downward TGFs that contains enough photons above 10 MeV have been experimentally shown to trigger atmospheric photonuclear reactions, namely producing neutrons and positron-emitting radioactive nuclei[13,14]. These photoneutrons can be observed as a short-duration gamma-ray burst lasting for several hundreds of milliseconds, as they are absorbed by atmospheric nuclei via neutron-capture processes[14,18].

Gamma-ray glows, also referred to as long bursts[19] or thunderstorm ground enhancements[20], are energetic radiation from thunderclouds with energies up to tens of MeVs, lasting for a few seconds to several minutes. They have been observed by airborne detectors[1,21–23], at mountain-top[20,24–29] and sea-level observation sites[19,30–33]. Gamma-ray glows usually coincide with passage of thunderclouds, and sometimes cease at the moment when lightning discharges take place[1,21–23,34–38].

Although TGFs and gamma-ray glows are distinguished clearly by duration, brightness, and timing with regard to lightning discharges, both of them are thought to originate from a common fundamental mechanism, called relativistic runaway electron avalanches (RREAs[39,40]). According to Wilson's hypothesis[41], seed electrons (provided by, e.g., cosmic rays) can be accelerated up to an energy of tens of MeVs in strong electric fields, producing secondary electrons. The number of multiplied and accelerated electrons exponentially increases, and the accelerated electrons finally emit bremsstrahlung gamma rays as they interact with ambient atmospheric nuclei. Dwyer[42] proposed additional electron-seeding processes by positrons and backscattered gamma rays into the RREA mechanism, called "relativistic feedback model". This model can achieve a higher multiplication factor than that of a RREA alone, and thus are thought to explain extraordinarily high brightness of TGFs.

Despite an increasing number of respective observation samples of TGFs and gamma-ray glows, connections between them remain poorly understood. This is primarily because there has been no report of simultaneous detection of both, except for a very recent short report on a marginal detection[17]. In this paper, we report the first unequivocal simultaneous detection of them at sea level and discuss its implications.

Results

Observation of high-energy phenomena in winter thunderstorms.
The Gamma-ray Observation of Winter Thunderclouds (GROWTH) collaboration[31,32,35,43] has been engaged with a multi-point observation campaign of atmospheric high-energy phenomena in coastal areas of Japan Sea[14,44]. Winter thunderstorms in Japan are ideal targets to observe this type of phenomena due to their unique characteristics; most notably typical altitude of clouds is significantly lower than ordinary[38,45,46], which makes sea-level observations of gamma-ray glows viable.

We have developed portable radiation detectors dedicated to the multi-point observation. They have a 25 cm × 8 cm × 2.5 cm

$Bi_4Ge_3O_{12}$ (BGO) scintillation crystal coupled with two photomultiplier tubes (PMTs; HAMAMATSU R1924A). Outputs from the PMTs are amplified, and then read out by a 50 MHz digitiser onboard a data acquisition system. The data acquisition system stores 20-μs waveforms of the amplified analogue outputs once a pulse is detected, and extracts the maximum and minimum value as well as the timing of the pulse (see also Detector calibration). The maximum value corresponds to the energies of the pulse, and the minimum the analogue baseline voltage. The data acquisition system also records counts of discarded photon events due to buffer overflow, which are used for dead-time correction. Three detectors were deployed at three observation sites in Kanazawa City, the capital of Ishikawa Prefecture, by the Japan Sea coast (Fig. 1) and have been operated since October 2016.

Lightning discharges were monitored by a broadband low-frequency (LF: 0.8–500 kHz) lightning mapping network (hereafter LF network), for which detectors are installed along Toyama Bay and in Noto peninsula. Another receiver in the extreme-low-frequency band (ELF: 1–100 Hz) is installed at Kuju, as summarised in the section Radio observations. We also utilise lightning location data of Japanese Lightning Detection Network (JLDN) operated by Franklin Japan Co., Ltd.

Detection of gamma-ray glow and downward TGF.
On 9 January 2018, two of our detectors shown in Fig. 1 recorded gamma-ray glows. Figure 2a, b shows long-term count-rate histories of detectors A and B, respectively. At around 17:54 in coordinated universal time (UTC), detector A at Kanazawa Izumigaoka High School (36.538°N, 136.649°E) recorded a radiation increase for ~60 s. Then, ~30 s later, detector B at Kanazawa University High School (36.539°N, 136.664°E, 1.3 km east from detector A) also recorded a gamma-ray glow. No radiation enhancements were observed by detector C at Kanazawa University Kakuma Campus (36.546°N, 136.709°E; 4 km from detector B) in the period. The glow then suddenly terminated, coincident with a lightning discharge, while it was still being observed by detector B.

An snapshot image of the X-band radar network at 17:55 shows a heavy precipitation area, corresponding to a thundercloud, located between detectors A and B (Fig. 1a). The radar data suggest that the thundercloud passed over the two detectors towards east-northeast with a speed of 19.3 ± 1.4 m s^{-1} (see Wind estimation with X-band radar). Since the temporal separation between the glow detection by the two detectors is consistent with the time for the thundercloud to travel the distance between the two detectors, we consider that the gamma-ray glows recorded by the two detectors are from the same cloud and hence of the same origin.

At the same time as the glow termination and the lightning discharge, both detectors A and B recorded a short-duration radiation burst lasting for ~200 ms simultaneously. The count-rate profiles of the 200-ms-lasting short burst shown in Fig. 2c, d exhibit a steep rise and decay with time constants of 52.0 ± 4.9 and 59.2 ± 1.7 ms for detectors A and B, respectively. Combining the timing analysis with spectral analysis (see Gamma-ray emission originating from neutrons), the short burst is found to originate from neutron captures by atmospheric nitrogen nuclei, which Rutjes et al.[18] predicted as "TGF afterglow", and Enoto et al.[14] observationally demonstrated. In addition, detector B recorded a faint annihilation emission at 511 keV for 10 s after the short burst (see Positron production by beta-plus decay). These features imply that atmospheric photonuclear reactions such as $^{14}N + \gamma \rightarrow {}^{13}N + n$ and $^{16}O + \gamma \rightarrow {}^{15}O + n$ took place coincident with the lightning discharge, as discussed in Bowers et al.[13] and Enoto et al.[14].
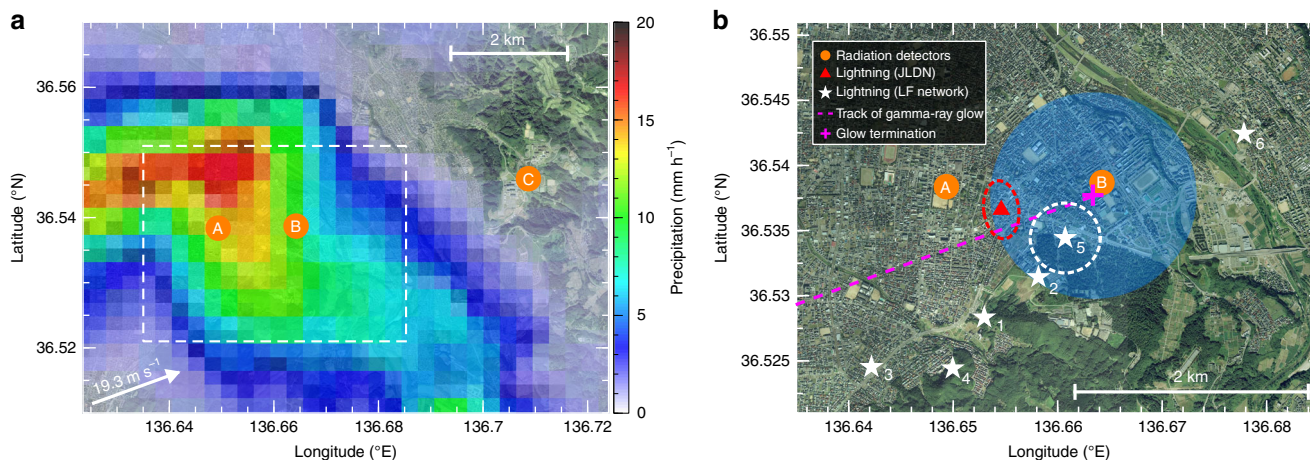
Fig. 1 Maps of observation sites in Kanazawa. **a** A precipitation map at 17:55 on 9 January 2018 in coordinated universal time, obtained by the extended radar information network. Orange circles show radiation monitors, the white arrow the wind speed and its direction, and the dashed-line rectangle the region of panel **b**. **b** A panoramic photograph around detectors A and B marked by filled orange circles. The lightning locations determined by Japanese Lightning Detection Network and our low-frequency network are marked by red triangles and white stars, respectively. The numbers beside the white stars correspond to the order of the low-frequency pulses. A typical locating error circle (~300 m in radius) is overlaid for the fifth pulse. The magenta dashed line shows a track of the centre of the gamma-ray glow, which ceased at the magenta cross marker. The shaded blue circle shows the region where 30-s-binned count rates in the 3.0–20.0 MeV band reached twice or more higher than the background rates when the glow disappeared, estimated with the simulation (see Simulation of gamma-ray glow). This corresponds to a detection significance of 8.1σ or higher. The radius of the region is 0.88 km. The background photographs are provided by the Geospatial Information Authority of Japan
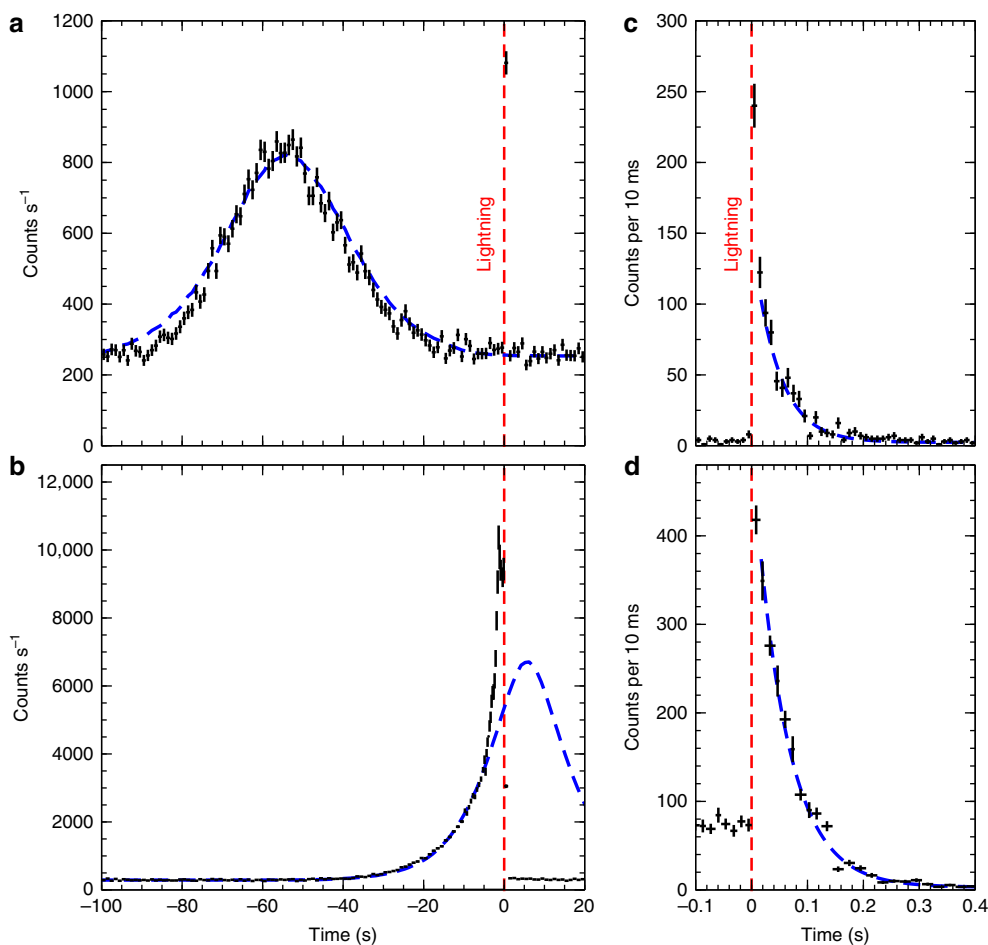
Fig. 2 Count-rate histories of gamma-ray glow and short-duration burst. **a**, **b** One-sec-binned histories of detectors A (**a**) and B (**b**) at around the events with ±1σ statistical errors for an energy range of 0.4–20.0 MeV. The origin of the X axis is 17:54:50.308892 in coordinated universal time. Blue lines show the best-prediction profile from Monte Carlo simulations. Red dashed lines show the timing of the lightning discharge. **c**, **d** Histories with finer bins for the same energy band. Blue lines show the best-fitting model of an exponential function with time constants of 52.0 ± 4.9 and 59.2 ± 1.7 ms for detectors A and B, respectively

Figure 3a, b shows the maximum and minimum waveform values of photon events during the short burst recorded by detectors A and B, respectively. At the very beginning of the short burst, both detectors A and B recorded saturated pulses (the maximum values exceeding >4 V), and then significant negative values of the baseline (the minimum values) called "undershoot" for ~10 ms. Although detector B failed to acquire the main part of the undershoot due to buffer overflow in the data acquisition system, it recorded the saturated pulses and the last part of the undershoot. As demonstrated in Methods: Initial flash of Enoto et al.[14], this feature manifests the existence of an extremely large energy deposit (much more than hundreds of

MeVs) in the scintillation crystal within a few milliseconds, which is a clear sign of a downward TGF. In the following analysis we employ an elapsed time t from the onset of the downward TGF at 17:54:50.308892 UTC, recorded by detector B.

The LF network recorded a consecutive series of waveforms of the lightning discharge lasting for ~400 ms (Fig. 3c). The downward TGF coincided with a large-amplitude pulse at the initial phase of the lightning discharge within 10 μs (Fig. 3d). We detected four or so precursory pulses shortly before the large-amplitude pulse. No pulses had been detected before the precursory pulses by the LF network. The ELF measurement also confirmed that the associated ELF pulse was coming from the LF source. In addition, JLDN also reported a negative intracloud/intercloud (IC) discharge of -197 kA at $t = -13$ μs, which is temporally associated with the large-amplitude pulse.

Figure 1b shows the source positions of the large-amplitude and precursory pulses determined by the LF network. At the beginning, the small precursory pulses took place in a southwest region less than 3 km away from detector B. Then, the main large-amplitude pulse (the fifth one in Figs. 1b and 3c) occurred 0.6 km southwest of detector B at $t = -5.5$ μs. JLDN also located the large-amplitude pulse within 0.9 km from detector B. These temporal and spatial correlations lead us to conclude that the large-amplitude LF pulse is associated with the downward TGF.

Production mechanism of gamma-ray glow. The multi-point observation enables us to investigate characteristics of the gamma-ray glow preceding the lightning initiation and the downward TGF. First, we perform spectral analysis. Figure 4 shows the background-subtracted gamma-ray energy spectra, extracted from -69 s $< t < -39$ s and -30 s $< t < -10$ s for detectors A and B, respectively. The detector response function is calculated with the GEANT4 Monte Carlo simulation framework[47], and is convolved with a model spectrum in spectral fitting using the XSPEC package[48]. The observed spectra, of which instrumental responses are corrected, are found to be well explained by an empirical power-law function with an exponential cutoff, $\varepsilon^{-\Gamma}\exp[(-\varepsilon/\varepsilon_{cut})^\alpha]$, where ε, Γ, ε_{cut}, and α are the photon energy (MeV), power-law photon index, cutoff energy (MeV), and cutoff index, respectively. The best-fitting parameters are $\Gamma = 0.90^{+0.06}_{-0.08}$ and $1.02^{+0.04}_{-0.05}$, $\varepsilon_{cut} = 6.4^{+1.0}_{-1.1}$ and $8.5^{+0.8}_{-0.9}$ MeV,
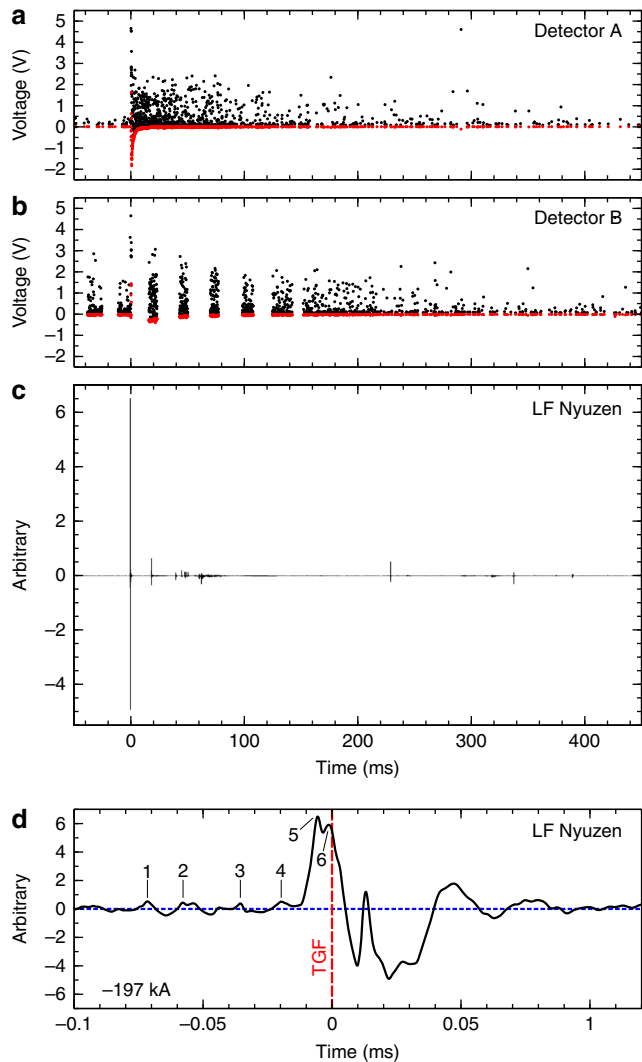

Fig. 3 Signature of downward terrestrial gamma-ray flash and associated lightning pulse. a, b Time histories of the (black) maximum and (red) minimum values of high-energy radiation waveforms recorded by detector A (**a**) and detector B (**b**). The minimum values normally present the baseline of the analogue waveforms. An energy of 10 MeV corresponds to 2.3 V in the normal (non-disturbed) operation condition. The time origin is at the TGF detection. **c** The low-frequency waveform (LF) of the lightning discharge recorded by the Nyuzen station (36.954°N, 137.498°N). The propagation time between the locations of the source of the large-amplitude pulse and the observation station is corrected. **d** LF waveform of the large-amplitude pulse associated with the downward TGF for a sub-millisecond period. Blue dashed line shows the waveform baseline. Number-assigned pulses are used for the location analysis

Fig. 4 Energy spectra of gamma-ray glow. Background-subtracted and deadtime-corrected energy spectra of the gamma-ray glow for the time region from -69 s $< t < -39$ s and -30 s $< t < -10$ s for detectors A (lower) and B (upper), respectively, where t is defined in text and is used in Fig. 2. The error of each data point is at 1σ confidence level. The spectrum of detector B is shifted upwards by a factor of 10 for visibility. The best-fitting model of the Monte Carlo simulation is overlaid with red dashed lines

$\alpha = 1.21^{+0.15}_{-0.14}$ and $1.43^{+0.15}_{-0.14}$, and the 0.4–20.0 MeV incident gamma-ray flux of $1.5^{+0.7}_{-0.5} \times 10^{-5}$ and $2.4^{+0.7}_{-0.6} \times 10^{-5}$ ergs cm^{-2} s^{-1} on average over $-69\,\text{s} < t < -39\,\text{s}$ and $-30\,\text{s} < t < -10\,\text{s}$ integration periods for detectors A and B, respectively. Here and after, all the errors are statistical at 1σ confidence level, unless otherwise mentioned.

We then perform another set of Monte Carlo simulations, using GEANT4, and compare the obtained energy spectra and count-rate histories with the simulated ones to investigate atmospheric interactions and propagation of electrons and gamma rays (see Simulation of gamma-ray glow). We find a model of spatial and energy spectral distribution for avalanche electrons in the RREA region which can reproduce both the obtained gamma-ray spectra and count-rate histories, and summarise the results in Figs. 1 and 4. The best-fit value of the RREA terminus altitude h_{base} is 400 m, which means the electron avalanche took place in the lower part of the winter thundercloud, and the offsets from the centre of the RREA region are 540 and 80 m for detectors A and B, respectively. The electron flux distribution is consistent with being proportional to a function of a distance from the RREA centre r, $\exp(-r/150\,\text{m})$, providing the circularly symmetric distribution. Figure 1b shows the centre position of the RREA region at the moment of the termination. Normalising the simulation result, we estimate the total production rate of 1–50 MeV avalanche electrons to be 3.66×10^{12} electrons s^{-1}. The electron flux $F(r, \varepsilon)$ at the terminus of RREA is also estimated to be a function of r and ε

$$F(r, \varepsilon) = 4.1 \times 10^2 \exp\left(-\frac{r}{150\,\text{m}}\right) \exp\left(-\frac{\varepsilon}{7.3\,\text{MeV}}\right) \text{electrons cm}^{-2}\,\text{s}^{-1}\,\text{MeV}^{-1}. \tag{1}$$

This model reproduces the observed count-rate histories and spectra, except the increase in the count rate of detector B during $-5\,\text{s} < t < 0\,\text{s}$. This period is discussed in the section Abrupt increase in count rates of gamma-ray glow before downward TGF.

Let us consider the electron multiplication factor $M = F_{\text{RREA}}/F_{\text{seed}}$, where F_{RREA} and F_{seed} are the average electron flux at the RREA terminus and seed electron flux, respectively. Integrating Eq. (1) yields the 0.3–50 MeV average flux within $r = 150\,\text{m}$ of $F_{\text{RREA}} = 7.5 \times 10^2$ electrons cm^{-2} s^{-1}. Assuming that the seed electrons are mainly produced by cosmic rays, the 0.3–50 MeV seed electron flux is a function of a vertical acceleration length L and h_{base} given by

$$F_{\text{seed}}(L) = 2.56 \times 10^{-3} \exp[(L + h_{\text{base}})/1890\,\text{m}]\text{electrons cm}^{-2}\,\text{s}^{-1} \tag{2}$$

(see Seed electrons). The multiplication factor M is thus a function of L, with the fixed h_{base} (400 m).

In the RREA region, electron flux is known to increase[39] exponentially as a function of L, $F_{\text{RREA}} = F_{\text{seed}} \exp(L/\lambda)$, assuming that change of the vertical atmospheric pressure is negligible for the RREA processes at the low altitude. The avalanche length λ is empirically determined (see ref. [49] and references therein) to be $\lambda = 7.3\,\text{MeV}/(eE - 0.276\,\text{MeV m}^{-1})$, where eE is a product of the elementary charge and strength of the electric field. The value of λ is then calculated to be 304, 99, and 59 m for $E = 0.3$, 0.35, and 0.4 MV m^{-1}, respectively. We note that the set of the trial values of E up to 0.4 MV m^{-1} we have assumed is suggested to be plausible inside thunderclouds[39]. Therefore, combining $M(L) = F_{\text{RREA}}/F_{\text{seed}}(L) = \exp(L/\lambda)$, L and M are derived to be $L = 3240$, 1160, and 710 m, $M = 4.3 \times 10^4$, 1.3×10^5, and 1.6×10^5 for $E = 0.3$, 0.35, and 0.4 MV m^{-1}, respectively.

As Dwyer[50] pointed out, the multiplication factor would not exceed $\sim 10^5$ in the RREA-only case because thunderclouds

cannot maintain an acceleration length required for it. Given that L can reach twice as high as the typical diameter of the RREA region[50], $L < 600\,\text{m}$ is required in this case, where the typical radius, $r = 150\,\text{m}$ is employed. The 0.3 MV m^{-1} case is not plausible because the required acceleration length $L = 3240\,\text{m}$ cannot be maintained inside the thundercloud. In the other cases, it is necessary to take into account the relativistic feedback processes to explain the estimated avalanche multiplication factor. The relativistic feedback processes are parameterised with a feedback factor γ, the fraction of the seed electrons provided by the steady-state relativistic feedback processes[50]. The flux of runaway electrons is then modified as $F_{\text{RREA}} = F_{\text{seed}}(L) \exp(L/\lambda)/(1 - \gamma)$. Figure 5 shows this relation between L and γ to explain the observed flux at the RREA terminus. To satisfy the condition $L < 600\,\text{m}$, γ should be larger than 0.998 and 0.846 for 0.35 and 0.4 MV m^{-1}, respectively. This suggests that the number of feedback-origin seed electrons is higher than that of cosmic-ray seed electrons by a factor of >5.5 for our event.

Abrupt increase in count rates of gamma-ray glow before TGF. The count-rate history of detector B exhibited an additional increase during $-5 < t < -0\,\text{s}$ (Fig. 6a). Figure 6b shows the ratio of the simulated model to the observed history. Although the observed history is well reproduced by the simulation up to $t = -5\,\text{s}$, the observed count rate is twice as high as the simulation in $-5\,\text{s} < t < -0\,\text{s}$. Figure 6c shows the three energy spectra extracted from the time regions of $-10\,\text{s} < t < -5\,\text{s}$, $-5\,\text{s} < t < -2\,\text{s}$, and $-2\,\text{s} < t < 0\,\text{s}$. All the spectra show a power-law function with an exponential cutoff, indicating that bremsstrahlung is still the main process of gamma-ray production. Since our simulations fail to reproduce this increase in count-rate, we speculate that the increase was caused by a fluctuation of the intrinsic electron fluxes, rather than by the movement of the RREA region with the ambient wind flow.

Based on the working hypothesis of the speculated increase of the accelerated electron flux, at least one of the following is required to have taken place: (1) stronger electric fields of the RREA region, (2) longer acceleration length, and/or (3) increase in the feedback factor γ. However, since lightning did not occur during this period ($-5\,\text{s} < t < 0\,\text{s}$), atmospheric mechanism could not drastically change the meteorological conditions, such as electric fields and acceleration length, within 5 s. We thus
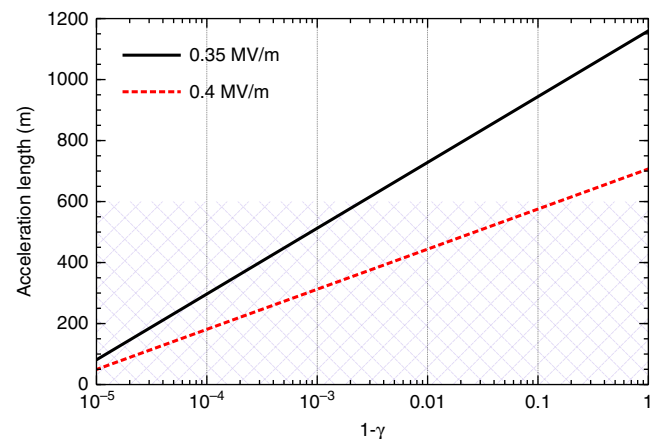

Fig. 5 Properties of relativistic runaway electron avalanche with relativistic feedback. The acceleration length as a function of the feedback factor γ. Black solid and red dashed lines indicate the cases with the electric field strengths of $E = 0.35$ and 0.4 MV m^{-1}, respectively. The blue-meshed region shows the plausible acceleration length in the case considered in this paper
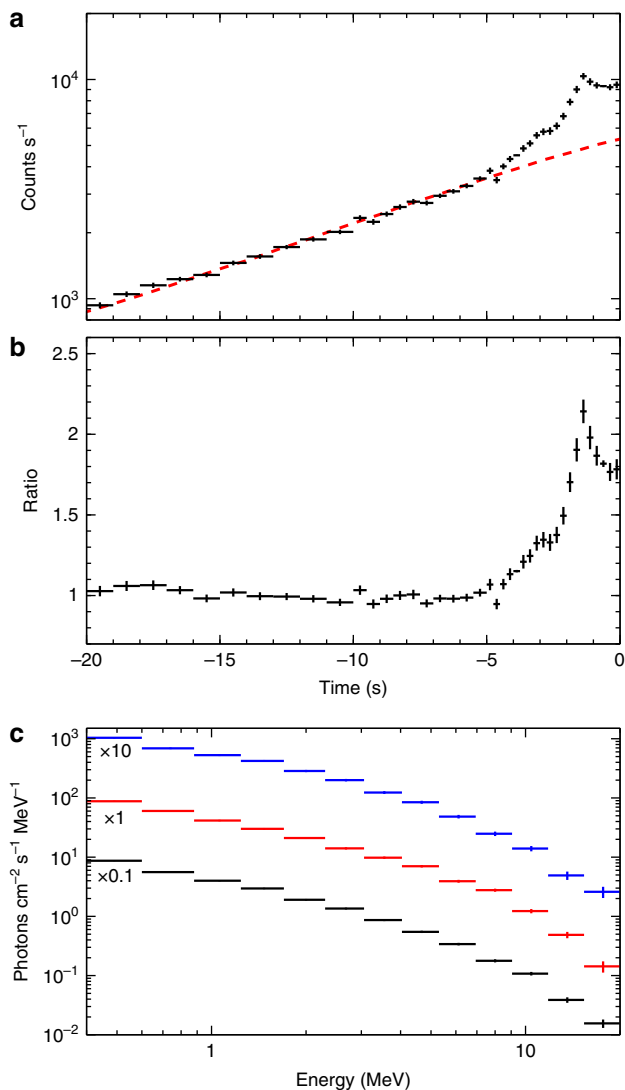
5

Fig. 6 Increase in count rates of detector B. **a** Comparison between the count-rate history of detector B and the exponential model (red dashed line). Background was subtracted. **b** Ratio of the Gaussian model to the observed count-rate history. **c** Background-subtracted spectra of detector B extracted from (black) $-10\,s < t < -5\,s$, (red) $-5\,s < t < -2\,s$, and (blue) $-2\,s < t < 0\,s$. The error of each data point is at 1σ confidence level. The spectra in $-10\,s < t < -5\,s$ and $-2\,s < t < 0\,s$ are shifted by a factor of 0.1 and 10, respectively, to avoid overlapping. Dead-time and detector responses are corrected

conjecture that temporal variations of the relativistic feedback processes played an important role for the electron flux increase, then the abrupt rise of gamma rays in the 5-s period before the lightning discharge. Assuming the electric field of $0.4\,MV\,m^{-1}$, the doubled rate of avalanche electrons can be explained by increasing γ from 0.846 to 0.923.

The RREA and relativistic feedback processes remained stable until $t = -5\,s$; this state corresponds to the "steady state" of relativistic feedback as defined by Dwyer[50], namely $\gamma < 1$. In general, when γ exceeds 1, an electron flux would spontaneously increase, and an RREA region should collapse. The timescale of the flux increase depends on the types of the relativistic feedback processes. The feedback process by positrons can discharge RREA regions within microseconds[50]. This timescale is close to that of TGFs, and is much shorter than that of the observed abrupt increase (i.e. 5 s). Alternatively, the feedback by backscattered

X-rays may trigger a second-order discharge in RREA regions[50]. At present, even though the 5-s abrupt flux rise seems to be of great importance, its origin is yet to be understood.

Discussion

To conclude the relation between the gamma-ray glow and the downward TGF, verifying their temporal and positional coincidence will give a strong clue. Our observation cannot clarify whether the glow termination or the downward TGF took place first because these phenomena seemed to be slightly overlapped. On the other hand, the positional coincidence of the gamma-ray glow and the downward TGF in the present case is precisely determined owing to the multiple gamma-ray detectors and the LF network. The discussion in the section Production mechanism of gamma-ray glow suggests that the gamma-ray glow ceased when the source cloud was moving 130 m southwest of detector B (Fig. 1b). Also, the TGF-associated LF pulse was located within 0.5 km from detector B. Therefore, it is clear that the two phenomena are physically related to one another.

Our interpretation of the observed gamma-ray glow suggests that the electron acceleration site should have electric fields of $0.35\,MV\,m^{-1}$ or higher in order to achieve the high electron multiplication factor of $>10^5$ with a plausible acceleration length. In such highly electrified regions, TGFs are thought to initiate more easily than in other less-electrified regions as Smith et al.[17] suggested. From another point of view, we speculate that the avalanche electrons of the gamma-ray glow can behave as seed electrons of the downward TGF. At the point where the TGF-associated LF pulse was located (point 5 in Fig. 1b), the 0.3–50 MeV electron flux at 400 m altitude is estimated to be 1.7×10^2 electrons $cm^{-2}\,s^{-1}$. By comparing this flux with that of the cosmic-ray-induced seed electrons (the canonical seed electron source), it is suggested that the highly-electrified region responsible for the gamma-ray glow can be the dominant source of seed electrons for the TGF which occurs in the close proximity of the gamma-ray glow. In addition, the abrupt count-rate increase monitored by detector B before the TGF (see section Abrupt increase in count rates of gamma-ray glow before downward TGF) suggests additional production of avalanche electrons for the gamma-ray glow, and might have predicted drastic changes in the electrified region such as the lightning discharge and the TGF.

In the present high-energy event, the discussion above suggests a possibility that the high electron current in the gamma-ray glow assisted the initiation of the downward TGF. However, it still remains observationally unclear how gamma-ray glows and TGFs are related with each other in general. Among an increasing sample of glow terminations, TGF-associated events are still quite rare, i.e. only Smith et al.[17] and the present event. For example, a termination event during a winter thunderstorm in 2017 (ref. [38]) was associated with an intracloud/intercloud discharge but not related with any signals for TGF-like emissions. As another example, a TGF-like intensive emission associated with photonuclear reactions was reported[14], where no gamma-ray glows were recorded before the event. In these cases, we lack sufficient evidences due to our present sparse observation sites on the ground to conclude that glow terminations are not always associated with TGFs. Our future gamma-ray monitoring network combined with radio-frequency lightning mapping systems will give a clue to reveal the relation between TGFs and gamma-ray glows.

In summary, we detected a gamma-ray glow, terminated with a downward TGF which triggered atmospheric photonuclear reactions. The gamma-ray glow was so bright that the relativistic feedback processes are required. Although we cannot determine whether the glow termination or the downward TGF occurred

first, the two high-energy phenomena in the atmosphere took place in an identical electrified region of a winter thundercloud, and hence are clearly related to each other in the present case.

Methods

Detector calibration. Energy calibration of the detectors was performed to convert the maximum value of a pulse into photon energy. We measured the centre of environmental background lines of ^{40}K (1.46 MeV) and ^{208}Tl (2.61 MeV), and built a linear calibration function which is utilised to assign the energy of each photon. All the detectors record 0.4–20.0 MeV gamma rays. See also Instrumental calibration in Enoto et al.[14] for details.

Absolute timing is conditioned by pulse-per-second signals of the Global Positioning System (GPS). The timing-assignment logic employed from 2017 to 2018 winter provides absolute timing accuracy of each photon better than 1 μs. However, detector A failed to receive the GPS signals during the experiment. Instead, we performed the calibration of detector A, using the internal clock time with ~1 s accuracy, and then corrected the absolute timing so that the detection time of the downward TGF matches that with detector B.

Wind estimation with X-band radar. We utilised data of eXtended RAdar Information Network (XRAIN). XRAIN is a polarimetric weather radar network in the X band and has a spatial resolution of 280 m (east–west) × 230 m (north–south) mesh. It records two-dimensional precipitation maps with a 1-min interval. XRAIN also obtains three-dimensional maps of radar echoes and particle types with a 5-min interval by the constant-altitude plan position indicator technique. However, the three-dimensional data are not utilised in the present paper because the XRAIN observations have a moderate spatial resolution of altitude (≥1 km), which is insufficient to discuss charge structures in the thundercloud.

Wind velocity and direction are estimated by overlaying and shifting precipitation maps at different time. First, 11 maps from 17:50 to 18:00 were extracted in the range of 36.4°N–36.7°N, 136.4°E–136.8°E. We then took a pair of maps with a 5-min interval (six pairs in total), and calculated the sum of precipitation residual at each mesh, given by $\Sigma_{i,j}(P_{ij}^1 - P_{ij}^2)^2$, where P_{ij}^1 and P_{ij}^2 are precipitation at each mesh on each map, and i and j are mesh indexes. With trial shifting of one map with several steps of the spatial resolution for four directions, we searched for the position which takes the minimum residual sum. The distance and direction for which the cloud moved in 5 min can be estimated from the amount of the map shift at the point of the minimum residual sum. Consequently, the wind direction and velocity at the moment of the glow detection were determined to be west-northwestwards and 19.3 ± 0.9 (systematic) ± 1.1 (statistic) m s^{-1}, respectively. Here, the quoted statistical error was calculated from the standard deviation (1σ) of six pairs. The systematic error was determined by the mesh size and temporal interval of the map pair. The wind velocity with the overall error is then calculated to be 19.3 ± 1.4 m s^{-1}, where the standard error propagation in quadrature between the systematic and statistical errors is assumed to hold. Since the statistic error is smaller than 10% and is comparable with the systematic error, it is reasonable to assume that the wind parameters did not change considerably during the glow observation.

Gamma-ray emission originating from neutrons. Photonuclear reactions such as $^{14}N + \gamma \rightarrow {}^{13}N + n$ and $^{16}O + \gamma \rightarrow {}^{15}O + n$ expel ~10 MeV neutrons from atmospheric nitrogen and oxygen nuclei[51–53]. The photoneutrons gradually lose their kinetic energy via elastic scatterings, and are eventually captured by atmospheric nuclei such as ^{14}N. In the dominant reaction $^{14}N + n \rightarrow {}^{15}N + \gamma$, ^{15}N nuclei in excited states emit various de-excitation gamma-ray lines up to 10.8 MeV. In addition, de-excitation gamma rays from other nuclei such as Si and Al should be also emitted when photoneutrons were captured by ambient nuclei in soil, buildings, and components of the detectors. These de-excitation gamma rays originating from neutron captures are thought to compose the short burst[13,18].

The timescale of the short burst is determined by neutron thermalisation[13,14,18]. A numerical calculation predicts the neutron-capturing rate of $\exp(-t/\tau)$ for 5 ms < t < 120 ms, where t is the elapsed time from the onset of the TGF and τ ≈ 56 ms is the decay constant[14]. The count-rate histories of the observed burst have decay constants of 52.0 ± 4.9 and 59.2 ± 1.7 ms for detectors A and B, respectively. These results are consistent with the calculation.

Supplementary Fig. 1 shows the energy spectra of the burst with detectors A and B. Enoto et al.[14] simulated the de-excitation emission, considering atmospheric scattering of the gamma rays and moderate energy resolution of BGO crystals. The emission model from ^{15}N and ambient nuclei, such as Al and Si, well reproduces the results of both detectors A and B. From the spectral and temporal analyses, we confirm that the observed short burst is caused by neutrons produced via atmospheric photonuclear reactions.

Positron production by beta-plus decay. After neutrons are expelled from ^{14}N and ^{16}O, unstable nuclei ^{13}N and ^{15}O start emitting positrons via β+ decay with half-lives of 10 and 2 min, respectively. Positrons immediately annihilate and emit 511 keV annihilation gamma rays. Supplementary Fig. 2a–d shows count-rate histories in the 0.4–0.65 and 0.65–30.0 MeV bands. Whereas detector A recorded

no enhancements after the short burst, detector B recorded an afterglow in the 0.4–0.65 MeV band for the period 0 s < t < 10 s. The count rates decreased with a decay constant of 6.0 ± 2.1 s. The background-subtracted photon count in the 0.4–0.65 MeV band for 1 s < t < 10 s is $(2.0 ± 0.4) \times 10^2$ photons. The background-subtracted energy spectrum is shown in Supplementary Fig. 2e. The centre energy of the line emission is 528 ± 14 keV, which is consistent with 511 keV of the annihilation line within error.

These results lead us to conclude that a positron-emitting region filled with ^{13}N and ^{15}O were produced in the atmosphere by the photonuclear reactions, and then passed over detector B flown by the ambient wind flow[14]. Considering that the count-rate history shows a monotonic decrease, the positron source might be generated somewhere above detector B or downwind.

Radio observations. The LF network has five stations (Supplementary Fig. 3a). Each station has a flat plate antenna sensitive to 0.8–500 kHz. Analogue outputs from the antenna are sampled by a 4 MHz digitiser, whose absolute timing is calibrated with the GPS signals. The LF network can locate radio pulses with the time-of-arrival technique. Supplementary Fig. 3b, c shows the entire LF waveforms of the observed lightning discharge.

The ELF receiver is installed in Kuju (33.059°N, 131.233°E) as a station of the Global ELF Observation Network operated by Hokkaido University. The station has two horizontal search coil magnetometers sensitive to 1–100 Hz magnetic-field perturbations in the east–west and north–south directions. The analogue output is sampled by a 400 Hz digitiser. The direction-of-arrival of the ELF pulses can be confirmed with the magnetic-detection-finder technique. Supplementary Fig. 3d shows the observed waveform in the ELF band.

The JLDN reported two other discharges besides the TGF-associated radio-frequency pulse: an IC of −14 kA at t = 18.7 ms and a CG of −13 kA at t = 228.6 ms. Supplementary Fig. 3b, c shows the corresponding LF pulses. Since these pulses occurred long after the observed TGF, we consider that they were not associated with the high-energy phenomena.

Simulation of gamma-ray glow. We performed Monte Carlo simulations of electron propagation in the atmosphere to reproduce the count-rate histories and energy spectra, using GEANT4 (ref. [47]). We assume that electron avalanches towards the ground developed in thundercloud, and that the electron spectrum of the RREA at the end of the region has the shape of $\exp(-\varepsilon/7.3$ MeV$)$[49], where ε is the electron energy. We also assume that the distribution of the electron flux in the avalanche region is circularly symmetric and has no intrinsic time fluctuation. These assumption should be reasonable, given that the count-rate history of detector A is symmetric about the peak, and that the wind velocity was approximately constant (see Wind estimation with X-band radar).

The energy spectra of bremsstrahlung gamma rays from the avalanche electrons approximately follow $\varepsilon^{-\Gamma}\exp(-\varepsilon/7.3$ MeV$)$[54]. The photon index Γ is determined from the source altitude h and offset from the source centre. Count-rate histories depend on the size of the RREA region, wind velocity, and h. The distribution of gamma rays is more diffuse at a higher source altitude due to atmospheric scattering, hence resulting in a longer and fainter gamma-ray glow.

First, we tested a disk-like region with a uniform electron flux, varying h and disk radius in our simulations. Supplementary Fig. 4a shows some examples of the simulation results at various altitudes. Comparing the simulation results with the observation, $h = 1500$ m is required to reproduce the observed count-rate histories, whereas Γ of the energy spectra indicates $h = 900$ m. Since any other conditions cannot satisfy both the spectra and count-rate histories, this uniformed-disk model is thus rejected in this analysis.

Then, we considered two disk-like models in which the spatial distribution of the electron flux follows either of the two functions of a distance from the RREA centre l: a Gaussian model, $\exp(-l^2/2\sigma^2)$ and an exponential model, $\exp(-l/L)$. The parameters σ and L are free parameters, which denote the spatial extent of the surface brightness of the emission.

We found that both models can reproduce the obtained count-rate histories and spectra; The estimated parameters are $h = 600$ m and $\sigma = 200$ m for the Gaussian model, and $h = 400$ m and $L = 150$ m for the exponential model. Comparing these two best models, we found that the exponential model explains the observation better, particularly for the count-rate histories of detector B (Supplementary Fig. 4b). Therefore, we employ the exponential model as a working hypothesis to interpret the observation.

Seed electrons. We assume that the seed electrons of the RREA processes are mainly produced by cosmic rays. To calculate the electron fluxes of secondary cosmic rays, we employed Excel-based Program for calculating Atmospheric Cosmic-ray Spectrum (EXPACS)[55,56], which calculates the flux and spectrum of cosmic-ray particles as a function of an altitude, latitude, longitude, and solar modulation. We extracted electron spectra at an altitude h of 300–2000 m, and then integrated the spectra to obtain the electron fluxes F_{seed} in the energy range of 0.3–50.0 MeV. The electron flux was found to increase exponentially as a positive function of altitude, given by $F_{seed} = 2.56 \times 10^{-3} \times \exp(h/1890$ m$)$ electrons cm^{-2} s^{-1}.

Carlson et al.[57] have considered 1 MeV seed electrons produced by cosmic rays. Kelley et al.[22] employed it, and derived the seed flux to be 0.25 cm^{-2} s^{-1} at

14.1 km. Our calculation with EXPACS gives the electron flux at 14.1 km of $0.86\,cm^{-2}\,s^{-1}$. Given that Carlson et al. took a more thorough approach than ours by simulating the effective seeding efficiency for various particles, energies, and geometries, our method might have overestimated the seed electron flux. Regardless of the potential errors in our method, our conclusion that the gamma-ray glow requires relativistic feedback is unaffected, because overestimation of the seed flux, even if it was the case, would result in an underestimation of the multiplication factor.

Data Availability

The data sets generated and analysed during the current study are available from the corresponding author on request.

References

1. McCarthy, M. & Parks, G. K. Further observations of x-rays inside thunderstorms. *Geophys. Res. Lett.* **12**, 393–396 (1985).
2. Fishman, G. J. et al. Discovery of intense gamma-ray flashes of atmospheric origin. *Science* **264**, 1313–1316 (1994).
3. Smith, D. M., Lopez, L. I., Lin, R. P. & Barrington-Leigh, C. P. Terrestrial gamma-ray flashes observed up to 20 mev. *Science* **307**, 1085–1088 (2005).
4. Marisaldi, M. et al. Detection of terrestrial gamma ray flashes up to 40 mev by the agile satellite. *J. Geophys. Res. Space Phys.* **115**, https://doi.org/10.1029/2009JA014502 (2010).
5. Briggs, M. S. et al. First results on terrestrial gamma ray flashes from the fermi gamma-ray burst monitor. *J. Geophys. Res. Space Phys.* **115**, https://doi.org/10.1029/2009JA015242 (2010).
6. Briggs, M. S. et al. Electron-positron beams from terrestrial lightning observed with fermi gbm. *Geophys. Res. Lett.* **38**, https://doi.org/10.1029/2010GL046259 (2011).
7. Tavani, M. et al. Terrestrial gamma-ray flashes as powerful particle accelerators. *Phys. Rev. Lett.* **106**, https://doi.org/10.1103/PhysRevLett.106.018501 (2011).
8. Mailyan, B. G. et al. The spectroscopy of individual terrestrial gamma-ray flashes: constraining the source properties. *J. Geophys. Res. Space Phys.* **121**, 11363–11363 (2016).
9. Dwyer, J. R. et al. A ground level gamma-ray burst observed in association with rocket-triggered lightning. *Geophys. Res. Lett.* **31**, https://doi.org/10.1029/2003GL018771 (2004).
10. Dwyer, J. R. et al. Observation of a gamma-ray flash at ground level in association with a cloud-to-ground lightning return stroke. *J. Geophys. Res. Space Phys.* **117**, https://doi.org/10.1029/2012JA017810 (2012).
11. Tran, M. et al. A terrestrial gamma-ray flash recorded at the lightning observatory in Gainesville, Florida. *J. Atmos. Sol. Terr. Phys.* **136**, 86–93 (2015).
12. Hare, B. M. et al. Ground-level observation of a terrestrial gamma ray flash initiated by a triggered lightning. *J. Geophys. Res. Atmospheres* **121**, 6511–6533 (2016).
13. Bowers, G. S. et al. Gamma ray signatures of neutrons from a terrestrial gamma ray flash. *Geophys. Res. Lett.* **44**, 10063–10070 (2017).
14. Enoto, T. et al. Photonuclear reactions triggered by lightning discharge. *Nature* **551**, 481–484 (2017).
15. Abbasi, R. et al. The bursts of high energy events observed by the telescope array surface detector. *Phys. Lett. A* **381**, 2565–2572 (2017).
16. Abbasi, R. U. et al. Gamma ray showers observed at ground level in coincidence with downward lightning leaders. *J. Geophys. Res. Atmospheres* **123**, 6864–6879 (2018).
17. Smith, D. M. et al. Characterizing upward lightning with and without a terrestrial gamma-ray flash. *J. Geophys. Res. Atmospheres*, https://doi.org/10.1029/2018jd029105 (2018).
18. Rutjes, C., Diniz, G., Ferreira, I. S. & Ebert, U. Tgf afterglows: a new radiation mechanism from thunderstorms. *Geophys. Res. Lett.* **44**, 10702–10712 (2017).
19. Torii, T., Sugita, T., Kamogawa, M., Watanabe, Y. & Kusunoki, K. Migrating source of energetic radiation generated by thunderstorm activity. *Geophys. Res. Lett.* **38**, https://doi.org/10.1029/2011GL049731 (2011).
20. Chilingarian, A., Hovsepyan, G. & Hovhannisyan, A. Particle bursts from thunderclouds: natural particle accelerators above our heads. *Phys. Rev. D* **83**, https://doi.org/10.1103/PhysRevD.83.062001 (2011).
21. Eack, K. B., Beasley, W. H., Rust, W. D., Marshall, T. C. & Stolzenburg, M. Initial results from simultaneous observation of x-rays and electric fields in a thunderstorm. *J. Geophys. Res. Atmospheres* **101**, 29637–29640 (1996).
22. Kelley, N. A. et al. Relativistic electron avalanches as a thunderstorm discharge competing with lightning. *Nat. Commun.* **6**, 7845 (2015).
23. Kochkin, P. et al. In-flight observation of gamma ray glows by ildas. *J. Geophys. Res. Atmospheres*, https://doi.org/10.1002/2017JD027405 (2017).
24. Brunetti, M., Cecchini, S., Galli, M., Giovannini, G. & Pagliarin, A. Gamma-ray bursts of atmospheric origin in the mev energy range. *Geophys. Res. Lett.* **27**, 1599–1602 (2000).
25. Torii, T. et al. Gradual increase of energetic radiation associated with thunderstorm activity at the top of Mt. Fuji. *Geophys. Res. Lett.* **36**, https://doi.org/10.1029/2008GL037105 (2009).
26. Tsuchiya, H. et al. Observation of an energetic radiation burst from mountain-top thunderclouds. *Phys. Rev. Lett.* **102**, https://doi.org/10.1103/PhysRevLett.102.255003 (2009).
27. Tsuchiya, H. et al. Observation of thundercloud-related gamma rays and neutrons in Tibet. *Phys. Rev. D* **85**, https://doi.org/10.1103/PhysRevD.85.092006 (2012).
28. Chilingarian, A. et al. Ground-based observations of thunderstorm-correlated fluxes of high-energy electrons, gamma rays, and neutrons. *Phys. Rev. D* **82**, https://doi.org/10.1103/PhysRevD.82.043009 (2010).
29. Chilingarian, A., Hovsepyan, G. & Mnatsakanyan, E. Mount Aragats as a stable electron accelerator for atmospheric high-energy physics research. *Phys. Rev. D* **9**, https://doi.org/10.1103/PhysRevD.93.052006 (2016).
30. Torii, T., Takeishi, M. & Hosono, T. Observation of gamma-ray dose increase associated with winter thunderstorm and lightning activity. *J. Geophys. Res. Atmospheres* **107**, ACL 2-1–ACL 2-13 (2002).
31. Tsuchiya, H. et al. Detection of high-energy gamma rays from winter thunderclouds. *Phys. Rev. Lett.* **99**, https://doi.org/10.1103/PhysRevLett.99.165002 (2007).
32. Tsuchiya, H. et al. Long-durationÎ³ray emissions from 2007 and 2008 winter thunderstorms. *J. Geophys. Res.* **116**, https://doi.org/10.1029/2010JD015161 (2011).
33. Kuroda, Y. et al. Observation of gamma ray bursts at ground level under the thunderclouds. *Phys. Lett. B* **758**, 286–291 (2016).
34. Alexeenko, V., Khaerdinov, N., Lidvansky, A. & Petkov, V. Transient variations of secondary cosmic rays due to atmospheric electric field and evidence for pre-lightning particle acceleration. *Phys. Lett. A* **301**, 299–306 (2002).
35. Tsuchiya, H. et al. Hardening and termination of long-durationÎ³rays detected prior to lightning. *Phys. Rev. Lett.* **111**, https://doi.org/10.1103/PhysRevLett.111.015001 (2013).
36. Chilingarian, A., Hovsepyan, G., Khanikyanc, G., Reymers, A. & Soghomonyan, S. Lightning origination and thunderstorm ground enhancements terminated by the lightning flash. *Europhys. Lett.* **110**, 49001 (2015).
37. Chilingarian, A. et al. Types of lightning discharges that abruptly terminate enhanced fluxes of energetic radiation and particles observed at ground level. *J. Geophys. Res. Atmospheres* **122**, 7582–7599 (2017).
38. Wada, Y. et al. Termination of electron acceleration in thundercloud by intracloud/intercloud discharge. *Geophys. Res. Lett.* **45**, 5700–5707 (2018).
39. Gurevich, A., Milikh, G. & Roussel-Dupre, R. Runaway electron mechanism of air breakdown and preconditioning during a thunderstorm. *Phys. Lett. A* **165**, 463–468 (1992).
40. Dwyer, J. R. A fundamental limit on electric fields in air. *Geophys. Res. Lett.* **30**, https://doi.org/10.1029/2003GL017781 (2003).
41. Wilson, C. T. R. The acceleration of Î²-particles in strong electric fields such as those of thunderclouds. *Math. Proc. Cambr. Philos. Soc.* **22**, 534 (1925).
42. Dwyer, J. R. The relativistic feedback discharge model of terrestrial gamma ray flashes. *J. Geophys. Res. Space Phys.* **117**, https://doi.org/10.1029/2011JA017160 (2012).
43. Umemoto, D. et al. On-ground detection of an electron-positron annihilation line from thunderclouds. *Phys. Rev. E* **93**, https://doi.org/10.1103/PhysRevE.93.021201 (2016).
44. Enoto, T. et al. Multi-point measurement campaigns of gamma rays from thunderclouds and lightning in Japan. In *Proc. XVI International Conference on Atmospheric Electricity* (2018).
45. Goto, Y. & Narita, K. Observations of winter lightning to an isolate tower. *Res. Lett. Atmos. Electr.* **12**, 57–60 (1992).
46. Rakov, V. A. & Uman, M. A. *Lightning: Physics and Effects* (Cambridge University Press, Cambridge, 2003).
47. Agostinelli, S. et al. Geant4—a simulation toolkit. *Nucl. Instrum. Methods Phys. Res. A* **506**, 250–303 (2003).
48. Arnaud, K. A. XSPEC: the first ten years. In *Astronomical Data Analysis Software and Systems V*, vol. 101 of *Astronomical Society of the Pacific Conference Series* (eds. Jacoby, G. H. & Barnes, J.), 17 (1996). http://adsabs.harvard.edu/abs/1996ASPC..101...17A.
49. Dwyer, J. R. & Babich, L. P. Low-energy electron production by relativistic runaway electron avalanches in air. *J. Geophys. Res. Space Physics* **116**, https://doi.org/10.1029/2011JA016494 (2011).
50. Dwyer, J. R. Relativistic breakdown in planetary atmospheres. *Phys. Plasmas* **14**, 042901 (2007).

51. Babich, L. P. Generation of neutrons in giant upward atmospheric discharges. *JETP Lett.* **84**, 285–288 (2006).
52. Babich, L. P. Neutron generation mechanism correlated with lightning discharges. *Geomagn. Aeron.* **47**, 664–670 (2007).
53. Carlson, B. E., Lehtinen, N. G. & Inan, U. S. Neutron production in terrestrial gamma ray flashes. *J. Geophys. Res. Space Phys.* **115**, https://doi.org/10.1029/2009JA014696 (2010).
54. Dwyer, J. R., Smith, D. M. & Cummer, S. A. High-energy atmospheric physics: terrestrial gamma-ray flashes and related phenomena. *Space Sci. Rev.* **173**, 133–196 (2012).
55. Sato, T. Analytical model for estimating terrestrial cosmic ray fluxes nearly anytime and anywhere in the world: extension of parma/expacs. *PLoS ONE* **10**, e0144679 (2015).
56. Sato, T. Analytical model for estimating the zenith angle dependence of terrestrial cosmic ray fluxes. *PLoS ONE* **11**, e0160390 (2016).
57. Carlson, B. E., Lehtinen, N. G. & Inan, U. S. Runaway relativistic electron avalanche seeding in the earth's atmosphere. *J. Geophys. Res. Space Phys.* **113**, https://doi.org/10.1029/2008JA013210 (2008).

Acknowledgements

Author contributions

Y.W., T.E., Y.F., T.Y., K.N., T. Matsumoto, and H.T. were responsible for the radiation detector developments, data analysis, and interpretation; T.E. is the project leader of the multi-point observation; Y.W. led the detector development, installation, analysis, simulations, and prepared the draft of the manuscript; Y.F. verified the Monte Carlo simulations using Geant4; T.Y. led the development of the data acquisition system; Y.N. and T. Morimoto were responsible for the LF observation; M.S. was responsible for the ELF observation; D.Y. and T.S contributed to the radiation detector operation; H.S. contributed to operation of the LF stations; K.N., M.K., T.U., K.M., and H.T contributed to the data interpretation.

Additional information

Publisher's note: Springer Nature remains neutral with regard to jurisdictional claims in published maps and institutional affiliations.